Measurement of the Neutron-Decay Lifetime of the ^{26}O Ground State

Messung der Lebensdauer des über Neutronenemission zerfallenden Grundzustands von ^{26}O
Zur Erlangung des Grades eines Doktors der Naturwissenschaften (Dr. rer. nat.)
Genehmigte Dissertation von Sonja Storck-Dutine aus Groß-Umstadt
Tag der Einreichung: 07.02.2023, Tag der Prüfung: 17.04.2023

1. Gutachten: Prof. Dr. Thomas Aumann
2. Gutachten: Prof. Alexandre Obertelli, Ph.D.
Darmstadt, Technische Universität Darmstadt – D17

TECHNISCHE UNIVERSITÄT DARMSTADT

Fachbereich Physik
Institut für Kernphysik
AG Aumann

Measurement of the Neutron-Decay Lifetime of the ^{26}O Ground State
Messung der Lebensdauer des über Neutronenemission zerfallenden Grundzustands von ^{26}O

Genehmigte Dissertation von Sonja Storck-Dutine

1. Gutachten: Prof. Dr. Thomas Aumann
2. Gutachten: Prof. Alexandre Obertelli, Ph.D.

Tag der Einreichung: 07.02.2023
Tag der Prüfung: 17.04.2023

Darmstadt, Technische Universität Darmstadt – D17

Bitte zitieren Sie dieses Dokument als:
URN: urn:nbn:de:tuda-tuprints-237685
URL: http://tuprints.ulb.tu-darmstadt.de/23768

Dieses Dokument wird bereitgestellt von TUprints,
E-Publishing-Service der TU Darmstadt
http://tuprints.ulb.tu-darmstadt.de
tuprints@ulb.tu-darmstadt.de
Jahr der Veröffentlichung der Dissertation auf TUprints: 2023

Abstract

The ground state of the two-neutron unbound nucleus ^{26}O has been speculated to have a rather long lifetime, in the picosecond regime, which would introduce potentially the first observation of a two-neutron radioactive decay. Previous measurements were able to place the lifetime at $6.5^{+4.6}_{-4.8}$ ps [Koh+13] and $7.2^{+3.5}_{-4.1}$ ps [Red19], though with large uncertainties. In order to determine the decay lifetime of the ^{26}O ground state with high sensitivity and precision, a new method has been applied.

The experiment presented in this work was performed at the Superconducting Analyzer for MUlti-particles from RAdio Isotope Beams (SAMURAI) at the Rare Isotope Beam Factory (RIBF) at RIKEN, Japan. A ^{27}F beam was produced in the fragment separator BigRIPS and impinged on a specially designed target, consisting of tungsten and platinum sheets, where ^{26}O was produced via a proton-knockout reaction. Following its lifetime, ^{26}O decayed into the ^{24}O fragment and two neutrons all measured in coincidence. The observable used in the measurement, which is sensitive to the lifetime, was the velocity difference between the fragment and the neutrons. The ratio between the number of decays occurring inside and outside of the target sheets changes according to the lifetime, strongly affecting the shape of the spectrum. Thus, the measured velocity difference delivers a characteristic spectrum from which the lifetime can be extracted.

The calibration and analysis techniques used in this work are presented in detail. In particular, a dedicated GEANT4 simulation was performed, where the full reaction process is modeled from the experimental setup with the lifetime as an input parameter. The proton knockout as well as the decay are considered, where the fragment recoil momentum is treated realistically according to theoretical calculations. Finally, the lifetime is extracted from the measured spectrum by comparison to simulated spectra. With this approach, a new upper limit on the ^{26}O lifetime could be determined with $\tau < 2.8$ ps at 5σ confidence level. A lifetime of $\tau = 0$ ps lies within the 1σ uncertainties ($\tau < 0.9$ ps) and therefore the observation of a two-neutron radioactivity of ^{26}O cannot be confirmed.

Zusammenfassung

Nach aktuellen Untersuchungen könnte der Grundzustand des ungebundenen Kerns von ^{26}O eine vergleichsweise lange Lebensdauer im Pikosekundenbereich haben. Damit eröffnet sich die Möglichkeit den ersten Fall von Zwei-Neutronen-Radioaktivität zu beobachten. Vorangegangene Messungen konnten die Lebensdauer eingrenzen zu $6.5^{+4.6}_{-4.8}$ ps [Koh+13] und $7.2^{+3.5}_{-4.1}$ ps [Red19], jedoch mit großen Unsicherheiten. Es wurde nun eine neue Methode angewandt, um die Lebensdauer des ^{26}O-Grundzustands präzise und mit hoher Sensitivität zu bestimmen.

Das in dieser Arbeit vorgestellte Experiment wurde am Superconducting Analyzer for MUlti-particles from RAdio Isotope Beams (SAMURAI) Aufbau am Rare Isotope Beam Factory (RIBF) am RIKEN, Japan, durchgeführt. Dabei wurde ein ^{27}F-Strahl im Fragmentseparator BigRIPS erzeugt und auf ein speziell entwickeltes Target aus Wolfram- und Platinplättchen geschossen, in denen ^{26}O durch eine Protonen-Knockout-Reaktion erzeugt wurde. Das entstandene ^{26}O zerfiel entsprechend der Lebensdauer in ein ^{24}O-Fragment sowie zwei Neutronen und alle Reaktionspartner wurden in Koinzidenz gemessen. Die Differenz der Geschwindigkeiten zwischen Neutronen und Fragment ist sensitiv auf die Lebensdauer von ^{26}O und diente in dieser Messung als Observable. Das Verhältnis der Zerfälle innerhalb und außerhalb der einzelnen Targetplättchen ist stark von der Lebensdauer abhängig und führt zu einem charakteristischen Geschwindigkeitsdifferenzspektrum, aus dem die Lebensdauer bestimmt werden kann.

In der vorgelegten Arbeit werden die verwendeten Kalibrierungen und Analysetechniken detailliert vorgestellt. Insbesondere wurde eine GEANT4-Simulation durchgeführt, die den gesamten Reaktionsprozess anhand des experimentellen Aufbaus nachbildet und in der eine Lebensdauer als Eingangsgröße angegeben werden kann. Die Protonen-Knockout-Reaktion als auch der Zerfall werden berücksichtigt und der Impulsübertrag auf das Fragment aufgrund des Rückstoßes wird anhand theoretischer Berechnungen mit einbezogen. Die Lebensdauer kann schlussendlich aus dem Vergleich des gemessenen und der simulierten Geschwindigkeitsdifferenzspektren extrahiert werden.

Mit dieser Methode konnte eine neue Obergrenze innerhalb des 5σ-Konfidenzintervalls für die Lebensdauer von ^{26}O bestimmt werden zu $\tau < 2.8$ ps. Eine Lebensdauer von $\tau = 0$ ps liegt innerhalb der 1σ-Unsicherheit ($\tau < 0.9$ ps) weshalb eine Beobachtung der Zwei-Neutronen-Radioaktivität nicht bestätigt werden kann.

Contents

1. Introduction

In the Geiger-Marsden experiments in the early 20$^{\text{th}}$ century, α-particles were scattered off a gold foil, leading to the discovery of the atomic nucleus [Rut11] and launching the new research field of nuclear physics. A nucleus is uniquely characterized by its number of protons and neutrons, the building blocks of nuclei. Over the years, more than 3000 nuclei were identified which occur either naturally on earth or were produced in the laboratory. Less than 300 of these nuclei are stable and the vast majority undergo radioactive decays by the emission of particles or spontaneously break into smaller constituents through fission.

Nowadays, most of the newly discovered nuclei are located far away from the valley of stability. The driving question of nuclear structure studies is to explore the limits of the nuclear landscape, *i.e.*, investigating how many protons and neutrons can be added to a nucleus until they are not bound any more. The limits of stability of nuclei are referred to as the proton and neutron drip lines. Here, the binding energy becomes negative and nucleons can escape the nucleus. The drip line on the neutron-deficient side of the nuclear chart is experimentally better explored since it is located closer to the valley of stability as compared to the neutron drip line. It is experimentally established up to neptunium ($Z = 93$) [Zha+19]. On the neutron-rich side most neutron numbers are experimentally not accessible, motivating the development of next-generation radioactive ion beam facilities [Pfü13]. The neutron drip line is experimentally only established up to neon ($Z = 10$) [Ahn+19]. According to theory predictions, the neutron drip line is located far away from the valley of stability. Around 6000 bound nuclei are predicted, where about half of them have not been discovered yet and are still in the ”terra incognita”, making this an exciting region to study [Erl+12]. The nuclear chart for the region of light isotopes is shown in Fig. 1.1, with the neutron drip line indicated by the yellow line.

The nuclear shell model, introduced by M. Goeppert-Mayer [May49] and O. Haxel, J. Jensen and H. Suess [Hax+49] in the late 1940s, was the first successful effective description of the atomic nucleus. It is based on the mean field approximation, where each nucleon moves independently in a field created by all remaining nucleons. Typical potentials used in this approximation are the harmonic oscillator or the Woods-Saxon potential. Including a spin-orbit interaction, that acts on the orbital angular momentum $\vec{l}$ and the spin $\vec{s}$, leads to single-particle energy levels, that can be occupied by a certain amount of nucleons, $2j + 1$, with the total angular momentum $\vec{j} = \vec{l} + \vec{s}$, following the Pauli principle. Neutrons and protons are treated individually and so-called ”magic numbers” evolve in this picture, where the number of nucleons corresponds to N or $Z = 2, 8, 20, 28, 50, 82$ and additionally $N = 126$ resulting in a shell structure. The shell closure is characterized by an increased energy gap to the next level, meaning that the nucleus is hard to excite and features an improved stability. The energy levels in the single-particle shell model up to $N = Z = 20$ are shown in Fig. 1.2a, with the magic numbers indicated by the gray boxes. The levels are labeled according to the quantum numbers nl_j, with s, p, d correspond to $l = 0, 1, 2$, respectively.

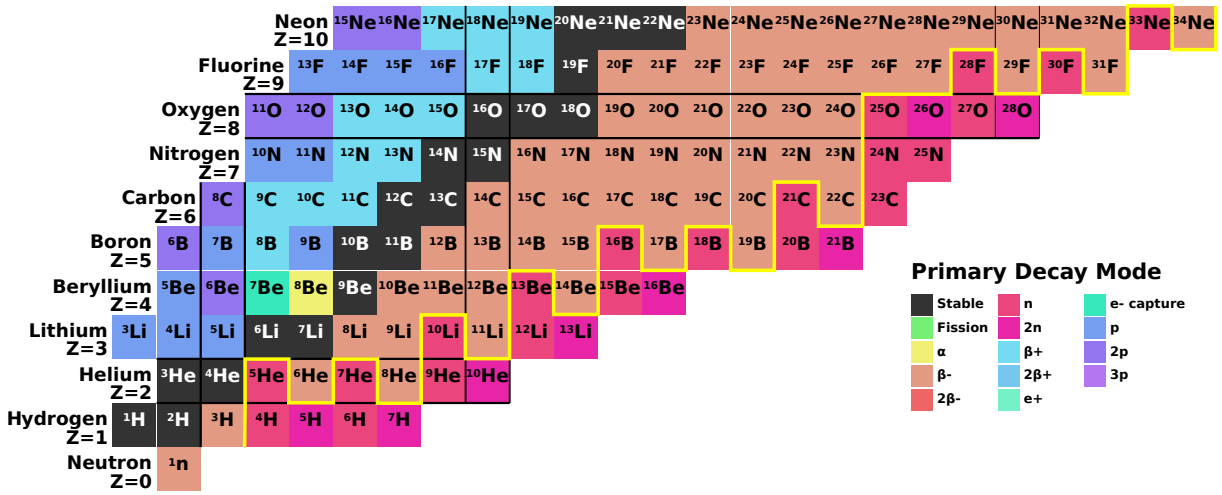

Figure 1.1.: Chart of nuclides for the region of light nuclei. The magic numbers in this region are indicated by the black lines, where the neutron drip line is indicated by the yellow line. The figure is taken and modified from [Cha23].

Of particular interest is the neutron drip line for oxygen due to the so-called ”oxygen anomaly” [Sak+99; Ots+10]. Experimentally, it was found that ^{24}O ($Z = 8, N = 16$) is a doubly-magic nucleus [Kan+09; Hof+09] and the last bound oxygen isotope, whereas ^{28}O is unbound [Sak+99]. Up to now, the ^{25,26}O ($N = 17, 18$) ground states (g.s.) have been observed as unbound resonances [Kon+16], where an experimental search for the ^{28}O g.s. resonance has been performed at RIKEN [Kon+15]. In the naive shell model used for stable nuclei, ^{28}O is predicted to be doubly magic with $Z = 8$ and $N = 20$. The $N = 20$ shell closure has long been known, however, to break down for isotopes with $Z = 10 - 12$ [Ots+20], leading to the conclusion that the magic numbers may be shifted for the neutron-rich region. This region is referred to as the ”island of inversion”, where intruder configurations are already dominant in the g.s. wave function. The term oxygen anomaly refers to the sudden change in stability for the oxygen isotopes. As shown in Fig. 1.1, the neutron drip line has a regular pattern, which is only broken for the oxygen isotopes. In the fluorine isotopic chain, with only one proton more, six more neutrons can be bound in ^{31}F [Sak+99]. This can be explained with the occupation of the proton (π) and neutron orbitals (ν). The shell gap between $\nu 1s_{1/2}$ and $\nu 0d_{3/2}$ decreases with $\pi 0d_{5/2}$ having a proton due to the additional binding of the tensor force [Hof+08; Ots+01].

Going towards the limits of stability changes the structure of nuclei and therefore they can benchmark nuclear theory. The mean-field approximation neglects residual interactions between the nucleons, as they are assumed to be small. For neutron-rich nuclei, including the nucleon-nucleon (NN) interaction, where valence neutrons interact with each other on top of the core potential, is important to describe the shell evolution. However, it was found that even three-body forces ($3N$) are necessary to explain the oxygen drip line [Ots+10], which are far less constraint experimentally. For single-particle energies calculated from the NN interaction, the $d_{3/2}$ orbital decreases when more neutrons are added, leading to bound oxygen isotopes up to $N = 20$. This is demonstrated in Fig. 1.2b by the dashed line for the oxygen isotopes ($Z = 8$) as a function of neutron number. The

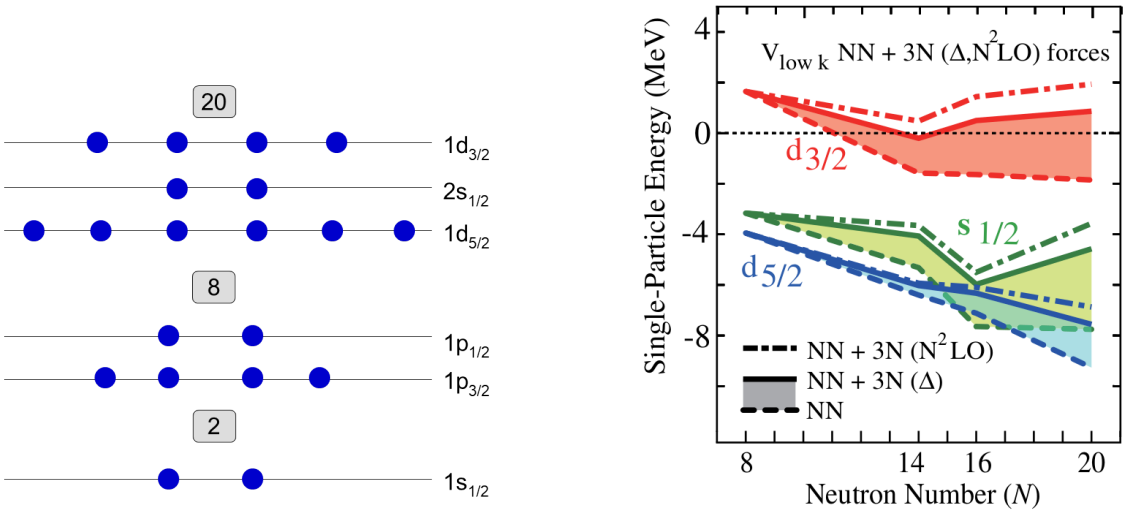

Figure 1.2.: (a) Energy levels in the single-particle shell model up to $N = Z = 20$. The magic numbers are indicated by the gray boxes, where each energy level can be occupied by $(2j + 1)$ protons or neutrons. The doubly magic nucleus ^{40}Ca with $N = Z = 20$, has a shell closure as shown here for both, protons and neutrons. (b) Calculated single-particle energies for oxygen isotopes ($Z = 8$) as a function of neutron number. Only by including $3N$ forces in the calculation (shaded areas), the unbound nature of ^{28}O can be reproduced. Figure (b) is taken and modified from [Ots+10].

single-particle energies are given in reference to the ^{16}O core. Including repulsive three-body forces, results in the shaded area in Fig. 1.2b. The single-particle energies changed sign and when filling the $d_{3/2}$ orbital with neutrons from $N = 16$ to $N = 20$ it remains unbound, in agreement with the experimental observations. The $3N$ forces included in this calculation are based on Δ excitation and chiral EFT interactions. A Δ excitation can be described as a virtual excitation of one nucleon induced by another nucleon, which is then scattered off a third nucleon. In consequence, a shell gap between the $s_{1/2}$ and $d_{3/2}$ orbital opens, giving rise to the magic number $N = 16$, whereas the magic number at $N = 20$ vanishes for the oxygen isotopes.

To investigate the structure of newly discovered exotic nuclei, one of the first properties to study is their radioactive decay. The decay modes, the lifetime and the decay energy give insights to the new nucleus. Nuclei beyond the drip line may present new kinds of radioactive decays at the limit of nuclear stability. The one-proton and the most recently discovered two-proton radioactivity are the most common decay mechanism beyond the proton drip line. It was first observed in ^{45}Fe [Pfü+02; Gio+02]. The term radioactivity refers to a sufficiently long lifetime as compared to a decay of unbound nuclei. In this work, a lifetime limit of $\tau > 10^{-14}$ s will be considered as radioactivity [Kah+17b; Wap91]. More details about radioactive decays will be described in Ch. 2.

So far, neutron radioactivity could not be conclusively observed. The nuclei beyond the proton drip line might have a long lifetime due to the additional Coulomb barrier [Pfü13]. For nuclei beyond the neutron drip line, the missing Coulomb barrier puts the expected lifetime of a one- or two-neutron unbound nucleus to much smaller values than the radioactive time frame. However,

a neutron decay could be hindered by a sufficiently large centrifugal barrier. Calculations by L. Grigorenko *et al.* [Gri+11; Gri+13], will be introduced in Sec. 2.2.1, predict a possible long half-life for the weakly two-neutron unbound ^{26}O, the focus of this work, depending on the decay energy, making it a promising candidate for the first observation of two-neutron radioactivity.

2. Physical Background

In this chapter, the physical background and the status of current research is presented. Radioactive decays, together with the decay law and the most common types of radioactive decays are briefly introduced in Sec. 2.1. More details can be found in [Kra88; Bet+08; May02]. Additionally, a brief overview of the decay of neutron-unbound states is presented. Details on the possible two-neutron radioactive decay of ^{26}O, the candidate of research in this work, are presented and discussed in Sec. 2.2.

2.1. Radioactive Decays

Radioactivity is defined as the spontaneous emission of radiation. A radioactive decay occurs in unstable nuclei reaching to more stable states and thus the daughter nucleus has a higher binding energy as the parent.

The binding energy of a nucleus is a unique characteristic and is defined by the difference of the masses individual constituents protons m_p, neutrons m_n and electrons m_e compared to the mass of the compound nucleus M:

$$E_B(Z,N) = (Zm_p + Nm_n + Zm_e - M(Z,N)) \cdot c^2, \tag{2.1}$$

and therefore it represents the energy gain by a nucleus compared to a collection of non-interacting nucleons.

2.1.1. Radioactive Decay Law

The activity A of a radioactive substance is given by the number of decays per time unit and is related to the decay constant λ as follows

$$A = -\frac{dN}{dt} = \lambda N, \tag{2.2}$$

with N being the number of nuclei at a given time t. The activity is measured in becquerel (Bq), with 1 Bq corresponding to one decay per second. The decay constant λ corresponds to the probability that a given nucleus will decay within a certain time. Integrating Eq. 2.2, results in the decay law

$$N(t) = N_0 \cdot e^{-\lambda t}, \tag{2.3}$$

with the initial number of nuclei N_0. After a time $t = \tau = 1/\lambda$ the amount of nuclei is reduced to N_0/e. The time τ is defined as the lifetime of the radioactive substance. Analogously the half-life

$T_{1/2}$ is defined as the time where half of the initial amount is left $N_0/2$, relating τ and $T_{1/2}$ as

$$\tau = \frac{T_{1/2}}{\ln 2}. \tag{2.4}$$

2.1.2. Types of Decay

The three common discovered decay types are α, β and γ decays. In the former decays, an α or a β particle is emitted, respectively, and the unstable nucleus tries to reach a stable species. In a γ decay, the nuclear species is not changed and instead an excited state decays towards the ground state of the same nucleus.

When a nucleus X undergoes an α decay, it emits a ^{4}He nucleus ($N = Z = 2$), defined as α particle. This means, the decay follows the process

$$^A_Z X \xrightarrow{\alpha} {}^{A-4}_{Z-2}Y + {}^4_2\mathrm{He}, \tag{2.5}$$

where Y is the daughter nucleus after the decay. α decays are most common in heavy nuclei. For the decay to occur, the α particle has to tunnel through the Coulomb barrier of the nucleus. This tunneling effect is forbidden in classical mechanics as the energy of the α particle is smaller than the barrier. In quantum mechanics on the other hand, the α particle has a small probability to tunnel through this barrier and makes the α emission possible. The lifetime of the parent nucleus is directly related to the available energy in the process, corresponding to the mass difference between the parent and the daughter nuclei. Heavy nuclei can also undergo a spontaneous fission process, where the parent nucleus splits into lighter daughter nuclei. During the fission process, neutrons can also be emitted, that can induce further fission processes. The α decay is considered as a type of fission process, where the α particle is one of the daughter nuclei.

During the β decay, a neutron is converted into a proton or vice versa, which can take place in three different processes. The β^- decay occurs in nuclei with a neutron excess. Here, a neutron in the nucleus is converted into a proton and due to the charge and lepton number conservation, also an electron e^- and an electron antineutrino $\overline{\nu}_e$ are produced and emitted. The β^- decay follows the process

$$^A_Z X \xrightarrow{\beta^-} {}^A_{Z+1}Y + e^- + \overline{\nu}_e. \tag{2.6}$$

Analogously, the β^+ decay occurs in neutron-deficient nuclei. A proton is converted into a neutron, positron e^+ and an electron neutrino ν_e. The charge number of the daughter nucleus is reduced by one:

$$^A_Z X \xrightarrow{\beta^+} {}^A_{Z-1}Y + e^+ + \nu_e. \tag{2.7}$$

In contrast to the α decay, the electron does not exist in the nucleus prior to the decay but is created out of the decay energy. Since the mass of the neutron is larger than the one of the proton, the neutron can also decay as a free particle with a half-life of $T_{1/2} \approx 10\,\mathrm{min}$. For the β^+ decay to occur, the proton has to be inside a bound nucleus, as the binding energy is necessary to permit the process. The β^+ decay competes with the electron capture (EC), where a neutron-deficient nucleus absorbs an electron from an inner atomic shell. A proton inside the nucleus is converted into a neutron and

an electron neutrino ν_e is emitted from the nucleus,

$$ {}^{A}_{Z}X + e^- \xrightarrow{\text{EC}} {}^{A}_{Z-1}Y + \nu_e. \tag{2.8} $$

γ radiation is emitted when a nucleus decays from an excited state to a lower lying state or the ground state. The energy of the emitted photon equals the difference in energy between the initial and the final level. An α or β decay process is usually accompanied by a γ decay, as the daughter nucleus can be in an excited state after the α or β decay and emits a γ ray to deexcite.

2.1.3. Neutron-unbound States

The limit of stability and therefore the location of the drip lines can be defined as the limits where the one-proton or one-neutron separation energy (S_p, S_n) crosses zero [Tho04]. The separation energy corresponds to the energy that is necessary to remove a single nucleon from a nucleus and is given by the difference of binding energies of two nuclei:

$$ S_p = E_B(Z, N) - E_B(Z-1, N), \tag{2.9} $$

$$ S_n = E_B(Z, N) - E_B(Z, N-1), \tag{2.10} $$

and is analogously defined for the removal of two nucleons as S_{2n} or S_{2p}. The nuclei of interest in this work, ^{25}O and ^{26}O, are one- and two-neutron unbound nuclei located beyond the neutron drip line. By adding more and more neutrons, the neutron separation energy decreases and the nuclei become weakly bound. Beyond the drip line, the one- or two-neutron separation energy becomes negative and neutrons can be spontaneously emitted. In this case, the absolute value of the separation energy corresponds to the decay energy:

$$ E_T = |S_{n,2n}|. \tag{2.11} $$

Neutron unbound decays usually have a short lifetime of about 10^{-22} s or less. These very short-lived nuclei are commonly referred to as resonances. Despite existing only momentarily, their state is defined and can be characterized by its energy, width and quantum numbers. Resonances appear as a significant increase in cross section at the resonance energy. The width Γ of the resonance is related to the lifetime τ as

$$ \Gamma = \frac{\hbar}{\tau}, \tag{2.12} $$

with the reduced Planck constant $\hbar$. The lifetime of a nucleus can be measured directly for sufficiently long time scales or indirectly using the uncertainty relation in Eq. 2.12. An overview of the different methods can be found in [Pfü+12; Nol+79]. Experimentally, resonances manifest themselves as peaks in the decay energy spectrum as shown in Fig. 2.4 for ^{25,26}O. In scattering theory, a commonly adopted definition of a resonance is a rapid increase of the phase-shift at $\pi/2$ [Mar+21]. A more general approach is to use the scattering S-matrix and determine the relevant pole in the complex-energy plane. This allows to define the resonance parameters as

$$ E = E_T - i\frac{\Gamma}{2}. \tag{2.13} $$

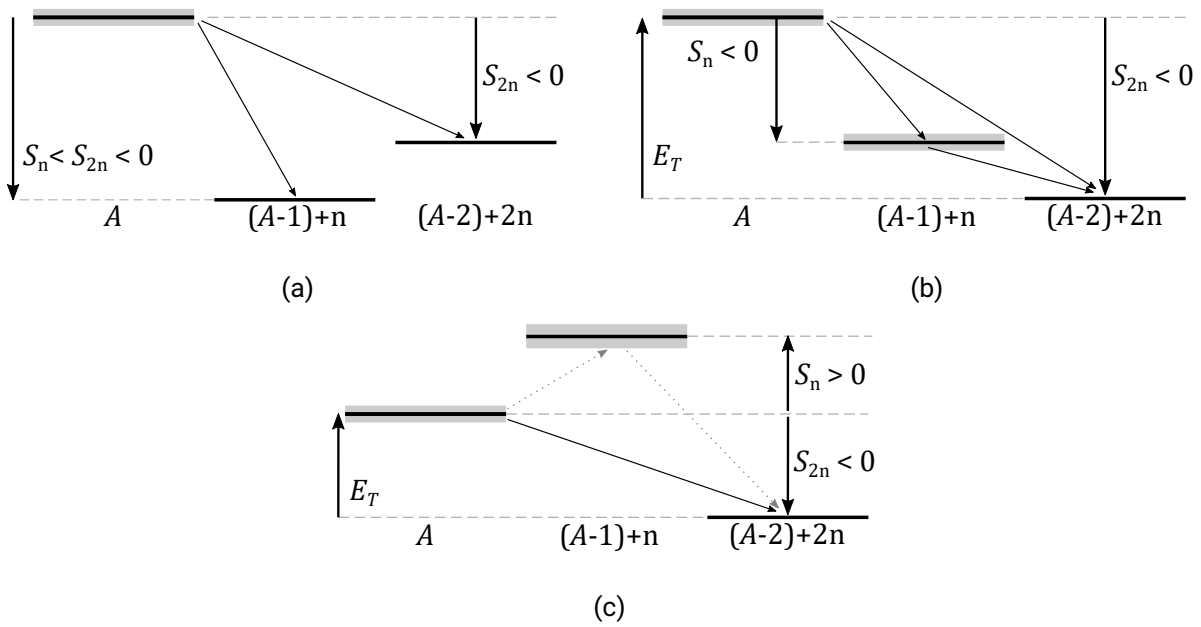

Figure 2.1.: Different decay schemes for a two neutron emission. (a) Decay from an excited state with the emission of one or two neutrons. (b) Sequential decay via an intermediate narrow resonance. (c) True two neutron decay, where the intermediate state cannot be reached energetically. The idea of the figure is adapted from [Pfü+12].

A bound state would be located at $E_T < 0$ and $\Gamma = 0$, whereas an unbound resonant state manifests as a pole at $E_T > 0$ and $\Gamma > 0$. The case of $E_T < 0$ and $\Gamma > 0$ is referred to as an unbound virtual state [Mar+21; Tay72].

The decay behavior of the neutron-unbound state can give insights on its structure. For a two-body decay, like the decay of ^{25}O into ^{24}O+1n, the available energy is shared between the decay partners, according to energy and momentum conservation. For a three-body decay, like the decay of ^{26}O into ^{24}O+2n, the decay dynamics is more complicated. Different decay schemes for the emission of two neutrons are shown in Fig. 2.1. Figure 2.1a shows the decay of an excited state, where also the emission of only one neutron is possible. In Fig. 2.1b the sequential decay via a narrow intermediate resonance is shown. Here, the parent nucleus (A) decays into the daughter nucleus ($A-2$) through an intermediate state ($A-1$) with the emission of only one neutron in the first step and a subsequent emission of the second neutron from the intermediate level. In Fig. 2.1c, the true two neutron decay is shown. The higher lying intermediate level is energetically forbidden and thus the two neutrons have to be emitted simultaneously. This scenario corresponds to ^{26}O as the sequential decay through ^{25}O is forbidden, making it a true two neutron emitter. The level scheme will be introduced in the next section and is shown in Fig. 2.5.

The decay could be hindered and thus increasing the lifetime, if certain conditions are fulfilled, qualifying the decay as radioactivity. In the case of proton radioactivity, the Coulomb barrier has to be overcome by the proton to escape the nucleus. Proton radioactive decays were briefly introduced in Ch. 1. The prospects of neutron radioactivity, especially for the case of the ^{26}O, will be presented in the next section.

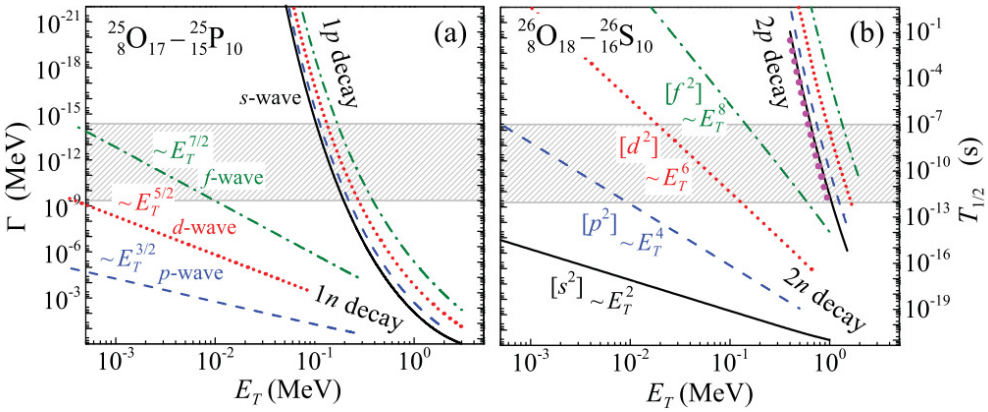

Figure 2.2.: Calculated half-lives for different orbital configurations as a function of the decay energy E_T and width Γ for (a) one-nucleon and (b) two-nucleon radioactivity. For the two-neutron emission, the possible energy window is much broader, making this the more realistic case of radioactivity. The figure is taken and modified from [Gri+11].

2.2. ^{26}O - A Promising Candidate for 2n Radioactivity

2.2.1. Lifetime Estimates from Theoretical Calculations

In the work by L. Grigorenko *et al.* [Gri+11], the lifetime of one- and two-neutron (1n and 2n) decays are estimated based on the behavior for the proton decay equivalent using a direct decay model. Considering the two-proton (2p) decay, where the one-proton emission is energetically forbidden due to the specific energy conditions of the daughter nucleus ($S_N > 0$ and $S_{2N} < 0$), leads to both protons being emitted simultaneously, called true 2p emission. This increases the lifetimes compared to sequential decays.

In Fig. 2.2, half-life ($T_{1/2}$) and width (Γ) predictions for one- and two-nucleon decay scenarios are shown as a function of the energy of the decayed nucleus. Half-lives being accessible with present detector technologies of $T_{1/2} > 1$ ps are indicated with the gray hatched areas. For 1n radioactivity of ^{25}O (Fig. 2.2a), the decay energy E_T would have to be 1 keV or smaller even for the d-wave. It was concluded that finding such a small energy is very unlikely. Experimentally, a decay energy of 749(10) keV was measured by [Kon+16] and will be presented in Sec. 2.2.2. More realistic scenarios of 1n radioactivity might appear for f-wave states or higher l states of heavier neutron-rich nuclei, which are not experimentally accessible yet. For the 2n radioactivity of ^{26}O (Fig. 2.2b), the possible energy window is much broader than for the 1n case. The decay energy could take values up to 200 keV for a d^2 configuration and 600 keV for a f^2 configuration. Additionally, the simultaneous emission of two neutrons, called true 2n decay, as compared to a sequential decay through the ^{25}O ground state creates an additional effective barrier and might hinder the decay. This makes the existence of a 2n radioactive decay much more probable [Gri+11].

In a further investigation of the ^{26}O decay by L. Grigorenko *et al.*, a three-body model was used [Gri+13]. It was found that the missing Coulomb barrier for long-lived 2n emitters makes the situation more complex as compared to the 2p case. The new prediction of the half-life includes additional effects, like configuration mixing, which shifts the upper limits of the decay energy to

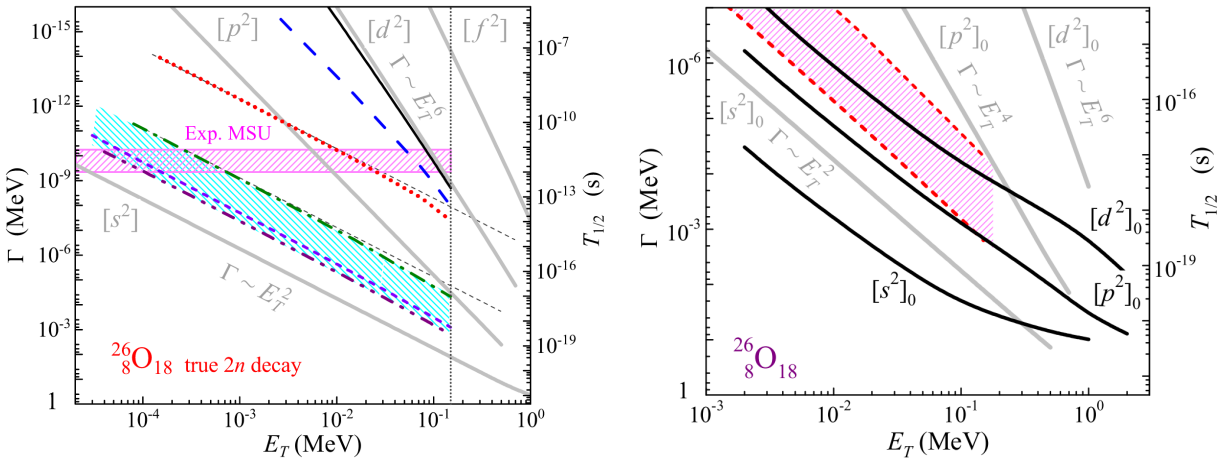

Figure 2.3.: (a) Half-life predictions of ^{26}O ground state for different models in the three-body calculation taking configuration mixing into account. The decay energies for a half-life > 1 ps are shifted to smaller values as compared to [Gri+11] (gray lines). (b) Predictions using the dineutron model for different structure assumption. The three-body calculation (blue hatched area in (a)) is indicated by the pink hatched area. The gray lines show the predictions from [Gri+11]. The figures are taken from (a) [Gri+13] and (b) [Gri+18].

smaller values and providing narrower limits on the half-life (blue hatched area), as shown in Fig. 2.3a.

With the lifetime value for ^{26}O measured in [Koh+13] (pink hatched area in Fig. 2.3a), which will be introduced in Sec. 2.2.3, an upper limit on the decay energy of ~ 1 keV is found, where the pink and the blue hatched area intersect. If the experimental result from [Koh+13] can be confirmed, the associated decay energy value is very small, meaning that it is at the 2n separation threshold. Such a behavior is an indicator for the formation of a halo structure. Since ^{26}O is unbound, the radius of the system is infinite. However, assuming a long-lived state, the Root Mean Square (RMS) radius of the valence neutrons of ^{26}O was calculated [Gri+13] and is comparable in size to the ^{11}Li radius, which is one of the most extreme 2n halo cases evidenced so far [Tan+85]. This could hint to an s-wave component analogously to ^{11}Li, shifting the decay energies to much smaller values in the prediction as compared to a pure d-wave state [Gri+13], cf. Fig. 2.3a. In the work of K. Hagino *et al.* [Hag+16], the ground state and excited state configurations of ^{26}O were calculated based on the experimental observation in [Kon+16]. It was found that the ground state is dominated by the $\nu(d_{3/2})^2$ configuration.

In the most recent calculation, L. Grigorenko *et al.* use a dynamic dineutron model [Gri+18]. The half-life and decay energy correlation is shown in Fig. 2.3b, together with the previous predictions. The pink hatched area in Fig. 2.3b corresponds to the blue hatched area in Fig. 2.3a. The dineutron model provides a more realistic assumption about the d^2 structure of ^{26}O and similarly puts the half-life to smaller values.

2.2.2. Experimental Overview

The ground state (g.s.) of the two-neutron unbound ^{26}O nucleus was observed for the first time by E. Lunderberg *et al.* in a proton-knockout reaction from ^{27}F at an energy of 82 MeV/u [Lun+12]. The ^{24}O fragment and the two neutrons were measured in coincidence with Modular Neutron Array (MoNA), located at the National Superconducting Cyclotron Laboratory (NSCL) at Michigan State University (MSU). The ground state resonance was observed at $E_T = 150^{+50}_{-150}$ keV. As presented in the previous section the half-life value is strongly related to the decay energy. With this g.s. energy, the estimation on the half-life presented above [Gri+11], leads to a value in the order of picoseconds for a pure $\nu(d_{3/2})^2$ configuration.

The ground state of the neutron unbound ^{25}O nucleus was measured for the first time by C. Hoffman *et al.* in an invariant-mass spectroscopy [Hof+08]. A ^{26}F beam with 85 MeV/u hit a Be target, where ^{25}O was produced in a proton-knockout reaction. A single resonance could be observed in the decay-energy spectrum with $E_T = 770^{+20}_{-10}$ keV and a width of $\Gamma = 172 \pm 30$ keV.

An experiment at the R^{3}B-LAND setup at Helmholtzzentrum für Schwerionenforschung (GSI) investigated both ^{26}O and ^{25}O, in a kinematically complete measurement [Cae+13a]. The isotopes of interest were produced from a proton-knockout of ^{27,26}F at energies of 414 MeV/u and 442 MeV/u, respectively. The ^{25}O g.s. resonance parameters were measured as $E_T = 725^{+54}_{-29}$ keV and a width of $\Gamma = 20^{+60}_{-20}$ keV. For the ^{26}O g.s. a new upper limit on the decay energy of $E \leq 120$ keV could be determined with 95 % confidence level (c.l.), in agreement with the previous measurement of [Lun+12]. This result provided a limit on the lifetime of $\tau \leq 5.7$ ns (95 % c.l.) together with the half-life estimation from L. Grigorenko *et al.* [Gri+11]. The experimental limit on the lifetime prior to this measurement was estimated by [Koh+13] to $\tau < 200$ ns, based on measurements by [Gui+90; Tar+97], where ^{26}O was not observed after passing a separator with the corresponding time-of-flight. Additionally, an indication for an excited state of ^{26}O at around 4 MeV was found in the GSI experiment though not conclusive [Cae+13a].

In the most recent spectroscopy experiment on ^{26,25}O at the SAMURAI setup at the RIKEN RIBF, the more precise results were obtained for the decay energies by Y. Kondo *et al.* [Kon+16]. ^{26}O (^{25}O) was investigated with the invariant-mass method, where it was produced from ^{27}F (^{26}F) via proton removal at 201 MeV/u. A very low lying ground-state resonance could be observed at only $E_T = 18 \pm 3(\text{stat}) \pm 4(\text{syst})$ keV above threshold. The decay energy spectrum is shown in Fig. 2.4a. The width of the state is assumed to be smaller than the experimental resolution. A higher lying level at $E_T = 1.28^{+0.11}_{-0.08}$ MeV could be observed for the first time, most likely belonging to the first 2^+ state. The decay energy of ^{25}O was remeasured with higher precision compared to previous measurements [Cae+13a; Hof+08], and was found to be located at $E_T = 749 \pm 10$ keV and a corresponding width of $\Gamma = 88 \pm 6$ keV, shown in Fig. 2.4b. The experimental findings are summarized in the level scheme of ^{26}O in Fig. 2.5. Comparing the low decay energy found in [Kon+16] to the calculations [Gri+13], results in a shift of the expected half-life to values of 10^{-17} s $- 10^{-15}$ s. However, as described in Sec. 2.2.1, the prediction is model dependent, making a precise dedicated lifetime measurement necessary to draw a conclusion.

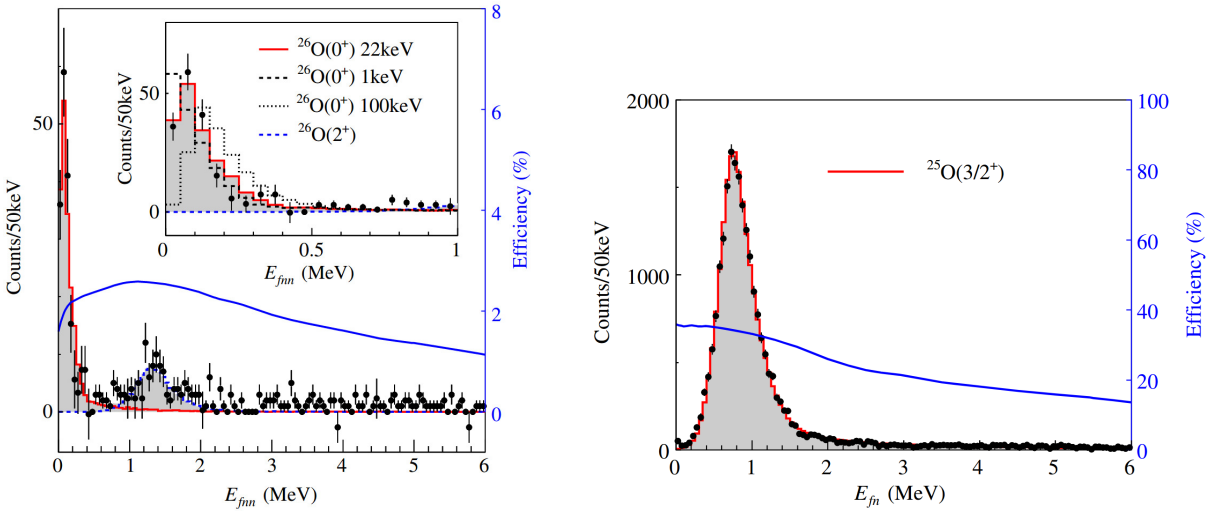

Figure 2.4.: Measured decay energy spectra of (a) ^{26}O and (b) ^{25}O reconstructed from the momentum vectors of the decay products (a) ^{24}O and two neutrons and (b) ^{24}O and one neutron. Both figures are taken from [Kon+16].

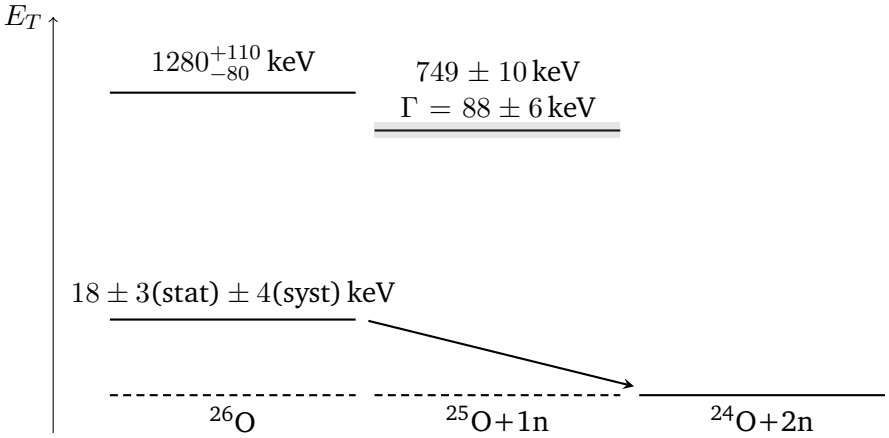

Figure 2.5.: Decay energy level scheme of ^{26}O relative to the ^{24}O ground state. As the g.s. of ^{25}O is located at higher energies than the ^{26}O g.s., the decay via this intermediate level to ^{24}O is energetically forbidden. The values are taken from [Kon+16].

2.2.3. Previous Lifetime Measurements

In an experiment by Z. Kohley *et al.* [Koh+13], performed at NSCL at MSU, a novel technique to measure half lives was applied, which was based on the Doppler-shift attenuation method [Tho+13]. In the Doppler-shift attenuation method [Sch+68], an excited nucleus is slowed down in a degrader, leading to a Doppler shift of the emitted γ-rays which is correlated to the lifetime. This method was extended for decays through the emission of neutrons. The relative velocity between the neutrons and the fragment is examined to extract the lifetime. In the measurement, an 82 MeV/u ^{27}F beam impinged on a thick Be target, where ^{26}O was produced in a proton-knockout reaction. Depending on the lifetime, the ^{26}O loses a different amount of energy in the target, causing a shift in the expected neutron velocity compared to the case with $T_{1/2} = 0$ ps. The reaction point in the target is not known, and thus the fragment velocity is calculated under the assumption that the knockout reaction occurs at the center of the target. For short lifetimes, the spectrum of the relative velocity V_{rel} would be centered at zero, whereas a shift would indicate a long-lived component of the decay. The experimental V_{rel} distribution is shown in Fig. 2.6a. The extracted half-life value from this measurement is $T_{1/2} = 4.5^{+1.1}_{-1.5}(\text{stat}) \pm 3(\text{syst})$ ps [Koh+13], which corresponds to a lifetime of $\tau = 6.5^{+1.6}_{-2.2}(\text{stat}) \pm 4.3(\text{syst})$ ps. This result suggests the possibility of a two-neutron radioactive decay, though the systematic uncertainty is too large to reach this conclusion.

In a more recent measurement by T. Redpath [Red19], the half-life of ^{26}O was remeasured with reduced uncertainties as $T_{1/2} = 5.0^{+1.7}_{-2.2}(\text{stat}) \pm 1.7(\text{syst})$ ps ($\tau = 7.2^{+2.5}_{-3.2}(\text{stat}) \pm 2.5(\text{syst})$ ps). The method from the previous measurement [Tho+13] was refined, using segmented Be targets intersected with silicon detectors. This allows for the identification of the specific Be target in which the proton knockout reaction occurred. In this way, the fragment velocity can be determined more accurately and the systematic uncertainty was reduced [Red+20].

In conclusion, ^{26}O is a well suited candidate for 2n radioactivity: (i) it has a very low decay energy, (ii) the valence neutrons could create an angular barrier, (iii) it is a true two-neutron emitter and (iv) it is experimentally accessible. The lifetime results obtained so far are in agreement with each other [Cae+13a; Koh+13; Red19]. However, none of them lead to an observation of the 2n radioactivity of ^{26}O. Additionally, as the theory estimation from the measured decay energy [Kon+16] puts the lifetime to much shorter values [Gri+13; Gri+18] than experimentally observed [Koh+13], an unambiguous measurement is necessary to draw a conclusion. In this work, a new method to measure the neutron-decay lifetime is applied, with the aim for a precise measurement with reduced uncertainties.

The thesis layout is as follows: in Ch. 3, the newly developed measurement method is introduced together with the experimental setup. Chapter 4 focuses on the calibration of the experimental detectors, and the analysis methods are presented in Ch. 5. The working principle of the simulations performed in this work, are introduced in Ch. 6. Finally, the results are discussed in Ch. 7 and summarized in Ch. 8.

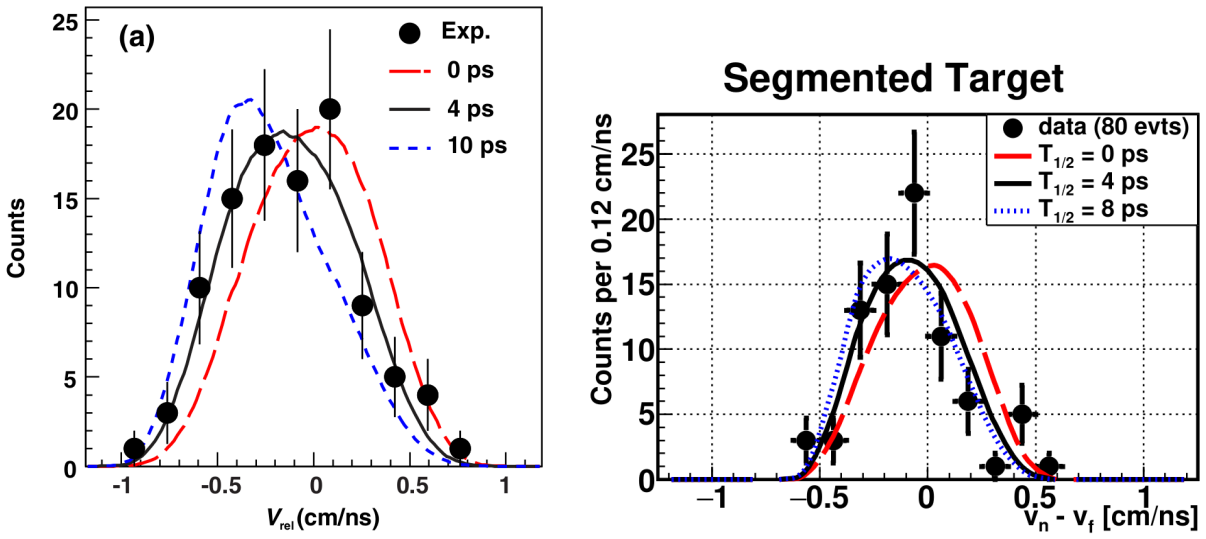

(a) (b)

Figure 2.6.: Measured relative velocity V_{rel} spectrum of the ^{24}O fragment and two neutrons from the decay of ^{26}O using different methods with (a) a single target and (b) a segmented target. A shift of V_{rel} away from zero, indicates a non-zero lifetime. The figures are taken from (a) [Koh+13] and (b) [Red+20].

3. Experimental Method and Setup

In 2016, a four day long experiment, called SAMURAI20 (S20), was performed with the goal to measure the lifetime of the ^{26}O ground state via a proton removal reaction from ^{27}F at the Rare Isotope Beam Factory (RIBF) at RIKEN, Japan [Acc22] (see Sec. 3.2). The secondary ^{27}F beam was provided by the RIKEN Projectile Fragment Separator (BigRIPS) [Kub03] and the reactions took place in inverse kinematics at relativistic energies at the Superconducting Analyzer for MUlti-particles from RAdio Isotope Beams (SAMURAI) experimental setup [Kob+13], described in Sec. 3.3 and 3.4, respectively. The detector setup allows to perform kinematically complete measurements where the momenta of all particles are measured, including those of the neutrons.

The experiment used a newly developed method to explore and study the neutron-radioactive decay of the candidate nucleus ^{26}O, described in more detail in Sec. 3.1. A prominent feature of the measurement technique is the use of a stack of thick targets allowing for the decay of ^{26}O inside and outside the target material according to its lifetime. For this purpose, it is necessary to measure the incoming ^{27}F, the outgoing ^{24}O and two neutrons in coincidence. The resulting spectrum is characteristic for a certain lifetime that is extracted by comparing to simulations.

3.1. Measurement Method

As discussed in Ch. 2, ^{26}O is a promising candidate for a radioactive decay via neutron emission. According to the estimates by Grigorenko *et al.* [Gri+13], a low-lying ground state of ^{26}O might be long-lived with a width of $\Gamma \leq 10^{-1}$ keV, see Fig. 2.3a. However, a direct measurement of its width is not possible with currently achievable energy resolutions of $\sigma_E \sim 10\,\text{keV}\,(\sigma)$ [Bor+21]. Consequently, a new measurement method was developed by J. Kahlbow *et al.* [Kah+17b] which was applied in this work and will be described in the following.

The method is based on the Doppler Shift Attenuation Method (DSAM) where nuclear lifetimes are measured by slowing down the nucleus of interest in a degrader where γ-rays might be emitted [Sch+68]. The velocity of the nucleus can be reconstructed by measuring the energy of the emitted γ-ray due to the Doppler effect.

The observable in the present experiment is the velocity difference between the neutrons and the fragment $\Delta\nu = \nu_\text{n} - \nu_\text{f}$. The ^{26}O, with a lifetime τ, is produced via a proton removal reaction from ^{27}F and then decays into ^{24}O and two neutrons. The decay will occur either inside or outside of the target material, producing a characteristic shape in the velocity-difference distribution. If the decay happens inside the target, the fragment will be slowed down in the material compared to the neutrons creating a broad distribution in the $\Delta\nu$-spectrum. For delayed decays outside the

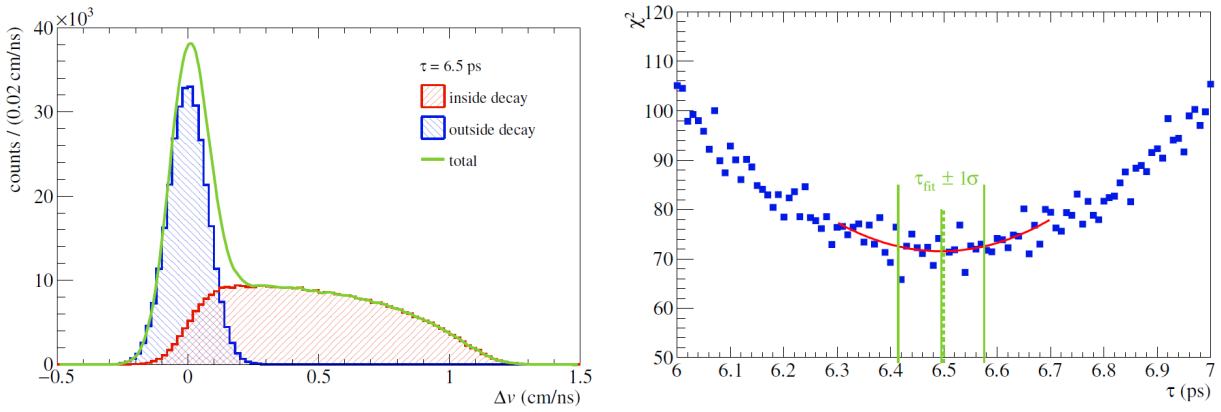

(a) (b)

Figure 3.1.: (a) Simulated velocity-difference spectrum for a lifetime of $\tau = 6.5\,\text{ps}$. Immediate decays inside the target material produce a broad distribution in the velocity-difference spectrum (red), whereas delayed decays outside the target produce a sharp peak (blue). The overall shape of the $\Delta\nu$ distribution depends on the lifetime of the isotope. (b) Hypothetical experimental data is compared to simulations for different lifetimes and from the minimum of the χ^2 distribution the lifetime is extracted. For the example in (a) the deduced lifetime with this method is $\tau = 6.49 \pm 0.08\,\text{ps}$. Both figures are taken from [Kah+17b].

material, a sharp peak will appear as shown in Fig. 3.1a. The shape of the $\Delta\nu$-spectrum depends on the lifetime, and therefore can be analyzed to extract its value from the experimental data.

For this reason, simulations for different lifetimes are essential to deduce the lifetime by comparing the experimental spectrum to the simulated ones. The chi-square χ^2 test is used as a measure to evaluate the agreement between the experimental data and the simulation. An example is shown in Fig. 3.1b where the χ^2 analysis leads to a lifetime value of $\tau = 6.49 \pm 0.08\,\text{ps}$ with the uncertainty given by $\chi^2_{\text{min}} + 1$.

In order to provide a high sensitivity in a certain region of τ, the beam energy, target material and target thickness were optimized. For the experiment, target sheets made of tungsten ($Z = 74$, $\rho = 19.25\,\text{g/cm}^3$) and platinum ($Z = 78$, $\rho = 21.45\,\text{g/cm}^3$) were chosen because of their high charge Z and mass density which provide a large energy loss over a short distance. From previous experiments, presented in Sec. 2.2.3, the lifetime of ^{26}O is expected to be in the low picosecond range for which the method is most sensitive. The measurable lifetime range can be increased by using several targets in a row, arranged in a stack. Short lifetimes are measured with low energies and thin targets to ensure that a reasonable amount of decays occur both inside and outside of the material. For the measurement, the beam energy, target material and target thickness were chosen to be most sensitive around the previously measured value of $\tau = 6.5\,\text{ps}$ [Koh+13] down to $\tau = 1\,\text{ps}$ [Cae+13b]. A picture of the target stack is shown in Fig. 3.6b where the individual target sheets are mounted with decreasing thickness.

A simulated velocity-difference spectrum is shown in Fig. 3.2 for a setup with eight Pt target sheets and an incoming ^{27}F beam with $200\,\text{MeV/u}$. Each material sheet creates a peak and box structure from outside and inside decays in the resulting spectrum. Additionally, the ratio of outside-to-inside decays is increased and the energy of the particle is decreased from target to target. The peak on the

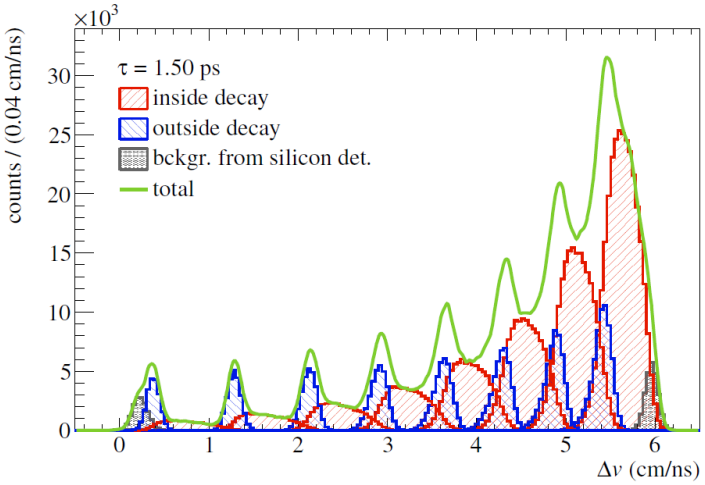

Figure 3.2.: Simulated velocity-difference spectrum for a lifetime of $1.5\,\mathrm{ps}$ with a target stack of eight platinum targets. The structure of the target stack is visible in the spectrum, where the peak with the largest velocity difference belongs to the first target. The ratio of outside to inside decays increases from target to target. The background from the silicon detectors is shown in gray. By using a stack of targets the precision of the method is increased and a range of lifetimes can be probed. The figure is taken from [Kah+17b].

right side of the spectrum with the largest velocity difference belongs to the first target.

The energy loss has to be measured before and after the target stack to identify the reactions and thus incoming and outgoing Z. For this, three single-sided silicon detectors of 300 µm thickness each are included, one in front and two behind the target stack (see Fig. 3.6a). However, the silicon detectors produce an additional background, since they act as targets themselves. This is also visible in Fig. 3.2 with the gray peaks on both ends of the spectrum. However, it is difficult to determine this background experimentally because in an empty target run the energy loss of the target stack will be missing and the backgrounds of the silicon detectors would therefore overlap. For this reason, a reference measurement with ^{25}O is performed where no lifetime is expected. This provides a velocity-difference spectrum for $\tau = 0\,\mathrm{ps}$ with the full background and can also be used to determine the systematic uncertainty of the measurement. The new method presented above is able to measure lifetimes down to $0.2\,\mathrm{ps}$ within 5σ using eight targets [Kah+17b].

3.2. Accelerator Facility

The accelerator complex at the RIKEN Nishina Center is located in the RIKEN Accelerator Research Facility (RARF) and in the RIBF. It can produce primary beams at high intensity up to uranium with an energy of $345\,\mathrm{MeV/u}$. After the acceleration, the in-flight radioactive-isotope beam separation takes place at BigRIPS which provides the secondary beams to the experiments. More information can be found in [Yan04]. The accelerator complex is shown schematically in Fig. 3.3 [Acc22].

The beam is produced with an Electron Cyclotron Resonance (ECR) ion source. In this procedure the ECR is used to ionize a plasma. The electrons are excited to the cyclotron frequency using electric

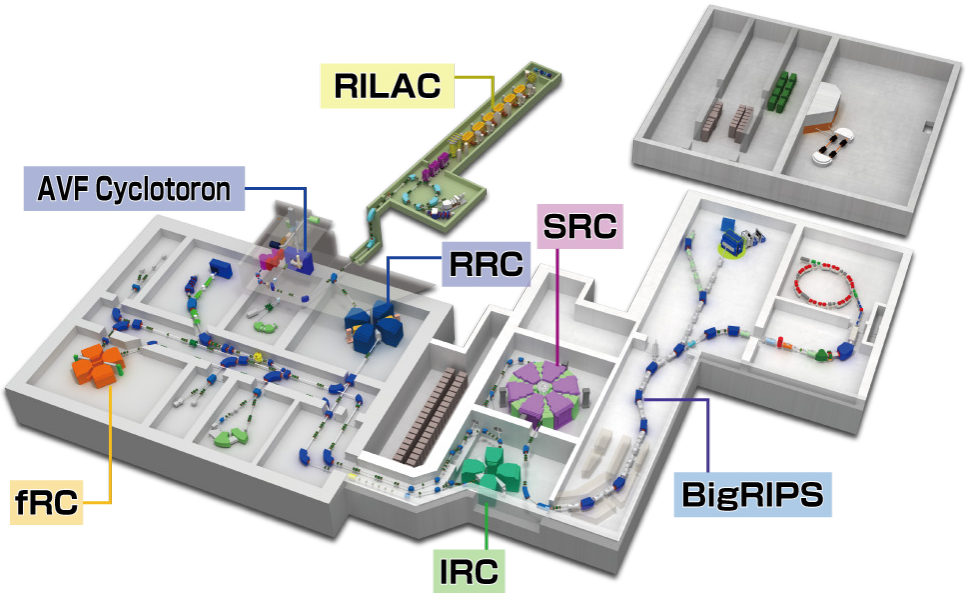

Figure 3.3.: The RIKEN accelerator complex. The ions are produced the the ion source and then injected into the RILAC. A series of different cyclotrons follows which is able to accelerate uranium ions up to 345 MeV/u. The figure is taken from [Acc22].

and magnetic fields. The ions are then accelerated in the RIKEN Linear Accelerator (RILAC) up to $6\,\mathrm{MeV/u}$. Several cyclotrons follow the linear accelerator. First, the RIKEN Ring Cyclotron (RRC), then the Intermediate-stage Ring Cyclotron (IRC) and last the Superconducting Ring Cyclotron (SRC).

In a cyclotron particles are injected in the center. The applied magnetic field (B) forces them on a spiral trajectory. The magnetic field is intersected with accelerating structures such as RF-cavities. During the acceleration the energy of the particle increases and thus the radius of its trajectory. The magnetic field is constant in the sector magnets. That means that at a given energy the particle cannot be further accelerated, since the radius would become too large. At this point the particle has to be extracted and forwarded to the next acceleration stage. The revolution frequency of a cyclotron for a particle with charge q and mass m is given by $\omega = q \cdot B/m$.

The RRC has four separated-sector magnets and a K-value of $540\,\mathrm{MeV}$. The K-value of a cyclotron gives its maximum bending power. After the RRC the ions are injected into the IRC with a K-value of $980\,\mathrm{MeV}$. Following the IRC is the final acceleration stage: the SRC is a superconducting cyclotron which was taken into operation in 2006. It consists of six sector-magnets, six accelerating structures and has a K-value of $2500\,\mathrm{MeV}$, with a maximum magnetic field of $3.8\,\mathrm{T}$. Along the acceleration line several strippers are installed to further ionize the particles.

3.3. Beam Production

After their acceleration the primary beams are injected into the BigRIPS setup shown in Fig. 3.4. There, the secondary beams are produced in a production target through fragmentation, selected according to their mass-to-charge ratio and then brought to the experimental area. BigRIPS is an in-flight beam separator where intense radioactive beams in a wide range of masses are produced using

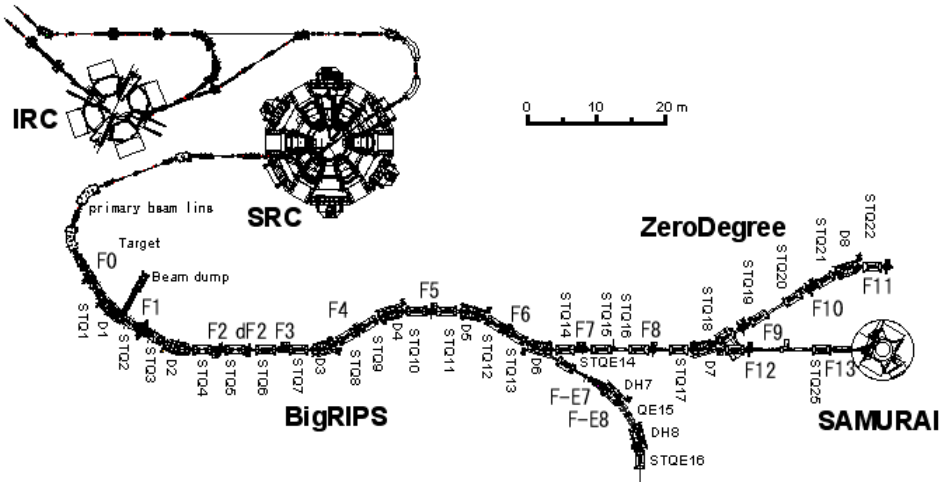

Figure 3.4.: The setup of the fragment separator BigRIPS. In the first stage from the production target F0 to the focal plane at F2 the secondary beam is produced. In the second stage from F3 to F7 the isotopes are separated according to their mass-to-charge ratio. The SAMURAI area is setup around the focal plane at F13 where the reaction target is installed. The total flight path from F0 to F13 is approx. 118 m. The picture is taken from [Big22].

a combination of magnetic dipoles (D) and Superconducting Triplet Quadrupoles (STQs). Different degraders and slits are available at various focal planes and are chosen according to the physics case. The two main features of BigRIPS are the large acceptance and the two-stage separator scheme: the angular acceptances are ± 40 mrad horizontally and ± 50 mrad vertically, with the momentum acceptance of ± 3 %. The maximum magnetic rigidity of BigRIPS is 9 Tm. The total flight path is about 118 m [Big22; Kub03].

For the present experiment, a ^{48}Ca primary beam with an energy of 345 MeV/u was used. In the first stage, the radioactive isotopes are produced and separated from its fragmentation on a beryllium production target, located at the focal plane at F0. An aluminum degrader was placed at the momentum-dispersive focal plane at F1 to separate the different isotopes.

The second stage from F3 to F7 is used for separating and identifying the different isotopes. It consists of eight quadrupole triplets and four dipoles with a bending angle of $30\,^{\circ}$. A second aluminum degrader was placed at the momentum-dispersive focal plane at F5. At the focal planes F3, F5, F7 and F13 plastic scintillator detectors were placed for Time-of-Flight (ToF) and energy loss measurements. The detector at F5 has an active volume of $240 \times 100 \times 3\,\mathrm{mm}^3$. The other plastic detectors have a smaller size of $100 \times 100\,\mathrm{mm}^2$ and different thicknesses: 3 mm (F3), 1 mm (F7) and 0.5 mm (F13). In addition, Parallel Plate Avalanche Counter (PPAC) detectors around the focal plane at F5 were used to calibrate the positions of the plastic detector at this position (see Sec. 4.2).

At BigRIPS PPACs are used for diagnosing the beam. These are position-sensitive detectors that allow to determine positions and angles of the isotopes at the different foci. Those are essential to determine the trajectories and thus the magnetic rigidity $B\rho$ which makes a precise particle identification possible. The PPACs in BigRIPS have two layers to measure the particle's x and y positions. The layers are thin parallel electrode films separated by 4 mm and are filled with a gas.

The sensitive area of one PPAC is $240 \times 150\,\mathrm{mm}^2$ [Kum+13]. After BigRIPS the beam is transported to the SAMURAI cave where the experiment took place.

In total, three different secondary beams were used in the experiment: ^{24}O, ^{27}F and ^{26}F. The ^{24}O beam lasted for $4.5\,\mathrm{h}$. As ^{24}O is the desired fragment to be detected from the main reaction, this beam is used for setting up and calibrating the fragment detectors. The beam had a sharp energy of 209 MeV/u with a spread of ≈0.4 % (RMS) and can be used for time-of-flight calibrations and sweep runs. The next beam was ^{27}F for the production of ^{26}O at the target, with a duration of $45.25\,\mathrm{h}$. The last beam, ^{26}F, took $17.5\,\mathrm{h}$. Both fluorine beams had an nominal energy of 220 MeV/u with a wide spread of about 3 % (RMS). As explained in Sec. 3.1, the ^{25}O spectrum will be used to deduce the systematic uncertainty of the measurement since it has no lifetime in the picosecond regime. The BigRIPS settings for all three beams are summarized in Appendix A.1.

3.4. SAMURAI20 Setup

3.4.1. Detectors

The SAMURAI setup is located behind BigRIPS (see Fig. 3.4) and consists of various detector systems which are installed to measure positions, energy losses and the time-of-flight of the particles. It is named after its main feature, the SAMURAI dipole magnet that separates the charged fragments from the neutrons after the reaction. Each detector system will be briefly explained in the following in the order of appearance in the beamline. More information about the SAMURAI setup can be found in [Kob+13].

The experimental setup is shown in Fig. 3.5 where the secondary beam enters from the left. The last quadrupole magnet STQ25 of BigRIPS is used for focusing the beam spot on the target position. At the beginning of the beamline two plastic scintillator detectors are installed, called Scintillators for Beam Time-of-Flight (SBT) hereafter. They serve as start detectors to trigger the Data AcQuisition (DAQ). They are followed by the Ion Chamber for Beam (ICB) which measures the energy loss of the incoming particles. Two Beam Drift Chambers (BDCs) are used to track the incoming beam from which the particles position at the target is extracted. The target is mounted between the silicon detectors in the target chambers. The two Forward Drift Chambers (FDCs) for the fragments follow the silicon detectors. They measure the positions before and after the deflection in the SAMURAI magnet. The particles are then detected in the HODoscope for Fragments (HODF) which measures the time-of-flight and the energy loss in the detector volume. Neutrons from the decays are not bent by the magnetic field and are detected by two neutron detection systems, the new Large Area Neutron Detector (NeuLAND) demonstrator and the NEutron Detection System for Breakup of Unstable Nuclei with Large Acceptance (NEBULA), which are placed at zero degree. The Caesium Iodide Array for γ-ray Transitions in Atomic Nuclei at high Isospin Asymmetry (CATANA), placed between BDC2 and the target area, was installed but not used in this experiment.

Start Detectors

The two start detectors are plastic scintillator detectors similar to the ones in BigRIPS. They are equipped with a PhotoMultiplier Tube (PMT) on the left and right side which is read out with a

Time-to-Digital Converter (TDC) and Charge(Q)-to-Digital Converter (QDC) after signal shaping. The active volume is $100 \times 100 \times 0.5\,\mathrm{mm}^3$ each. The start time is the average of the times at which the four signals from the PMTs occurred. The difference of the time signals from the left and right PMT is proportional to the position at which the particle passed the detector. The average charge is given by the square root of the product of the individual charges measured in the left and right PMTs. These relations can be deduced from the behaviour in the scintillator material. The charges measured on the left q_L and right q_R side are given by

$$q_\mathrm{L} = q_0 \cdot \exp\left(-\frac{L/2 - x}{\lambda}\right) \qquad \text{and} \qquad q_\mathrm{R} = q_0 \cdot \exp\left(-\frac{L/2 + x}{\lambda}\right), \tag{3.1}$$

where q_0 is the deposited charge by the particle, L the total length of the plastic scintillator, x the point of incidence and λ the attenuation in the scintillator material [Fuk+13; Sua16]. By multiplying these two relations, one can calculate the incident charge q_0 with

$$q_0 = \sqrt{q_\mathrm{L}\, q_\mathrm{R}} \cdot \exp\left(\frac{L}{2\lambda}\right). \tag{3.2}$$

If no absolute charge calibration is necessary, this can be approximated to $q_0 \propto \sqrt{q_\mathrm{L}\, q_\mathrm{R}}$. From the time signals measured at the left and right end of the scintillator the point of incidence x of the particle can be calculated. Since the velocity of light in the scintillator v stays constant during the travel from x to the left and right PMTs, it follows that

$$x = \frac{v}{2} \cdot (t_\mathrm{L} - t_\mathrm{R}) \propto \Delta t. \tag{3.3}$$

ICB

The ICB is a multi-layer ionization chamber. It has an active volume of $140 \times 140 \times 420\,\mathrm{mm}^3$ and is filled with P10 gas mixture which consists of $10\,\%$ methane and $90\,\%$ argon. It has 10 anode and 11 cathode planes which are $21\,\mathrm{mm}$ apart. A voltage is applied to create a potential difference between the anodes and cathodes. If a charged particle passes the detector, it will ionize the gas. The positive and negative charges will separate and will drift towards the electrodes. This will create a measurable signal in the detector and will give information on the energy loss of the particle. The nuclear charge can be determined by using the Bethe-Bloch formula with the measured energy loss ΔE and the velocity β as input:

$$-\frac{\Delta E}{\Delta x} = \frac{4\,\pi\, e^4\, Z^2}{m_e\, c^2\, \beta^2} \cdot N\, z \cdot \left[\ln\left(\frac{2 m_e\, c^2\, \beta^2}{I}\right) - \ln\left(1 - \beta^2\right) - \beta^2\right], \tag{3.4}$$

where Δx is the distance traveled within the material, e the elementary charge, m_e the electron mass, c the speed-of-light and Z the charge state of the passing particle. The quantities N, z and I represent the properties of the material which are atomic density, atomic number and the mean excitation potential respectively [Fuk+13].

BDCs

The BDCs are Multi-Wire Drift Chambers (MWDCs). Each BDC consists of eight planes which are

arranged in the x and y direction to track the path of the particles through the detector. Each plane has 16 wires mounted parallel to each other. The BDCs have an active area of $80 \times 80\,\mathrm{mm}^2$ where the anodes and cathodes are 2.5 mm apart. This defines the drift length of the charges. The detector volume is filled with a gas mixture of $40\,\%$ helium and $60\,\%$ methane.

Target Area
Two vacuum chambers were installed in the beamline containing the target surrounded by three silicon detectors. The detectors and the target were mounted on remote controllable drives to be able to move them out of the beamline. The detailed setup of the target area is explained in Sec. 3.4.2 and shown in Fig. 3.6a.

FDCs
The FDCs are multi-wire drift chambers like the BDCs. The operation gas for both FDCs is a mixture of $40\,\%$ helium and $60\,\%$ methane. The first FDC is placed between the target and the magnet to measure the angle and position of the emitted fragments entering the magnet. It has a circular active area with a diameter of 315 mm and an opening for neutrons in the size of $620 \times 340\,\mathrm{mm}^2$. In total, there are 14 planes with 32 wires each. Six planes are arranged in x direction, the other eight planes are rotated by $\pm 30\,^\circ$. The drift length between the wires is 5 mm.

The second FDC is placed behind the magnet at $90\,^\circ$ to measure the outgoing positions of the fragments. From the measurements of the two FDCs the bending radii can be determined and therefore the magnetic rigidity of the particles. The wires are arranged in a hexagonal cell structure with 10 mm drift length on the detection planes. These planes are oriented in x direction as well as rotated by $\pm 30\,^\circ$. Two planes with the same orientation are separated by shield wires. There are in total 14 planes and 8 shield wires. The FDC2 has an active volume of $2296 \times 836 \times 860\,\mathrm{mm}^3$.

SAMURAI Magnet
The SAMURAI spectrometer is a multi-purpose device. It is build on a rotational stage and can be rotated from $0\,^\circ$ to $90\,^\circ$. The dipole magnet has cylindrical poles with diameters of 2 m and superconducting coils around it which are cooled with liquid helium. The maximum magnetic field in the center of the poles can reach 3 T, with a maximum field integral of 7 Tm [Shi+11]. The vacuum chamber inside the magnet has a large gap space of 3 m horizontally and 0.8 m vertically to allow for large acceptance measurements. It has two exit windows for the charged fragments and the neutrons [Shi+13]. The magnetic field during the experiment was 2.2 T and the magnet was rotated by $60\,^\circ$.

Hodoscope HODF
The hodoscope is used to measure the time-of-flight and the energy loss for the particle identification of charged fragments. It is placed behind the FDC2 at $60\,^\circ$ and consists of 24 plastic scintillator bars with a size of $1200 \times 100 \times 10\,\mathrm{mm}^3$ which are aligned vertically. The ends of the bars are coupled to PMTs via light guides. Scintillation light will be detected at both ends of the bars and allows for a position and energy loss measurement. The time difference of the two signals is proportional to the position in the detector and the integral of the signal to the energy loss.

NeuLAND and NEBULA
NeuLAND is a neutron detector designed for the Reactions with Relativistic Radioactive Beams (R^3B)

setup at GSI/FAIR [Bor+21]. It is designed to have a high efficiency, high resolution and is able to reconstruct multiple neutrons. In the present experiment the NeuLAND demonstrator was used with 4 double-planes with 100 plastic scintillator bars each. It was placed at $0\,^\circ$ deflection angle. The final detector for R^{3}B will have 30 double-planes [Col11a]. Each double-plane consists of 50 horizontally and 50 vertically oriented scintillator bars with a size of $2500 \times 50 \times 50\,\mathrm{mm}^3$. The ends of each bar are connected to a PMT. The scintillator bar and the light guides are produced in one piece to reduce losses between them. A veto detector with eight paddles of size $1900 \times 320 \times 10\,\mathrm{mm}^3$ was placed in front of the NeuLAND demonstrator. The NEBULA detector is placed behind NeuLAND. It consists of 120 bars of plastic scintillators for neutron detection and 24 bars for the veto detector. All bars are oriented vertically and have a size of $1800 \times 120 \times 120\,\mathrm{mm}^3$, where the veto bars are the same as for NeuLAND. The ends of each bar are connected to PMTs. The detector is build in six layers, one veto layer is followed by two neutron layers.

The neutron detectors measure the time-of-flight, position and energy deposition of the neutrons. The position in beam and horizontal direction (vertical for every second layer in NeuLAND) is given by the scintillator bar. The position along the bar length is determined by the time difference between both ends of the bar.

The NeuLAND demonstrator was shipped to RIKEN in 2015 where it was commissioned [Kah+16] and used in a two year long campaign of experiments [Kah+17a]. With the combination of the NEBULA detector and the NeuLAND demonstrator the detection and reconstruction of four neutrons was possible for the first time [Leh21].

3.4.2. Target Area

Reaction Target

The target used for this experiment consisted of six sheets of material in order to see the difference of in- and out-of-target decays and to be sensitive to a range of lifetimes as described in Sec. 3.1. The first four sheets were made of tungsten, whereas the last two sheets were made of platinum. The distance between the individual target sheets was reduced to $8\,\mathrm{mm}$. The size of each target sheet was $60 \times 65\,\mathrm{mm}^2$. The thickness of each target decreased with beam direction. The target area with the reaction target is schematically illustrated in Fig. 3.6a.

The target stack was mounted on a drive which could remove the target from the beam axis. On the top and bottom of the holding structure, the target sheets were clamped together between spacing bars made of aluminum to have an equal distance between the sheets. The bars were threaded on four rods and fixed with nuts. At the front and end, the rods were fixed with thin aluminum strips as an additional security measure which did not overlap with the target area. The spacing bars had additional noses on top and bottom to guarantee a proper alignment during the assembly. A special box was designed to simplify the mounting and the transport of the target stack. The assembled target with the holding structure is shown in Fig. 3.6b.

Every sheet was checked with a spectral photometer by the target laboratory at GSI for quality and uniformity of the materials. The best ones were used for the experiment. It was necessary that the thickness of one sheet corresponds to its design value and that is does not vary over the area of the sheet since the target thicknesses are matched to each other. It was found in [Kah+17b] that a deviation in thickness of $\pm 5\,\%$ would smear out the velocity-difference distribution such that the

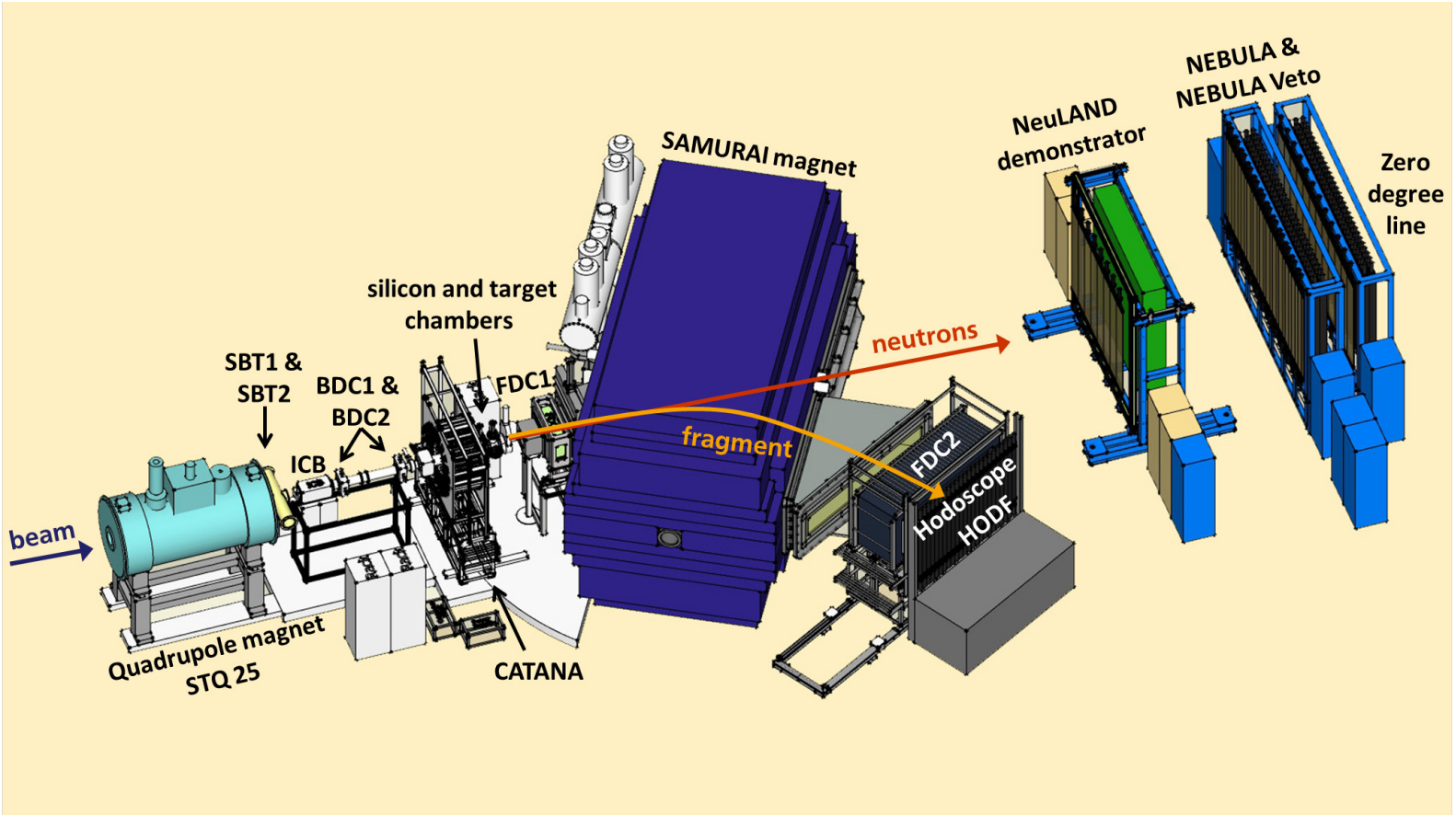

Figure 3.5.: Schematic setup of the SAMURAI20 experiment. After the last quadrupole magnet of BigRIPS the start detectors SBT1 and SBT2 are placed. They are followed by the ICB for energy loss measurement and the two BDCs for tracking. The CATANA γ-detector was not used in the experiment. The target is placed between silicon detectors in the two target chambers. The FDCs track the charged particles through the SAMURAI magnet which are measured in the hodoscope. The neutrons are not bend by the magnetic field and are detected by the NeuLAND and NEBULA neutron detectors which are placed at zero degree.

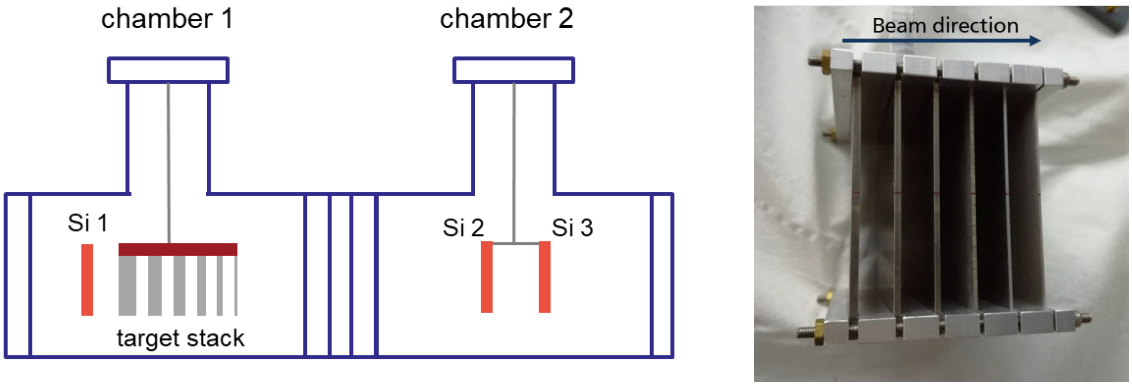

(a) (b)

Figure 3.6.: (a) Schematic setup of the target area with the beam coming from the left. One silicon detector is installed in front of the target stack and two silicon detectors are installed behind the target in the second chamber. (b) A picture of the target stack. Six target sheets decreasing in thickness are mounted together in a stack forming the reaction target. The first four sheets are made of tungsten and the last two of platinum.

Table 3.1.: Nominal and measured thicknesses of target sheets in use. The target sheets are numbered according to their order in beam direction. The average thickness was measured by the target laboratory at GSI. The sheets that matched their design value best and did not have a large deviation throughout the material were used for the experiment.

nr.	material	nominal thickness in mm	average thickness (measured) in mm	area density in g/cm^2	deviation in %
1	W	2.032	2.042	3.931	0.49
2	W	1.524	1.586	3.053	4.07
3	W	1.270	1.354	2.606	6.61
4	W	1.016	1.055	2.031	3.84
5	Pt	0.770	0.777	1.667	0.91
6	Pt	0.610	0.614	1.317	0.66

(a)

(b)

Figure 3.7.: (a) Micron MSX25 silicon detector with 2 channels, one for the back side and one for the front side. (b) Canberra type RF/PF 50*50 detector. The Micron silicon detector was mounted in front of and two Canberra detectors were mounted behind the target.

required precision could not be reached. The final target characteristics are summarized in Tab. 3.1. The last column in the table give the mean deviation from the design value. All values except for the third target lie within the constraint.

Silicon Pin Diodes

For the experiment, three silicon pin diode detectors were used. One was mounted in front of the target and two behind. They are used to measure the energy loss directly in front and behind the target, hence to determine the nuclear charge Z before and after the reaction. More details about the working principle of silicon detectors are presented in App. D. These are single sided silicon pin diodes with a thickness of 300 µm which are available from Micron Semiconductor Ltd of type MSX25 shown in Fig. 3.7a (Si 1) and from Canberra of type RF/PF 50*50 shown in Fig. 3.7b (Si 2 & Si 3). They have an active area of $5 \times 5\,\mathrm{cm}^2$ and are n-type semiconductors. During the preparation time before the measurement, all available silicon detectors were tested with an α-source. Based on these tests, the three best detectors were selected for the experiment. More details about the tests are described in [Sto18].

3.4.3. Trigger Logic

During the experiment the data was taken by the DAQ system. It is able to store data on an event-by-event basis. Since not all data is interesting for the analysis, different trigger settings are available. The trigger is a logical signal that starts the data recording when some user-specified conditions are met, *e.g.*, detectors firing in coincidence. The different trigger settings are summarized in Tab. 3.2.

The beam trigger is released when the start detector (SBT) measures a signal and no other detector fires. For the fluorine beams, the beam trigger was downscaled by a factor of 100 which means that only every 100th event is recorded. In addition, triggers including the fragment and the neutron detectors were available. The second trigger included the HODF and the NEBULA detector in addition to the start detector and the third trigger included NeuLAND instead of NEBULA. For these reaction triggers, the beam trigger was not downscaled. In order to select a specific trigger, the

Table 3.2.: Trigger conditions available during the experiment. The selected detectors need to fire at the same time for the trigger to be released. Trigger bit seven was used for the data acquisition during the experiment and trigger bit one or two are used for the analysis.

Trigger Bit n	Detectors				
	Beam (SBT)	HODF	NEBULA	NeuLAND	HIME
0	X/100				
1	X	X	X		
2	X	X		X	
6	X	X			X
7	$n = 0$ or 1 or 2 or 6				

respective trigger bit can be enabled. During the experiment, trigger bit seven was selected meaning that an event is recorded if one of the conditions is fulfilled. For the analysis, trigger bit $n = 1$ or $n = 2$ are selected. The HIME prototype detector was running parasitic during the experiment. It was placed behind the neutron detectors and is not used for the analysis. More details about the setup of the RIBF DAQ can be found in [Bab+10].

4. Calibration

During the experiment, the data is stored in a raw format. In order to analyze the data, it has to be converted into physical units. This is achieved by the calibration of the data, where conversion parameters and corrections are applied and the data is synchronized. The goal of the calibration procedures is to determine these parameters.

The software used for the calibration and later for the data analysis is ROOT developed by the European Organization for Nuclear Research (CERN) [Bru+97]. It is an object-oriented software, based on the programming language C++ and used for large scale data analysis on an event-by-event basis. During the experiment the raw data was stored in `ridf`-files which are produced by the RIBF DAQ system using AnaROOT. AnaROOT is a ROOT based analysis framework developed at RIKEN [Iso13]. It is used for online and offline analysis of RIBF experiments since it is optimized for reading the `ridf`-files and it includes experiment specific data classes with which the calibration parameters for the different detector systems can be applied.

The calibration procedures of the SAMURAI detectors will be presented in this chapter. In Sec. 4.1 the photogrammetry measurement is performed, where the exact detector positions are determined and the coordinate system is introduced. Next, the calibration of the in-beam plastic detectors of BigRIPS and SAMURAI is introduced in Sec. 4.2. In Sec. 4.3, the energy loss detectors before the SAMURAI magnet are calibrated to identify the charges of the incoming and the reacted particles. The energy loss and the time-of-flight of the incoming beam are evaluated at the assumed reaction position in Sec. 4.5. The MWDCs, used for tracking of the particles before and after the magnet, are introduced in Sec. 4.6. Afterwards, the calibration of the fragment hodoscope behind the SAMURAI magnet is explained in Sec. 4.7 and the neutron detectors NeuLAND and NEBULA in Sec. 4.8. Finally, the stability of the time measurements over the duration of the experiment is investigated in Sec. 4.9. The figures shown in this chapter during the calibration processes are using data from the ^{27}F setting unless stated differently.

The calibration of certain in-beam detectors, *e.g.*, the PPAC, the plastic detectors, the MWDCs, and the ICB, was already done during my Master's thesis and are shown here again for completeness. A more detailed description of the individual calibration steps of these detectors can be found in [Sto18].

4.1. Photogrammetry Measurement

For many of the calibration procedures the exact positions of the detectors and the distances between them need to be known. For this, a photogrammetry measurement is performed using a commercial solution of a PhotoGrammetry System (PGS) called V-STARS [Pro22]. With this measurement, the positions can be determined very accurately with an uncertainty in the order of 100 μm.

Each detector and other important structures are equipped with phosphorescent markers, called targets. In addition, two scale bars with the length of 1 m are placed in the setup that are used as a reference to scale distances among the different measurement points. The program can recognize the targets and scale bars from a large number of photos. Using the recognized structures, a 3D model of the setup is produced where distances between targets can be measured accurately.

All detectors are placed in a common coordinate system. The system used for SAMURAI experiments has its origin in the center of the SAMURAI magnet with the z-axis being in beam direction, the y-axis pointing upwards and the x-axis pointing to the left (looking in beam direction), forming a right-handed coordinate system. For the fragment detectors behind the magnet, the coordinate system is rotated by $60\,^\circ$ and labeled with (x', y', z') in the following. In order to improve the measurement, misidentified targets and reflections from shiny surfaces are removed manually in the PGS program. From this, the identified points are used to place geometrical objects in the model, *e.g.*, planes modeling the detector surfaces, with which distances and angles between objects can be measured.

The S20 experiment was running in a campaign of three experiments where PGS measurements were already performed. Only FDC2 and the hodoscope were moved between experiments and therefore only this area was remeasured, see Fig. 4.1. The position information of the detectors in front of the magnet are taken from the measurement of the experiment that took place before (S27) and are shown in Fig. 4.2. In cases where it was not possible to reconstruct a distance, values were also taken from the design sheets or measured by tape.

NeuLAND and NEBULA have not been moved between the experiments. By comparing the results of both measurements the accuracy of this method can be estimated. The extracted lengths from the center of SAMURAI to NeuLAND and NEBULA differ at maximum by 0.03 %. The distance from the center of the magnet to FDC2 could not be measured directly. On the detector side facing the magnet no photogrammetric targets could be recognized. Instead, points located on one side of the detector frame were used.

In addition, the offset of the center of the fragment detectors to the 60 ° line can be determined. The FDC2 offset value in x direction from the photogrammetry is -104 mm. This value is comparable to the value of -105 mm determined with tape measure after moving the detector. On the side planes of the HODF not many points were recognized by the program. For this reason, the position of the side planes could not be determined very precisely. The deduced offset value is -165 mm. If this value is compared to the one measured by tape which is -155 mm, the discrepancy is very large. Under the assumption that the FDC2 value is correct, the HODF offset can be determined from data. For this, a position cut on the center of FDC2 with small outgoing angles is performed. Then, the transition from one HODF bar to the next can be determined by looking at the ratio of entries in neighboring bars. If the ratio is equal to 1, the transition between two bars is hit. With this method the HODF x offset was determined to be -152 mm. This value is much smaller than the one deduced from the photogrammetry and fits to the manually measured value and is therefore used for the analysis.

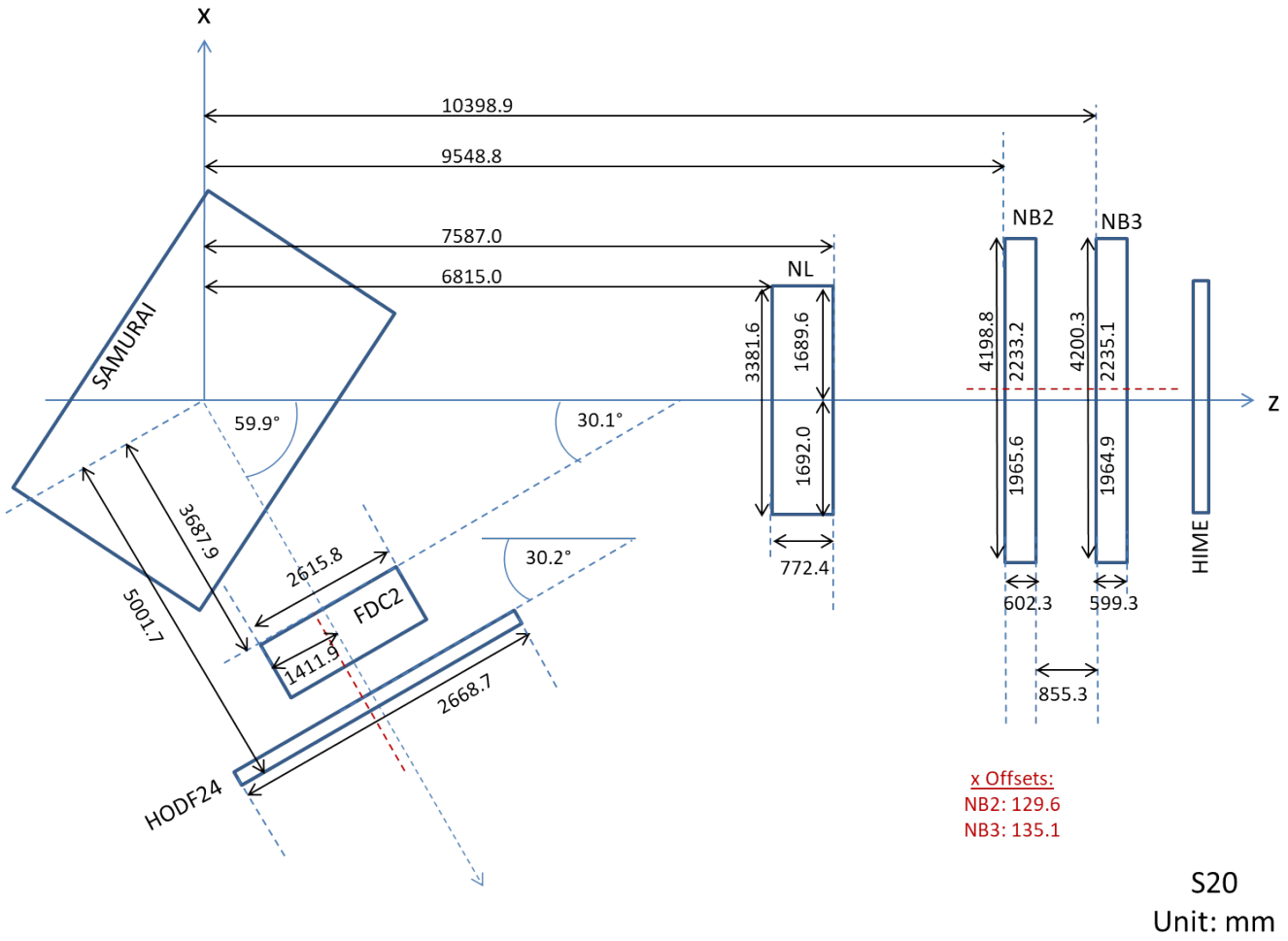

Figure 4.1.: Result of the photogrammetry measurement of the S20 experiment for the region behind the magnet. All lengths are given in mm. Detector sizes are not drawn to scale.

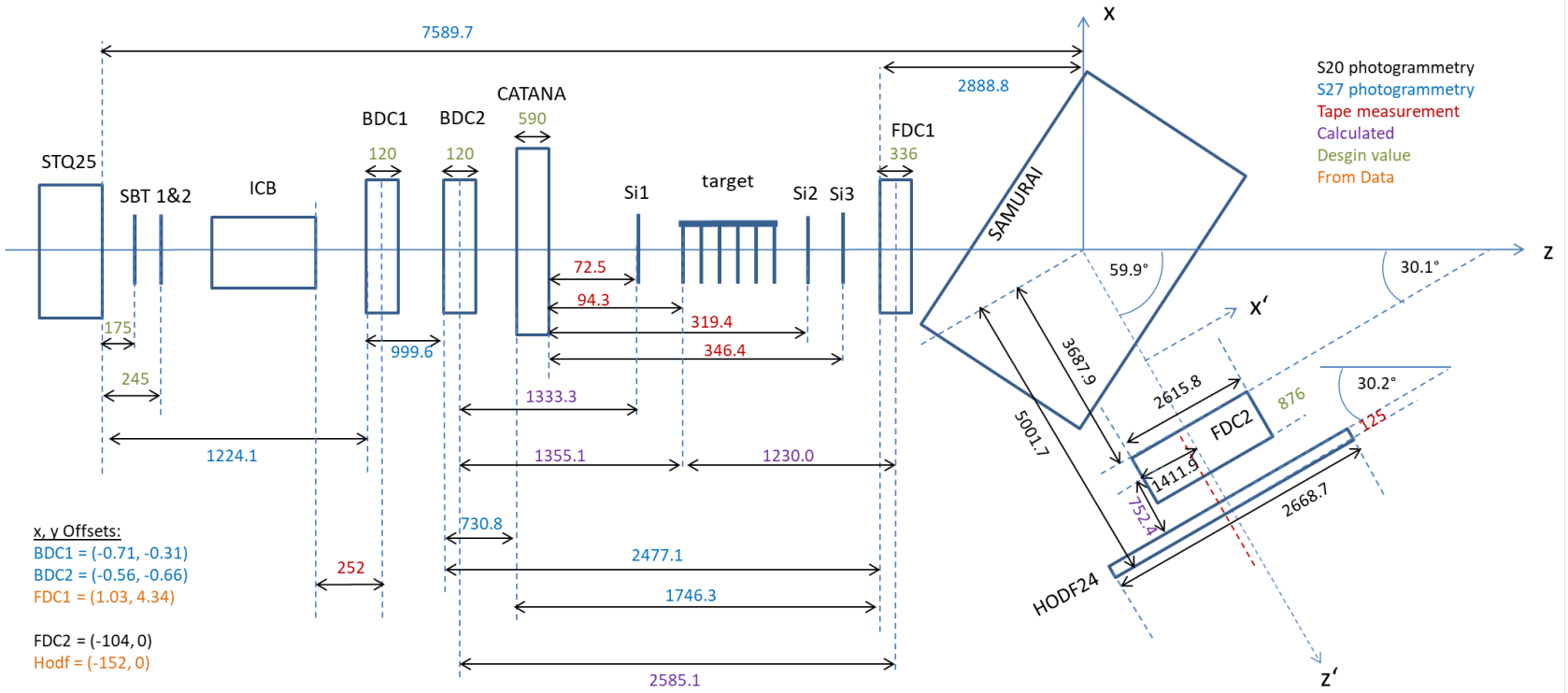

Figure 4.2.: Schematic setup of S20 experiment with the detectors in front of the magnet. All lengths are given in mm. Detector sizes are not drawn to scale.

4.2. BigRIPS Plastic Scintillation Detectors

The BigRIPS separator has several plastic scintillation detectors installed close to the different focal planes. The ones used during the experiment were installed at the focal planes F3, F5 and F7, cf. Fig. 3.4 to measure the time-of-flight of the incoming ions. The plastic detectors at F13, also called SBTs, close to the target focal plane at the entrance to the SAMURAI cave are used as start detectors for the experiment.

First, the raw signal from the TDC has to be converted into a time. With this, the absolute time-of-flight from the different focal planes of BigRIPS to the SAMURAI setup can be calibrated. Finally, the plastic scintillator at F5 is calibrated in position. With the position information of this detector the mass-to-charge ratio can be determined, since they will appear at different positions at the momentum-dispersive focal plane at F5. Together with energy loss detectors and the absolute time-of-flight, this information can be used for the incoming particle identification.

4.2.1. Time Calibration

At the beginning of the experiment, time calibration runs are performed where a pulse is given to the electronics of the detectors every 10 ns. The pulses are very sharp and since their distance in time is known, one can assign the correct time in ns to the TDC channels. Each pulse in the uncalibrated spectrum is fitted with a Gaussian function to determine the mean position and is assigned to its expected value. The slope of this linear correlation gives the conversion parameter from the raw signal to the time in ns. The measured charge does not need to be converted from raw values to physical units since an absolute calibration is not needed.

The start detectors (SBTs) at the entrance of the SAMURAI beamline generate the signal which is used as beam trigger for the DAQ and time reference. In order to improve the resolution, the time and charge measurements of both SBTs are averaged

$$t_{\mathrm{SBT}} = \frac{1}{4}(t_{0,\mathrm{SBT1}} + t_{1,\mathrm{SBT1}} + t_{0,\mathrm{SBT2}} + t_{1,\mathrm{SBT2}}) \quad \text{and} \quad q_{\mathrm{SBT}} = \frac{1}{2}(q_{\mathrm{SBT1}} + q_{\mathrm{SBT2}}). \tag{4.1}$$

The time resolution, determined using the ^{24}O beam with a very narrow energy ($\sim 3\,\mathrm{MeV/u}$), is 101 ps, given by the standard deviation of a Gaussian fit. This value includes the resolution of both detectors. Under the assumption that both detectors have the same resolution, the individual resolution can be calculated and is given by 71 ps (σ).

4.2.2. Position Calibration with the Parallel Plate Avalanche Counter (PPAC)

During the experiment, two PPACs around the plastic detector at F5 were used. One PPAC is positioned in front and one after the plastic scintillator. They are used to calibrate the position of the plastic detector and are then removed from the beamline for the production runs of the experiment.

For light beams, the position resolution required to determine the magnetic rigidity is not critical, such that only the F5 plastic scintillator with high efficiency was used. The data of a dedicated calibration run (run 462) with full acceptance and low intensity, where both PPAC and plastic

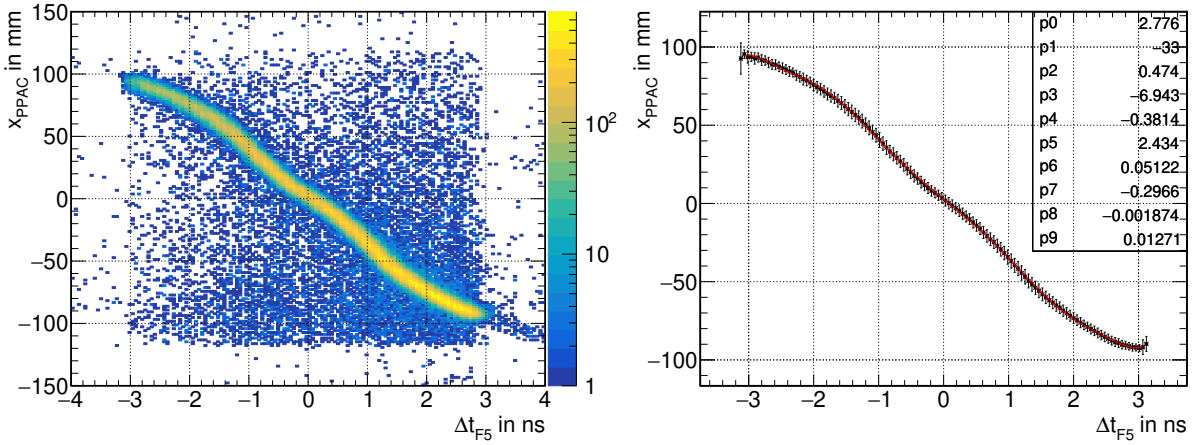

Figure 4.3.: (a) Position on the PPAC vs. position on the plastic detector at F5. The plastic detector shows a position dependence which will be corrected with the PPAC. (b) The histogram in (a) is cut into slices along the x axis and each slice is projected to the y axis. The projection is fitted with a Gaussian function. (b) The mean of each fit is filled into a graph used for the correction.

detectors, were in operation, are used to calibrate the position of the plastic detector. For the calibration, the measured PPAC positions are plotted against the time difference measured by left and right PMTs of the plastic scintillator, which is proportional to the position $x_{F5} \propto t_{0,F5} - t_{1,F5}$. This plot is shown in Fig. 4.3a for a ^{27}F beam. One can see a position dependence of the plastic detector which has to be corrected for further analysis. Each bin on the x axis is projected onto the y axis and fitted with a Gaussian function. The mean of each fit is then filled into a graph and fitted with a polynomial, see Fig. 4.3b. In this case, a polynomial of 9th order produces the best fit results which is used to correct the position dependence of the plastic detector.

4.2.3. Background Reduction

Background stemming from reactions in the beam line or electronic effects can already be reduced for the calibration procedure. More details about the background reduction are described in [Fuk+13]. The plastic scintillator detectors at the different focal planes F3, F5 and F7 of BigRIPS and both SBTs at SAMURAI are used for background cuts in time. The raw PMT signals within each detector are correlated, as shown in Figs. 4.4a and 4.4b for the detectors at F3 and F5 as an example, with the graphical cuts indicated by the red boxes. The signals appearing off the diagonal and at smaller values on the diagonal are produced by incomplete measurements in one or both of the PMTs and electronic artifacts. Additionally, background cuts are applied to the correlation of different energy loss detectors: the energy loss measured at F7, the ICB and the first silicon detector in front of the target and are shown in Figs. 4.4c and 4.4d. With these cuts, reactions along the beam line and within the detectors can be removed. The background cuts in time and charge are applied in all calibration and analysis steps.

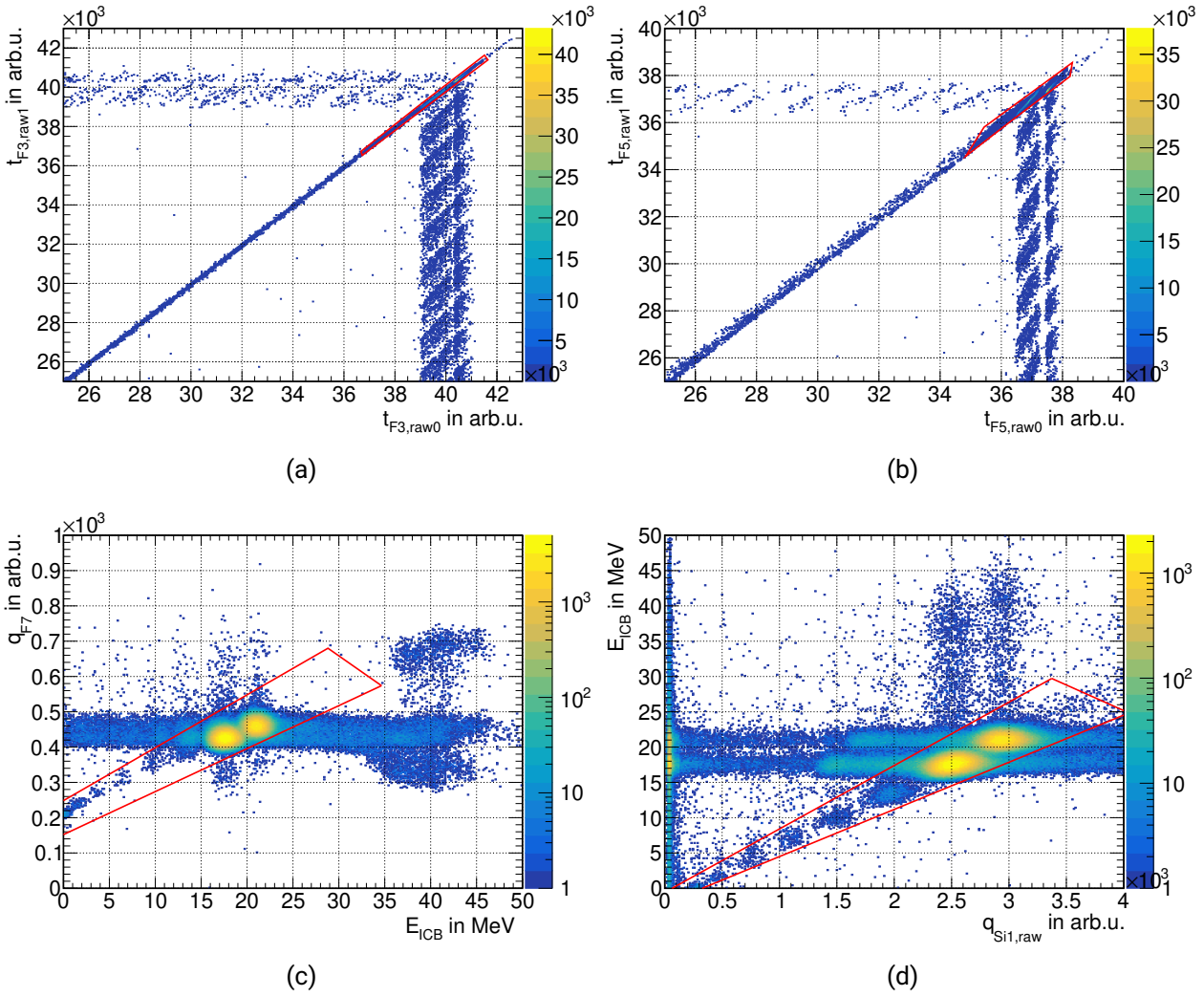

Figure 4.4.: Background reduction cuts for correlations in raw PMT times in the plastic scintillator detectors at (a) F3 and (b) F5. Background stemming from reactions along the beam line is removed with the energy loss correlations between (c) ICB and F7 and (d) Si1 and ICB. The graphical cuts are indicated by the red boxes.

4.3. Energy-loss Detectors before the Magnet

If a charged particle passes through material, it will lose energy according to the Bethe-Bloch formula (Eq. 3.4). This information can be used to determine the charge of the incoming particles and thus identification of the particle. In the S20 experiment, the ICB and the silicon detectors were installed for this purpose and are calibrated as described in the following.

4.3.1. Ion Chamber for Beam (ICB)

The ICB is a multi-layer ionization chamber which measures the energy loss of the passing particles. The conversion from raw Analog-to-Digital Converter (ADC) channels to energy in MeV was already done during the experiment and does not have to be done again since it is a hardware specific conversion. The raw signal for one event is given by the average charge per channel and is then converted into MeV by a linear function.

In order to determine the nuclear charge Z of a passing ion, the energy loss in the ICB is plotted against the time-of-flight between the F7 and the SBT plastic detectors, see Fig. 4.5. Several peaks are visible that belong to the different isotopes in the beam. A dependence on the ToF can be seen in the distribution which is corrected to improve the resolution. The Bethe-Bloch formula can be approximated as $Z \propto \sqrt{\Delta E}\beta$ with which the nuclear charge can be calculated. It follows that the β-dependence on the charge can be removed by multiplying the energy loss with β or performing a correction of the time-of-flight. Since the β was not yet available at this point of the calibration the latter method was chosen. For this, the most prominent peak which belongs to ^{27}F is fitted with a linear function to determine the slope of the dependence. Each event is shifted by the distance to an arbitrarily determined mean. This ensures that the distances of the peaks stay constant. The corrected histogram is shown in Fig. 4.5b. No further correction is needed, since the charge peaks are already uniform. The three most prominent peaks are projected to the y axis and fitted with a Gaussian function. Since the components of the beam are known, each peak can be assigned with the correct Z value. The means derived from the fit are then plotted in a graph at the correct Z value. A linear fit determines the parameters for the conversion from the ICB energy signal to the Z value of the particle, where the result is shown in Fig. 4.6. The ICB has a charge resolution of $\sigma(Z)/Z = 1.5\,\%$ for $Z = 9$.

4.3.2. Silicon Pin Diodes

In addition to the ICB, three single-sided silicon detectors were used to identify the Z of each passing particle. The first, placed in front of the target, identifies the incoming particle and the two detectors after the target help to identify the reaction of interest. At the beginning and at the end of the experiment, the pedestals of each silicon detector had to be determined. Pedestals are the signals produced by the detector and the electronics without beam but with applied voltage to the detectors and electronics. For the analysis, this creates an offset which has to be subtracted. Therefore, data without beam, taken in advance of the ^{27}F beam (run 397) and after the last fluorine beam, was used (runs 493 and 497). The pedestal value of each detector is determined from a Gaussian fit and is given by the mean value plus one standard deviation. In comparison to after the experiment only

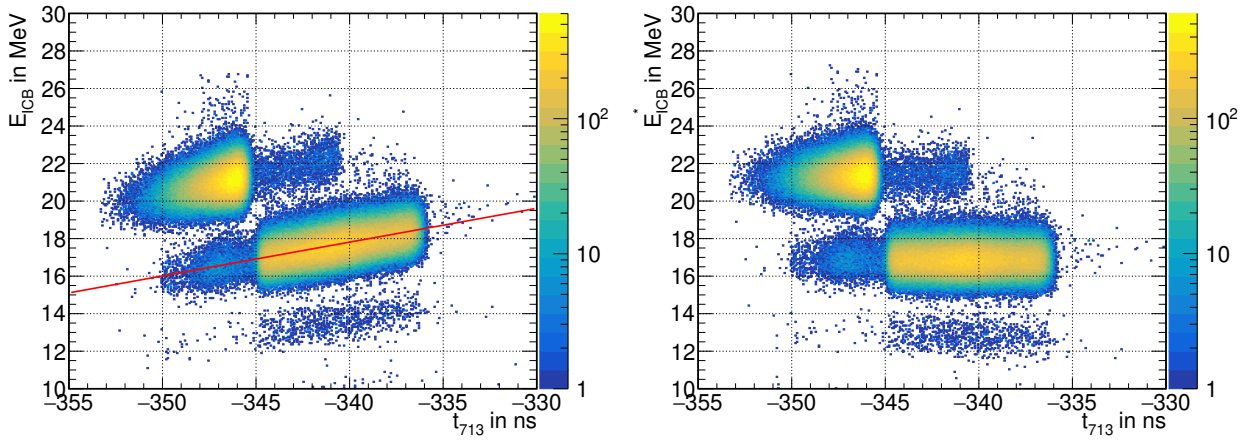

(a) (b)

Figure 4.5.: Z calibration with the ICB. (a) The ICB energy is plotted against the ToF from the plastic detector at F7 to SBT. The slope of the ToF dependence at the most prominent peak ($Z = 9$) is determined with a linear fit for the correction (red line). (b) Corrected histogram.

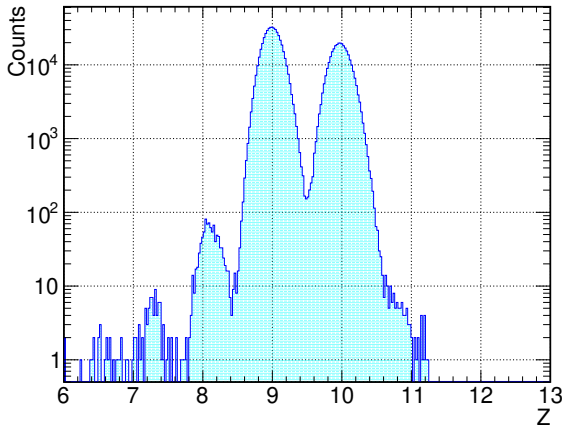

Figure 4.6.: Result of the Z calibration with the ICB, determined by a linear fit to the expected Z values.

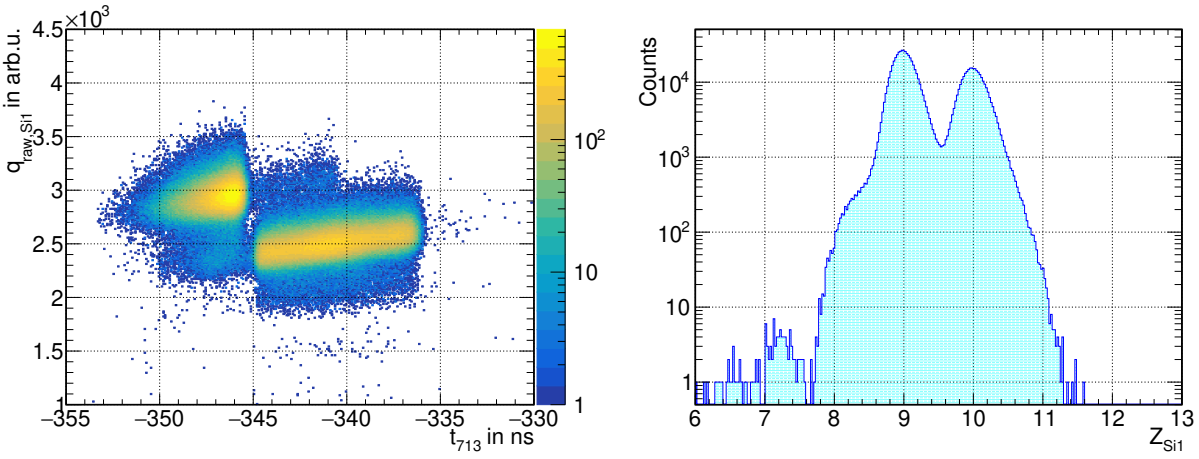

(a) (b)

Figure 4.7.: (a) Silicon energy signal from the first detector vs. the ToF from the plastic detectors at F7 to F13. The events are shifted according to the correction function and then projected to one axis. (b) Result of the Z calibration with the first silicon detector.

the third detector had a slight increase which can be neglected.

After the pedestal are subtraction, the calibration for the charge identification is applied directly. The calibration is performed similarly to the one with the ICB in Sec. 4.3.1. The raw signal of the first silicon detector is plotted against the time-of-flight from F7 to the SBTs, see Fig. 4.7a. The most prominent peak around 2500 arb.u. belongs to ^{27}F. A linear function is fitted to this distribution. Since the peaks are uniform without any distortion, no other correction besides the ToF correction is necessary. Each peak is then projected to the y axis and fitted with a Gaussian function. The means of these fits can be assigned to the expected Z values and converted with a linear fit. The result is shown in Fig. 4.7. The resulting charge resolution of the first silicon is $\sigma(Z)/Z = 1.8\,\%$ for $Z = 9$.

For the silicon detectors located behind the target, the measured charges are smeared out due to the large energy loss in the material and the associated ToF dependence. This is shown in Fig. 4.8a where the measured charge is plotted over the fragment time-of-flight for the second silicon detector. The fragment time-of-flight is obtained as described in Sec. 4.7.3. For the correction, a cut on the incoming isotope ^{27}F is performed. The peak with the largest measured charge belongs to the unreacted beam $Z = 9$. To be able to cut on the charge of interest after the target, the dependence on the time-of-flight is corrected with a linear function indicated by the red line. The correction is optimized for fragments with $Z = 8$. The resulting charge distribution is shown in Fig. 4.8b. With this correction the charge $Z = 8$ can be separated from the charges $Z = 7$ and $Z = 9$ in the projection on the y axis. Charges smaller than $Z = 7$ can not be separated with the silicon detectors, as the correction was only optimized for $Z = 8$. Again, the measured charges are converted into expected Z with a linear fit. The projection is shown in Fig. 4.8c. The charge resolution of the two silicon detectors behind the target is $\sigma(Z)/Z = 1.7\,\%$ for $Z = 8$.

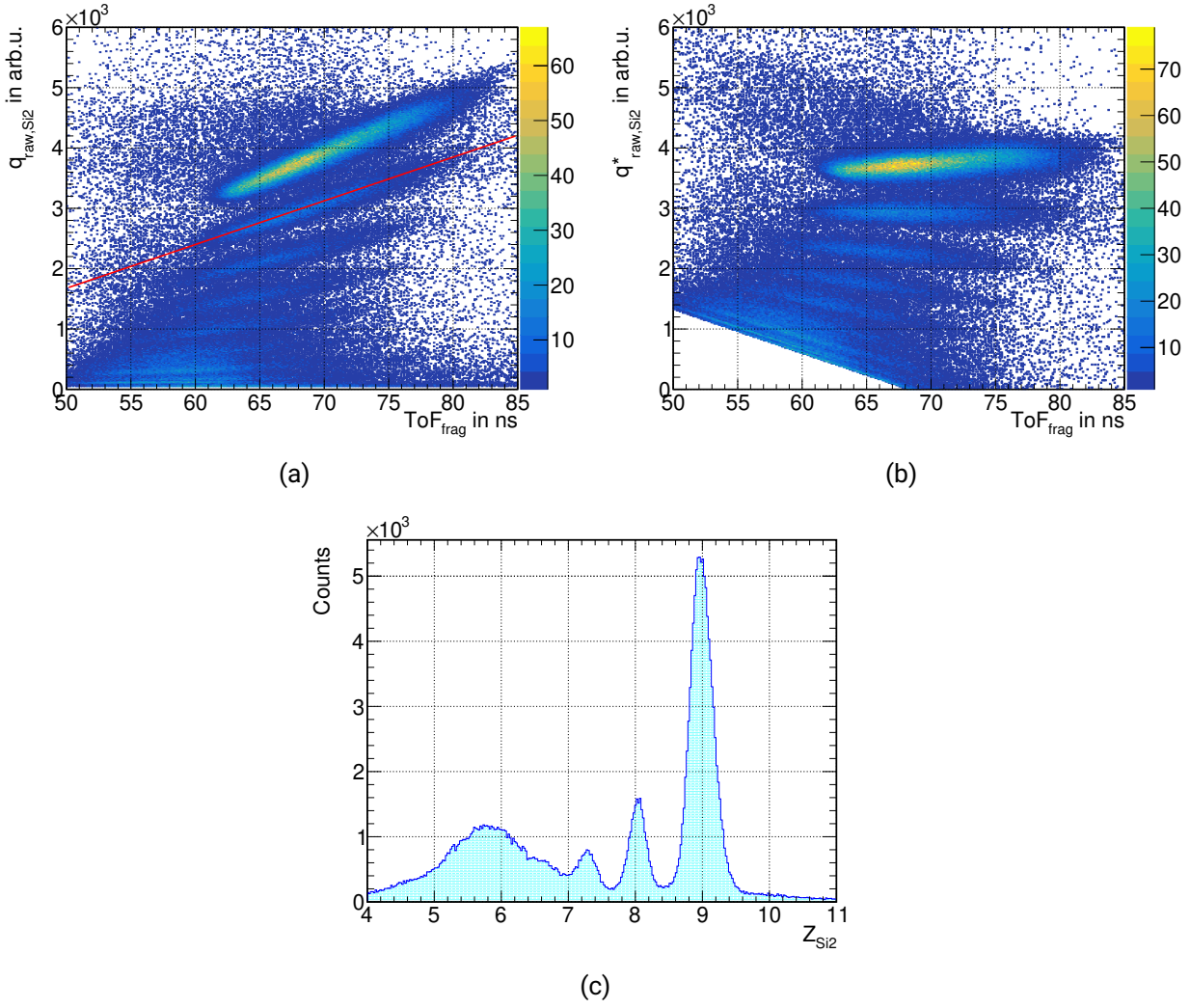

Figure 4.8.: (a) Dependence of the measured charge on the time-of-flight for Si2. This dependence is corrected with a linear fit to $Z = 8$ (red line). (b) Resulting charge distribution of Si2. The correction for Si3 is applied analogously. (c) Projection of calibrated spectrum. Charge $Z = 8$ can be separated from $Z = 9$ and $Z = 7$.

4.4. Incoming Beam Energy

The energy of the projectiles at the entrance of the SAMURAI setup, is determined using the following relation

$$E_{\text{kin}} = \left(\frac{1}{\sqrt{1 - \beta_{713}^2}} - 1 \right) \cdot m_u c^2 \tag{4.2}$$

with the unit mass $m_u = 931.494\,\text{MeV/c}^2$ and the velocity β_{713} between the focal planes at F7 to F13. For this, the velocity β_{713} has to be calibrated absolutely. This is done using the second stage of BigRIPS. In BigRIPS the particles are separated according to their mass-to-charge ratio:

$$\frac{A}{Q} = \frac{B\rho}{\beta\gamma m_u\, c} \tag{4.3}$$

with the magnetic rigidity $B\rho$ and the Lorentz factor γ. This relation can be derived from comparing the Lorentz force which acts on a particle in a magnetic field to the centripetal force. These two forces let the particle stay on a circular trajectory as long as it is deflected by the magnetic field of a dipole. This is done in the chicane of the BigRIPS from the focal plane at F3 to F5 and from F5 to F7. For fully stripped ions as is it was the case in the S20 experiment, $Q = Z$, which leads to $A/Q = A/Z$.

With this relation, the absolute time-of-flight is calibrated. The expected mass-to-charge ratio and the nominal $B\rho_0$ from the BigRIPS settings, see Tab. A.1, are used to calculate the expected velocity β and from this the expected ToF. Eq. 4.3 is solved for β to calculate the expected velocity between the different focal planes. The distance L between the plastic detectors that measure the ToF is given in [Big22]. The expected time-of-flight is given by

$$\text{ToF} = \frac{L}{\beta \cdot c}. \tag{4.4}$$

The values used for the calculations and the results are given in Tab. A.3. To calibrate the measured time-of-flight absolutely, an offset has to be determined. This is done using the uncalibrated time-of-flight between the different focal planes, determining the mean of the distribution and subtracting the expected value. With the calibrated ToF, the exact β of the individual projectiles can be calculated using again Eq. 4.4. From this, the energy of the incoming projectiles can be determined with Eq. 4.2. The resulting energy distributions for all three secondary beam settings are shown in Fig. 4.9. The ^{27}F and ^{26}F beams have a similar shape that is caused by the BigRIPS settings with a wide energy spread of about 3 % (RMS). The ^{24}O beam is much sharper in energy with a spread of about 0.4 % (RMS).

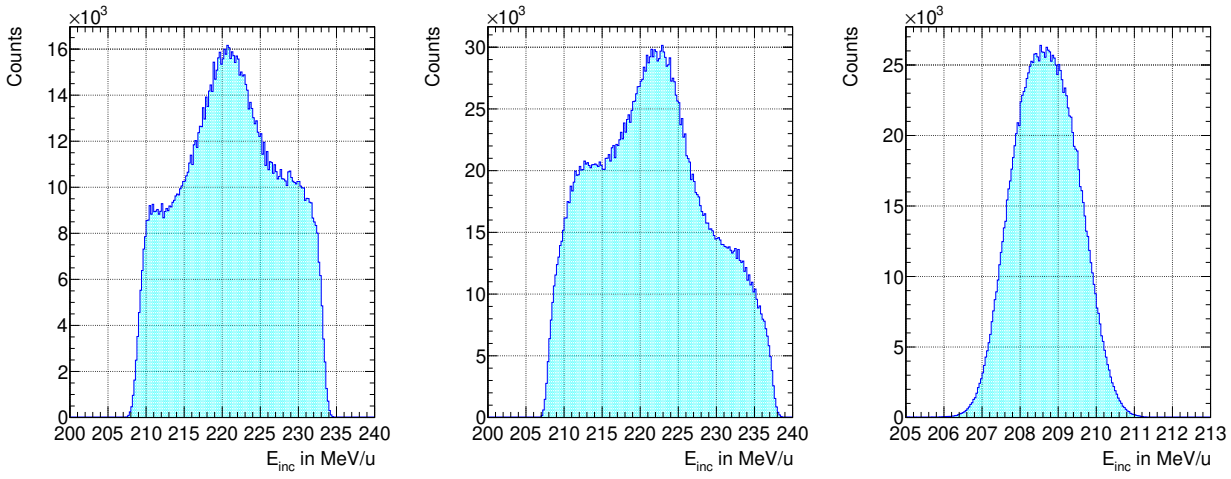

Figure 4.9.: Incoming energy distributions for (a) ^{27}F, (b) ^{26}F and (c)^{24}O beam setting with a cut on the respective isotope.

4.5. Beamline Energy Loss and Time-of-flight

As the HODF, NeuLAND and NEBULA times are measured relative to the start time and no time measurement close to the target is available, the ToF from the SBTs to the assumed reaction point has to be subtracted. In order to determine this ToF and the energy loss up to this point, a simulation, including all materials in the beamline between the SBTs and the last silicon detector, is performed. Details on the simulation are given in Sec. 6.1. Since the reaction point of the proton removal and the decay point of the ^{26}O are not known in the experimental data, an assumption has to be made. For this analysis, it will be assumed that the ^{24}O fragment starts flying from the last silicon detector, which is positioned behind the target. This means that in the simulation, the ^{27}F projectile is transported up to this point at which the energy loss and the ToF are evaluated. There are several options for valid assumptions, but since the experimental $\Delta\nu$ spectrum will be compared to a simulated one, it is only important that they are treated in the same way.

With the simulation, the ToF and the energy loss are extracted as a function of the incoming beam energy, which was determined in Sec. 4.4. By fitting the ToF from the start to the last silicon detector as well as the respective energy loss with a parabolic function, they can be estimated event-by-event based on the incoming energy of the projectile. The simulation results with the parabolic fit are shown in Fig. 4.10.

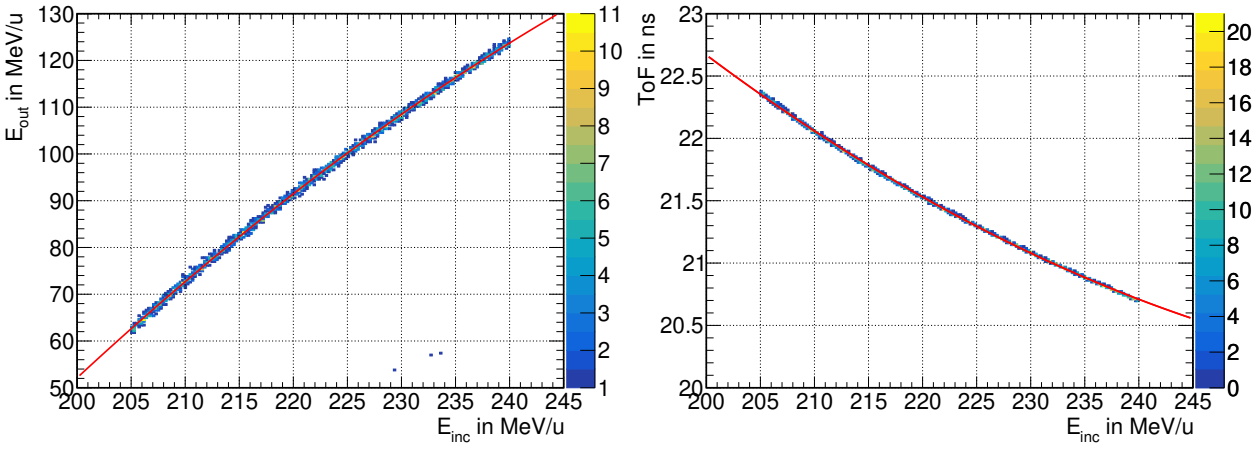

(a) (b)

Figure 4.10.: Simulated relation of the projectile (a) energy and (b) time-of-flight at the position of the last silicon detector after the target as a function of the incoming energy at the entrance of the SAMURAI cave. Each distribution is fitted with a parabolic function, which is used for the calibration of the experimental data.

4.6. Multi-Wire Drift Chambers (MWDC)

In order to determine the path of the particle through the detector, the track of the particle has to be reconstructed. If a charged particle is passing the MWDC, it will ionize the gas in the detector. The electrons will drift to the wires of the different layers and create a signal in the raw TDC spectrum. In the first step of the calibration, this raw time signal needs to be converted into a drift length. Since the distance of the individual wires in each MWDC is known, the range of the raw signal can be assigned to this length. The drift length for BDC is $2.5\,\text{mm}$, $5\,\text{mm}$ for FDC1, and $10\,\text{mm}$ for FDC2. The raw time signal of one layer of the first BDC is shown in Fig. 4.11 as an example. Cuts are applied on the raw spectrum to set the window for the maximum drift length which is indicated by the dotted lines. The events left of this window are falsely accepted because of the large trigger window of the MWDCs. The drift length for each event is then calculated by integrating the measured TDC distribution and normalizing it to the integral of the maximum drift length.

The produced signal by the passing particle corresponds to a radius around the wire in which the particle must have passed. For tracking of the particle, these radii are taken into account and a track (linear function) is fit among the wires. The track with the best fit (lowest χ^2) is assumed to be the real track. The residuum of one plane is defined as the difference between the measured radius and the reconstructed track of the particle relative to the position of each wire. The residuum is shown in Fig. 4.12a for the first layer of FDC1. In the second step of the MWDC calibration, a correction function is determined with which the dependence of the residuum on the drift length can be corrected and thus the resolution can be improved. For this, each bin along the x axis is projected to the y axis and fitted with a Gaussian function. The mean of each bin is then filled into the graph shown in Fig. 4.12b in black. The profile is used as a correction function for the drift length before the tracking procedure, such that effects like a position offset of the wires from the design value and

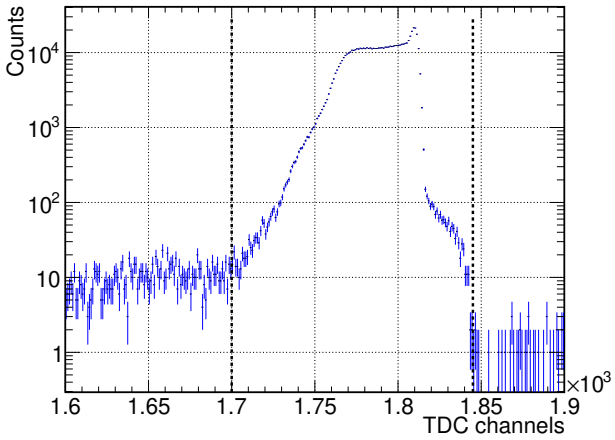

Figure 4.11.: Raw time signal in TDC channels of the first BDC for layer 1. The TDC window is set to the section marked by the dotted lines. This length determines the maximum drift length.

Table 4.1.: Position and angular resolutions of the MWDCs. Compared to the FDCs the BDCs have a large angular resolution due to their small depth in z direction. This information is not used in the experimental analysis.

MWDC	Total Residual in µm		Position Resolution (σ)	Angular Resolution (σ)
	before correction	after correction	in µm	in mrad
BDC1	91	72	104	5.25
BDC2	91	76	110	5.56
FDC1	575	177	211	1.75
FDC2	394	280	334	0.56

a drift length dependent charge collection are corrected.

With the MWDCs calibrated, the position and angular resolutions can be extracted. The position resolution for each layer is calculated from the total residuum using conversion factors. A detailed derivation of these conversion factors and the calculation of the position resolution can be found in [Kah19]. The width of the residuum is determined for each layer with a Gaussian fit to the distribution which is then converted into the position resolution. In order to extract the angular resolution, points with an error bar corresponding to the position resolution are placed on a straight line and fit with a linear function. The angular resolution is given by the fit uncertainty, that corresponds to the slope of the linear fit. The resulting resolutions are shown in Tab. 4.1. The large value for the angular resolution of the BDCs comes from their small depth in beam direction. For the experimental analysis, this information is not necessary and therefore not used.

4.6.1. Projection on the Target and Si3

After the BDC calibration, the position of the particles can be extrapolated to the target and detectors behind the BDCs. From the distance between the BDCs of $D_1 = 999.6\,\text{mm}$ and the measured positions

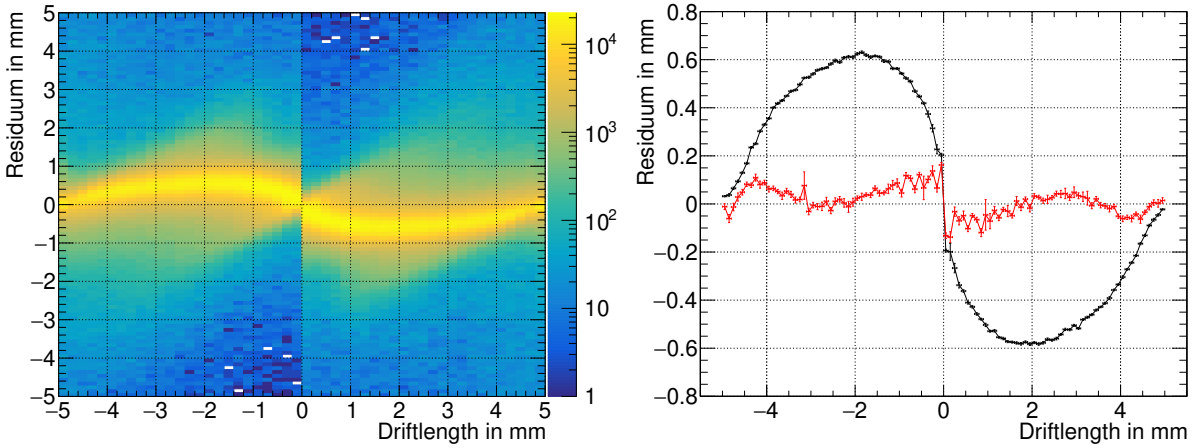

(a) (b)

Figure 4.12.: Residual vs. drift length plots for FDC1 (a) For both detectors the residuum distribution shows a strong dependence on the drift length. (b) The profile before the correction is shown in black and after the correction in red.

x_1 and x_2 in BDC1 and BDC2 respectively, the angle α_x is calculated using

$$\alpha_x = \arctan\left(\frac{x_2 - x_1}{D_1}\right). \tag{4.5}$$

As discussed in Sec. 4.5, the position of the reaction point is not known and therefore assumed to be at the last silicon detector for this analysis. The distance from the second BDC to the last silicon is $D_{\text{Si3}} = 1607.2\,\text{mm}$. From this, the position on the last silicon detector x_{Si3} is calculated using

$$x_{\text{Si3}} = \tan\alpha_x \cdot D_{\text{Si3}} + x_2. \tag{4.6}$$

and analogously for the y position. In the same way, the position can be extrapolated to the target using the distance from the second BDC to the first target sheet of $D_{\text{tgt}} = 1355.1\,\text{mm}$. With the extrapolated position at the target, a cut is applied on the size of the silicon detector which is $50 \times 50\,\text{mm}^2$ for the analysis. The size of the cut is indicated in Fig. 4.13 by the box. As shown, events are cut on the top and bottom of the beam spot. The events lost due to the size of the silicon detector are approximately $5.6\,\%$.

4.6.2. FDC1 Position Offset

The offset from the center of the beamline of the first FDC could not be determined from the PGS measurement due to lack of points (cf. Sec. 4.1). Therefore, it is determined using data from an empty target run. The offsets of the drift chambers before the target (BDCs) could be deduced from the PGS measurement and therefore used as a reference. From the BDC positions, the position on the target is extrapolated as described in the previous section. The same is done with the measured FDC1 position and angle. Comparing both extrapolated positions, gives the FDC offsets in x and y direction with $+1.03\,\text{mm}$ for x and $+4.34\,\text{mm}$ for y. The large offset is produced by the reconstructed

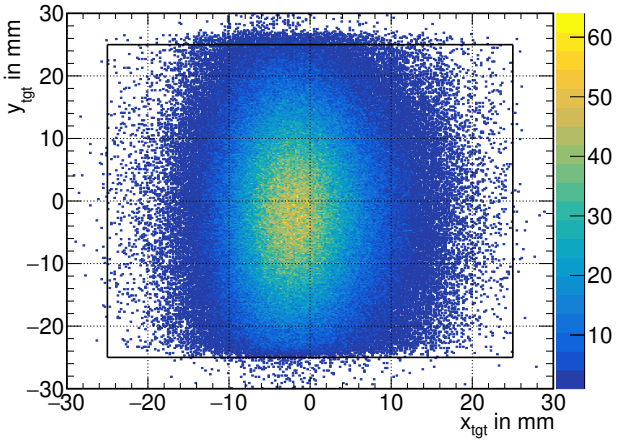

Figure 4.13.: Projected position on the target. The cut on the size of the silicon detector is indicated by the box. It removes $5.6\,\%$ of the events.

FDC1 angle. If the position is extrapolated from BDCs to FDC1, the positions agree with a small offset. Since FDC1 angle is used for the fragment reconstruction, the large offset is included into the analysis and the simulation.

4.7. Fragment Hodoscope

For the measurement of the fragment time-of-flight and charge Z, HODF is used. As explained in Sec. 3.4, the HODF consists of scintillator bars making the calibration similar to the plastic detectors. Also here, the raw time is converted into ns using time calibration runs. Afterwards, the bars have to be aligned in time and charge using magnet sweep runs and the hit position on the HODF. Finally, the absolute value of the time-of-flight is calibrated using empty target runs and comparing to simulations. With the ToF calibrated, the mass-to-charge ratio of the fragment can be determined, as explained in Sec. 5.1.

4.7.1. Charge Calibration

For the charge calibration of the HODF, the measured charges in each bar have to be aligned and corrected. This is done in several steps with sweep runs where the ^{24}O beam was swept over all bars of the HODF by changing the magnetic field. After the pedestal subtraction, the y position dependence of the charge is corrected and the bars are matched with each other. The difference between the times measured at the top and the bottom of one bar is proportional to the y position within the bar where the particle hit the detector. If the measured charge is plotted over this position, a dependence in Δt is visible as shown in Fig. 4.14a for the first bar of the HODF. This dependence comes from difference in path length for the different bars and is called ”smiley”-effect. The smiley-effect has to be corrected for each bar individually. A parabolic fit is used as a correction function which is fitted to incoming ^{24}O isotopes. For the correction, the value of the correction function is subtracted from the measured charge and in the same step shifted to an arbitrarily chosen value. This correction

is necessary since the measured charges are very close together and would smear out otherwise. The corrected distribution is shown in Fig. 4.14b for all bars as a function of the x position. The x position of the HODF is extrapolated from the x position and angle measured in FDC2. The distance between the two detectors is known from the PGS measurement.

In the next step, the charge is converted into charge number Z. For this, the charge distribution of each bar is fit with Gaussian functions to determine the mean positions. This done with the ^{27}F beam since the it contains more different isotopes with sufficient statistics and allows for a more precise calibration.

In addition, the dependence of the energy loss on the time-of-flight is visible for the production runs since it contains the target and can be improved in the same step. For this, the isotopes with charge equal to eight are fitted with a parabolic correction function. Then, the Z values can be converted into the expected charge number. This is done with a linear fit to the charges from $Z = 5$ to $Z = 9$. The result is shown in Fig. 4.16b. For large position values, the charge alignment shows some irregularities due to small statistics. However, this is not critical as these charges are not used for the analysis and with a cut on the silicon detectors after the target they can be removed, cf. Sec. 5.1.2. The resulting charge resolution is $\sigma(Z)/Z = 1.9\%$ for $Z = 8$.

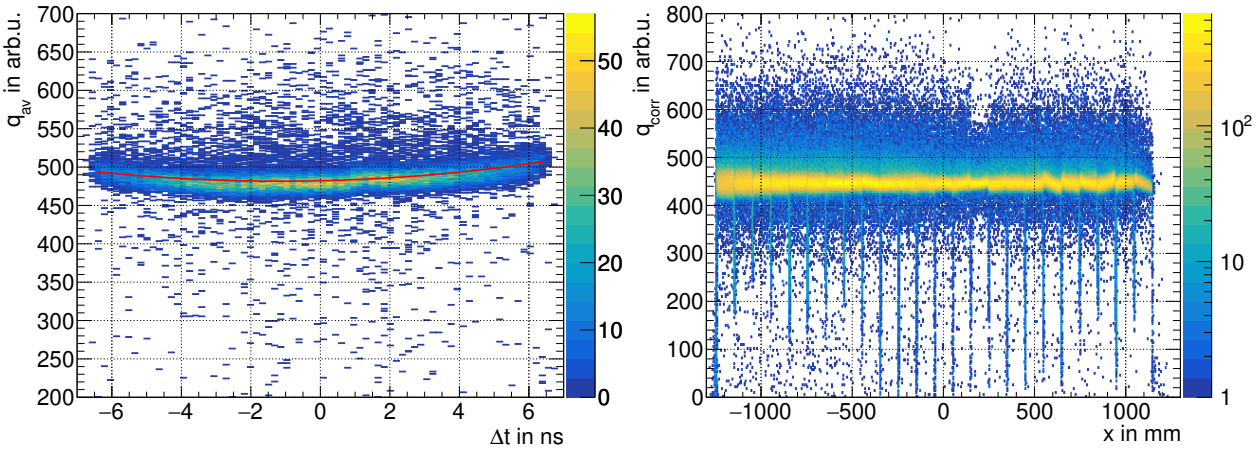

(a) (b)

Figure 4.14.: (a) The measured charge q_{av} shows a dependence on the y position within the HODF where bar 12 is shown as an example. The position is measured using the time difference between top and bottom PMTs. This is called "smiley"-effect and is corrected by using a parabola fitted to the distribution (red line). (b) After the correction of the position dependence for the sweep run, the individual bars, presented by the x position, are matched in charge. Data from the ^{24}O setting is shown.

4.7.2. Timing Synchronization

After the raw time is converted into ns in the same way as the plastic detectors in Sec. 4.2, the bars have to be synchronized. For this, the x positions of the gaps between the bars can be used. Using the sweep runs of the ^{24}O beam, the areas between the bars become visible, see Fig. 4.14b. The narrow lines at small charges belong to events that hit the area between the bars and only deposit

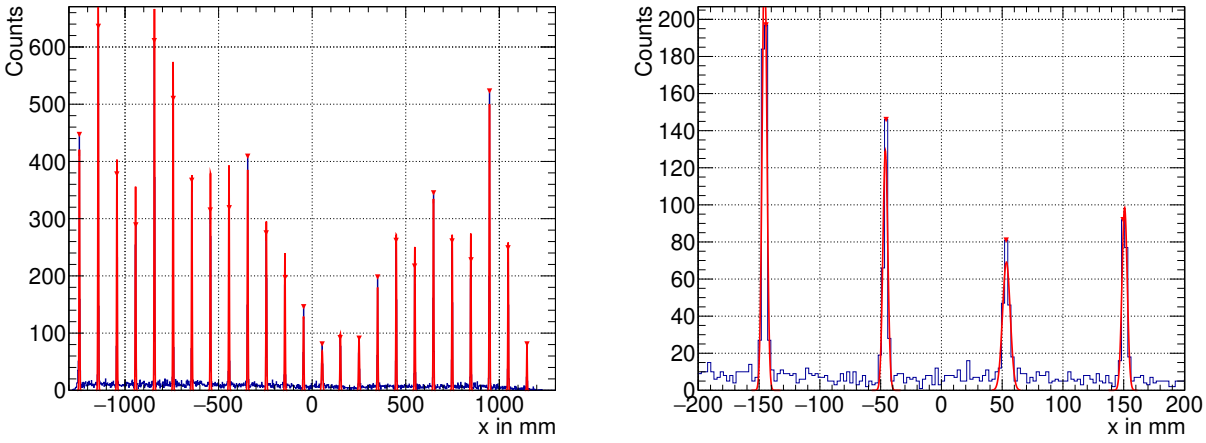

(a) (b)

Figure 4.15.: (a) Positions of the ”interbar” areas. With the sweep runs, the positions of the bar edges become visible as only small energies are deposited here. Each bar edge is fitted with a Gaussian function to determine the exact positions used for the calibration. (b) Zoom on the central region. Data from the ^{24}O setting is shown.

part of their energy in the bar material. Projecting these events onto the x axis, reveals the exact positions of the ”interbar” areas as shown in Fig. 4.15. Each peak is fitted with a Gaussian function from which the mean gives the exact x' position.

The timing synchronization is done using these transition areas from one bar to the next. The offset of the detector center from the 60 ° line was already determined from data as explained in Sec. 4.1 and can be verified. The region of ± 10 mm distance from the bar edge is defined as the transition region. Events that hit the hodoscope in these regions are selected. Under the assumption that the events in these regions on one bar arrive simultaneously with events on the next bar, the bars can be matched. For this, the mean of the two distributions belonging to the left and right side of the transition region is determined and serves as an offset. The first bar is taken as a point of reference and for all following bars the relative offset has to be subtracted. Looking at data from production runs, the matched timing has some irregularities for certain bars. This could be due to changes in the electronics between the oxygen and fluorine beam. These bars are corrected manually with the physics data. The result of the synchronization is shown in Fig. 4.16a.

4.7.3. Fragment Time-of-Flight

For the fragment mass-to-charge ratio and the final velocity-difference spectrum $\Delta\nu$ the velocity is needed and therefore the absolute time-of-flight. In order to find the expected time-of-flight from the last silicon detector to the hodoscope, a simulation was performed as explained in Sec. 6.1. With the simulation, the expected ToF for this distance can be determined.

For this calibration, empty target run 391 of ^{24}O beam is used. With a cut on the incoming energy, the expected $B\rho$ can be calculated. The incoming energy is calculated as explained in Sec. 4.4. The simulated particles with the same $B\rho$ give the expected time-of-flight for this energy. The distribution of the expected time-of-flight for the simulation has its mean at 49.8 ns. From this, the offset t_{offset} of

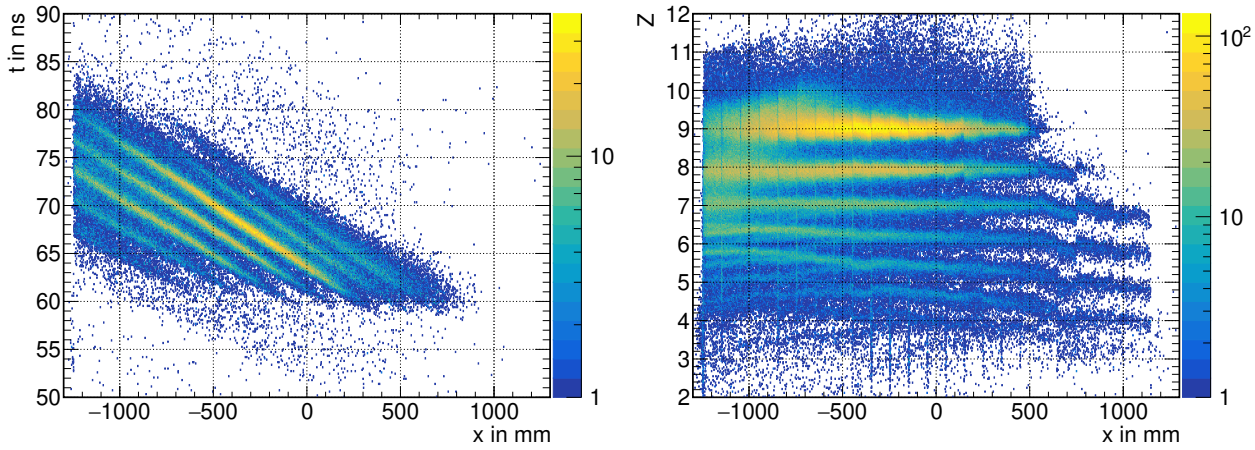

(a) (b)

Figure 4.16.: (a) Calibrated fragment time-of-flight after the time synchronization of the HODF bars with a cut on $Z = 8$ after the target. The distribution is smooth over the area of the detector with no steps visible. (b) Calibrated fragment charge Z vs. x position in HODF. The charge alignment of the bars shows some deviation for large positions due to small statistics. However, this is not critical as these charges will be removed by the fragment cut.

the measured HODF time t_f to the expected time-of-flight can be calculated taking the start time t_SBT and the time-of-flight from the SBT to the last silicon detector $\mathrm{ToF}_\mathrm{SBT\text{-}Si3}$ into account. The absolute time-of-flight of the HODF is given by

$$\mathrm{ToF}_\mathrm{f} = t_\mathrm{f} - t_\mathrm{SBT} - \mathrm{ToF}_\mathrm{SBT\text{-}Si3} - t_\mathrm{offset} + t_\mathrm{sync} + t_\mathrm{run}, \tag{4.7}$$

with t_sync being the bar dependent offset from the synchronization of the bars and t_run being the run dependent offset to have a consistent ToF over the duration of the measurement, cf. Sec. 4.9. The fragment time-of-flight resolution can be determined from the standard deviation of the Gaussian fit leading to $\sigma(t_\mathrm{ToF}) = 135\,\mathrm{ps}$, $\sigma(t_\mathrm{ToF})/t_\mathrm{ToF} = 0.27\%$ using the ^{24}O beam and no target.

4.8. Neutron Detectors

The neutron detectors are calibrated in several steps as the other plastic detectors. Also here, the raw time and charge measurements have to be converted into physical units. This was already performed during the experiment with pulser runs and cosmic muon data by I. Gašparić for NeuLAND [Gaš17] and by Y. Kondo for NEBULA [Kon17].
Since the measured charge in the neutron detectors covers a wide range, in contrast to the HODF, a walk correction has to be performed. Here, the time difference between two PMTs with the same orientation is plotted vs. the charge measured in one of the PMTs with a narrow cut on the charge in the other PMT. For NeuLAND, in which the bars in one double-plane are arranged perpendicularly, not the PMTs from the same plane are compared but the ones with the same orientation in the next plane behind. For each PMT a correction function is determined and applied. The result of the

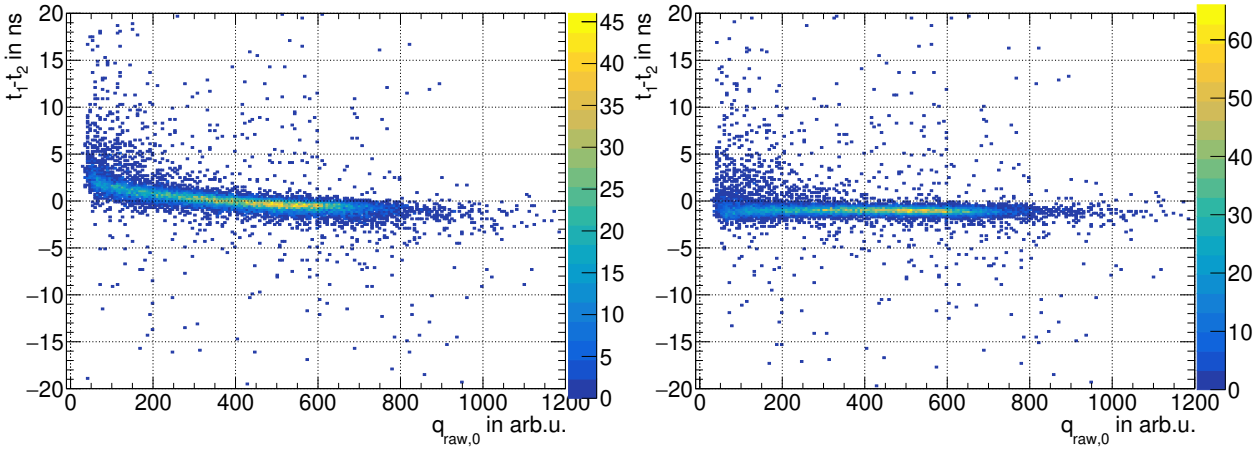

Figure 4.17.: (a) Before and (b) after the walk correction for one bar in NeuLAND. This calibration was performed during the experiment and was not done again for the current analysis as the walk effect was sufficiently corrected.

calibration that was done during the experiment is shown for NeuLAND in Fig. 4.17a before and Fig. 4.17b after the correction. Since no walk effect is visible anymore, this correction is kept and not redone.

4.8.1. Time Jumps

In the NeuLAND data, jumps or shifts in time are observed. They are at the order of $\approx 200\,\mathrm{ps}$ and thus have to be corrected. This effect could be attributed to the electronics of the NeuLAND demonstrator which show drifts or jumps in threshold over the duration of the experiment. It was not feasible to correct each channel (PMT) individually, thus the combined times of t_0 and t_1 of each bar are corrected. For the position measurement the time difference $\Delta t = t_0 - t_1$ and for the time-of-flight the average of both time measurements $t = \frac{1}{2}(t_0 + t_1)$ is used.

In order to find the correction parameter for each bar, the time difference $t - t'$ to each bar in the perpendicular layer directly behind is plotted over run number. The jump of the bar of interest is revealed and possible jumps of individual bars in the layer behind are averaged out by this comparison. The correction parameter is given by the offset of the time difference for each run compared to an arbitrarily chosen reference run (in this analysis run 450) and is shown in Fig. 4.18, where a time jump is visible around run 426. For short runs, the statistics are too low to determine a correction parameter, as indicated by the large error bars in Fig. 4.18. For these runs therefore no correction is applied.

The jump correction is done in a similar way for the time difference within a bar Δt. The position measurement of the layer behind the bar of interest is converted into a time difference $\Delta t'$. For this, a preliminary position calibration is performed as described in Sec. 4.8.2. With the parameters obtained from this calibration, the position can be converted into time difference again. For NEBULA the time jump effect was not observed.

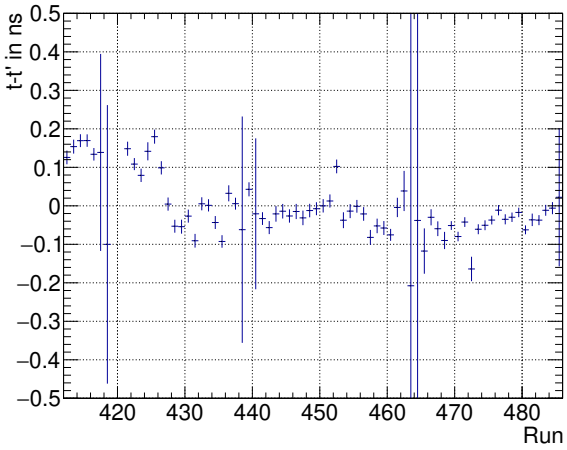

Figure 4.18.: Offsets for the jump correction in NeuLAND are given by the comparison to the time of each bar in the layer behind by $t - t'$. The offsets are calculated for each run and each bar, here bar 25 is shown as an example. For some runs, *e.g.*, run 465, the statistics are very low and the offset parameter has a large error. In such cases, no correction is applied.

4.8.2. Position Calibration

The goal of the position calibration is to convert the time difference between the top and the bottom PMTs in the two neutron detectors into a position in mm. The remaining position coordinate (x or y depending on the orientation of the bar) is randomized within the size of the bar.

For NeuLAND, the setup structure of the detector is used again, as a bar with perpendicular orientation is mounted directly in front or behind. Plotting the time difference within a bar over the position of the bar behind, gives a linear correlation between the two quantities, shown in Fig. 4.19a. Every bin of the time-difference distribution is fitted with a Gaussian function. For the distribution of the means, the conversion parameters are found with a linear fit. The resulting position distribution is shown in Fig. 4.19b. The rectangular structure in the position distribution is attributed to the neutron exit window of the SAMURAI magnet.

For NEBULA, the individual bars are only oriented vertically, meaning that there is no reference position measurement in a neighboring bar. Instead, the time difference spectrum is used. Here, the maximum time spread is assigned to the maximum bar length, as shown in Fig. 4.20a. The rising and falling edges belong to the ends of the bar. A cut, indicated by the black lines, is applied on the edges at half (orange line) of the distribution's flat top (red line). This time difference corresponds to the maximum bar length of 1800 mm. From here, conversion parameters are calculated to transform the time difference into a position. The result of the calibration is shown in Fig. 4.20b.

4.8.3. Timing Synchronization

With the position calibration finished, the timing of the individual bars needs to be synchronized in order to have a consistent ToF measurement. This can be done with gamma rays that are produced in the target, as a very thick and dense target was used in this experiment and the gamma peak can be observed in almost all NeuLAND and NEBULA bars. A few NeuLAND bars were not hit by the

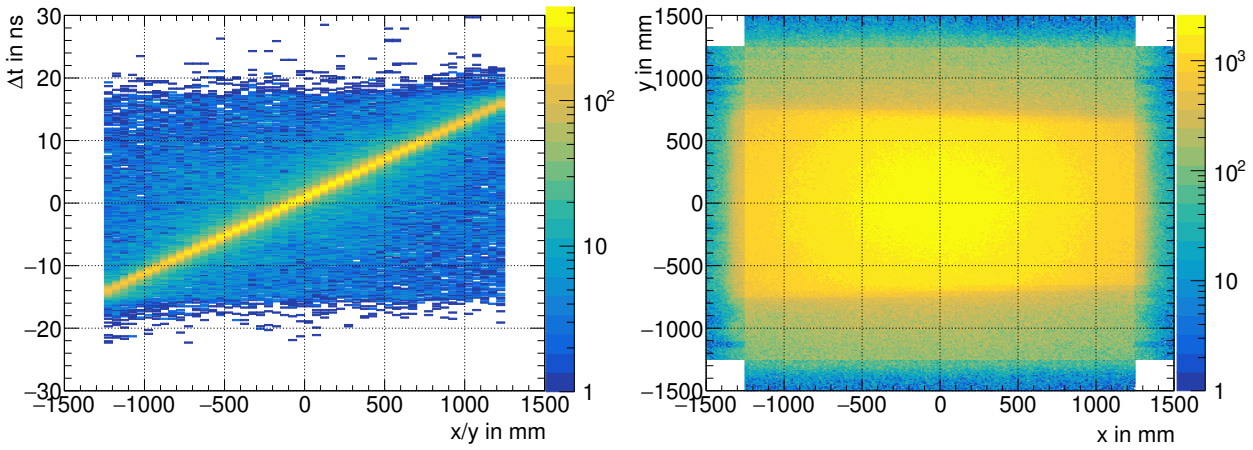

(a) (b)

Figure 4.19.: (a) The correlation between time difference and position in the double-planes in NeuLAND is used for the calibration, as the bars are mounted perpendicularly within a double-plane. (b) NeuLAND x and y position distribution after the calibration.

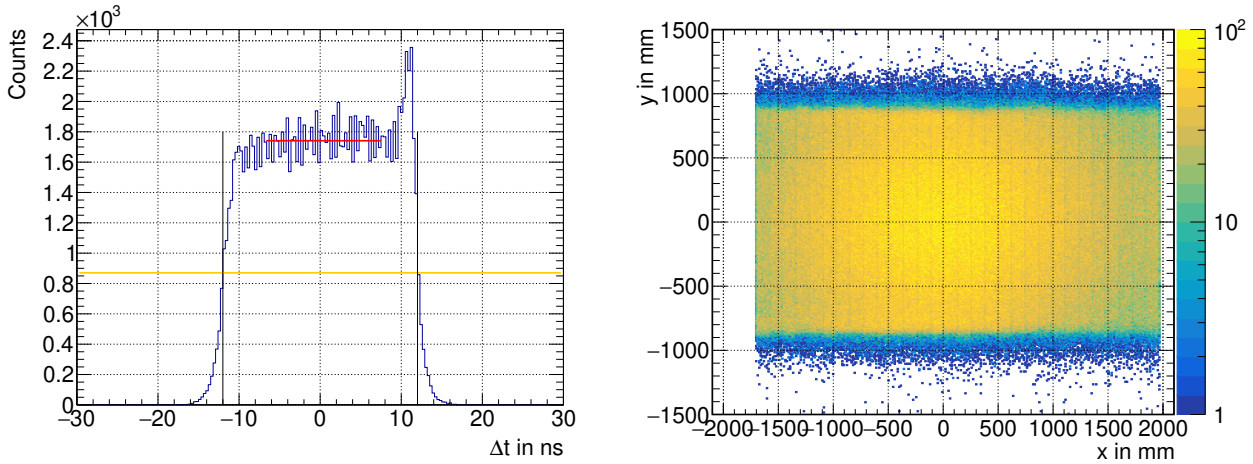

(a) (b)

Figure 4.20.: (a) Time difference distribution in NEBULA between the top and bottom PMTs. The maximum bar length is assigned to the spread in the time difference distribution, indicated by the black lines. (b) Resulting position distribution of NEBULA after the calibration.

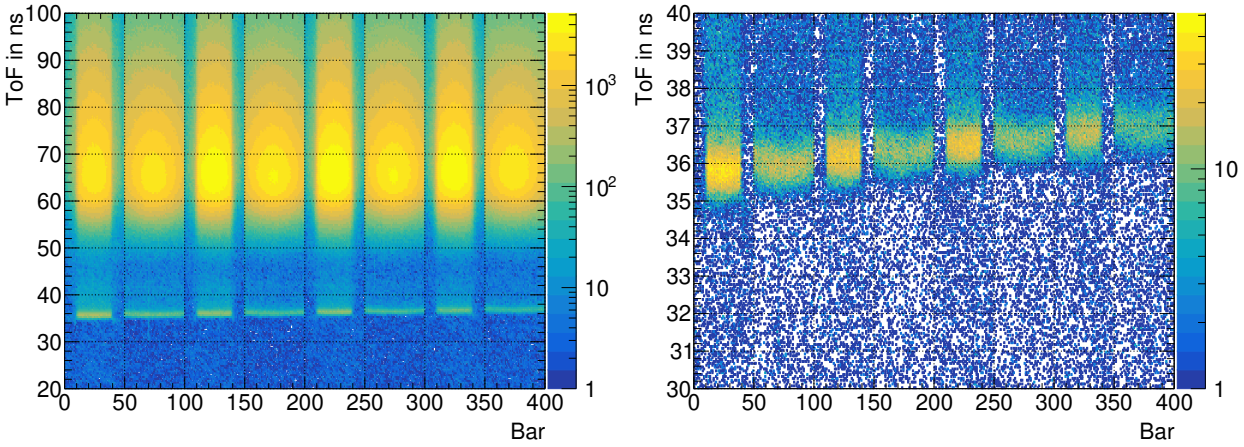

(a) (b)

Figure 4.21.: (a) NeuLAND time-of-flight distribution vs. bar number after the synchronization. The neutron peak appears at around 70 ps whereas the peak of the gamma rays is at around 35 ps. (b) Zoom in on the gamma time-of-flight distribution. A slight smiley-effect becomes visible after the calibration coming from the longer flight times for bars positioned on the edge of a scintillator plane.

gamma rays, as they were blocked by the SAMURAI exit window. The calibration parameters which were obtained with cosmic rays by I. Gasparic [Gaš17] are used for these bars.

With the gamma peak, the expected time-of-flight to each bar is calculated using the measured flight length, as calibrated in Sec. 4.8.2, and the speed of light. The flight length of the particle is given by the hit position in the neutron detector and the hit position that was extrapolated on the third silicon detector. The resulting gamma peaks in the spectrum appear at around 35 ps, as can be seen in Fig. 4.21a, whereas the neutron peak is located at around 70 ps. The peak is fitted with a Gaussian function for each bar. The difference of the mean of the fit and the expected ToF from the gamma rays results in the calibration parameter used for the bar synchronization. Using the gamma rays as a reference also allows for the absolute time calibration in the same step. The total time of the neutron detectors is then calculated analogously to the fragment time-of-flight as follows:

$$\mathrm{ToF_n} = t_\mathrm{n} - t_\mathrm{SBT} - \mathrm{ToF_{SBT\text{-}Si3}} - t_\mathrm{offset}, \tag{4.8}$$

where $\mathrm{ToF_n}$ of the neutrons is measured from the third silicon detector to the respective neutron hit. t_n and t_SBT are the times measured by the SBT and the neutron detectors, t_offset is the bar dependent calibration parameter determined during the synchronization and $\mathrm{ToF_{SBT\text{-}Si3}}$ is the time-of-flight from the start detector to the last silicon after the target. The slight smiley-effect created with this calibration step, cf. Fig. 4.21b, originates from the longer flight length for bars on the edges.

4.8.4. Time-of-Flight Resolution

The time-of-flight resolution is also determined using the gamma rays created in the target. The gamma peak is plotted for all bars at once. To remove the position dependence on the absolute ToF

value, the expected ToF is subtracted again. Since the absolute calibration was already performed, the gamma peak is then centered at zero. In addition, a cut on gammas with a high energy is applied ($q > 10\,\text{MeVee}$). Gammas with a small energy have a worse resolution and are removed anyhow by the neutron reconstruction algorithm later in the analysis (see Sec. 6.3), making this a valid cut. The time-of-flight resolution of the neutrons is given by the width of the gamma peak. The resulting resolution values are $\sigma(t_{\text{ToF, NL}}) = 278\,\text{ps}$ and $\sigma(t_{\text{ToF, NB}}) = 251\,\text{ps}$.

4.9. Time-calibration Stability

During the analysis it appeared that the time measurements for some detectors, *e.g.*, SBTs and the HODF, are not stable over the duration of the experiment. The drifts observed in the time measurements, could be attributed to temperature changes of the electronics. Since the measured ToF is very critical for this analysis, the drifts have to be corrected.

As the SBTs are used as the start detector, the measured time has to be comparable throughout the experiment. With a cut on the isotope of interest, the SBT time is plotted over the run number in Fig. 4.22a for the ^{27}F production runs (run 398 - 462) and the ^{26}F setting (run 463 - 485). Since the beam energy did not change within one setting, the time should be stable over the runs. The time drift is corrected by using the mean of the distribution for each run and comparing this to an arbitrarily chosen reference run. The result of the correction is shown in Fig. 4.22b. The time drift also has to be corrected for the HODF time. The procedure is the same as for the SBT time where a reference run is chosen for each beam setting and times are corrected comparing to this run. For NeuLAND and NEBULA no time fluctuations could be identified within the ToF resolution.

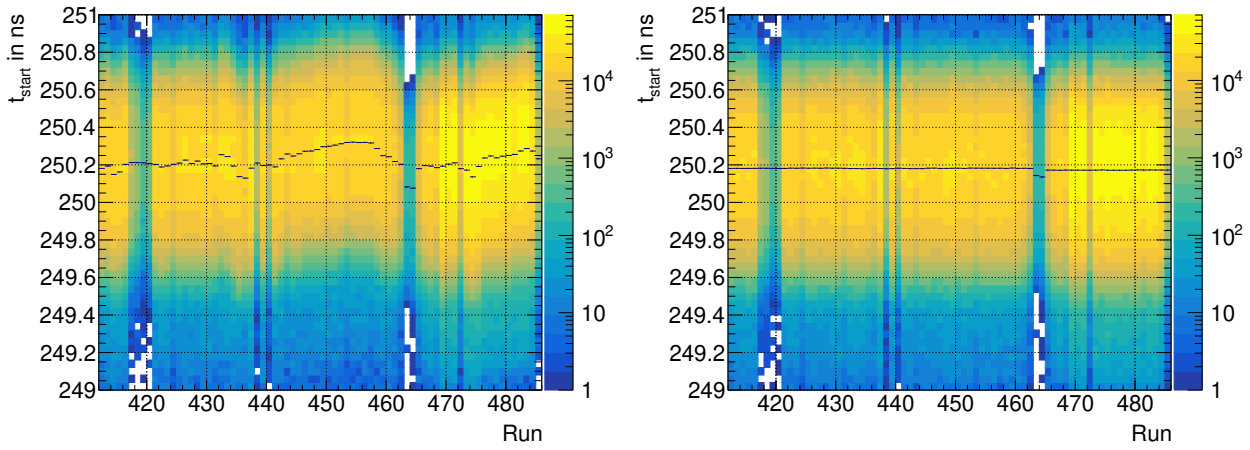

Figure 4.22.: The events start time (a) before and (b) after the correction as a function of the run number. The start time drifts over the duration of the experiment due to temperature changes of the electronics. A correction is applied to ensure a consistent start time during the duration of the data taking. This effect is corrected by using the mean of the distribution for each run. Data from the ^{27}F and ^{26}F settings is shown.

5. Analysis Techniques

5.1. Particle Identification (PID)

With the calibration of the individual detectors, it is possible to perform the Particle IDentification (PID). The particles are identified based on two quantities, their nuclear charge Z and their mass-to-charge ratio A/Z. In this work the A/Z is calculated using the ToF-$B\rho$-ΔE method, as described in [Fuk+13]. The quantities A/Z and Z are determined by measuring the time-of-flight ToF, the magnetic rigidity $B\rho$ and the energy loss in the detector material ΔE. Since the nuclear charges were already determined with a simple β correction in Ch. 4, the last step of the method will not be explained again. Particles that are impinging on the target will be called incoming particles and fragments as well as unreacted beam particles will be called outgoing particles hereafter.

5.1.1. Incoming PID with the ToF-$B\rho$-ΔE method

The absolute ToF and therefore the velocity β was already calibrated in Sec. 4.4 to obtain the incoming energy and is used here again for the PID. Since not all particles have the same energy, their magnetic rigidity is different. Thus, the exact $B\rho$ values have to be calculated. This is done using a simplified procedure compared to the one described in [Fuk+13]. The magnetic rigidity is calculated from the nominal $B\rho_0$ using the following relation:

$$B\rho = B\rho_0\,(1+\delta), \tag{5.1}$$

where the shift δ is determined from the measured position at the plastic detector at F5 which was calibrated with the PPACs and the matrix element $\langle x|\delta\rangle$ of the first order optical transfer matrix when going from F5 to F7

$$x_{\mathrm{F5}} = \langle x|\delta\rangle\,\delta. \tag{5.2}$$

Only the PPACs at F5 were used during the experiment, since this simplified procedure is sufficient for light nuclei. The value of this matrix element was determined to be -34.4457 mm during the experiment. With the deduced $B\rho$ and β, the mass-to-charge ratio can be calculated following Eq. 4.3.

In Fig. 5.1a the resulted A/Z calibration is shown for ^{27}F setting. For ^{27,26}F the reconstructed A/Z values match to the expected ones which means that the calculated time offset is correct. For the ^{24}O setting the resulting values are shifted. This effect occurs because of a transversal offset of

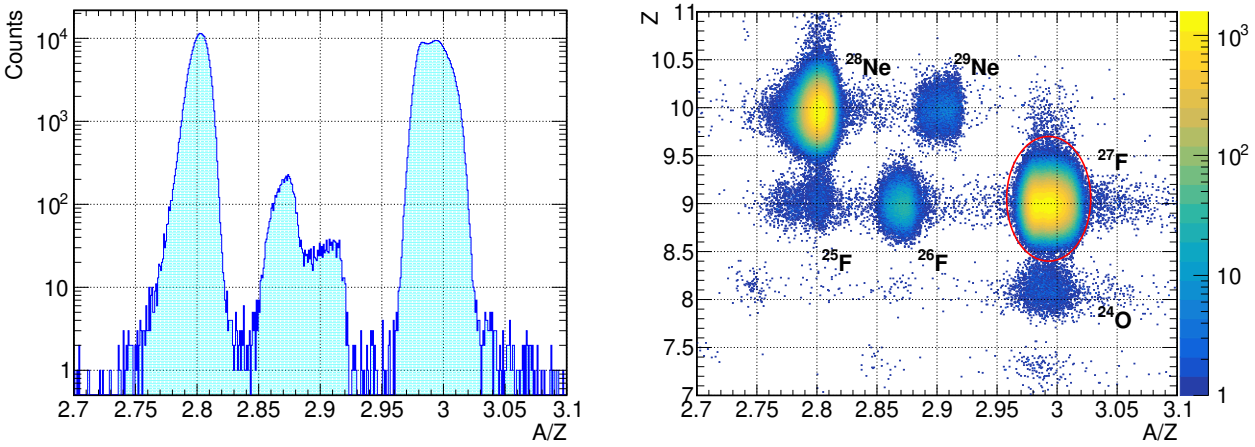

(a) (b)

Figure 5.1.: (a) Result of the A/Z calibration using the ToF and $B\rho$ for the ^{27}F setting. The resulting mass-to-charge ratio of $A/Z = 3$ corresponds to the expected one. (b) Incoming PID of the ^{27}F beam setting. The four most prominent isotopes in this cocktail beam are ^{27}F, ^{28}Ne, ^{29}Ne and ^{26}F. The energy loss in the ICB is used for the charge information, as it has the best resolution of the available detectors. The selection cut of ^{27}F is shown by the red ellipse.

the beam which implies that the nominal $B\rho_0$ does not correspond to the real one. The shift can be corrected with a linear function to get the expected A/Z values. With the reconstructed A/Z and the calibrated Z values from the ICB, the incoming particle identification can be performed. The resolution is $\sigma(A/Z)/A/Z = 0.3\,\%$ for both fluorine settings and the respective mass-to-charge ratio of the isotope of interest.

The incoming PID of the ^{27}F beam is shown in Fig. 5.1b. As described in Sec. 4.2.3, already some incoming cuts are applied on the raw time of all plastic detectors and the charge of the plastic detector at F7, the ICB and the first silicon detector. Different isotopes were present in this beam setting, though all can be well separated. ^{27}F and ^{28}Ne are the two main admixtures. In addition, there were ^{29}Ne and ^{26}F in the cocktail beam. Peaks appearing at lower charges $Z < 8$ become only visible with high statistics. These events are caused by effects in the detectors and are cut off the analysis by the selection of ^{27}F, indicated by the red ellipse. The A/Z distribution for the fluorine isotopes is broad compared to neon isotopes, which can be explained by a wider range of time-of-flights.

The incoming PIDs of the two other beam settings ^{26}F and ^{24}O are shown in Fig. 5.2a and 5.2b respectively, using the energy loss of the ICB for the charge information. In the ^{26}F cocktail beam the main admixtures were ^{27}Ne, ^{28}Ne, ^{25}F, ^{27}F and ^{24}O besides ^{26}F. The PID of the ^{24}O setting shows the presence of isotopes ^{25}F, ^{26}F, ^{23}O, ^{24}O, ^{22}N and ^{23}N. The isotopic fraction for the isotopes of interest and intensity of each beam setting are summarized in Tab. 5.1.

For all three settings the energy loss in the ICB is used for the charge information, since is has a better Z resolution as compared to the silicon detector in front of the target. The selection cuts for the isotope of interest are shown in the respective PID plots by the red ellipses and have size of 3.5σ for A/Z and 5σ for Z for all three settings.

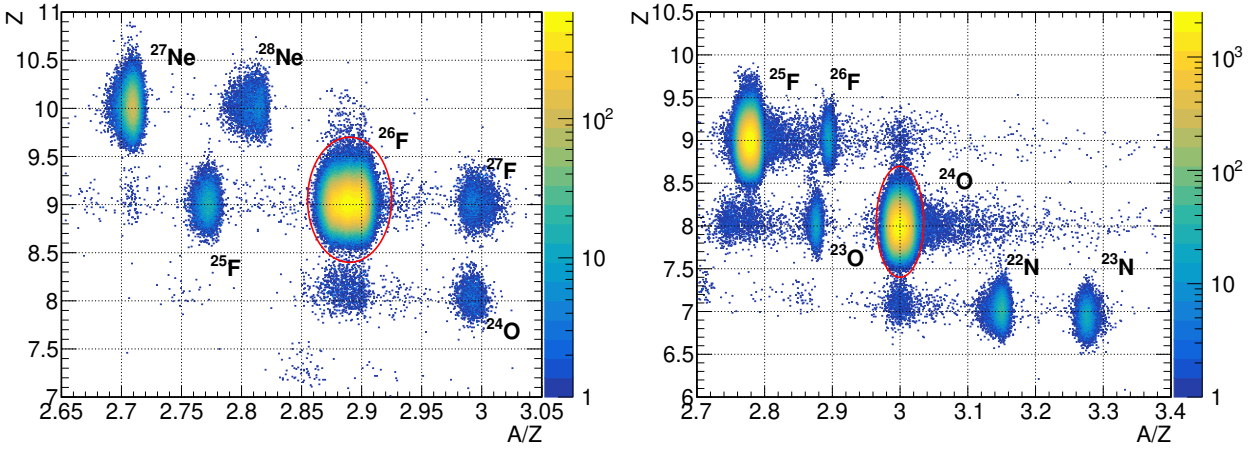

(a) (b)

Figure 5.2.: Particle identification for the (a) ^{26}F and (b) ^{24}O beam setting using energy loss information of the ICB to determine the Z. The selection cut on the isotope of interest is indicated by the red ellipse.

Table 5.1.: Isotopic fraction and intensity for the isotopes of interest from the different beam settings. The values are determined by the selection cut on the respective isotope in the PID plot. The intensity values are deadtime corrected.

Isotope	Isotopic Fraction in %	Intensity in Hz
^{27}F	60.5	3073
^{26}F	89.9	9024
^{24}O	51.1	995

5.1.2. Fragment PID

The A/Z of the ^{24}O fragment is reconstructed using the multi-dimensional fit routine of ROOT. In the first step, the maximum phase space covered by the setup was simulated using the measured distances of the detectors, cf. Sec. 4.1 and SAMURAI magnetic field map. Then, two functions for the $B\rho$ and the flight length l_f were determined by the multi-dimensional fit to the simulated data. The fit was already performed during my Master's thesis by J. Kahlbow [Kah18]. The obtained fits are a function of the positions and angles before the SAMURAI magnet at FDC1 and after the magnet, at FDC2 x position and angle.

$$B\rho = f(x_{\mathrm{FDC1}}, y_{\mathrm{FDC1}}, \alpha_{x,\mathrm{FDC1}}, \alpha_{y,\mathrm{FDC1}}, x_{\mathrm{FDC2}}, \alpha_{x,\mathrm{FDC2}}), \tag{5.3}$$

$$l_\mathrm{f} = g(x_{\mathrm{FDC1}}, y_{\mathrm{FDC1}}, \alpha_{x,\mathrm{FDC1}}, \alpha_{y,\mathrm{FDC1}}, x_{\mathrm{FDC2}}, \alpha_{x,\mathrm{FDC2}}). \tag{5.4}$$

These functions can then be evaluated with experimental data to get the $B\rho$ and the flight length of each particle. From this, the mass-to-charge ratio A/Z, the velocity β and the kinetic energy can be reconstructed.

In Fig. 5.3 the resulting fragment identification is shown for the ^{27}F beam using the Z values calibrated with HODF as explained in Sec. 4.7. A cut on the incoming ^{27}F isotopes as well as the reaction trigger is applied. The fragment with the highest charge and mass-to-charge ratio is the unreacted beam. Various reaction products can be identified and separated besides the fragment of interest ^{24}O, reaching from fluorine to beryllium. For charges lower than $Z = 8$, the HODF charge calibration is not precise, cf. Sec. 4.7. However, a higher precision is not necessary since an additional cut on the silicon detectors after the target is applied to select the oxygen isotopes. The cut on the silicon detectors is shown in Fig. 5.4a and the resulting fragment PID in Fig. 5.4b. The produced oxygen isotopes are well separable when the cut on the silicon detectors is applied with a mass-to-charge resolution of $\sigma(A/Z)/A/Z = 0.4\,\%$ for ^{24}O. The selection cuts are shown by the red ellipses in Fig. 5.4. The cut applied to the silicon detectors is 3σ in Z and the fragment cut has a size of 5σ in A/Z and Z.

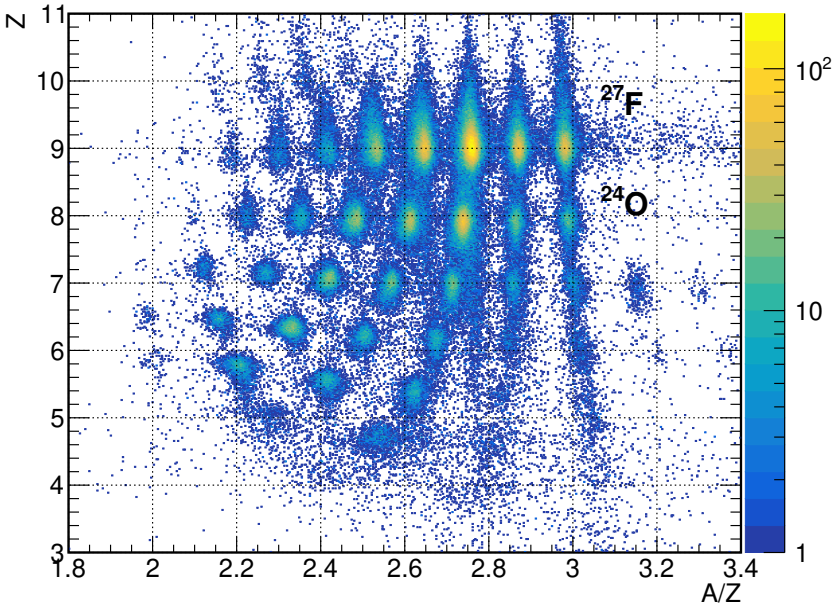

Figure 5.3.: Fragment identification after the selection of incoming ^{27}F isotopes and the reaction trigger. The unreacted ^{27}F and the desired fragment ^{24}O are labeled.

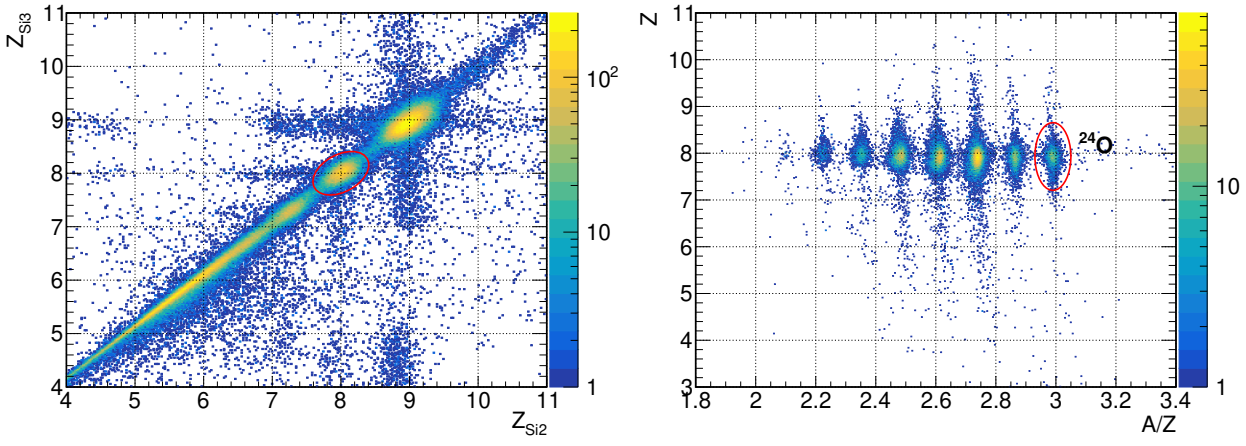

(a) (b)

Figure 5.4.: (a) Charge correlation of the silicon detectors behind the target with the cut on $Z = 8$ indicated by the red ellipse. (b) Resulting fragment identification with the additional cut on the silicons after the target. The oxygen isotopes are well separated, with ^{24}O being marked by the red ellipse.

5.2. Invariant-Mass Method

The invariant-mass method is commonly used in low-energy nuclear physics experiments to study the excitation energy spectrum of exotic nuclei, that are short-lived or even unbound. The excitation energy cannot be measured directly in contrast to other quantities, like the time-of-flight or the energy loss of a particle. However, as this experiment was carried out in inverse kinematics, it can be reconstructed from the measured velocities and trajectories of the particles in the final state.

When measuring all necessary quantities with high precision, the excitation energy spectrum can be used to investigate resonant states, identify new states or study their decay dynamics. For instance, this method was applied in [Kon+16] where the decay energies of the ground state and the first excited state of ^{26}O were found (cf. Fig. 2.4). In this analysis this is not possible as the momentum resolution is lowered due to the thick target material. Here, the relative energy spectrum is only used as a consistency check for the simulation and will be presented and discussed in Ch. 7. More details on the invariant-mass method can be found in [Leh21; Sch15; Obe+21].

The invariant mass M_{inv} of a system is, as the name indicates, invariant under Lorentz transformation. It corresponds to the mass of the particle in the center-of-mass frame. An incoming projectile with rest mass m_p that has been excited in a reaction with a target has an invariant mass of

$$M_{\text{inv}} = m_p + E^*, \tag{5.5}$$

where E^* is the excitation energy. During the decay of the particle, the invariant mass is conserved and can be calculated from the four momenta $\vec{P}$ of all particles N in the final state:

$$M_{\text{inv}} = \sqrt{\left(\sum_i^N \vec{P}_i\right)^2} = \sqrt{\left(\sum_i^N E_i\right)^2 - \left(\sum_i^N \vec{p}_i\right)^2}, \tag{5.6}$$

with the energy E_i and the three momenta $\vec{p}_i$ of the individual particles in a reference system with $c = 1$. The energy and the total momentum of a relativistic particles is given by

$$E_i = \gamma_i m_i, \tag{5.7}$$

$$p_i = \beta_i \gamma_i m_i, \tag{5.8}$$

with the Lorentz factor $\gamma = \frac{1}{\sqrt{1-\beta^2}}$. With this, the sums in Eq. 5.6 can be rewritten to

$$\left(\sum_i^N E_i\right)^2 = \sum_i^N (\gamma_i m_i)^2 + \sum_{i \neq j}^N \gamma_i \gamma_j m_i m_j, \tag{5.9}$$

$$\left(\sum_i^N \vec{p}_i\right)^2 = \sum_i^N (\beta_i \gamma_i m_i)^2 + \sum_{i \neq j}^N \beta_i \beta_j \gamma_i \gamma_j m_i m_j \cos\Theta_{ij}, \tag{5.10}$$

where Θ_{ij} is the angle between the outgoing particles i and j in the laboratory frame. In case γ rays are emitted, their energy has to be added to the invariant mass. It follows that the invariant mass of

the final state is expressed by

$$M_{\text{inv}} = \sqrt{\sum_i m_i^2 + \sum_{i \neq j} \gamma_i \gamma_j m_i m_j (1 - \beta_i \beta_j \cos \Theta_{ij})} + E_\gamma, \tag{5.11}$$

using $\gamma^2(1-\beta^2) = 1$. Substituting into Eq. 5.5, the excitation energy is expressed as

$$E^* = \sqrt{\sum_i m_i^2 + \sum_{i \neq j} \gamma_i \gamma_j m_i m_j (1 - \beta_i \beta_j \cos \Theta_{ij})} + E_\gamma - m_p. \tag{5.12}$$

In the S20 experiment, no γ rays are expected and therefore no γ detector was used around the target. The excitation energy is then given by the relative energy E_{rel} of the final state particles. Additionally, the mass of the initial particle m_p is replaced by the sum of the masses of the final state particles $\sum_i m_i$. This leads to E_{rel} starting from zero in contrast to the particle separation threshold S.

$$E_{\text{rel}} = \sqrt{\sum_i m_i^2 + \sum_{i \neq j} \gamma_i \gamma_j m_i m_j (1 - \beta_i \beta_j \cos \Theta_{ij})} - \sum_i^N m_i \tag{5.13}$$

5.3. Chi-Square (χ^2) Method

The χ^2 method is often used to determine how good a model function describes the data. If a fit is performed with for example ROOT, a χ^2 reduction is used to determine the best fitting parameters of the model function. The description in this section follows [Bev+03], where the following notations will be used:

- n: total number of bins in a histogram of experimental data
- h_i: number of events in bin i of experimental histogram
- N: total number of events in histogram, $\sum_{i=1}^{n} h_i = N$
- σ_i: spread of events of each bin h_i
- y_i: number of events in bin i predicted by the model.

The χ^2 is a weighted sum of the squared differences between experimental data points and a model function and is defined as

$$\chi^2 = \sum_{i=1}^{n} \frac{(h_i - y_i)^2}{\sigma_i^2}. \tag{5.14}$$

The uncertainty σ_i of each bin is Poisson distributed in a counting experiment, leading to the variance being $\sigma_i^2 = y_i$. This is illustrated in Fig. 5.5a. A histogram is drawn from a Gaussian distribution. The parent distribution is indicated by the solid black line with mean $\mu = 5$ and standard deviation $\sigma = 1$. The dotted curves represent the Poisson distribution of events in each bin

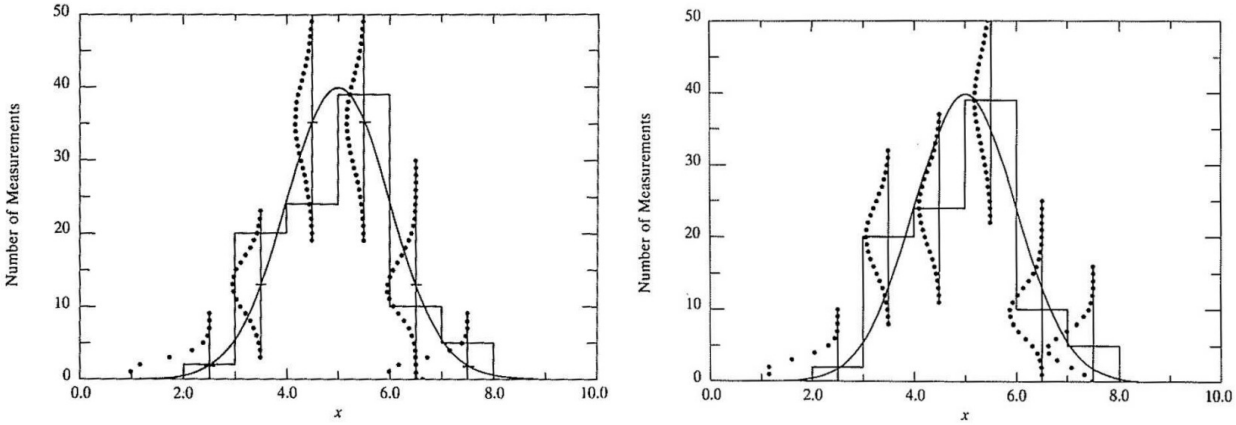

(a) (b)

Figure 5.5.: Histograms drawn from a Gaussian distribution. The parent distribution is shown by the black solid line with mean $\mu = 5$ and standard deviation $\sigma = 1$. (a) The dotted curves represent the Poisson distribution of events in each bin based on the parent distribution. (b) The Poisson distributions represents the spread of events in each bin based on the sampled data. Both figures are taken from [Bev+03].

based on the parent distribution. In an experiment, the parent distribution is not known and therefore also the uncertainty σ_i is unknown. However, it can be estimated from the data with $\sigma_i^2 = h_i$. The corresponding histogram is shown in Fig. 5.5b. The dotted curves of the Poisson distribution are centered at each bin instead of the parent distribution. This simplifies Eq. 5.14 to

$$\chi^2 = \sum_{i=1}^{n} \frac{(h_i - y_i)^2}{h_i}. \tag{5.15}$$

If a measurement agrees perfectly with a model function, the χ^2 would be zero, which is impossible for a real experiment. The expectation value of χ^2 is

$$\langle \chi^2 \rangle = \nu = n - n_c, \tag{5.16}$$

where ν is the number of degrees of freedom and n_c the number of constraints. The reduced χ^2_ν is defined as $\chi^2_\nu = \chi^2/\nu$ with an expectation value of $\langle \chi^2_\nu \rangle = 1$. The 1σ uncertainty is determined by the values of the distribution at $\chi^2 + 1$ [Bev+03].

In Ch. 7, the χ^2 method is applied to compare the experimental data with the simulated spectra and extract the lifetime value from the χ^2 minimum.

6. Simulation

The simulations in this work are performed using the GEometry ANd Tracking (GEANT4) toolkit [Ago+03]. With the simulations, calibration steps for the experimental data can be performed, see Sec. 6.1, the $\Delta\nu$ spectra for different lifetimes are created in Sec. 6.2, and the neutron reconstruction algorithm is developed in Sec. 6.3.

In the GEANT4 framework, particles are transported through matter. For this, the geometry of the experimental setup has to be implemented using geometric objects that have the size and material of the detectors and other structures used in the experiment. A simulation starts by giving the initial position and momentum vector of every particle in an event as an input. GEANT4 transports the particles through the individual structures and calculates the flight path and the interaction with the materials using an implemented physics list. The physics list used in this work is QGSP_INCLXX_HP. The particle's properties are evaluated at certain steps. The lengths of these steps can be chosen according to a physics condition, *e.g.*, the mean free path of the particle, at a material change, or it can be fixed as it was partially done in this work. Finally, the information is given to the detectors, for which the response is calculated. In this work, the SAMURAI simulator (smsimulator) was used for the simulations. This is a simulation toolkit based on GEANT4, including ROOT libraries, which was developed by the SAMURAI collaboration [SAM22]. It includes the SAMURAI magnet as well as the standard SAMURAI detectors. The SAMURAI simulator was modified to meet the specifics of the present work. All remaining detectors of the S20 setup were implemented and placed according to the photogrammetry measurement in Sec. 4.1. The field maps for the magnet are taken from [Map22] and modified with a field factor to match the experimental data, cf. Sec. 6.1.3.

The setup is shown in Fig. 6.1 with a typical event for the last step of the lifetime simulation (cf. Sec. 6.2) with a ^{24}O fragment and two neutrons starting from their initial position after the decay from ^{26}O. The fragment trajectory, indicated with the gray line, is bent by the magnetic field towards FDC2 and HODF. The two neutrons, displayed by the blue lines, are unaffected by the magnetic field and move towards NeuLAND and NEBULA.

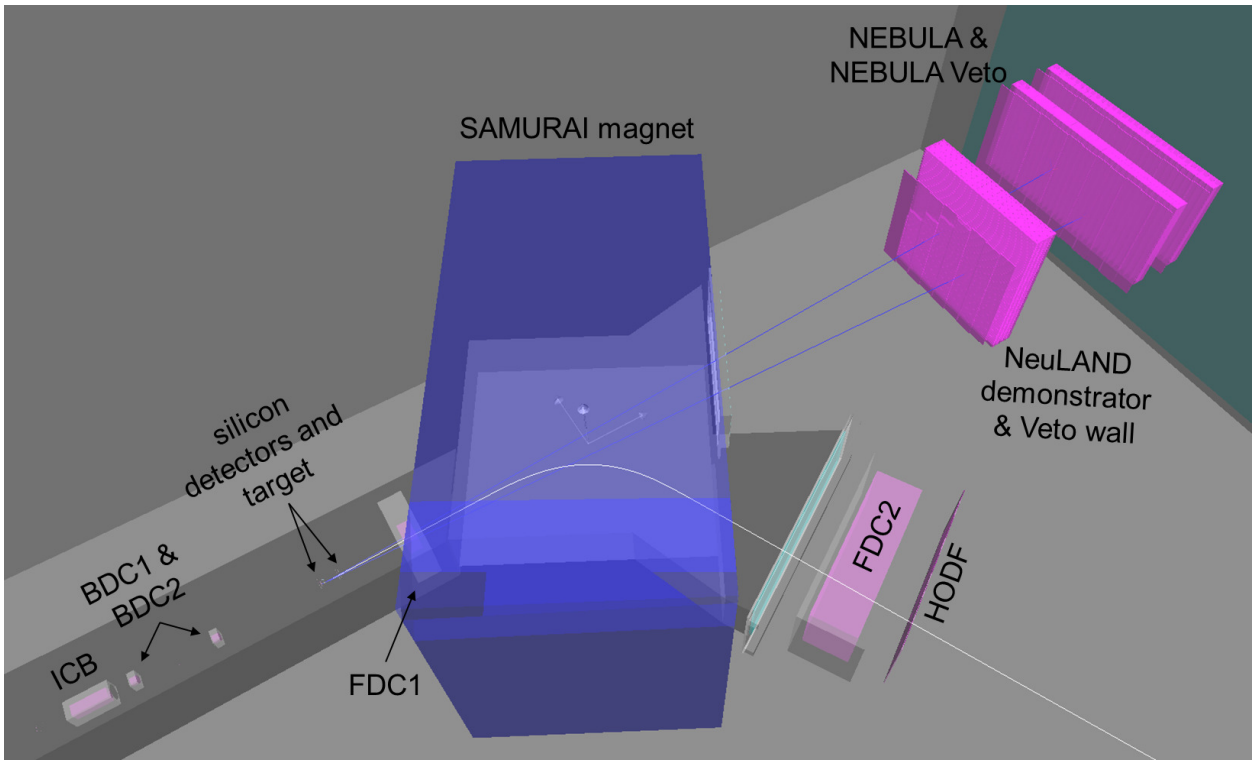

Figure 6.1.: Simulation setup with a typical event of a ^{24}O fragment and two neutrons, that were produced in the decay of ^{26}O. The fragment (gray line) is bent towards FDC2 and HODF by the magnetic field, whereas the neutrons (blue lines) are unaffected and move towards NeuLAND and NEBULA.

6.1. Simulations for Calibration

6.1.1. Incoming Beam Energy Loss and Time-of-flight

The simulation can be used to calibrate the experimental data. This is done as described in Sec. 4.5, where the energy loss and the time-of-flight of the projectile to the assumed reaction point are simulated depending on the incoming energy of the beam particle. The input for the simulation is generated using a uniform energy distribution over the range of experimental energies of 205 - 240 MeV/u. The ^{27}F particles start flying in front of the SBTs and are transported up to the last silicon detector. All detectors and beamline materials positioned along this path in the experiment, including vacuum foils and air gaps, are included. The energy loss and time-of-flight up to the last silicon detector are determined with this simulation and used for the experimental calibration, as this information is not available in the experimental data. The resulting distributions are shown in Fig. 4.10.

In the same simulation, the energy loss and time-of-flight up to the first target can also be determined. This is not needed for the experimental calibration but for the lifetime simulation described in Sec. 6.2. The lifetime simulation starts at the first target and the experimental input distributions can be projected up to this point.

6.1.2. Fragment Time-of-Flight Correction

As the position of the decay is not known in the experiment, the assumption is made that the decay happens at the last silicon detector, meaning that the ^{24}O fragment and neutron time-of-flight are calculated from this point (see Sec. 4.5). A schematic drawing of the different flight times is shown in Fig. 6.2. The fragment time-of-flight $\mathrm{ToF_f}$ is determined from the measured times of HODF and the SBTs ($t_\mathrm{f} - t_\mathrm{SBT}$) and the simulated time-of-flight from the SBTs to Si3 ($\mathrm{ToF_{SBT\text{-}Si3}}$), assuming an ^{27}F beam, with additional calibration correction parameters (cf. Sec. 4.7.3). In the lifetime simulation, the decay point is known but cannot be used for the analysis. To guarantee an equal treatment of the simulation and experimental data, the same assumption has to be applied. In the last step of the simulation, the fragment is transported from the decay point z_τ to HODF ($\mathrm{ToF_{HODF}}$). The ToF measured by HODF in the simulation includes the time between the decay point z_τ to the last silicon detector Si3 and then to HODF. For this reason, the ToF to Si3 has to be subtracted from the HODF time-of-flight. The same procedure is applied to the NeuLAND and NEBULA ToF. A comparison of the time-of-flights between the simulation and the experimental data is shown in Fig. 6.3a for HODF and in Fig. 6.12a for NeuLAND. The NeuLAND time-of-flight agrees very well with the simulation, see Sec. 6.3.1. The HODF time-of-flight is shifted to smaller values.

Since the lifetime simulation consists of several steps and only starts at the first target (z_i), the information of the total time-of-flight of the particle is lost. However, the total ToF can be estimated. The ToF from the decay point to the third silicon detector is known from the last step of the lifetime simulation. The ToF between SBTs to the first silicon detector and also to z_i is known from the simulation used for calibration described above. What is missing for the total ToF, is the time-of-flight from the start of the simulation z_i, to the decay position z_τ. This can be estimated from the first step of the lifetime simulation process, where ^{27}F is transported from the start z_i to the position of the proton removal z_r. The time-of-flight can be evaluated from the start to each of the targets (ToF_r),

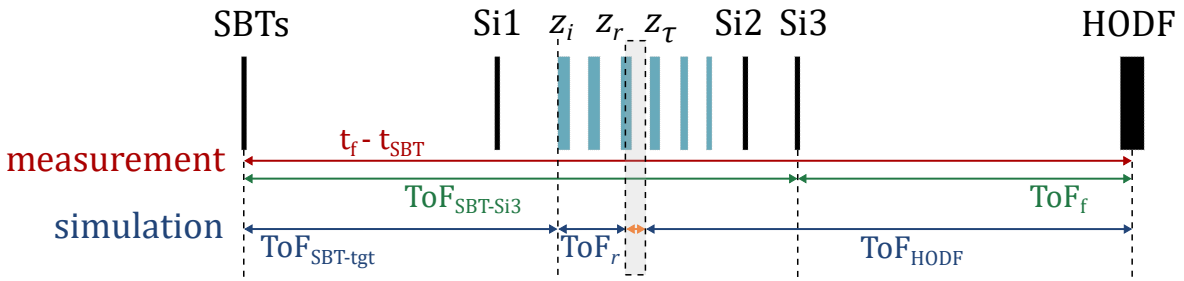

Figure 6.2.: Schematic drawing of the different flight times, used in the measurement and the simulation. The fragment ToF (ToF_f) is calculated as indicated by the green lines from the measured HODF and SBT times (red) for the experimental analysis. The simulated ToF_f has an offset and is corrected using the total ToF indicated with the blue lines. Sizes are not drawn to scale.

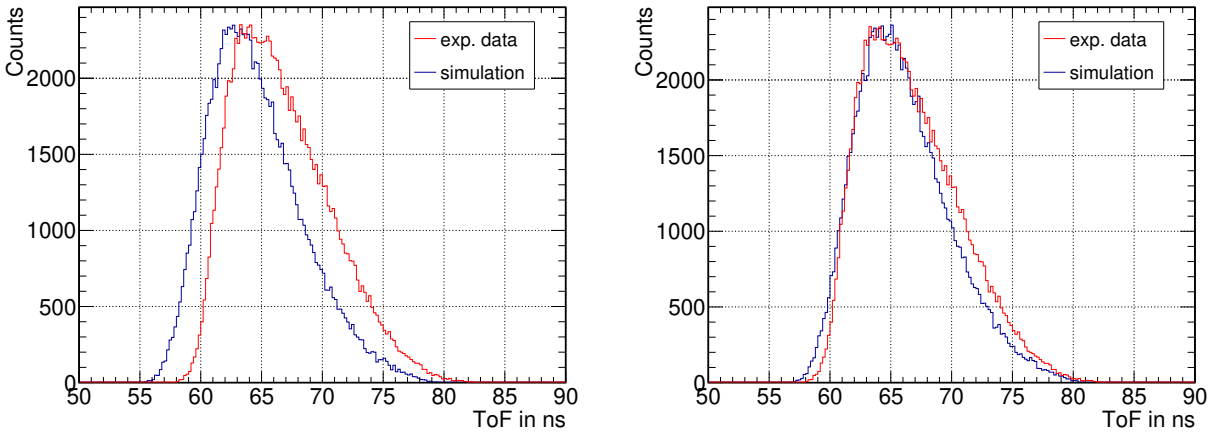

Figure 6.3.: Comparison between simulated (blue) and experimental data (red) of ^{24}O for the HODF time-of-flight (a) without and (b) with including an offset to match the distributions.

providing the missing contribution to the total ToF. Since this is done within a different simulation step, the ToF cannot be attributed to the individual particles but can only be estimated depending on where the proton removal happened. The decay will happen either inside the target, where the proton removal happened or directly after, in the gap between targets. Hence, the contribution to the ToF from the point of the proton removal to the decay point is very small, indicated by the orange arrow in Fig. 6.2, and therefore neglected in the estimation. For future simulations, the ToF for each simulation step is recommended to be included to be able to apply a precise correction. With this estimation, the total ToF can be calculated and the HODF ToF can be corrected. However, this contribution is small compared to the offset in Fig. 6.3a and is not sufficient to correct it.

The shifted HODF ToF is shown in Fig. 6.3b in comparison to the experimental distribution, with an offset determined to be 1.5 ns. For the reference spectrum of ^{25}O, the necessary ToF offset of the detected ^{24}O fragment in HODF, is even larger at 2.4 ns. These offsets are substantial and need further investigation. The effect of including this offset on the resulting velocity-difference spectrum is shifting the absolute position of the spectrum. However, the further analysis and the lifetime determination are independent on the absolute position of the $\Delta\nu$ spectrum. Therefore, the offset in the HODF ToF does not influence the lifetime result.

6.1.3. Magnetic Field Factor Determination

Comparing the experimental and simulated spectra for the FDC2 and HODF x position distribution reveals that the field map of the SAMURAI magnet used in the simulation does not fit perfectly. The HODF x position distribution using the SAMURAI field map of 2.2 T is shown in Fig. 6.4a. The simulated HODF x position (blue) is shifted by around 200 mm and does not agree with the experimental spectrum. To correct this, a scaling factor for the magnetic field can be included in the simulation. The idea is to use the unreacted ^{27}F to determine this field factor. For this, a simulation with ^{27}F is performed, where the projectile does not undergo any reaction up to HODF. The experimental energy distribution, as described in Sec. 6.2.1, is used as an input and the beam is transported up to HODF with all detectors and materials included. The simulated spectra are compared to the experimental data from the ^{27}F setting with a cut on the unreacted beam at HODF. The field factor was not determined using the lifetime simulation with the ^{24}O projectile, as described in Sec. 6.2, such that the extracted lifetime is not influenced by this matching process. The optimal field factor is found iteratively. For this, the simulation is performed with different field factors and FDC2 and HODF x position distributions are used as a measure for the field factor. With a linear fit to the field factor distribution in dependence on the HODF x position, the correct field factor at the expected HODF x position can be interpolated. The obtained field factor for the unreacted setting is 1.039. If this field factor is applied to the lifetime simulation, the resulting x position distribution in comparison to the experimental data (red) is shown in Fig. 6.4b. As shown, it improves the agreement between simulation and experiment but the positions in the simulation are still shifted to higher values.

The same investigation is done with the simulation of the reference channel, described in Sec. 6.2.6. The incoming projectile is ^{26}F, a proton knockout occurs in the target where ^{25}O is produced and the fragment ^{24}O is transported up to HODF. The field factor is only used in the last step of the lifetime simulation, where the fragment has to pass the magnet. The field factor is determined in the

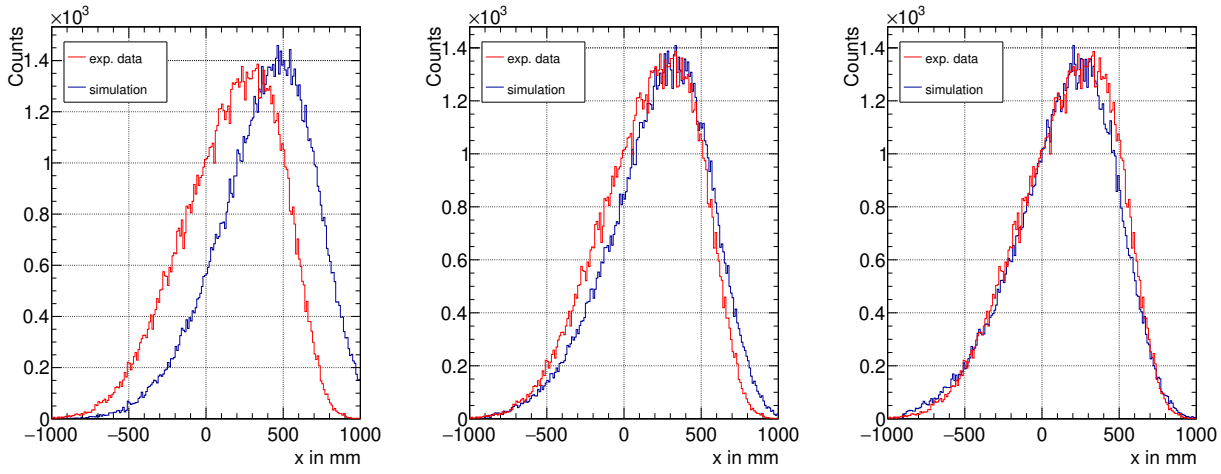

Figure 6.4.: Comparison between simulated (blue) and experimental data (red) of the x position distribution at HODF for different field factors applied to the magnetic field of SAMURAI. (a) The field map taken from [Map22] is used for the lifetime simulation without an additional correction factor. (b) The field factor determined from the simulation with the unreacted ^{27}F beam is used. The agreement is better than in (a) but the x position in the simulation is still shifted. (c) The field factor determined with the reference channel is used. The agreement of the HODF positions is best and therefore this field factor will be used in the last step of the lifetime simulation.

same way as described before, and is found to be 1.060 for the reference channel. The x position distribution of HODF with this field factor applied to the lifetime simulation is shown in Fig. 6.4c. The HODF position from the simulation and the experiment agree very well and this factor will be used in the lifetime simulation. In the simulation of the reference channel, the lifetime does not play a role, and therefore the result for the lifetime will not be influenced. Additionally, the HODF calibration was optimized for the ^{24}O fragment and not for a ^{27}F projectile. This could explain the different result for the field factor based on the two different approaches.

6.2. Lifetime Simulation

In the experiment, the incoming ^{27}F is transformed into ^{26}O via proton removal which then decays into ^{24}O and two neutrons. In the simulation, these processes have to be modeled as realistically as possible to guarantee a comparability between experiment and simulation. A schematic of the process is shown in Fig. 6.5. The lifetime simulation starts at the beginning of first target z_i with a ^{27}F beam. The proton removal occurs at the position z_r, where ^{26}O is created. ^{26}O decays at the position z_τ into ^{24}O and two neutrons. The position z_τ depends on the lifetime and can be inside target, where the proton removal took place or outside in the gap between two targets. In order to implement this process, the simulation is set up in several steps, following the processes in the experiment. As the simulation has to be performed for different lifetimes, a lifetime value is required as an input. A sketch of the different simulation steps is shown in Fig. 6.6.

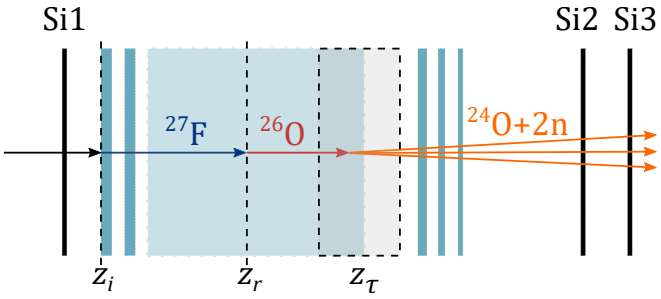

Figure 6.5.: Reaction processes that are implemented in the lifetime simulation to model the processes in the experiment. The simulation starts at the beginning of the first target z_i with ^{27}F, from which a proton is removed at the position z_r to create ^{26}O. ^{26}O decays at the position z_τ into ^{24}O+2n. z_τ depends on the lifetime and can be inside or outside the target. Sizes are not drawn to scale.

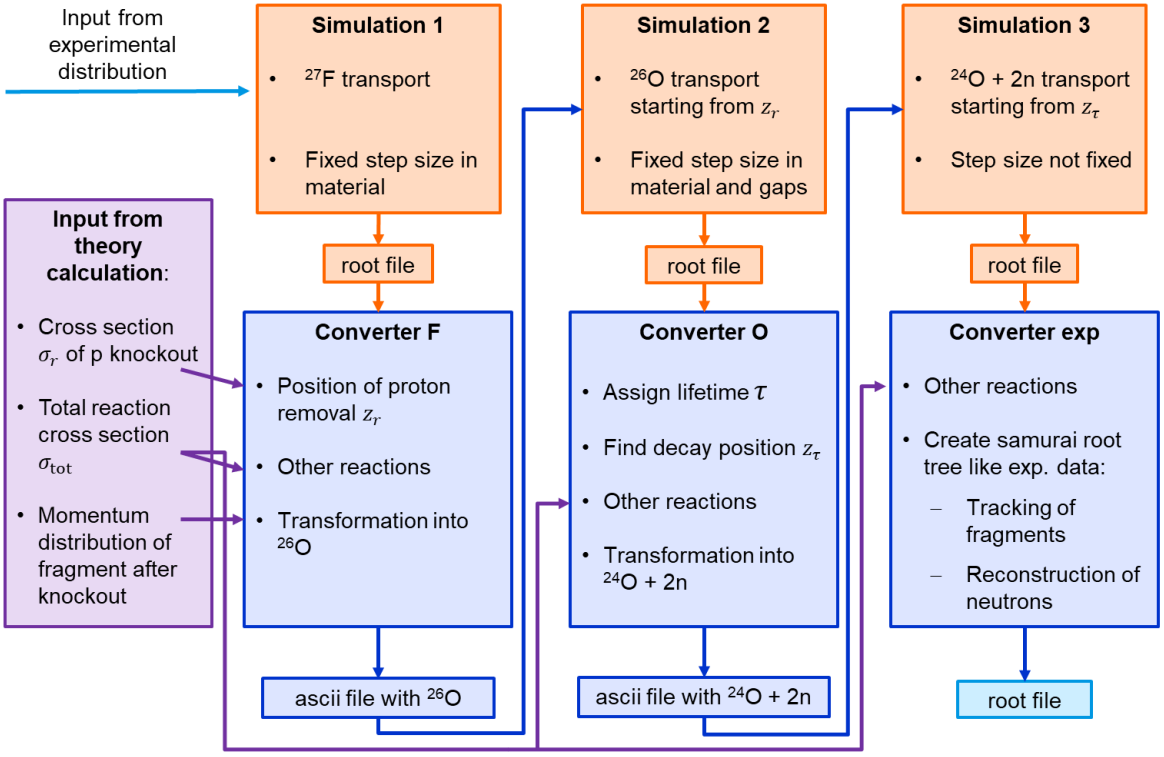

Figure 6.6.: Overview of lifetime simulation process. The input into the first simulation is modeled based on the experimental energy and position distributions. The transport of each isotope is done in a separate simulation with converters in between, where the proton removal and the decay take place.

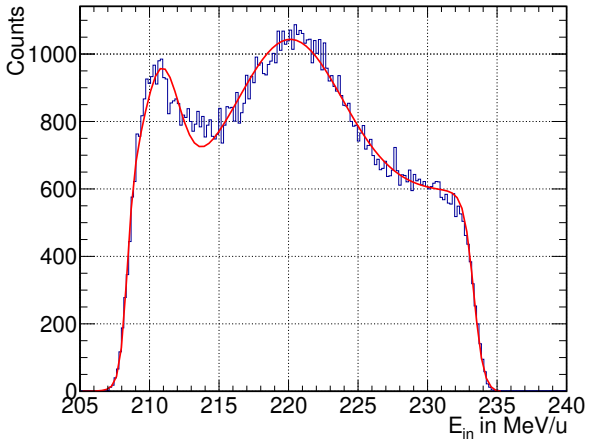

Figure 6.7.: Experimental energy distribution of incoming ^{27}F ions fitted with a sum of sigmoid and Gaussian functions in red. The resulting function is used to generate energy values for events in the simulation. The incoming energy distribution is evaluated with a selection cut on the outgoing ^{24}O fragment.

6.2.1. Event Generator

A simulation in the `smsimulator` can be performed by giving a list of events as an input. The input list is an `ascii`-file which contains the momentum vector, position vector, energy, charge and mass number of each particle in an event at the start position of the simulation. As the resulting $\Delta\nu$ spectrum for each lifetime requires to have at least comparable statistics and events are lost in the simulation as they do not fall in the acceptance of the setup, using the events from the experimental data only is not sufficient. As a consequence, the events are generated based on the experimental distributions.

The first simulation step, cf. Sec. 6.2.2, will start with the ^{27}F incoming ion at the beginning of the first target sheet. To model the particles distributions, the experimental distributions at the start position are extracted. The position of the particle at the start is extracted using the BDCs as described in Sec. 4.6.1. The x and y distributions are fit with Gaussian functions from which random values can be sampled. The energy of the particle is obtained from the calibration simulation described in Sec. 6.1. As this distribution does not follow a Gaussian distribution, a more sophisticated fit has to be performed. The best fitting function is a sum of sigmoid and Gaussian functions, shown in Fig. 6.7. This function is used to generate input energy values for the simulated events. The velocity and the total momentum are calculated with this energy value. The components of the momentum vector are again sampled from the respective experimental distributions, scaled with the total momentum.

With this approach of generating the events, the experimental distributions are modeled but the correlation between the individual properties is lost as the values are independently sampled. However, in the experimental data, only a slight correlation between position and angle is visible which can therefore be neglected in the event generator.

6.2.2. Transport of ^{27}F and Proton Removal

With the events generated, the first simulation is performed where the incoming isotope, ^{27}F, is transported through the reaction target. In GEANT4, the particle is transported in steps where the information, *e.g.*, time-of-flight, energy, position, etc., is made available at every step. For this simulation, the step length is fixed at $100\,\mu$m within the target material. Since the number of steps increases the duration of the simulation, this length is a compromise between simulation time and having a sufficient number of steps per target sheet.

The simulation is only used to transport the particles, while the proton removal is implemented afterwards, in a so-called converter, cf. Fig. 6.6. For this, the information at the individual steps is essential. To find the point of the proton removal z_r, input from theory calculations is used. The proton knockout cross sections for this analysis σ_r, in addition to the total reaction cross sections σ_{tot} and the ^{26}O fragment momentum distributions after the knockout were calculated by C. Bertulani [Ber21]. More details about the theory calculations are described in Sec. 6.2.5 and App. B. From the proton knockout cross section, the reaction probability is calculated for each step of the simulation, depending on the target material. It is decided for each step if the proton knockout occurred by comparing the reaction probability for this step to a reference value. The reference probability is randomly generated from a uniform distribution of values between zero and one. If the reaction probability is larger than the reference probability, it is interpreted that a reaction has occurred and the event is kept for the next step, otherwise it is rejected. For the same step, the reaction probability from the total reaction cross section is also calculated to include beam losses due to other reactions, and is again compared to a randomly generated reference value. Here, the event is kept, if the reaction probability is smaller than the reference value, because this means that the reaction did not happen. The resulting position distribution z_r of the proton removal is shown in Fig. 6.8. As expected, the peaks appear at the target positions with decreasing width as also the thickness of the target sheets decreases with beam direction. Furthermore, the proton removal only happens within the target material as it was required in the converter. The red spectrum includes the beam loss, calculated from the total reaction cross section σ_{tot} in contrast to the blue spectrum. It can be seen, that the further the beam passes through the target material, the higher the probability of particle loss, as expected from the calculations.

Finally, the particle has to be transformed into ^{26}O. This is done using the calculated momentum distributions, shown in Fig. 6.11 for the Pt target. For each of the three spatial directions, a momentum value is randomly sampled from the distribution of the respective energy of the particle. To obtain a uniform direction distribution in the center-of-mass frame, the angle of the final momentum is chosen from a normalized sphere around the position of the proton removal z_r. After the knockout, the particle is boosted in beam direction. Finally, the particles properties are written to an `ascii`-file to be used as an input for the next simulation. In total, approximately 1 billion events were simulated in this step, as the reaction probability for the proton knockout is very small at an order of $\approx 0.001\,\%$ and a sufficient amount of reactions in each target sheet is necessary for the analysis. With this approach it is assured that the generated particles are independent of each other and no accidental structures are created by reusing generated events with the same properties.

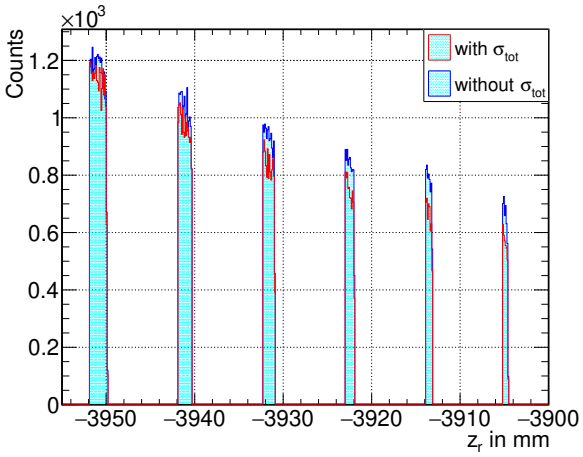

Figure 6.8.: Position distribution z_r of the proton knockout from ^{27}F. The red spectrum includes beam losses due to the total reaction cross section σ_{tot} that decreases the number of proton removal reactions with beam direction.

6.2.3. Transport of ^{26}O and Neutron Decay

In the next step of the lifetime simulation, the ^{26}O particles are transported through the target again with the starting point at the position of the proton removal z_r. For this simulation it is necessary to get the information from each step also in the gap between the targets which is essential for finding the decay position of ^{26}O which takes place both inside and outside of the material, cf. Sec. 3.1. To do so, "gap detectors" between the target sheets are implemented in the simulation. They consist of vacuum but also act as a sensitive volume in GEANT4.

After the simulation, another converter is used to create the input for the next simulation step. Here, a lifetime value τ is assigned to each event, which is randomly sampled from a uniform distribution of lifetime values in the interval $\{0\,\text{ps} < \tau \leq 15\,\text{ps}\}$. The lifetime of the particle is then generated from an exponential distribution with the decay constant τ. To identify the step of the simulation and thus the position z_τ where the decay happened, the lifetime is compared to the Lorentz corrected time-of-flight of the particle. In addition, the reaction probability of the ^{26}O particle is calculated from the total reaction cross section for each step. The decision is made similarly to the method described in Sec. 6.2.2. If the particle undergoes a secondary reaction, it is rejected for further processing. The decay position distribution z_τ is shown in Fig. 6.9 for a short (red) and a long (blue) lifetime. The width of the targets is indicated by the black lines. For the short lifetime, the decay mainly happens inside the material, and the contribution from outside decays is small. For a long lifetime, the ratio from outside to inside decays is expected to increase, cf. Sec. 3.1, which is also reflected in the position distribution as a substantial amount of decays occur between the targets.

Finally, the decay is implemented using the phase space decay routine of ROOT which is a tool to generate the decay kinematics of an initial nucleus, in this work ^{26}O, decaying into a number of daughter nuclei, here ^{24}O and two neutrons. A relative energy of 18 keV is used in this decay according to [Kon+16]. The decay is performed in the center-of-mass frame. Afterwards, each particle in the final state is boosted in beam direction using the velocity β of the initial particle.

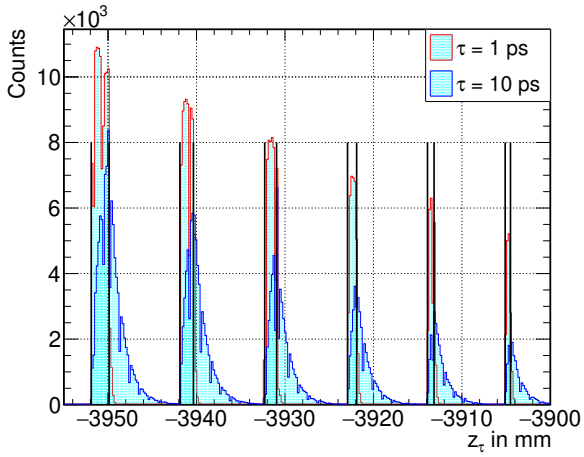

Figure 6.9.: Position distribution of the decay position z_τ for two different lifetimes. The black lines indicate the size of the six target sheets. For the small lifetime of 1 ps (red) the decays mainly happen inside the targets as compared to the long lifetime of 10 ps (blue), where the number of outside decays between the targets is increased.

6.2.4. Transport of ^{24}O and 2n

In the last step of the simulation process, the decay components are transported through the rest of the setup including all detectors and materials after the target. The simulation starts at the decay position z_τ and each event consists of three particles, ^{24}O and two neutrons. For this simulation, a fixed step size of the particle transport is not necessary anymore.

Again, particles are rejected for the analysis based on the total reaction cross section of ^{24}O with the tungsten and platinum material. The number of secondary reactions that could occur in the materials of the detectors after the target, *e.g.*, the FDCs gas mixture, is assumed to be small compared to the target materials and is neglected. Furthermore, the experimental resolutions, determined in Ch. 4, are included in the last converter to make the simulation data comparable to the experimental one. Additionally, during the experimental analysis, certain assumptions were made, that have to be included into the simulation analysis. Firstly, the position from where the time-of-flight of the fragment and the neutrons is measured (see Sec. 4.5) and secondly how the flight path of the fragment is reconstructed through the magnet (see Sec. 5.1.2). The resulting $\Delta\nu$-spectrum over the simulated lifetime range is shown in Fig. 6.10. For longer lifetimes, the individual contributions from outside decays after the target sheets become visible and the peak structure explained in Sec. 3.1 is created.

6.2.5. Input from Theory Calculations

To make the simulation as realistic as possible, theory calculations were included to estimate certain quantities: the proton knockout cross sections, the total reaction cross sections and the fragment momentum distributions after the knockout were calculated by C. Bertulani [Ber21]. Details are described in App. B.

The total reaction cross section σ_{tot} is used in every step of the simulation process to estimate the beam loss in the target material due to different reactions. The full list of calculated cross sections

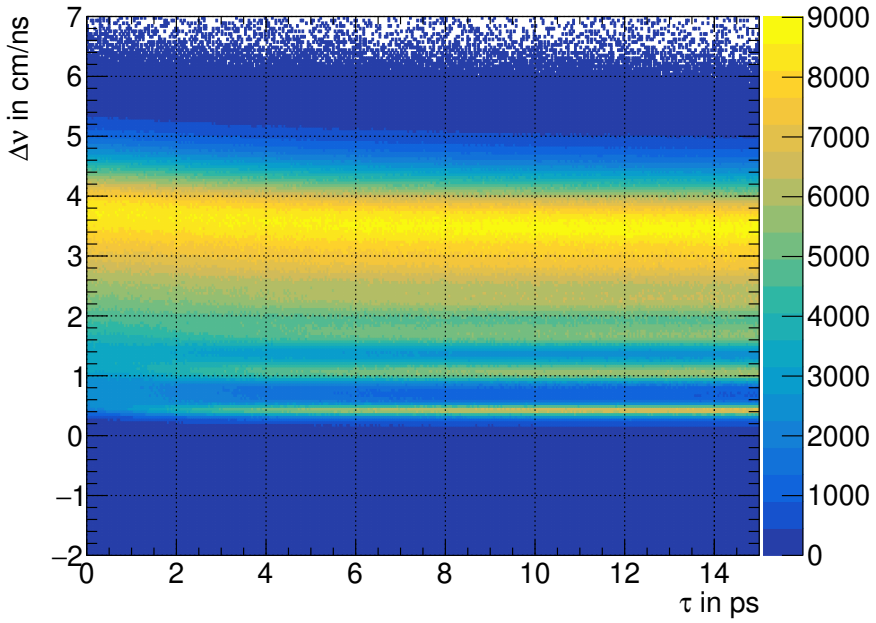

Figure 6.10.: Result of the lifetime simulation. The velocity difference $\Delta\nu$ is shown over the range of simulated lifetime values. For long lifetimes the number of outside decays increases, creating the sharp peak contributions.

is shown in Tab. B.1 and B.2. The cross sections were calculated for a discrete set of energies that corresponds to the experimental energy range. For each isotope and material the cross section distribution is fit with a power function to get a continuous distribution as a function of energy. An example fit is shown in Fig. B.1. For each event at each step in the simulation, the cross section value is evaluated from the fit function. From this, the reaction probability p_r of each step with length l_{step} is calculated as:

$$p_r = \sigma_{\text{tot}} \cdot N_A \cdot \rho_{\text{tgt}} \cdot \frac{l_{\text{step}}}{M_{\text{mol}}}, \tag{6.1}$$

with the Avogardo constant N_A, the molar mass M_{mol}, and the density ρ_{tgt} of the target. With the reaction probability, it is decided for each step if the reaction occurred, as explained in Sec. 6.2.2. This is done analogously for the proton knockout cross sections σ_r, listed in App. B.1.2.

The ^{26}O fragment momentum after the knockout is sampled from the calculated theory distributions. The longitudinal and transversal momentum distributions after the knockout in the platinum material are shown in Fig. 6.11. The corresponding distributions for the tungsten material are shown in Fig. B.2. As they were calculated for discrete energies, the distributions must first be interpolated for the desired energy of each event. In the simulation, a random value will be chosen from the distributions at the interpolated energy. For the longitudinal momentum, the shape at different energies is very similar. Here, it is sufficient to use the distribution of only one discrete energy to sample values for every event as the difference in shape is not significant. This is not the case however, for the transversal direction, where the dependence of the shape on the energy is significant. For smaller beam energies, the peak shifts to larger momenta and the distribution gets broader. A possible

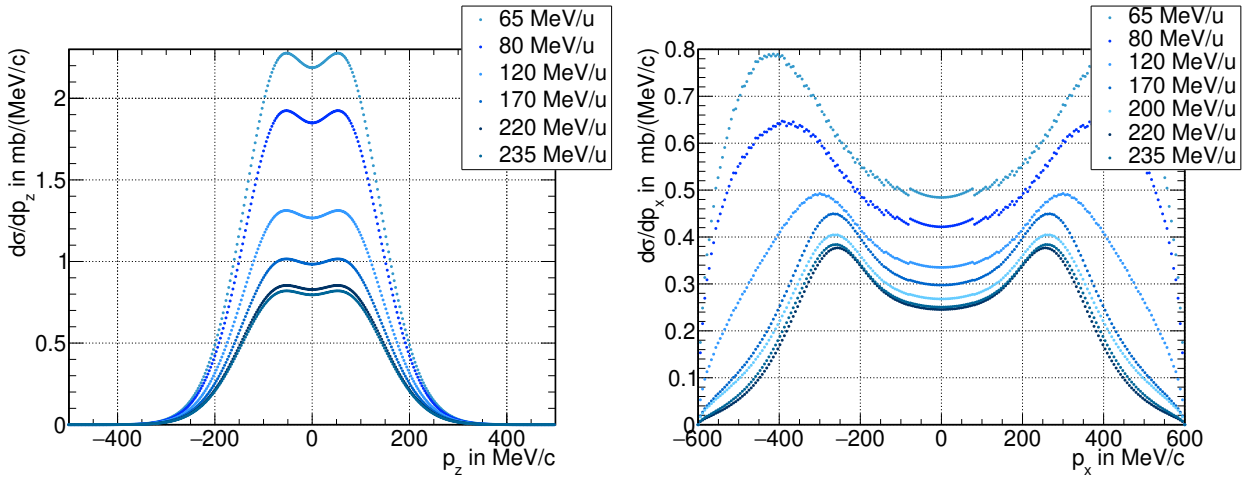

(a) (b)

Figure 6.11.: Calculated (a) longitudinal and (b) transversal momentum distributions of ^{26}O after the proton knockout at the platinum target for different beam energies.

explanation for this is the larger influence of the Coulomb barrier in this component. In consequence, for the energy of each particle, the corresponding momentum distribution is interpolated. The resulting distributions are used to sample a momentum value for the transversal and the longitudinal direction. The shape of the distribution reflects the probability of how often a value on the momentum axis is chosen in the sampling process. The absolute value of the amplitude is not important for this application and is therefore not normalized.

For the calculations, it is assumed that the proton is knocked out from the $d_{5/2}$ shell. This corresponds to the outermost proton in the core and the other protons occupy the closed shell at $Z = 8$. Further inputs for the calculations are the one proton separation energies, which are $S_p = 16.82\,\text{MeV}$ for ^{27}F and $S_p = 15.94\,\text{MeV}$ for ^{26}F [Lab22].

6.2.6. Reference Channel

The same simulation procedure is repeated to the reference channel. Here, ^{26}F is transported to the point of the proton removal. Then ^{25}O is produced with zero lifetime which decays into ^{24}O and one neutron. Compared to the lifetime simulation of ^{26}O, the ^{25}O decays in the same GEANT4-step after it is produced from the proton knockout. The decay energy of the ground state of 749 keV [Kon+16] is implemented in the phase space decay. This simulation is performed to develop the neutron reconstruction procedure for the case where only one neutron is detected, and to be able to compare the shape of the resulting $\Delta\nu$-spectrum of the experiment to the simulation. The corresponding input from theory calculations is shown in App. B. The simulated $\Delta\nu$-spectrum is presented in Fig. 7.16 in comparison to the experimental reference spectrum with the ^{26}F setting.

6.3. Neutron Reconstruction

6.3.1. Matching Simulation

The interaction of particles with the material is modeled by the physics list. If the readout of the detector is special, creating additional effects in the data, this has to be included into the simulation manually. For the neutron data, the processes in the scintillator bars have to be included. For this, the light output of the energy deposition is calculated using Birk's law [Bir51]. This light is transported to each end of the scintillator bar using the effective speed-of-light in the material. The signals from the individual sides are smeared with the ToF resolution of the neutron detectors, as determined in Sec. 4.8.4. The ToF is calculated from the average of the two measurements, as it is done for the experimental data, and corrected with the time of the transport from the hit position to the ends of the bars. The hit position is calculated from the time difference, c.f. Eq. 3.3. The remaining two position coordinates are again randomized within the bar thickness. For the charge measurement, the attenuation of the light is taken into account with the attenuation coefficient of the material and the travelled distance within the bar. PMT thresholds are applied according to the experimental data and the total charge is calculated using Eq. 3.2.

Figure 6.12 shows the comparison between the simulated (blue) and the experimental data (red) of certain properties of the neutron detectors. The simulation was performed as described in Sec. 6.2. Overall, the simulated distributions are in agreement with the experimental data, especially for the measured charge (Fig. 6.12c), the longitudinal hit position (Fig. 6.12d) and the hit multiplicity in NeuLAND. For NEBULA the agreement is even better. Small differences could be explained by the used physics list. However, a difference between the ToF spectra, c.f. Fig. 6.12a and 6.12b, can be observed, where the rising edge of the experimental spectrum has an additional contribution that is not reproduced in the simulation.

The additional contribution appears at smaller ToF values, corresponding to faster particles. This could come from reactions that happen in front of the target. In such a reaction, the neutron would be faster than other neutrons that are produced later due to the missing energy loss of the initial particle. This kind of reaction can be excluded with a cut on the charge $Z = 9$ on the ICB and the silicon detector, that is placed just in front of the target. However, if this cut is applied, the contribution in the ToF spectra of the neutron detectors does not vanish. The ToF resolution could be another explanation, as it was determined with the γ-peak in the experimental data. Since the energy deposition of the neutrons is larger, the resolution value determined from γ-rays acts as an upper limit. Nevertheless, it is tested if the additional contribution in the ToF distribution could come from a too small resolution value in the simulation. This is done by increasing the resolution in the simulation by 10 %. As the difference in the ToF spectra could not be explained by this, the ToF resolution was increased even further to an unrealistically high value of 1 ns which was again not sufficient to explain the additional contribution.

6.3.2. Neutron Reconstruction Algorithm

When a neutron hits the neutron detectors, it needs to undergo an interaction creating charged particles, such as protons, that can produce scintillation light and can be detected in the scintillator

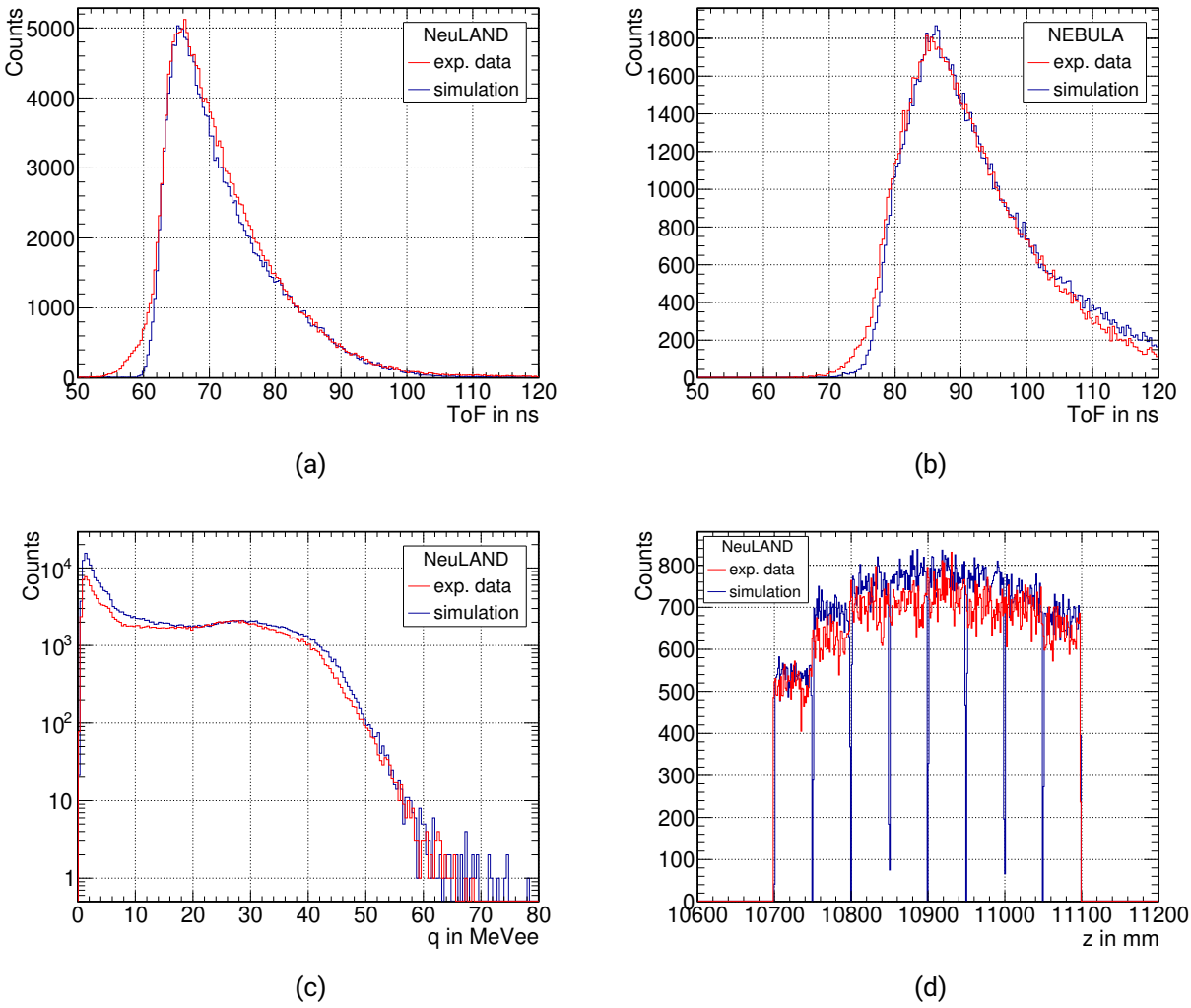

Figure 6.12.: Comparison between simulated (blue) and experimental data (red) of basic distributions in the neutron detectors. Shown are the time-of-flight distributions in (a) NeuLAND and (b) NEBULA, (c) the measured charge and (d) the hit distribution in z direction in NeuLAND. The agreement is overall good. For the ToF, an additional contribution in the experimental data appears at smallest ToF values.

material. The knocked-out proton is possibly scattered further and produces several hits in the detectors which belong to the same initial neutron. The goal of the neutron reconstruction procedure is to develop an algorithm that is able to identify the initial neutrons. The hits that belong to the same neutron have to be clustered together, to reconstruct the neutron energy, hit position and time-of-flight. Signals originating from particles produced in the process, *e.g.*, protons or γ-rays, which do not belong to the initial hit, are called cross talk, which has to be identified and rejected. The reconstruction procedure was originally developed by T. Nakamura *et al.* [Nak+16] for the SAMURAI setup with the NEBULA detector and was adjusted for the combined neutron detection with NeuLAND and NEBULA by C. Lehr [Leh21]. The algorithm used in this analysis is adapted to the requirements of this measurement from both mentioned algorithms and is described in this section.

To develop the reconstruction algorithm, the simulated data from the lifetime simulation is used for the two-neutron case and data from the reference channel simulation is used for the one-neutron case. In the simulated data, the initial neutrons produced in the decay, called primary neutrons, are marked with a flag. With this flag, it is possible to check if the reconstructed hit came from a primary or a falsely identified neutron. This is used to determine the efficiency of the algorithm and the remaining cross talk contribution. Finally, the algorithm is applied to the experimental data, to reconstruct the neutron hits in the same way.

Time-of-flight

In the first step, a cut is applied on the time-of-flight to exclude unrealistically low and high ToF values that are produced by random coincidences with cosmic rays. However, the ToF cut in the analysis of the two neutron case is not very strict but relaxed, to ensure that the second neutron is not cut away.

Clustering and Charge Cut

During the clustering, hits that are close in space Δr and time Δt are grouped to the same cluster. For this, limits are defined for NeuLAND and NEBULA individually in which hits are considered close. The spatial distance is defined by a sphere with radius Δr around the hit and is 200 mm for NeuLAND and 330 mm for NEBULA. The difference Δt in time is 1.33 ns for NeuLAND and 2.2 ns for NEBULA. The distribution of pairs of hits in time difference versus spacial distance is shown in Fig. 6.13a. The values for Δr and Δt are estimated from the velocity of the neutrons and by eye from Fig. 6.13a. All hits within these constraints are sorted into the same cluster by starting with the first hit of an event and checking all remaining hits. The next hit of the remaining hits starts a new cluster if the Δr and Δt conditions cannot be fulfilled anymore. This procedure is repeated until all hits are sorted into clusters.

The hits within one cluster are sorted according to the time-of-flight, such that the ToF of the first hit in the cluster determines the ToF of the whole cluster. The total energy of the cluster is given by the summed energies of all hits in one cluster. After the clustering, a cut is applied on clusters with a charge smaller than 5 MeVee as they are coming from low energy γ-rays produced in other processes and are considered cross talk.

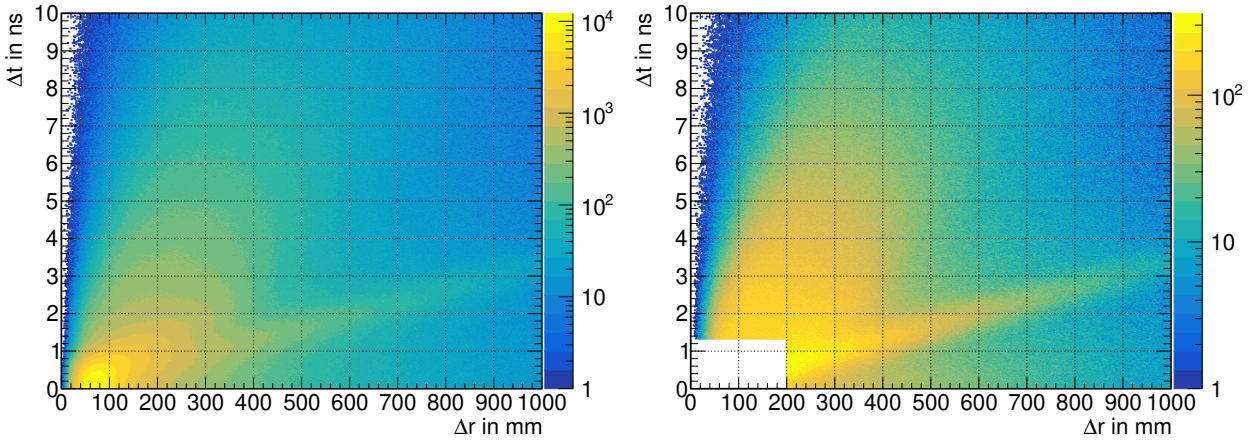

(a) (b)

Figure 6.13.: Distance in space Δr and time Δt between hits/clusters in NeuLAND (a) before and (b) after the clustering. The clustering combines hits that meet the conditions for Δr and Δt. After the clustering, the cross talk produced by γ-rays becomes visible by the diagonal line. Shown is data from the lifetime simulation with the two neutron case.

Cross Talk from γ-rays

The cross talk produced from high energy γ-rays is visible in Fig. 6.13b. The γ-rays travel with the speed of light and are therefore faster than the neutrons, creating the diagonal line in Fig. 6.13b. Their energy is high enough to survive the charge cut but still small compared to the neutrons. To separate them better from the neutron hits, the velocity β_{12} between the first and the second cluster is used. β_{12} is calculated from the distance in space and time between the two clusters: $\beta_{12} = \Delta r/(\Delta t \cdot c)$. The inverse of the velocity is plotted versus the charge q_2 of the second cluster in Fig. 6.14a. The cross talk from the γ-rays appears at $^1/_{\beta_{12}} \approx 1$. The black lines in Fig. 6.14a indicate the cut to remove the γ cross talk. This cut is applied to clusters within the same wall of scintillator bars and then to clusters in all walls, *i.e.*, between NeuLAND and NEBULA.

Cross Talk from Neutrons

To remove the cross talk produced by the neutrons themselves, a causality cut is applied. If a neutron is scattered in the detector material, it will lose energy and travel slower than before the scattering process. Therefore, the velocity β_{01} from the decay point to the first cluster, calculated from the hit position and the ToF to the first cluster, would be larger than the velocity between the first and the second cluster β_{12}. To identify the neutrons that fulfill the condition, the ratio $^{\beta_{01}}/_{\beta_{12}}$ is plotted versus the charge q_1 of the first cluster in Fig. 6.14b. The neutron can have a maximum velocity β_{12} after the first interaction (black line), corresponding to the energy loss of the first cluster. The cross talk appears at large values for $^{\beta_{01}}/_{\beta_{12}}$ (right side of black line), since the second cluster fulfills the condition and could be produced by a scattered neutron. This condition is again applied to the clusters in the same detector wall and afterwards to clusters in different detector walls.

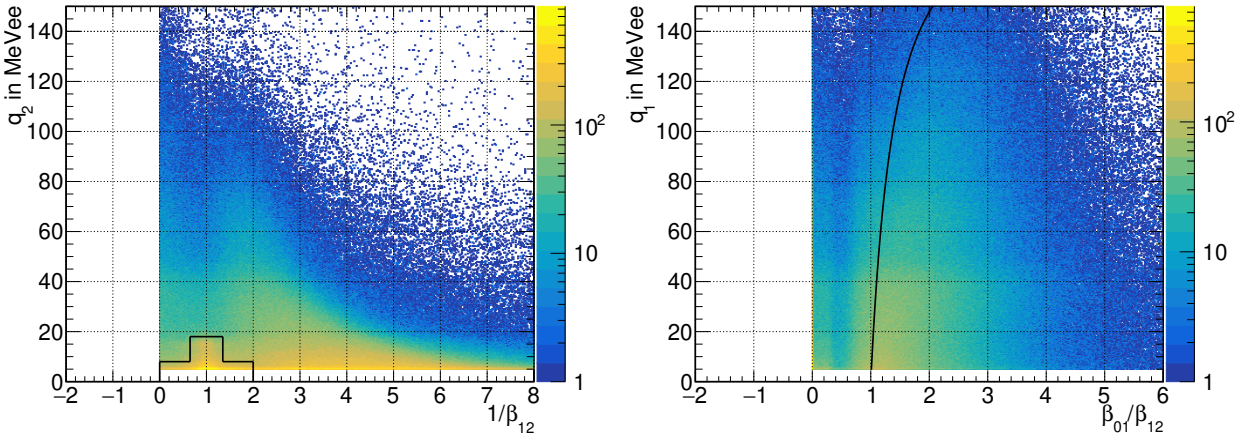

(a) (b)

Figure 6.14.: (a) Cross talk produced from γ-rays can be identified when plotting the charge measured in the second cluster versus the inverse velocity between the first and the second cluster. It accumulates around $1/\beta_{12} \approx 1$ and is removed by the cut indicated by the black box. (b) Cross talk produced by scattered neutrons. If the velocity β_{12} between the first and the second cluster is smaller than the velocity β_{01} between the reaction point and the first cluster, it is possible that the second cluster is produced by a scattered neutron and therefore all clusters to the right of the black line are removed. Shown is data from the lifetime simulation with the two neutron case for NeuLAND.

Veto Condition

Finally, a veto condition is applied. If a particle hits the veto wall, hits in a certain area in the detector wall behind are discarded. For this analysis, the maximum distance of 400 mm between the veto hit and the hit in the detector produced the best results. Alternatively, the veto hit can also be used to remove the entire event. However, this approach is too strict for this analysis. The veto wall of NeuLAND did not work properly during the experiment which means its data cannot be used. Only the veto walls of NEBULA are used in this analysis. Nevertheless, the background coming from the fragment side appears later in time and is removed by the ToF cut, such that the missing NeuLAND veto wall is not critical for the analysis.

6.3.3. Reconstruction Efficiency and Algorithm Performance

The performance of the reconstruction algorithm is determined using the simulation again, since the amount of primary neutrons is known and can be compared to the number of reconstructed neutrons. For a neutron to be detected, it has to undergo a measurable interaction with the detector material. This depends on the energy of the neutron, the thickness of the material and if the particle passes through the geometrical acceptance of the setup. The acceptance is defined as the probability of the particles in the final state to hit the detector that they are supposed to be measured in. Considering only the neutrons, the detection efficiency for the 1n case is around 56 % and around 37 % for the 2n case, including the acceptance of the neutrons. However, taking the fragment into account, meaning that it hits FDC2 and HODF, the detection efficiency decreases to 38 % (1n) and 27 % (2n). A possible

explanation is that due to the thick and dense target, the fragment undergoes a lot of scattering processes and is often scattered out of the setup's acceptance. Consequently, the fragment is taken into account for the acceptance in this analysis.

The efficiency of the reconstruction algorithm is determined using the primary neutrons of the simulation. It takes the acceptance into account, so that the reconstruction efficiency is given by the number of reconstructed neutrons out of the accepted ones. The reconstruction efficiency for the 2n case is 42 % and 88 % for the 1n case. The total efficiency, given the number of reconstructed 2n events out of the total 2n events, is 12 %, and for the 1n case, 33 %.

The cross talk contribution is determined by the number of reconstructed 2n events, where only one neutron was accepted, meaning that one of the reconstructed neutrons is falsely identified. The cross talk contribution is 4.8 % for the 2n case.

7. Results and Discussion

In this chapter, the results of the analysis are presented and discussed, where a comparison between the experimental and simulated spectra is performed to determine the lifetime of ^{26}O. The analysis is performed for the range of simulated lifetimes $\tau = 0 - 15$ ps. For the comparison of the experimental and simulated distributions, simulated selected lifetime values are presented, in particular, $\tau = 6.5$ ps, which is the current literature value measured by Kohley *et al.* [Koh+13]. The analysis is done for different ranges of initial energies to take the energy dependence of the velocity difference into account for the lifetime value. Finally, the result is compared to the reference measurement and simulation of ^{25}O to deduce the uncertainty of the method.

7.1. Experimental $\Delta\nu$ Spectrum

After the calibration procedures, the essential ingredients to extract the velocity difference spectrum are available and the reaction channel, in which ^{26}O is produced from a proton knockout of ^{27}F and decays into ^{24}O and two neutrons, is tagged and identified. First, the desired fragment, ^{24}O, is selected according to the fragment identification cut shown in Fig. 5.4b and its ToF and flight length are measured as described in Sec. 4.7.3 and Sec. 5.1.2. Then, only events where two neutrons are detected in coincidence are considered further. The neutron's ToF and flight length are obtained after the neutron reconstruction. The reconstruction algorithm was explained in Sec. 6.3 for the simulated data and is applied in the exact same way to the experimental data. As explained in Sec. 3.1, the measurement principle is based on the shape of the $\Delta\nu$ spectrum, which is sensitive to the lifetime of ^{26}O, and is therefore used to assess it. Finally, the velocities of the fragment and neutrons are calculated and the velocity difference spectrum $\Delta\nu$ is obtained by subtracting the fragment velocity from that of the neutrons, $\Delta\nu = \nu_{\mathrm{n}} - \nu_{\mathrm{f}}$.

7.1.1. ^{26}O Decay Channel

The measured $\Delta\nu$ spectrum is shown in Fig. 7.1. The peak of the spectrum is located at ~ 3.5 cm/ns, with a sharp falling edge towards higher $\Delta\nu$ values and a slower rising edge towards lower $\Delta\nu$ values. A peak structure, produced by the different target sheets, which would indicate a long lifetime, would appear in the rising edge part of the spectrum. In Fig. 7.1, a prominent peak structure cannot be observed. Two broad "bumps" might be visible at ~ 0.5 cm/ns and ~ 1.5 cm/ns, with a sharp rising edge at ~ 0 cm/ns. The range of incoming energies was broad (≈ 30 MeV/u) in this experiment, leading to an energy dependence of the velocity-difference spectrum due to the energy loss of the fragment in the thick targets. This energy dependence will be discussed in Sec. 7.1.2 and Sec. 7.2.2. The spectrum in Fig. 7.1 is shown for the full range of incoming energies.

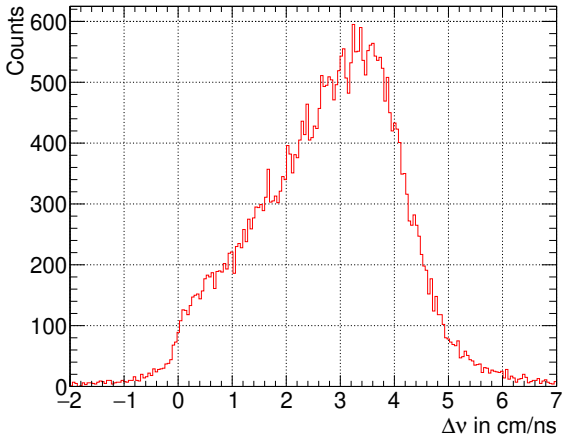

Figure 7.1.: Measured velocity-difference spectrum ($\Delta\nu = \nu_n - \nu_f$) from ^{26}O decay with a sharp falling edge towards high $\Delta\nu$ values and a slower rising edge between $\Delta\nu \approx 0 - 3.5\,\mathrm{cm/ns}$, where the peak structure created by the target sheets would appear for long lifetimes.

7.1.2. Reference Decay Channel ^{25}O

During the experimental campaign, an additional spectrum was measured, where ^{25}O decays into ^{24}O and one neutron, cf. Ch. 3. Its velocity-difference spectrum serves as a reference for zero lifetime ($\tau = 0\,\mathrm{ps}$), as the lifetime of the neutron unbound ^{25}O is much smaller ($\tau(^{25}\mathrm{O}) = 9 \cdot 10^{-9}\,\mathrm{ps}$ [Lab22]), which is well beyond the experimental sensitivity.

The comparison of the two experimental spectra is shown in Fig. 7.2a, again for the full range of incoming energies. The peak position of both spectra agrees, and is located at $\sim 3.5\,\mathrm{cm/ns}$. However, both edges of the spectrum show a clear difference. First, in the ^{26}O spectrum, the falling edge at high $\Delta\nu$ values drops faster than in the reference spectrum. The second and main difference is observed at the rising edges. Both spectra agree up to $\sim 0\,\mathrm{cm/ns}$, where the ^{26}O spectrum shows a "bump", as described above. These differences to the overall shape might hint to a small lifetime, since no clear peak structure can be observed in the ^{26}O spectrum but the shape is considerably different from the shape of the reference spectrum for ^{25}O.

The relative energy spectrum of ^{25}O is shown in Fig. 7.2b. Also here, a broad structure up to $\sim 10\,\mathrm{MeV}$ can be observed. Additionally, a peak at $\sim 1\,\mathrm{MeV}$ is visible, consistent with the ground state of ^{25}O, which is located at 749 keV [Kon+16]. The relative energy spectra for ^{26}O will be presented together with the simulation in Sec. 7.2.3.

As the velocity-difference is energy dependent due to the energy loss of the fragment in the targets, the same comparison is done with different slices of incoming energies. The incoming energy distribution as a function of the velocity-difference is shown in Fig. 7.3 for the ^{26}O decay, as well as the reference channel of ^{25}O. The range of incoming energies is divided into slices of 5 MeV, chosen as a compromise between the statistics and the reduction of the energy dependence. The resulting $\Delta\nu$ spectra are shown in Fig. 7.4 for the lowest and highest energy regions, together with an intermediate energy. The spectra still show differences at both edges. On the rising edge of both spectra, a peak structure becomes slightly visible though not very prominent.

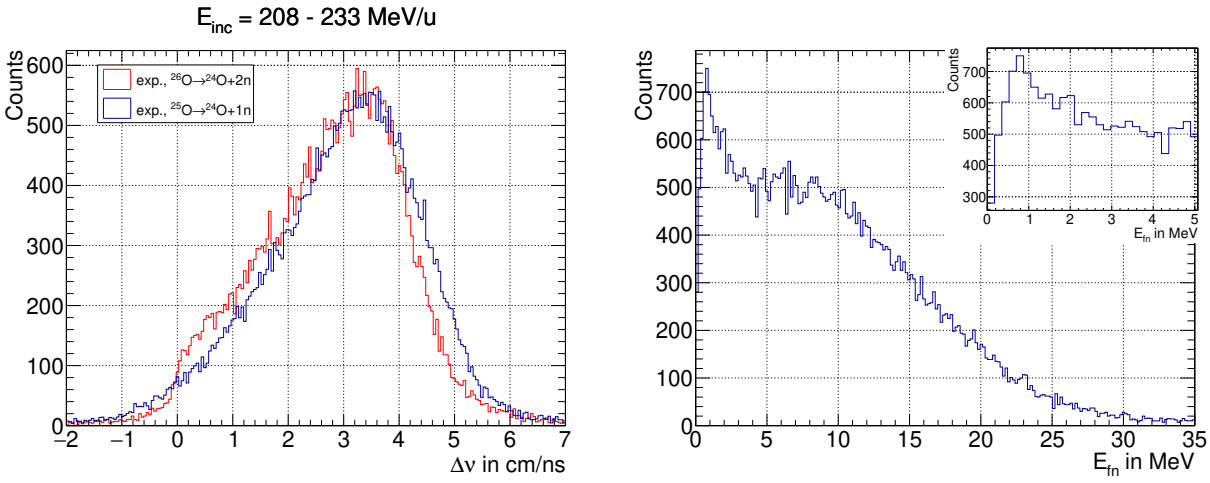

(a) (b)

Figure 7.2.: (a) Comparison of the ^{26}O (red) $\Delta\nu$ channel to the reference spectrum of ^{25}O (blue). The ^{25}O spectrum is downscaled for the comparison. Although the peaks are located at the same position, both, the rising and the falling edges, show a difference in shape. (b) Two-body relative energy spectrum E_{fn} from ^{25}O decay. A peak at around 1 MeV is visible, consistent with the ground state of ^{25}O. The inset shows the low energy region up to 5 MeV, where the ground state would be located.

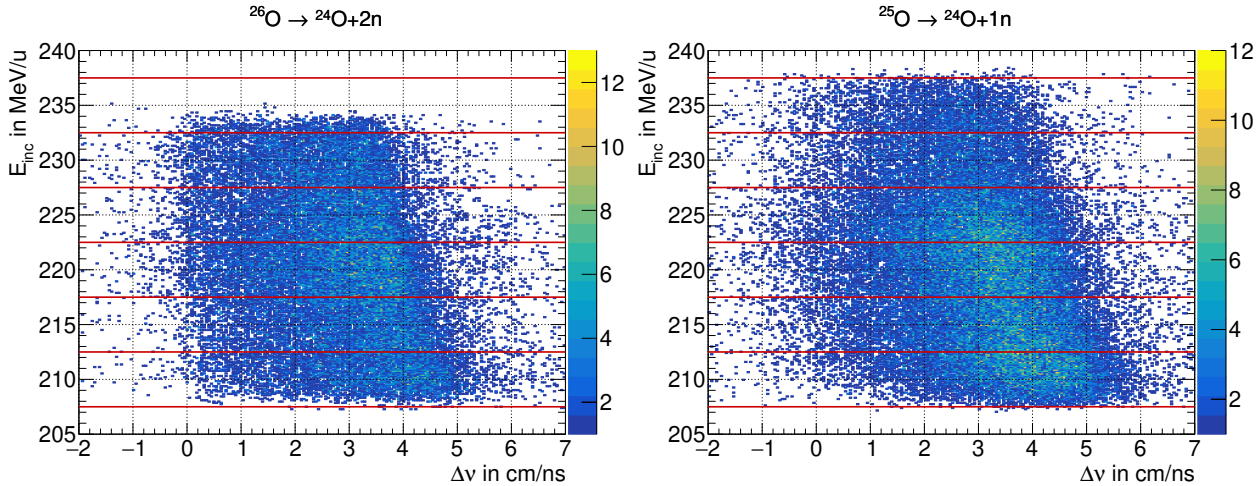

(a) (b)

Figure 7.3.: Incoming energy E_{inc} as a function of the velocity-difference for the decay of (a) ^{26}O and (b) ^{25}O. The velocity-difference is energy dependent due to the energy loss of the fragment in the target. To reduce this energy dependence for a comparison of the spectra, the distribution is cut into slices of 5 MeV, indicated by the red lines.

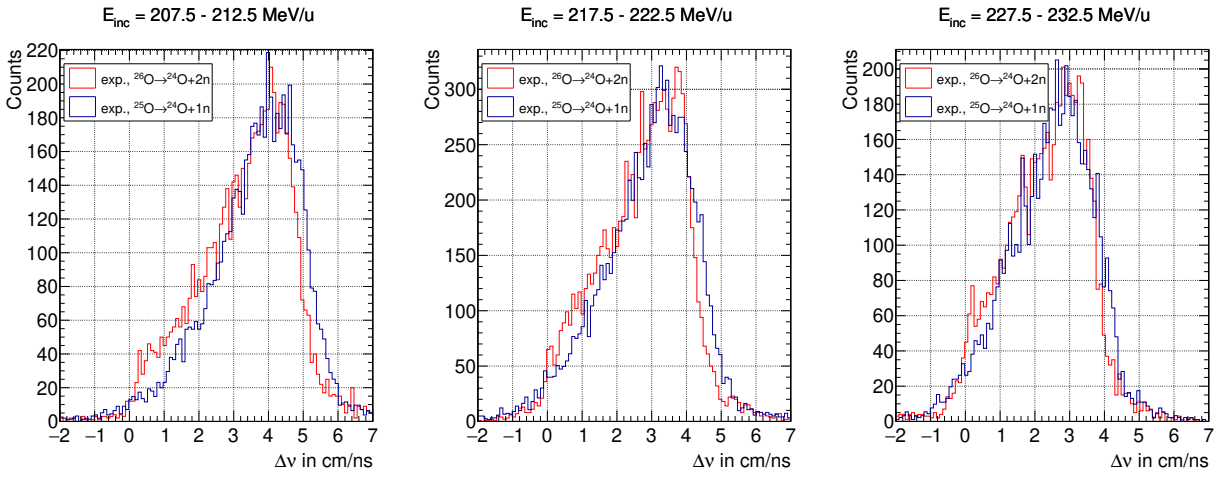

Figure 7.4.: Comparison of the measured velocity-difference spectra for ^{26}O (red) and ^{25}O (blue) decay for different ranges of incoming energy. The ^{25}O spectra are downscaled to match the statistics of ^{26}O.

7.2. Lifetime Determination using χ^2 Analysis

7.2.1. ^{26}O Decay Channel

The result of the lifetime simulation was presented in Fig. 6.10, in terms of the velocity difference as a function of the lifetime. The range of simulated lifetimes is $\tau = 0 - 15$ ps with a bin width of 0.04 ps. For the comparison of the simulated spectra with the measured one, each bin on the lifetime axis in Fig. 6.10 is projected onto the $\Delta\nu$ axis, resulting in discrete $\Delta\nu$ spectra for the range of simulated lifetimes. These projections are shown in Fig. 7.5 for $\tau = 0.02$ ps, 6.5 ps and 14.98 ps, corresponding to the first bin $(0 - 0.04$ ps), the previously measured value by Z. Kohley *et al.* [Koh+13], and the last bin $(14.96 - 15$ ps). The lifetime values indicated in the text and figures correspond to the center of the projected bin. For the shortest lifetime, the velocity-difference spectrum is positioned at the highest $\Delta\nu$, shifting towards lower values for longer lifetimes. In addition, the peak structure on the rising edge is more prominent for long lifetimes.

The more prominent peak structure for longer lifetimes can be explained with the increasing ratio of outside-to-inside decays presented in Sec. 3.1. The longer the lifetime of the particle, the longer it takes to traverse the target, leading to a decay between the target sheets. This is demonstrated in Fig. 7.6, where the inside and outside contribution from each target sheet is shown for a lifetime of $\tau = 1$ ps (a) and $\tau = 6.5$ ps (b). For the shorter lifetime, the inside contributions (solid line) are dominating, whereas for the longer lifetime the outside contributions (hatched area) develop, creating the prominent peak pattern in the sum spectrum. Furthermore, the peaks from the inside decays are wider than those from the outside decays due to the additional energy loss of the fragment after the decay.

Each of the projected histograms (*e.g.* Fig. 7.5) is converted into a function to fit the experimental spectrum. In this process, additional parameters are added that will act as fit parameters in the fitting procedure. Here, two parameters are have to be considered, a scaling factor p_0, as the simulated

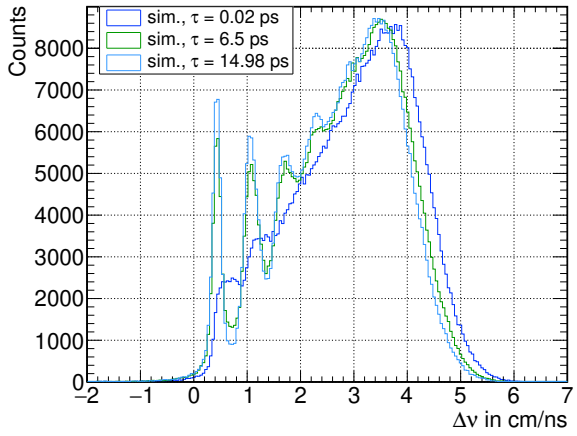

Figure 7.5.: Simulated velocity-difference spectra for the different lifetimes of $\tau = 0.02\,\mathrm{ps}, 6.5\,\mathrm{ps}$ and $14.98\,\mathrm{ps}$.

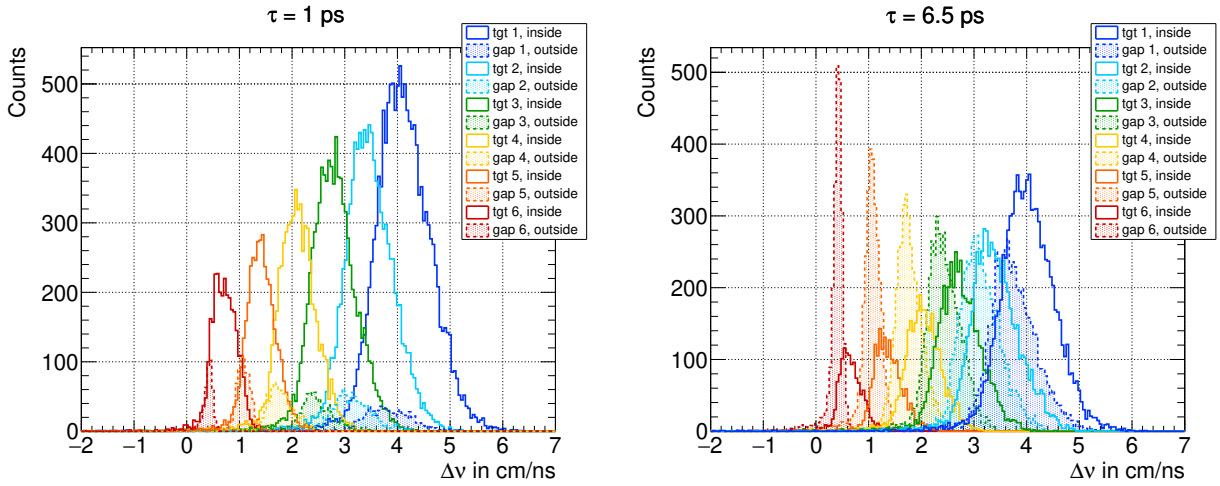

(a) (b)

Figure 7.6.: Simulated inside (solid) and outside (dashed, filled) contributions to the velocity-difference spectrum $\Delta\nu$ from every target sheet for (a) a short lifetime of 1 ps and (b) a long lifetime of 6.5 ps. For the short lifetime, the inside contributions are dominating, whereas for the long lifetime the sharp outside peaks are emerging, creating the prominent peak pattern in the sum spectrum.

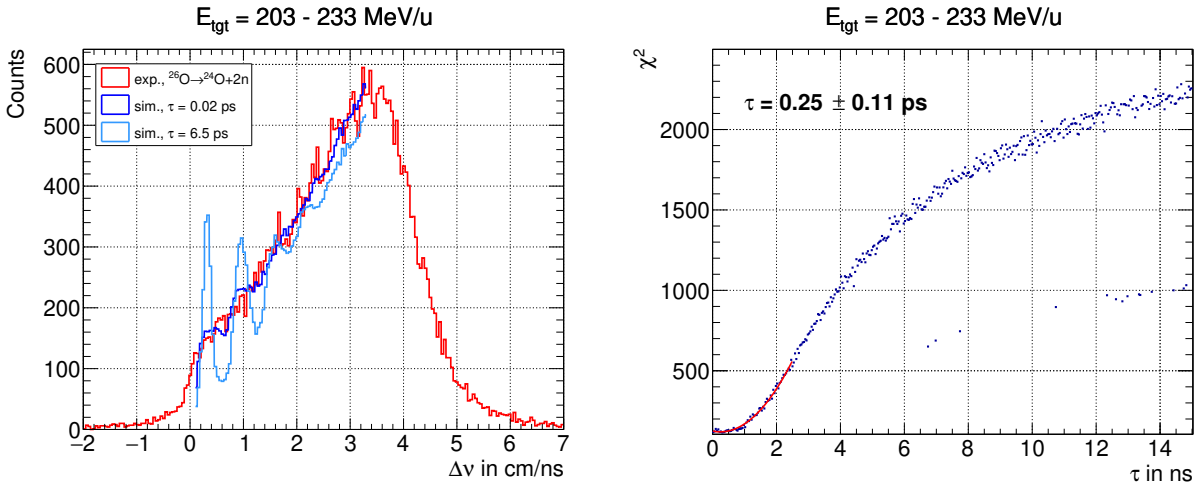

Figure 7.7.: (a) Measured velocity-difference spectrum (red) together with fitted simulated functions for lifetimes of $\tau = 0.02\,\text{ps}$ (dark blue) and $\tau = 6.5\,\text{ps}$ (light blue). The fit is performed with two parameters, a scaling factor and an x offset in the $\Delta\nu$ range presented ($\Delta\nu = 0.1 - 3.3\,\text{cm/ns}$). (b) Resulting χ^2 distribution as a function of lifetime τ. The minimum is determined with a parabolic fit resulting in a value of $\tau = 0.25 \pm 0.11\,\text{ps}$, with an associated uncertainty given by $\chi^2 + 1$.

spectra have around 10 times more statistics than the experimental plots and an offset p_1 on the x axis. The latter is included to make the fitting independent on the absolute position of the $\Delta\nu$ spectrum. As discussed in Sec. 6.1.2, the simulated and the experimental HODF time-of-flight do not match and the applied shift (see Fig. 6.3) has an influence on the absolute position of the resulting $\Delta\nu$ spectrum. Since the measurement method, introduced in Sec. 3.1, does not rely on absolute calibrations, the left side of the spectrum, which introduces the peak pattern, is of higher importance for the analysis and the structure itself is most sensitive to the lifetime. Therefore, the χ^2 analysis is performed without including the absolute position of the velocity-difference spectrum.

As the experimental spectrum has slightly different edges compared to the simulated ones, the fit range is limited to $\Delta\nu$ values of 0.1 - 5 cm/ns, cf. Fig. 7.11, where the full range is shown. These differences are possibly coming from the missing contributions of the silicon detectors. In the experiment, they can also act as additional targets in which the proton knockout from ^{27}F could take place with a subsequent decay of ^{26}O. In the simulation, however, the proton knockout and the decay can only happen in the tungsten and platinum targets. This part will be implemented as part of the next steps when finalizing the analysis results, cf. Ch. 8.

For the determination of the lifetime, only the area sensitive to the peak structure from the target contributions is considered. To be independent from the absolute position, the peak of the spectrum (at $\sim 3.5\,\text{cm/ns}$) is excluded, limiting the fit range further to $\Delta\nu = 0.1 - 3.3\,\text{cm/ns}$. The fit functions for two selected lifetimes $\tau = 0.02\,\text{ps}$ and $\tau = 6.5\,\text{ps}$ are shown in Fig. 7.7a together with the experimental spectrum. In order to determine the parameters with the best fit to the data, the minimal χ^2 is used as a measure, calculated according to Eq. 5.15. The resulting distribution of the minimal χ^2 values for each lifetime fit is shown in Fig. 7.7b. The minimum of this distribution is determined with a parabolic fit, where the uncertainty is given by the corresponding lifetime values

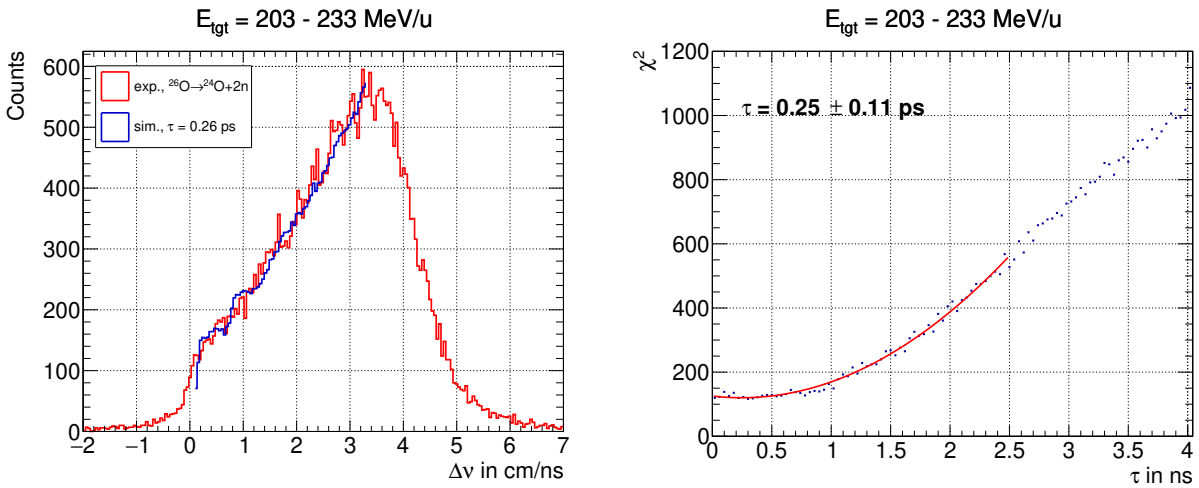

Figure 7.8.: (a) Measured velocity-difference spectrum (red) with the best fitting simulated function (blue). (b) The χ^2 distribution from Fig. 7.7b zoomed into the region of short lifetimes. The distribution appears to be nearly flat up to $\approx 1\,\mathrm{ps}$.

at $\chi^2 + 1$, as explained in Sec. 5.3. The lifetime, using this method with two fit parameters and the full range of incoming energies, is located at $\tau = 0.25 \pm 0.11\,\mathrm{ps}$. The experimental spectrum in comparison with the simulated function that corresponds to the fitted lifetime value is shown in Fig. 7.8a. The simulated distribution has broad peaks at $\sim 0.3\,\mathrm{cm/ns}$ and $\sim 1\,\mathrm{cm/ns}$, that are not visible in the experimental distribution. Here, a slight broad structure might appear at $\sim 0.5\,\mathrm{cm/ns}$. This part of the distribution is not reproduced well by the fit function and might also be shifted to higher $\Delta\nu$ values. This is also reflected in the χ^2 distribution, shown again in Fig. 7.8b with a zoom into the region of lifetimes up to 4 ps. The χ^2 distribution appears to be nearly flat up to $\sim 1\,\mathrm{ps}$.

7.2.2. Incoming Energy Dependence

As the energy loss of the fragment in the targets depends on the initial energy of the particle, the velocity-difference is also energy dependent, as shown in Fig. 7.9 for the measured and simulated distributions for lifetimes of 1 ps and 6.5 ps. For the longer lifetime, the peak structure created by the outside decays becomes visible, which cannot be observed for the shorter lifetime and the experimental distribution. In the analysis described above, the full energy range was used for the $\Delta\nu$ spectra. To investigate the effect of the incoming energy on the result, the same analysis is performed with a cut on the energy. The energy at the start point of the simulation, *i.e.*, the position of the first target, referred to as E_{tgt} hereafter, is divided into 5 MeV slices, indicated by the red lines in Fig. 7.9. The 5 MeV range is chosen to obtain sufficient amount of statistics but also to reduce the energy dependence at the same time. As an example, the result for the slice with an incoming energy between $E_{\mathrm{tgt}} = 208 - 213\,\mathrm{MeV/u}$ is shown in Fig. 7.10. With the cut on the energy, a structure with broad peaks becomes visible at the rising edge of the experimental distribution, which agrees with the simulated function for small lifetimes. The minimum of the χ^2 distribution is found at $\tau = 0.43\,\mathrm{ps}$ for this energy range. The flat trend which was visible in the distribution of the full energy range is not visible anymore and the distribution around the minimum follows the expected quadratic

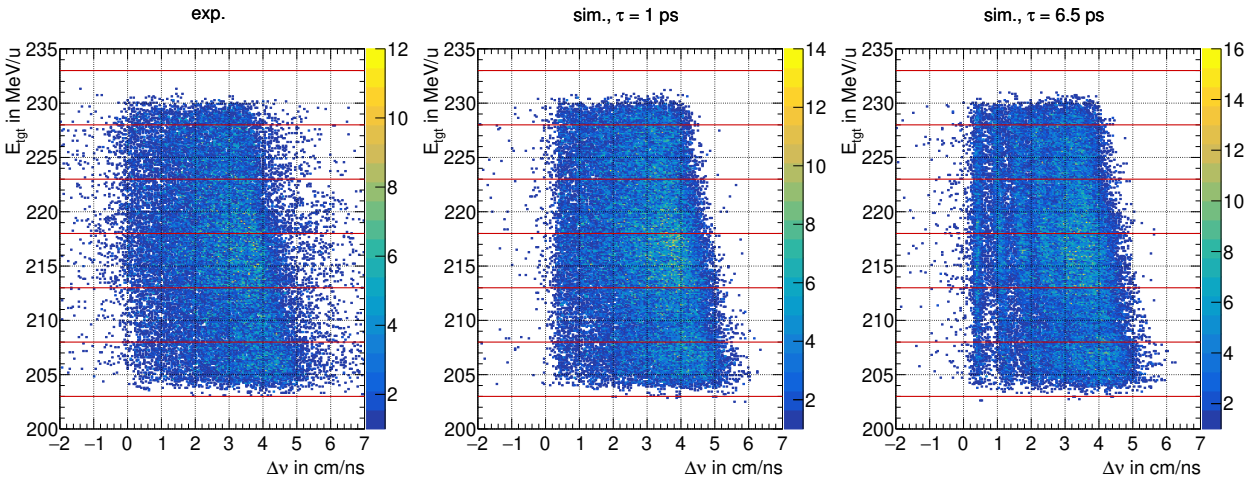

Figure 7.9.: Incoming energy E_{tgt} as a function of velocity-difference $\Delta\nu$ for (a) the experimental data and simulated data with (b) $\tau = 1\,\text{ps}$ and (c) $\tau = 6.5\,\text{ps}$. The influence of the incoming energy on $\Delta\nu$ and consequently on the lifetime result is investigated using slices of 5 MeV incoming energy indicated by the red lines.

dependence. The uncertainty, determined from $\chi^2 + 1$, is larger due to the lower statistics and the therefore stronger scattering of the χ^2 values. The results for all energy slices are summarized in App. C.

The resulting lifetime value averaged over all energy slices, leads to $\tau = 0.44\,\text{ps}$. The arithmetic mean and the corresponding uncertainty is calculated according to Eq. C.1 and C.2. Due to the reduced energy dependence, the χ^2 distributions for each slice do not show a flat behavior anymore (cf. Figs. C.1 and C.2), which was observed using the full energy range (cf. Fig. 7.10b). In conclusion, the χ^2 analysis of the experimental velocity-difference $\Delta\nu$ spectrum leads to a small lifetime of $\tau(^{26}\text{O}) = 0.44 \pm 0.11\,\text{ps}$. For comparison, simulated spectra corresponding to the resulting lifetime value (0.46 ps) and the previously measured value of 6.5 ps are shown over the full $\Delta\nu$ range together with the experimental spectrum in Fig. 7.11. The spectrum of the current literature value of 6.5 ps [Koh+13], shows a prominent peak structure at the rising edge missing in the experimental spectrum. The spectrum of the small lifetime compares well with the experimental finding, as compared to the spectrum for the previously measured lifetime of $6.5\,\text{ps}$.

7.2.3. Invariant-Mass Spectroscopy

As discussed in Sec. 5.2 the invariant-mass method can be used to extract the relative energy between different particles in the final state. The measured relative-energy spectra are shown in Fig. 7.12: (a) the three-body (^{24}O+2n) relative energy E_{fnn}, (b) the two-body subsystem, ^{24}O fragment and only one neutron E_{fn} and (c) the two-neutron subsystem E_{nn}. As explained in Sec. 5.2, a precise analysis of the relative energy cannot be performed in this analysis, due to the limited momentum resolution induced by the thick targets. Yet, it is used as a cross check for the simulation procedure and analysis.

In all three relative energy spectra, a peak at low energies ($< 1\,\text{MeV}$) is visible, related to the ground state of ^{26}O located at 18 keV [Kon+16]. Additionally, a peak at around 2 MeV, can be

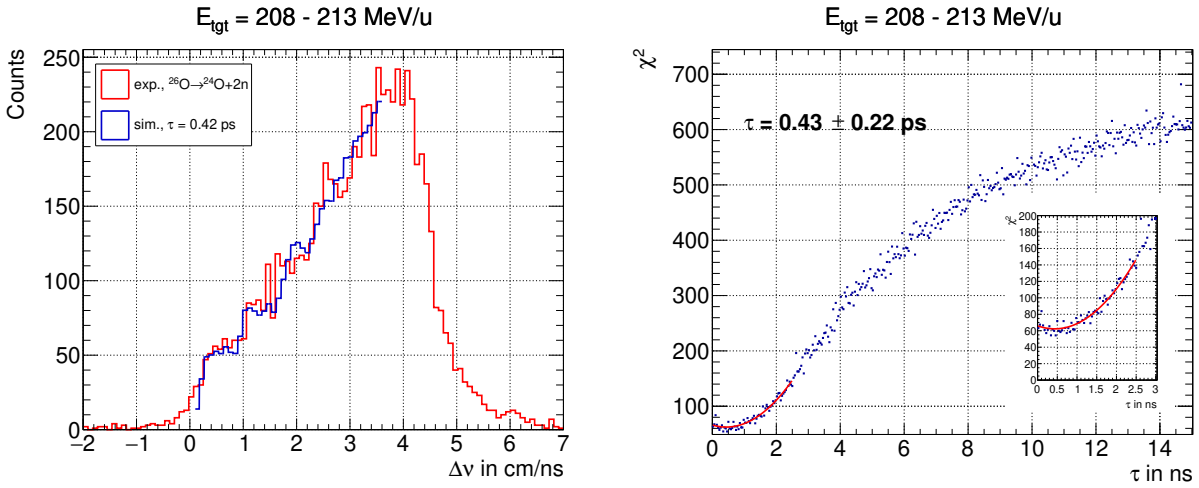

Figure 7.10.: (a) Measured $\Delta\nu$ spectrum (red) for incoming energies between $E_{\text{tgt}} = 208{-}213\,\text{MeV/u}$ with the simulated function (blue), corresponding to the best fit. (b) χ^2 analysis with the minimum at $\tau = 0.43 \pm 0.22\,\text{ps}$ for this energy range.

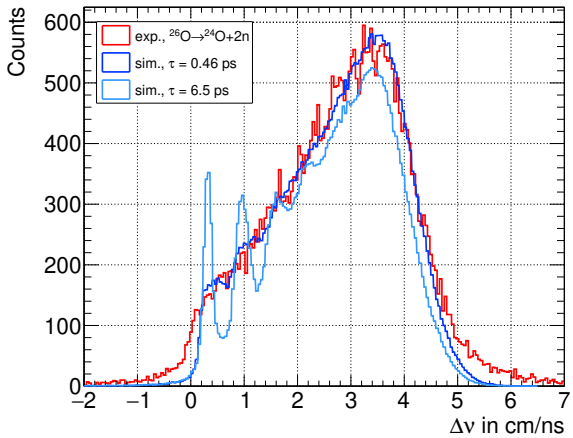

Figure 7.11.: Comparison of the measured velocity-difference spectrum together with the simulated ones for the lifetime of $\tau = 0.46\,\text{ps}$ (best fitted value) and $\tau = 6.5\,\text{ps}$ (previous measurement [Koh+13]). The fit is performed in the range of $\Delta\nu = 0.1 - 3.3\,\text{cm/ns}$. The experimental distribution is wider, which might be due to the missing contributions from the silicon detectors in the simulation. The simulated spectrum for the literature lifetime value has a very prominent peak structure, not observed in the experimental one.

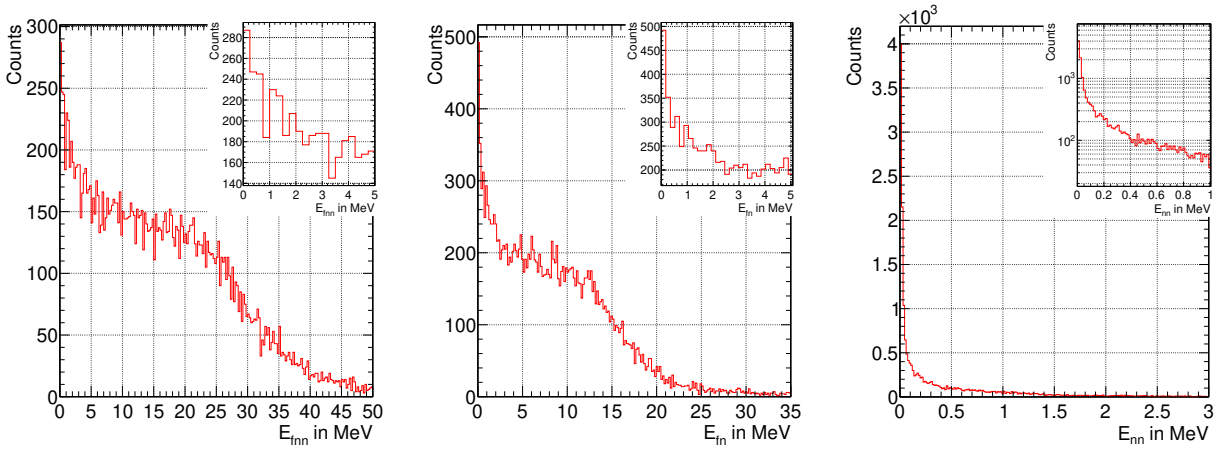

Figure 7.12.: Measured relative energy spectra from ^{26}O decay for (a) the three-body system, ^{24}O and the two neutrons E_{fnn}, (b) the fragment and only one neutron E_{fn} and (c) the subsystem of only the two neutrons E_{nn}. A peak at low relative energies can be observed in all three spectra, indicating for the ground state of ^{26}O. The inset shows the low energy regions for the individual spectra, where the ground state is expected. The excited state at $1.28\,\mathrm{MeV}$ cannot be clearly identified.

observed in the E_{fnn} spectrum. This peak could be produced by the excited 2^+ state of ^{26}O, which is located at 1.28 MeV. However, the resolution is not sufficient to identify this state. In the E_{fnn} and E_{fn} spectra, a broad structure is visible up to $\sim 20\,\mathrm{MeV}$ and $\sim 15\,\mathrm{MeV}$. To investigate this structure, the measured spectra are compared to the simulation.

A comparison of the relative-energy spectra is shown in Fig. 7.13 for a lifetime of 6.5 ps in the simulated spectra. The two-neutron relative energy has a peak at low relative-energy values (blue), in good agreement with the experimental spectrum (red). The three-body relative energy of the fragment and the two neutrons also presents the low-energy peak of the ^{26}O ground state. An additional peak appears at approximately 2 MeV. The excited state of ^{26}O is located at 1.28 MeV. However, a second peak is clearly visible in the simulated spectrum in which the excited state was not included. Therefore, this peak is produced due to the target configuration. In Fig. 7.13c, the relative energy is shown versus the decay position z_τ. For the last target, the simulated three-body relative energy is the sharpest, whereas it gets broadened for the previous targets due to the additional energy loss of the fragment compared to the neutrons. In conclusion, the second peak in the spectrum E_{fnn} involving the fragment and the two neutrons, originated from the target segments. Additional structures are slightly visible, created by the remaining target sheets, explaining also the broad peak up to $\sim 20\,\mathrm{MeV}$.

Since the ground state of ^{25}O is located at 749 keV [Kon+16], the excited state of ^{26}O, in contrast to its ground state, could sequentially decay through the ^{25}O ground state. In this work, the lifetime of the ground state is to be determined and therefore the sequential decay from the excited state should be excluded. However, the excited state cannot be clearly identified in the relative-energy spectra involving the fragment due to the energy loss of the fragment. The two-neutron relative-energy spectrum is free from the large energy-loss difference in the target. Thus, it can be used to exclude

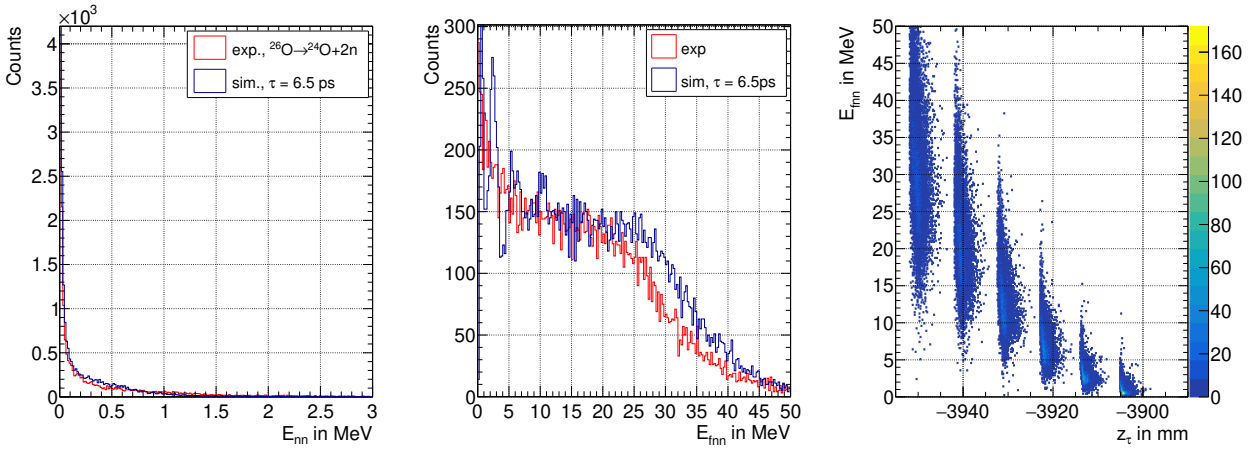

Figure 7.13.: Measured (red) and simulated (blue) relative energy E_{rel} spectra for (a) the two neutron system and (b) the three-body system (^{24}O+2n). The peak structure at $\sim 2\,\text{MeV}$ is created by the target sheets. (c) Simulated three-body relative energy versus the decay position z_τ of ^{26}O. The distributions for the first targets are broadened due to the additional energy loss of the fragment after the decay.

the excited state of ^{26}O, though it is not visible in the spectrum. The χ^2 analysis is performed again with a cut on the two neutron relative energy $E_{\text{nn}} < 1\,\text{MeV}$. With the lower uncertainty of the location of the excited state given in [Kon+16], this cut is below the 3σ uncertainty and therefore a possible contamination of the excited state is reduced to a minimum. The resulting lifetime value does not change. The statistical uncertainty is slightly larger, due to the reduced statistics. The obtained lifetime results including the cut on E_{nn} are summarized in Tab. C.2.

7.2.4. Reference Decay Channel ^{25}O

To determine the systematic uncertainty of the method, the χ^2 analysis is repeated for the reference channel, where ^{25}O was produced from the proton knockout from ^{26}F and decayed into ^{24}O and one neutron. For this, the same analysis is performed with the experimental velocity-difference spectrum of ^{25}O, using the lifetime simulation with ^{26}O and the χ^2 analysis with two fit parameters, as explained in Sec. 7.2.1. For each lifetime function, the best fit parameters are determined from the minimal χ^2 of the fit. To find the lifetime value, again a parabolic fit is performed. Here, the parameter that corresponds to the x position of the minimum of the parabola is limited to values $x \in [0, 15]$, such that negative values for the resulting lifetime are excluded. The extracted lifetime value is $\tau = 0 \pm 0.09\,\text{ps}$ for the full range of incoming energies.

The resulting χ^2 distribution as a function of lifetime is shown in Fig. 7.14 together with the best fit to the experimental spectrum. The best fit function corresponds to the first bin of Fig. 6.10, *i.e.*, the smallest simulated lifetime range of $\tau = 0 - 0.04\,\text{ps}$. One can see that the simulated function has a peak structure that is not observed in the experimental distribution. Additionally, the slope of the rising edge is different. Overall, the agreement is not good, which is also reflected in the reduced χ^2 value of $\chi^2_\nu = 9.5$.

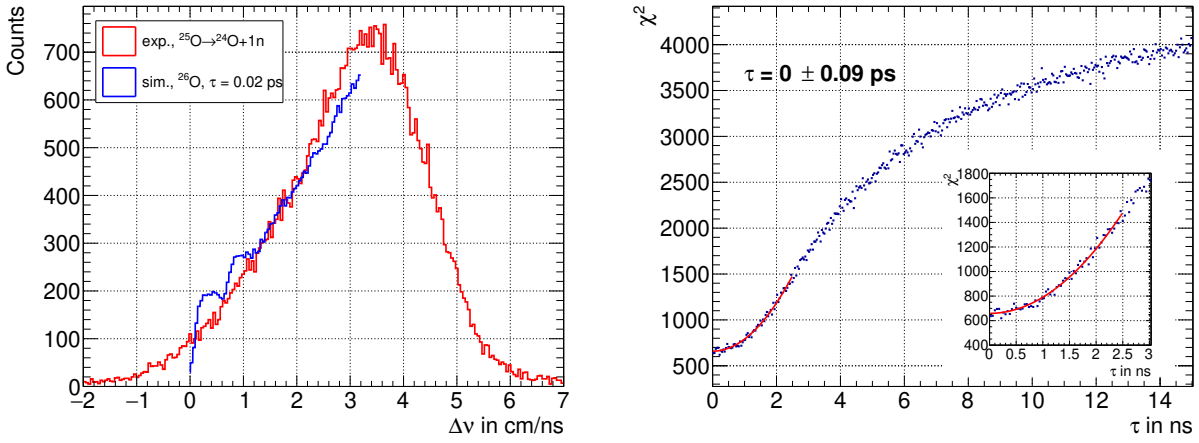

(a) (b)

Figure 7.14.: (a) Comparison of the velocity-difference spectrum for the reference measurement from ^{25}O (red) to the lifetime simulation. The best fit result (blue) is shown, which corresponds to the smallest simulated lifetime region. (b) Resulting χ^2 distribution with a minimum at $\tau = 0 \pm 0.09$ ps. The uncertainty is given by $\chi^2 + 1$.

As the energy dependence of the velocity difference was considered for the extraction of the lifetime value of ^{26}O in Sec. 7.2.2, it has to be taken into account also for the determination of the systematic uncertainty. Therefore, the χ^2 analysis is repeated with the measured spectrum of ^{25}O, where the incoming energy is divided again into 5 MeV slices. The $\Delta\nu$ spectrum of each energy range is fitted to the simulated functions for the same energy range. The resulting fits and χ^2 distributions are shown in Figs. C.3 and C.4 and the results are summarized in Tab. C.3. The fit of the first energy range is shown as an example in Fig. 7.15. The shape of the fit function and the $\Delta\nu$ spectrum agree better for the individual slices as compared to the full energy range. The mean of the extracted lifetime values is $\tau = 0.34 \pm 0.12$ ps, according to Eqs. C.1 and C.2. This result is very different from the value obtained with the fit to the full energy range, *i.e.*, the energy dependence of the velocity difference has a large influence on its shape. Thus, for a consistent determination of the systematic uncertainty, the energy dependence has to be taken into account.

Due to the bin width in the lifetime axis of 0.04 ps (cf. Fig. 6.10), a comparison with a lifetime of exactly zero is not possible. For this purpose, an additional simulation for the ^{25}O case with no lifetime was performed, as described in Sec. 6.2.6. The differences between the lifetime simulation and the one for ^{25}O are: (i) the different particles and therefore different energy losses in the material, (ii) the different input parameters, *i.e.*, the fragment momentum distribution after the proton knockout, the proton knockout and total reaction cross sections, and (iii) the different flight paths of the isotope of interest. As explained in Sec. 6.2.6, ^{25}O decays immediately after the proton removal, which leads to $z_r = z_\tau$. In the lifetime simulation ^{26}O can, depending on the lifetime, travel further through the target and lose energy. However, the step size is limited in the simulation, leading discrete values of the decay position z_τ. Thus, the step size could have an influence on the shape of the simulated $\Delta\nu$ spectrum and should be further investigated.

The comparison of the measured and simulated spectra of ^{25}O is shown in Fig. 7.16. Here,

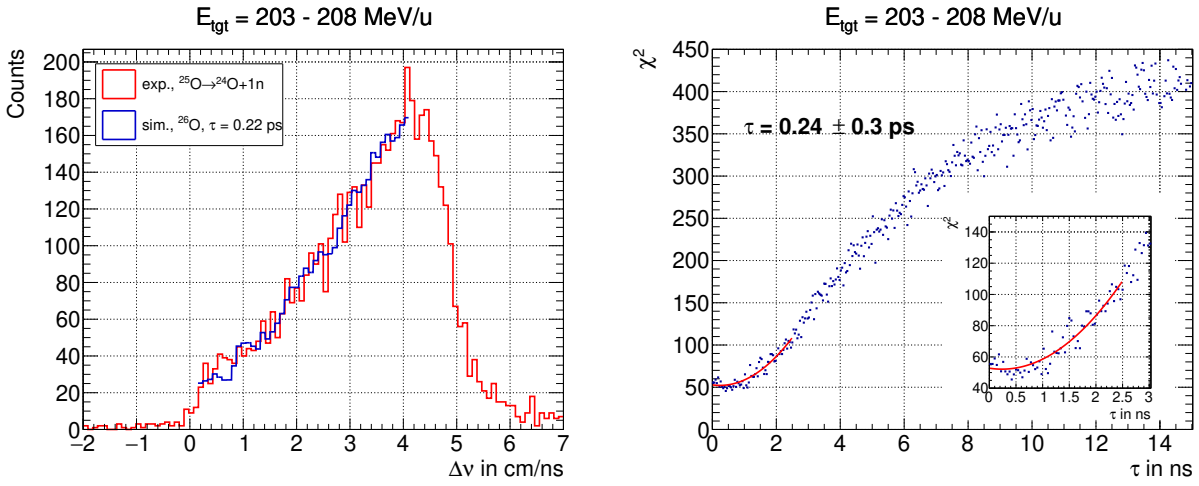

(a) (b)

Figure 7.15.: (a) Measured ^{25}O $\Delta\nu$ spectrum (red) for incoming energies between $E_{\text{tgt}} = 203 - 208\,\text{MeV/u}$ with the simulated function (blue), corresponding to the best fit. (b) χ^2 analysis with the minimum at $\tau = 0.24 \pm 0.30\,\text{ps}$ for this energy range.

the shape of both distributions agrees well, especially for the range which is most sensitive to the lifetime, where the peak structure would appear. However, the outer ranges at $\Delta\nu \lesssim 0\,\text{cm/ns}$ and $\Delta\nu \gtrsim 5\,\text{cm/ns}$ are underestimated in the simulation, as already pointed out and discussed in Sec. 7.2.1. In conclusion, the simulation is able to reproduce the experimental spectra well in the range of the velocity difference which is sensitive to the lifetime.

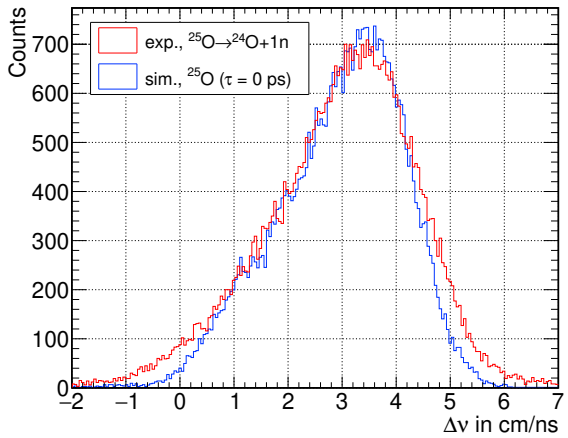

Figure 7.16.: Comparison of the experimental (red) and simulated (blue) velocity-difference spectrum of the reference channel ^{25}O using a lifetime value of $\tau = 0\,\text{ps}$ as an input.

7.2.5. Conclusion

The lifetime value of ^{26}O, extracted with the χ^2 analysis taking the energy dependence of the velocity-difference into account is $\tau(^{26}\text{O}) = 0.44 \pm 0.11(\text{stat})\,\text{ps}$. The statistical uncertainty of $\Delta\tau_{\text{stat}} = 0.11\,\text{ps}$ is given by the corresponding lifetime value at $\chi^2 + 1$, as described in Sec. 5.3.

The resulting lifetime value from the fit of the simulation to the measured spectrum of ^{25}O is used to estimate the systematic uncertainty of the method. The measured velocity-difference spectrum of ^{25}O features no lifetime in the picosecond range. Therefore, applying the χ^2 analysis analogously as for the ^{26}O spectrum sets a lower limit on the lifetime the method is sensitive for. A lifetime value of $\tau(^{25}\mathrm{O}) = 0.34 \pm 0.12(\mathrm{stat})$ ps was extracted, leading to a systematical uncertainty of $\Delta\tau_{\mathrm{syst}} = 0.46$ ps.

Following the presented measurement and analysis in this work, a new upper limit on the lifetime of the ^{26}O g.s. is determined as $\tau < 0.9$ ps at 1σ confidence level (c.l.) ($68.3\,\%$), $\tau < 1.9$ ps at 3σ c.l. ($99.7\,\%$) and $\tau < 2.8$ ps at 5σ c.l. ($> 99.9\,\%$). This result is in agreement with all previously measured lifetime values of $\tau = 6.5^{+4.6}_{-4.8}$ ps [Koh+13], $\tau = 7.2^{+3.5}_{-4.1}$ ps [Red19] and $\tau \leq 5.7$ ns (at $95\,\%$ c.l.) [Cae+13a].

The new measurement method applied in this work, is able to reduce the upper limit of the measured lifetime value by one order of magnitude, as compared to previous measurements [Koh+13; Red19]. Additionally, it does not rely on absolute calibrations as only the shape of the velocity-difference distribution is needed for the determination of the lifetime. A lifetime of $\tau = 0$ ps lies within the 1σ confidence level and therefore the observation of two-neutron radioactivity of ^{26}O cannot be confirmed.

7.3. Sensitivity to Theory Input

In the lifetime simulation, different theoretical calculations are used as input (cf. Sec. 6.2.5): the cross section for the proton removal from ^{27}F, the total reaction cross sections, and the recoil motion of the ^{26}O fragment after the proton removal. In this section, the sensitivity of the velocity-difference spectrum to the theoretical inputs is investigated together with a comparison to the expected simulated spectrum from the originally proposed method in [Kah+17b]. The differences between the simulations in this work compared to the original idea reside in the treatment of the recoil of the fragment after proton removal, the energy dependence of the cross sections, the material of the targets and the range of the incoming energy.

The resulting velocity-difference spectrum has a low sensitivity to the absolute value of the cross sections. It, however, plays an important role if the beam loss effect modeled with the cross sections is included. If the cross section values are different, this would lead to more or less particles being lost in the process, but would however not change the shape of the spectrum. In [Kah+17b], the cross sections were assumed to be constant as a function of energy. In this work this is not the case, cf. App. B. The total reaction cross section becomes larger towards smaller energies, which means that more particles are lost in the last targets. The differences however are in the order of a few percent and do not make a substantial contribution to the shape of the $\Delta\nu$ spectrum. Yet, the beam loss due to the total reaction cross section has to be included to model realistically the beam losses in the thick targets.

The main difference between the simulations is the treatment of the recoil after proton removal. In the work of Kahlbow *et al.* (Fig. 7.17a), this was not included, whereas in this work the recoil was explicitly treated with the calculated ^{26}O fragment momentum distributions after proton knockout (Sec. 6.2.5). To investigate the influence of the calculated distributions on the final $\Delta\nu$ spectrum, the simulation is performed without taking them into account. The comparison is shown in Fig. 7.17,

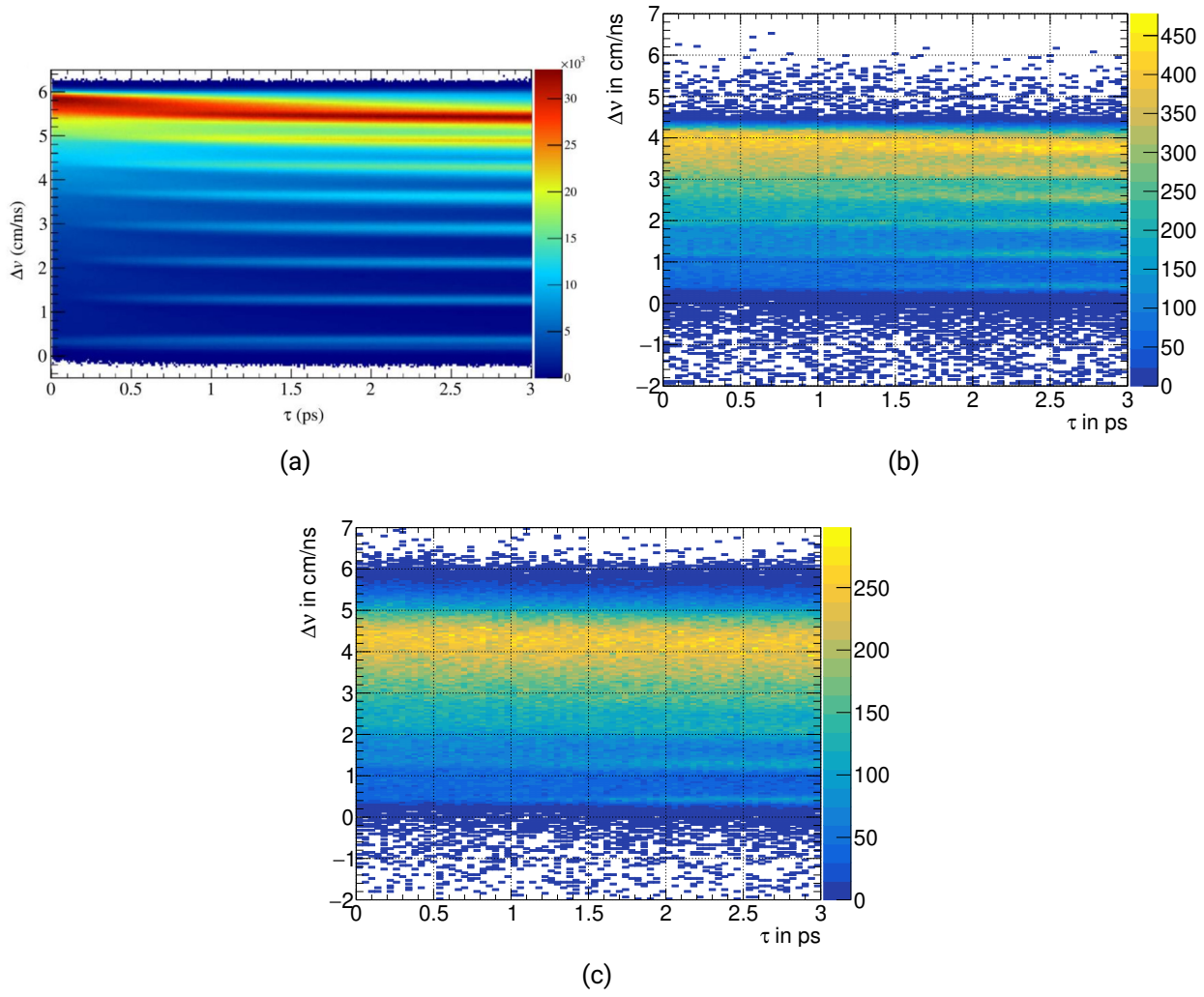

Figure 7.17.: Comparison of the velocity-difference distribution as a function of the lifetime for (a) the original expectation from [Kah+17b] (simulation with 8 targets, no recoil motion) and this work (b) without and (c) with taking the recoil motion from the proton removal into account. The range of energies at the entrance to the target is limited to energies of 203-208 MeV/u. (a) is taken from [Kah+17b].

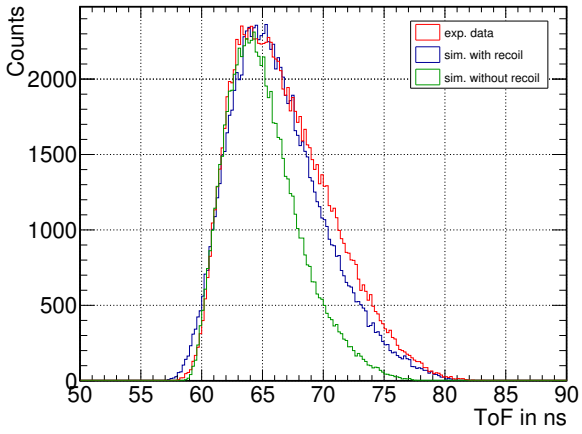

Figure 7.18.: Experimental (red) HODF time-of-flight comparing to the simulation with (blue) and without the recoil included (green). The simulated distribution without the recoil is to narrow to reproduce the experimental one.

with and without including the fragment recoil. For this comparison, the simulation in this work is considered for only an energy interval of incoming energies between 203 - 208 MeV/u. The incoming energy in [Kah+17b] was 200 MeV/u, not within the present experimental energy range. Therefore the energy interval closest to this value is chosen for the comparison. Additionally, the lifetime range is restricted to 3 ps in Fig. 7.17. The full range of simulated lifetimes was discussed in the previous section.

From the comparison of Fig. 7.17b and Fig. 7.17c, it becomes clear that including the recoil broadens the resulting velocity-difference spectrum. The peak structure in Fig. 7.17b is more prominent and all six outside peaks from the targets are visible as in the initial study (Fig. 7.17a). However, this treatment of the fragment momentum is too simplistic as fundamental kinematical distributions cannot be reproduced, as shown in Fig. 7.18 for the HODF ToF distribution. The simulated distribution without including the recoil (green) is too narrow compared to the experimental one (red). The resolutions included in the simulation are the same as explained in Ch. 6 and were extracted from the experimental distributions in Ch. 4. The ToF distribution of the lifetime simulation is shown in blue, where the recoil from the proton removal is included and the width agrees well with the experiment.

In conclusion, including the ^{26}O fragment momentum distributions from the proton knockout into the simulation has a substantial influence on the resulting $\Delta\nu$ spectrum. The broadening is necessary to reproduce the experimental distributions more realistically, since including only the experimental resolutions into the simulation is not sufficient.

8. Summary and Outlook

In this work, the lifetime of the ^{26}O ground state was successfully measured applying a new measurement method. The uncertainties compared to previous measurements could be reduced and a new upper limit was extracted.

In the experiment, performed at the SAMURAI setup at RIKEN, ^{26}O was produced in a proton knockout reaction from ^{27}F at $220\,\mathrm{MeV/u}$, then decayed into ^{24}O via two-neutron emission. A target stack, consisting of four W and two Pt targets, was used. With this setting, the ratio of the number of decays which take place inside and outside of the target changes according to the lifetime. The velocity difference between the neutrons and the ^{24}O fragment delivers a characteristic spectrum, which is sensitive to the lifetime. A dedicated GEANT4 simulation was developed, where the full reaction process, which includes both the proton knockout and the subsequent decay, was modeled according to the experimental setup and the lifetime was given as an input parameter. From the comparison between the shapes of the measured and simulated velocity-difference spectra, a new upper limit of the ^{26}O g.s. was determined. The systematic uncertainty of the method was deduced from a reference measurement with the ^{25}O channel, where not lifetime in the picosecond regime is expected. The resulting upper limit on the lifetime is $\tau < 0.9\,\mathrm{ps}$ at 1σ c.l. ($68.3\,\%$) and $\tau < 2.8\,\mathrm{ps}$ at 5σ c.l. ($> 99.9\,\%$).

This result is in agreement with all previously measured lifetime values of $\tau = 6.5^{+4.6}_{-4.8}\,\mathrm{ps}$ [Koh+13], $\tau = 7.2^{+3.5}_{-4.1}\,\mathrm{ps}$ [Red19] and $\tau \leq 5.7\,\mathrm{ns}$ (at $95\,\%$ c.l.) [Cae+13a]. The upper limit of the lifetime could be reduced by one order of magnitude. A lifetime of $\tau = 0\,\mathrm{ps}$ lies within the 1σ uncertainties and therefore the observation of a two-neutron radioactivity of ^{26}O cannot be confirmed. Additionally, the result is in agreement with the theory estimation on the lifetime for the measured decay energy of the ^{26}O g.s. [Kon+16; Gri+13], from which a lifetime value of $10^{-5} - 10^{-3}\,\mathrm{ps}$ is expected.

To finalize the results, the simulation will include proton knockout also in the silicon detectors, which were located in front and behind the target stack. The silicon detectors also act as targets and create additional structures at the edges of the velocity-difference spectrum. This might provide a better agreement of the simulated and measured spectra at the edges of the $\Delta\nu$ spectrum. Moreover, the influence of the step size in the lifetime simulation on the resulting velocity-difference can be further studied and understanding the origin of the time-of-flight offset of the HODF requires further investigation.

For future measurements of the ^{26}O lifetime using the presented method, a target stack optimized for a lifetime in the low picosecond region, around the value obtained in this work, would increase the sensitivity. Additionally, the reconstruction of the decay position would allow for a more precise velocity-difference spectrum and could reduce the systematic uncertainties. This could be achieved by integrating the knockout targets into an active target. The individual target sheets would act as cathodes with thin anodes in between, which are read out to identify fragments between the target

sheets and thus determine in which target sheet the proton knockout occurred. Such an active target was developed by the Studies On FIssion with ALADIN (SOFIA) collaboration [Mar+15] and is used for fission experiments.

A. SAMURAI Setup and Calibration

A.1. BigRIPS settings

The BigRIPS settings for the three different beams are shown in the tables below. The used runs for the calibration were run 450 for ^{27}F, run 477 for ^{26}F and run 375 for ^{24}O.

Table A.1.: Nominal magnetic rigidities $B\rho_0$ for all secondary beams

	$B\rho_0$ in Tm		
magnet	^{27}F beam	^{26}F beam	^{24}O beam
D1	7.9848	7.7398	7.8808
D2	7.4500	7.2172	7.2290
D3	7.2708	7.0393	7.0553
D4	7.2708	7.0393	7.0554
D5	6.7814	6.5575	6.6026
D6	6.7814	6.5575	6.6026

Table A.2.: Slit settings for all secondary beams

	slit opening in mm		
slit	^{27}F beam	^{26}F beam	^{24}O beam
F1	-120, +120	-120, +120	-5.4, +5.4
F2	-120, +120	-4, +4	-5, +5
F5	-55, +55	-95, +94.8	-110, +110
F7	-25, +25	-25, +25	-25, +25

A.2. Time-of-Flight Calibration

The procedure of the absolute time-of-flight calibration is described in Sec. 4.4. In the first step the expected ToF has to be calculated with the nominal path length between the plastic detectors and the nominal $B\rho$. These distances are given in Tab. A.3 together with the calculated values for the offset between the uncalibrated and calibrated ToF for the different beams. The used runs for this calculation are run 450 for ^{27}F, run 477 for ^{26}F and run 375 for ^{24}O.

Table A.3.: Nominal flight path and offset in time-of-flight between the plastic detectors between the different focal planes. The distances between the focal planes are given in [Big22] together with the positions of the plastic detectors relative to the focal planes.

	F3-F5	F5-F7	F3-F7	F7-F13	F3-F13
path length in m	23.888	23.088	46.976	36.013	82.989
offset in ns for ^{27}F	171.796	116.009	287.805	544.803	832.567
offset in ns for ^{26}F	171.614	116.083	287.717	544.737	832.414
offset in ns for ^{24}O	171.450	117.378	288.528	545.312	833.780

B. Theory Calculations for Simulation

The theory calculations used in this work were performed by C. Bertulani [Ber21] within the Glauber model. The Glauber model is commonly used to describe nuclear scattering at high energies based on eikonal wave functions. In the eikonal approximation it is assumed that the projectile passes the field of the target on a straight-line trajectory up to the interaction point, *i.e.*, the energy transfer in the collision is much smaller than the projectile energy. When a projectile nucleus impinges on a target nucleus with a certain displacement of the center-of-mass, called the impact parameter, each projectile nucleon is considered individually. From this, the probability that a projectile and a target nucleon are in the overlapping area of the two nuclei can be evaluated. To infer whether an interaction has occurred, the nucleon-nucleon interaction is included. The nucleon-nucleon interaction probability for a certain impact parameter is given by the number of possible collisions out of the number of participating nucleons and their collision probability together with the probability that the remaining nucleons do not interact and remain as spectators. With that, the total reaction cross section can be calculated. A detailed description and the deduction of the formalism is presented in [Ber+21] and [Sch17]. More details on the cross section calculation can be found in [Ber+04], [Ber+19] and [Tei+22].

B.1. Cross Sections

B.1.1. Total Reaction Cross Section

The relevant total reaction cross sections are presented in Tab. B.1 for the ^{27}F setting and Tab. B.2 for the ^{26}F setting, where the values for ^{24}O are used in both simulations. The cross sections were calculated for a discrete set of particle energies. However, a continuous distribution is necessary in the simulation as all energies within the experimental range need to be considered. For this, the values for each isotope and each target material are fitted with a power law as shown in Fig. B.1 for ^{27}F and ^{26}F. The function is then evaluated at the desired energy E of the particle to extract the respective cross section.

It should be noted that for ^{26}F, the cross section at 65 MeV/u is smaller than the ones at higher energies. This is due to the Pauli blocking, included in the calculation, which reduces the cross section towards low energies [Ber+10].

Table B.1.: Calculated total reaction cross sections σ_{tot} for isotopes relevant to the ^{26}O lifetime simulation for the two target materials at different energies.

E in MeV/u	σ_{tot} in mb					
	^{27}F, W	^{27}F, Pt	^{26}O, W	^{26}O, Pt	^{24}O, W	^{24}O, Pt
65	4067	4115	3915	3921	3694	3744
80	4046	4094	3903	3916	3693	3742
150	3923	3972	3797	3822	3613	3662
220	3901	3949	3779	3807	3600	3648
250	3910	3958	3787	3817	3609	3657

Table B.2.: Calculated total reaction cross sections σ_{tot} for isotopes relevant to the lifetime simulation of the reference channel ^{25}O for the two different target materials at different energies.

E in MeV/u	σ_{tot} in mb			
	^{26}F, W	^{26}F, Pt	^{25}O, W	^{25}O, Pt
65	3720	3772	3763	3817
80	3722	3781	3759	3820
150	3651	3721	3674	3745
220	3640	3713	3660	3734
250	3649	3722	3668	3744

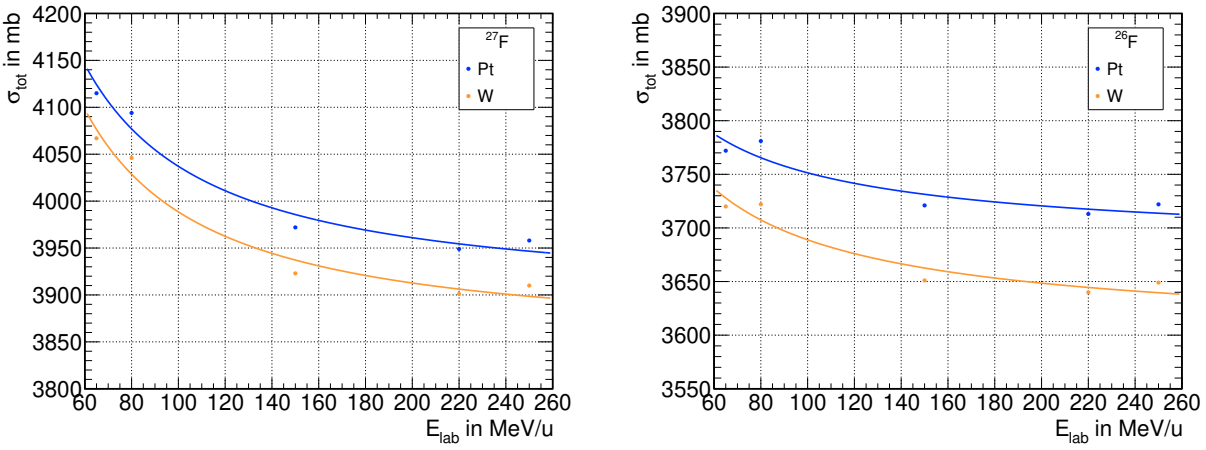

(a) (b)

Figure B.1.: Calculated total reaction cross sections σ_{tot} for (a) ^{27}F and (b) ^{26}F with platinum (blue) and tungsten (orange) for different energies. To get a continuous energy dependence of the cross section, the distributions are fitted with a power law.

B.1.2. Proton Knockout Cross Section

The calculated cross section of the proton knockout consists of a stripping and a diffraction dissociation contribution. As this theory has been developed for light targets [Ber+04], the contribution from the diffraction dissociation is not accurate for the targets in the experiment and is thus not used in this work. Therefore, the values presented in Tab. B.3 contain only the stripping part of the cross section. Again, a polynomial function is fitted for every isotope and target-material combination, which is used to interpolate the cross section values at the desired energies.

Table B.3.: Calculated proton removal cross sections σ_r for both fluorine isotopes and the two target materials.

E in MeV/u	σ_r in mb			
	^{27}F, W	^{27}F, Pt	^{26}F, W	^{26}F, Pt
65	7.02	6.74	8.10	7.80
80	8.63	8.34	9.84	9.53
120	14.73	14.51	16.51	16.29
170	18.19	18.11	19.91	19.90
200	-	-	20.98	21.01
220	19.55	19.57	21.24	21.25
235	19.62	19.59	21.25	21.28

B.2. Fragment Momentum Distributions

The resulting momentum distributions of the ^{26}O fragment after the proton knockout from ^{27}F have been presented in Sec. 6.2.5. The momentum distributions of the ^{25}O reference channel, in which the proton is knocked out from ^{26}F, are shown in Figs. B.3 and B.4. The width of the longitudinal momentum distribution does not change for different beam energies, in contrast to the transversal contribution. Here, the distributions get broader with lower energies. In [Ber+92] and [Ber+04], it was found that the width of the transverse momentum distribution is dominated by the size of the target nucleus, whereas the longitudinal momentum distribution is insensitive to it. As the targets in this work were made of heavy nuclei, this has a large influence on the transverse momentum distribution. Furthermore, the transversal component can be additionally broadened by the Coulomb repulsion and diffractive effects [Ber+04].

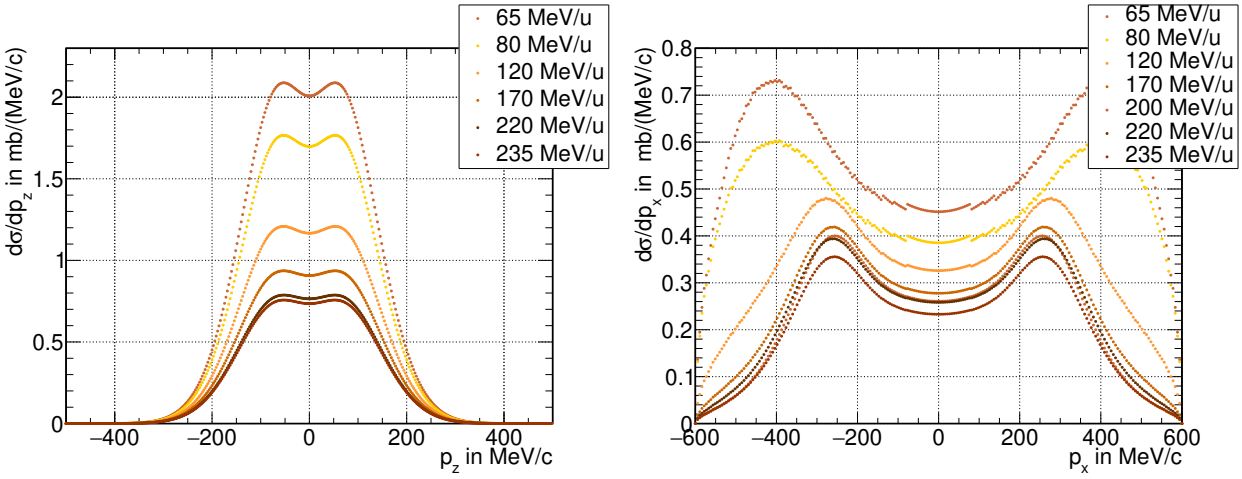

(a) (b)

Figure B.2.: Calculated (a) longitudinal and (b) transversal momentum distributions of ^{26}O after the proton knockout from ^{27}F at the W target for different beam energies.

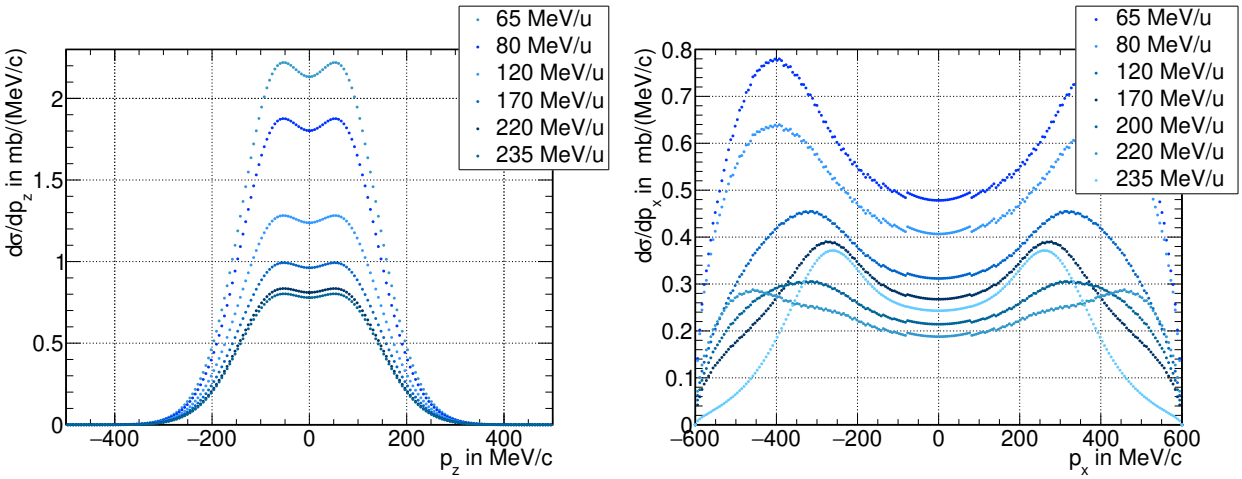

(a) (b)

Figure B.3.: Calculated (a) longitudinal and (b) transversal momentum distributions of ^{25}O after the proton knockout from ^{26}F at the Pt target for different beam energies.

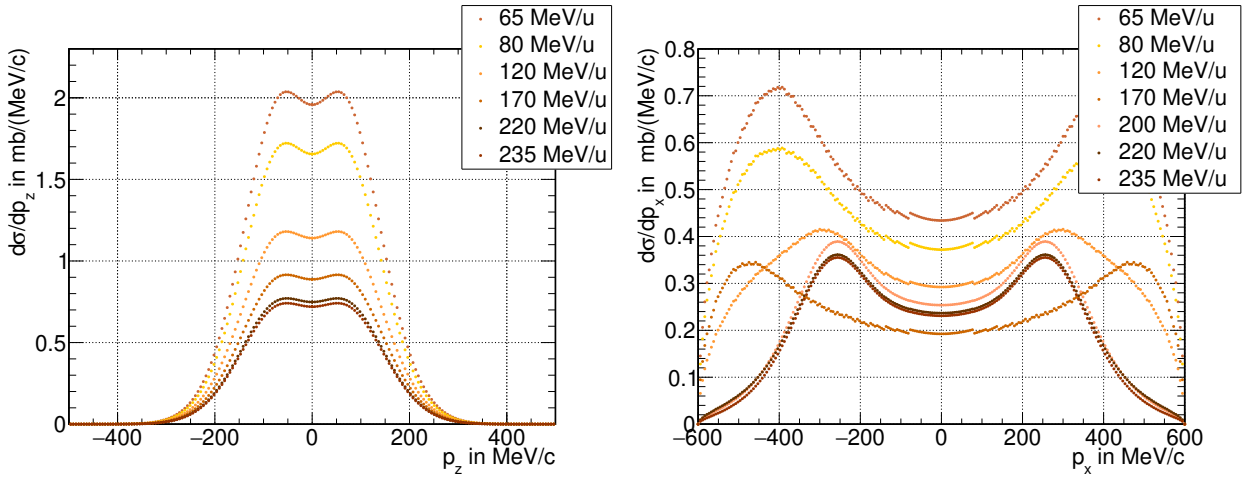

Figure B.4.: Calculated (a) longitudinal and (b) transversal momentum distributions of ^{25}O after the proton knockout from ^{26}F at the W target for different beam energies.

C. Incoming Energy Dependence of the Lifetime Analysis

In this appendix, the results of the lifetime analysis from the ^{26}O decay for each incoming energy range are presented. The range of incoming energy is divided as described in Sec. 7.2.1. The χ^2 analysis is shown in the right column in Figs. C.1 and C.2, with the minimum τ determined from a parabolic fit with the uncertainty given by χ^2+1. The left column shows the experimental distribution of the respective energy range with the simulated function that corresponds to the bin in Fig. 6.10 closest to the lifetime minimum. The lifetime values τ indicated in the plots, correspond to the center of the bin with width 0.04 ps. The results are summarized in Tab. C.1. The average lifetime value over all six energy slices is $\overline{\tau} = 0.44 \pm 0.11$ ps.

The same χ^2 analysis is performed with an additional cut on the two-neutron relative energy $E_{\mathrm{nn}} < 1$ MeV to exclude the sequential decay from the excited state of ^{26}O, as described in Sec. 7.2.3. The results are summarized in Tab. C.2. The extracted lifetime values is $\overline{\tau} = 0.42 \pm 0.12$ ps and thus agrees with the lifetime value determined above.

To estimate the uncertainty of the method, the same analysis is performed with the reference channel ^{25}O, as explained in Sec. 7.2.4. As the lifetime value of ^{26}O was extracted taking the energy dependence of $\Delta\nu$ into account, it also has to be taken into account for the systematic uncertainty. The results are presented in Tab. C.3. The averaged value over all six energy slices is $\overline{\tau}(^{25}\mathrm{O}) = 0.34 \pm 0.12$ ps.

The average lifetime value $\overline{\tau}$ is calculated using the arithmetic mean

$$\overline{\tau} = \frac{1}{N} \sum \tau_i, \tag{C.1}$$

with the lifetime values τ_i of the N individual energy slices [Bev+03]. The uncertainty of the average lifetime value is determined from the error propagation of Eq. C.1

$$\Delta\overline{\tau} = \frac{1}{N} \sqrt{\sum \Delta\tau_i^2}, \tag{C.2}$$

with the uncertainty of the individual lifetimes $\Delta\tau_i$, measured for each slice. $\Delta\tau_i$ is determined from the lifetime values at $\chi^2_{\mathrm{min}} + 1$.

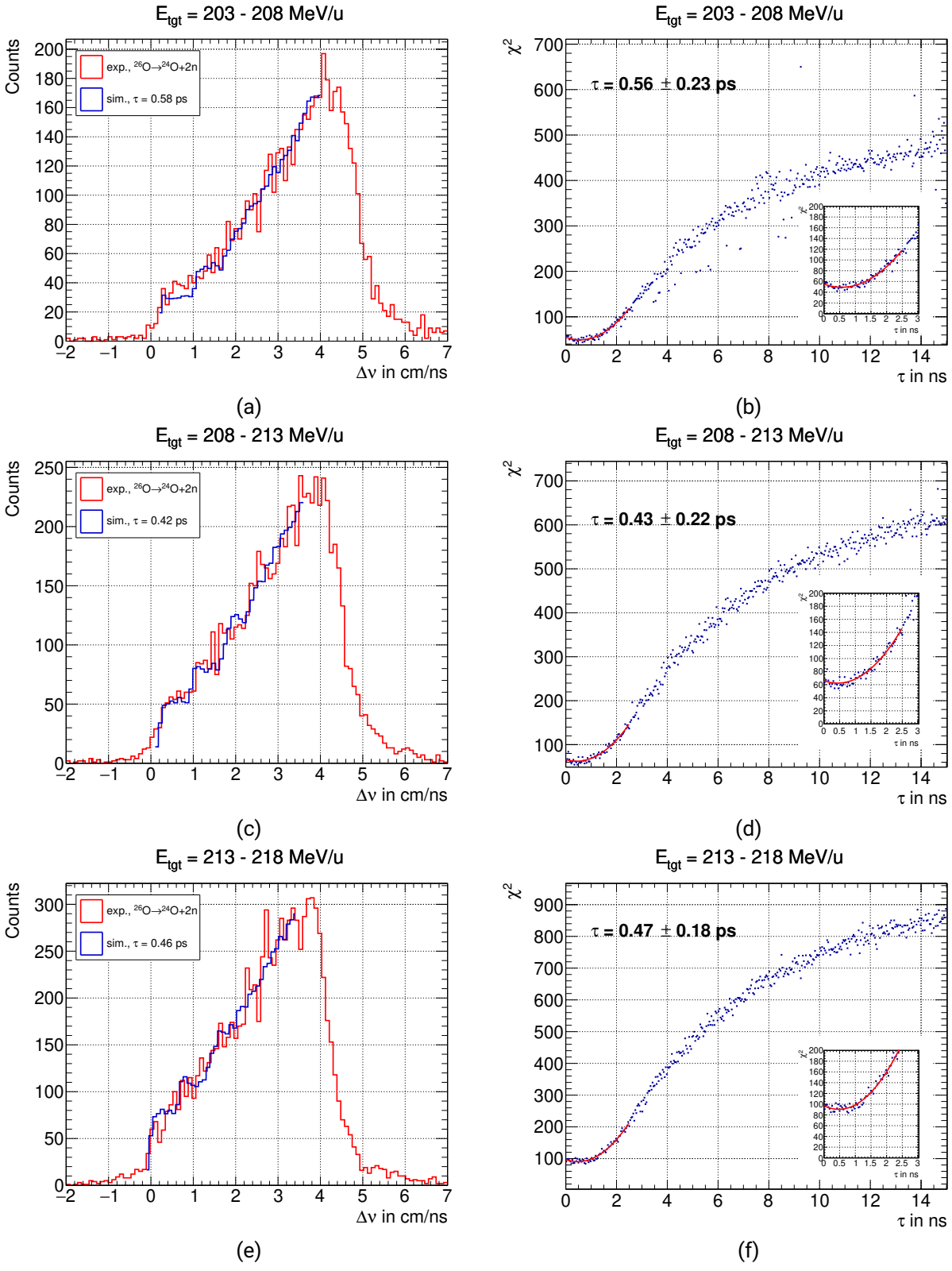

Figure C.1.: Lifetime analysis results for each 5 MeV interval of the incoming energy for $203\,\mathrm{MeV/u} < E_{\mathrm{tgt}} < 218\,\mathrm{MeV/u}$. The left column shows the comparison of the experimental distribution to the simulated function with the best χ^2. The right column shows the χ^2 distribution with a parabolic fit to the minimum. The uncertainty in the plots is given by $\chi^2 + 1$.

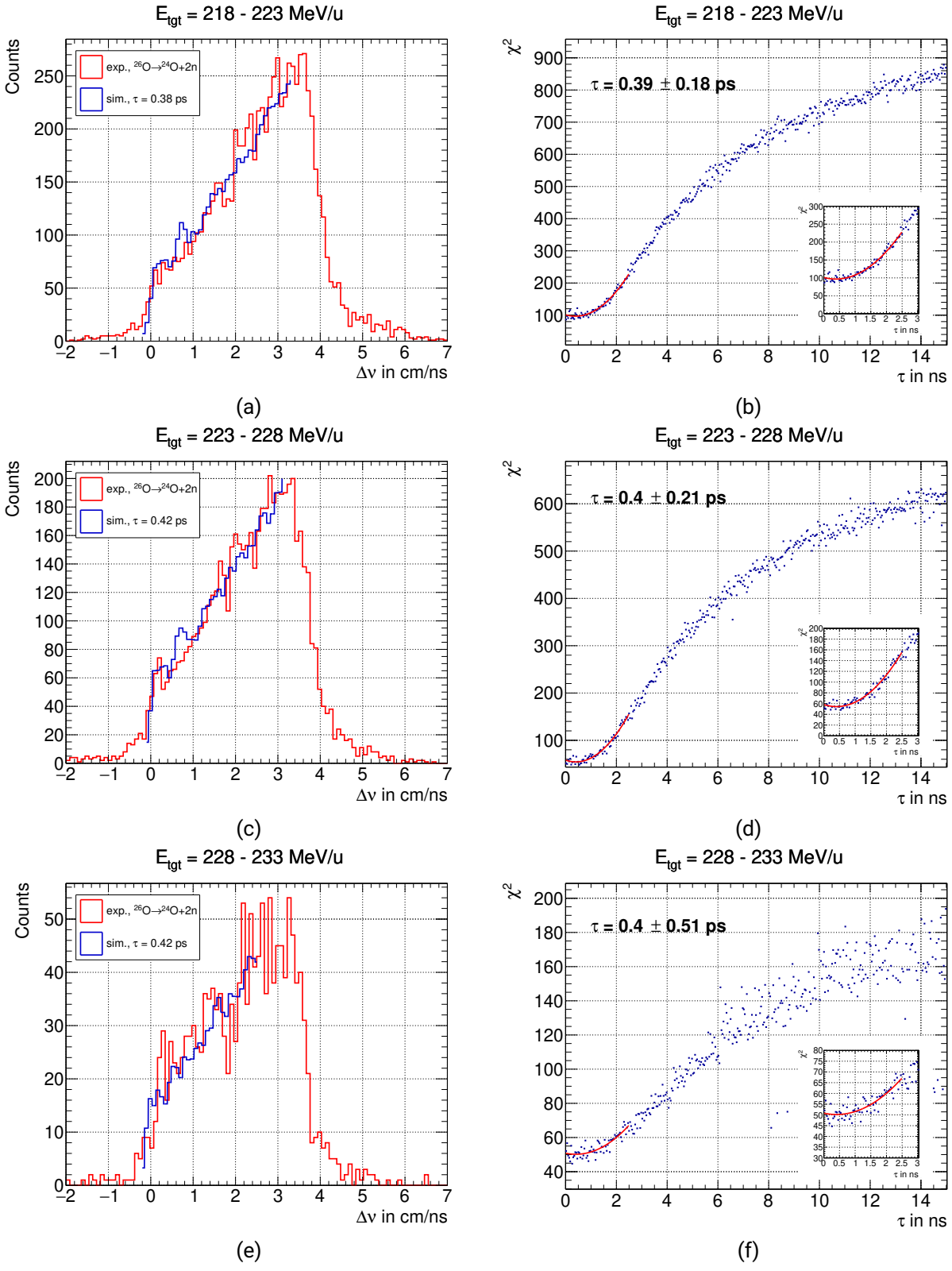

Figure C.2.: Lifetime analysis results for each 5 MeV interval of the incoming energy for $218\,\mathrm{MeV/u} < E_{\mathrm{tgt}} < 233\,\mathrm{MeV/u}$. The left column shows the comparison of the experimental distribution to the simulated function with the best χ^2. The right column shows the χ^2 distribution with a parabolic fit to the minimum. The uncertainty in the plots is given by $\chi^2 + 1$.

Table C.1.: Extracted lifetime values of ^{26}O for the different incoming energy ranges.

slice N	energy range in MeV/u	τ in ps	$\Delta\tau$ in ps from $\chi^2_{\text{min}}+1$	χ^2_{min}	χ^2_ν
1	203 - 208	0.56	0.23	49	1.2
2	208 - 213	0.43	0.23	62	1.7
3	213 - 218	0.47	0.18	90	2.4
4	218 - 223	0.39	0.18	97	2.6
5	223 - 228	0.40	0.21	54	1.6
6	228 - 233	0.40	0.51	50	1.8
full	203 - 233	0.25	0.11	120	1.7

Table C.2.: Extracted lifetime values of ^{26}O for the different incoming energy ranges with an additional cut on the two-neutron relative energy of $E_{\text{nn}} < 1\,\text{MeV}$.

slice N	energy range in MeV/u	τ in ps	$\Delta\tau$ in ps from $\chi^2_{\text{min}}+1$	χ^2_{min}	χ^2_ν
1	203 - 208	0.56	0.23	49	1.2
2	208 - 213	0.43	0.24	67	1.8
3	213 - 218	0.50	0.19	93	2.5
4	218 - 223	0.37	0.19	90	2.4
5	223 - 228	0.29	0.22	55	1.6
6	228 - 233	0.41	0.57	50	1.8
full	203 - 233	0.22	0.11	117	1.7

Table C.3.: Extracted lifetime values of ^{25}O for the different incoming energy ranges.

slice N	energy range in MeV/u	τ in ps	$\Delta\tau$ in ps from $\chi^2_{\text{min}}+1$	χ^2_{min}	χ^2_ν
1	203 - 208	0.24	0.30	52	1.2
2	208 - 213	0	0.37	73	1.9
3	213 - 218	0.43	0.19	86	2.3
4	218 - 223	0.37	0.18	97	2.6
5	223 - 228	0.43	0.21	55	1.6
6	228 - 233	0.58	0.36	58	1.7
full	203 - 233	0	0.09	663	9.5

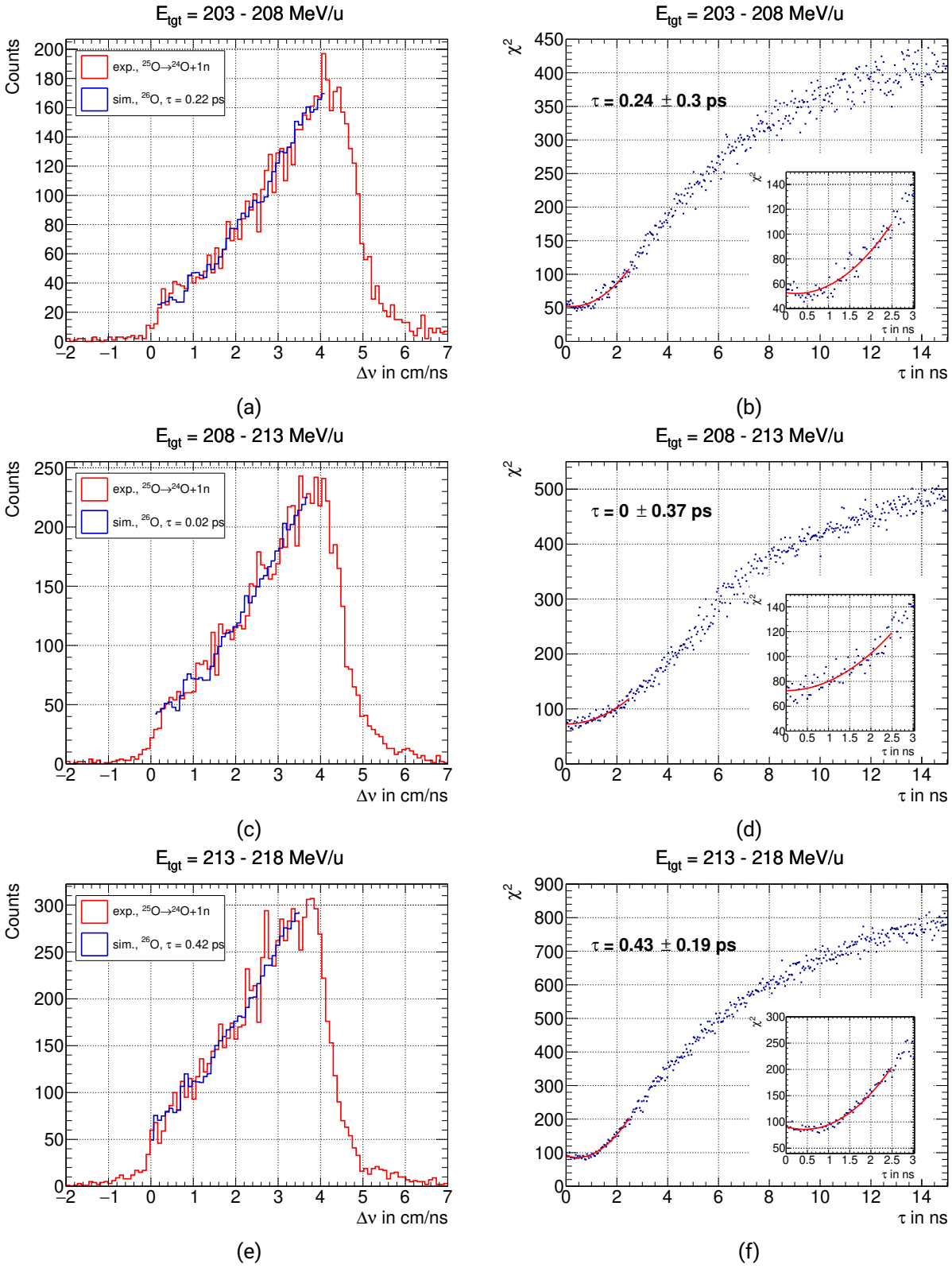

Figure C.3.: Lifetime analysis results for the reference channel ^{25}O for each 5 MeV interval of the incoming energy for $203\,\mathrm{MeV/u} < E_{\mathrm{tgt}} < 218\,\mathrm{MeV/u}$. The left column shows the comparison of the experimental distribution to the simulated function with the best χ^2. The right column shows the χ^2 distribution with a parabolic fit to the minimum. The uncertainty in the plots is given by $\chi^2 + 1$.

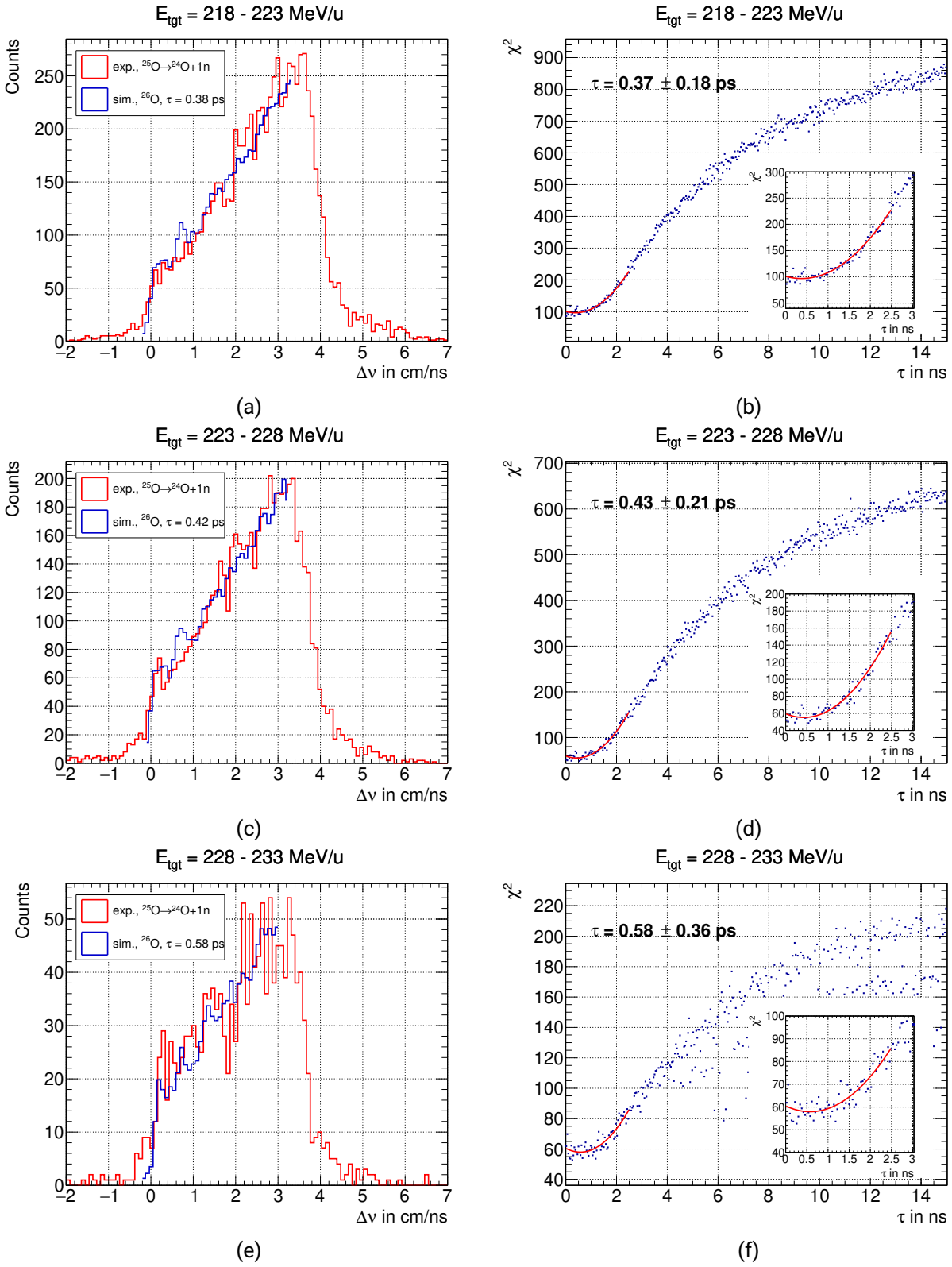

Figure C.4.: Lifetime analysis results for the reference channel ^{25}O for each 5 MeV interval of the incoming energy for $218\,\mathrm{MeV/u} < E_{\mathrm{tgt}} < 233\,\mathrm{MeV/u}$. The left column shows the comparison of the experimental distribution to the simulated function with the best χ^2. The right column shows the χ^2 distribution with a parabolic fit to the minimum. The uncertainty in the plots is given by $\chi^2 + 1$.

D. Detector Characterization for R^3B

In addition to the main topic of my PhD presented in this thesis, I was involved in a project where a prototype detector was tested and characterized. Currently, the new Facility for Antiproton and Ion Research (FAIR) is being build as an extension of GSI with an upgraded accelerator complex to study heavier ions at higher energies and intensities. A new R^3B setup is being commissioned with which the first FAIR Phase-0 experiments took place in 2019. This chapter focuses on the tests performed with the Position-Sensitive Pin detectors (PSPs) used in the R^3B setup [Col14]. The R^3B setup, located at the GSI facility, is built similar to the SAMURAI setup. With the R^3B setup, kinematically complete measurements of heavy neutron-rich nuclei can be performed at high energies up to 1 GeV/u, whereas higher intensities for lower energies up to a few 100 MeV/u can be achieved with the SAMURAI setup. Heavy ions are measured in various detection systems and are deflected by the R^3B magnet GSI Large-Acceptance Dipole (GLAD) after a reaction. To identify the projectile and fragment before and after the reaction, respectively, and track them through the magnet, various tracking detectors are used. The detectors used for specific experiments can change depending on the physics case. The standard R^3B detectors in front of the GLAD magnet that were used during the test beam times of 2018 and 2019 are described in the following. A scheme of the setups is shown in Fig. D.1: at the entrance to the setup the LOS detector is located, a plastic scintillator that is used for the start time. The ROLU detector is a veto detector. It consists of four plastic scintillators on the right, left, top, and bottom which can be moved with a drive. They open a window where the particles pass through without hitting the detector. The PSPs are placed in front of (Fig. D.1a) or around the target (Fig. D.1b) to identify and track the particles in front of the magnet. Additionally, CALorimeter for In-Flight Gamma-ray and PArticle Detection (CALIFA) is located around the target. It measures γ-rays and light charged particles, like protons [Col11b]. Behind the GLAD magnet the neutron detector NeuLAND [Col11a] and the time-of-flight wall are located. The later measures the energy loss and ToF of the fragments.

In this Chapter, a prototype detector design of a silicon tracking detector, called PSP, is investigated. Its working principle and design are explained in Sec. D.1. One specialty of the detector is the calibration procedure, explained in Sec. D.2, where so-called ”interstrip” events are used, making it possible to calibrate the detector with itself. No dedicated calibration runs are necessary. The electronic readout is introduced in Sec. D.3 together with findings from previous tests of the PSP in Sec. D.4. Sec. D.5 focuses on tests performed with the detector during the test beam time in 2018 and the experiments in 2019 where the new detector design was used for the first time in a physics experiment. The goal of these tests is to incorporate the previous findings into the electronic readout and confirm them with different projectiles. From the test results, recommendations for future R^3B experiments are made. Finally, an overview of ongoing activities and ideas for future improvements are discussed in Sec. D.6.

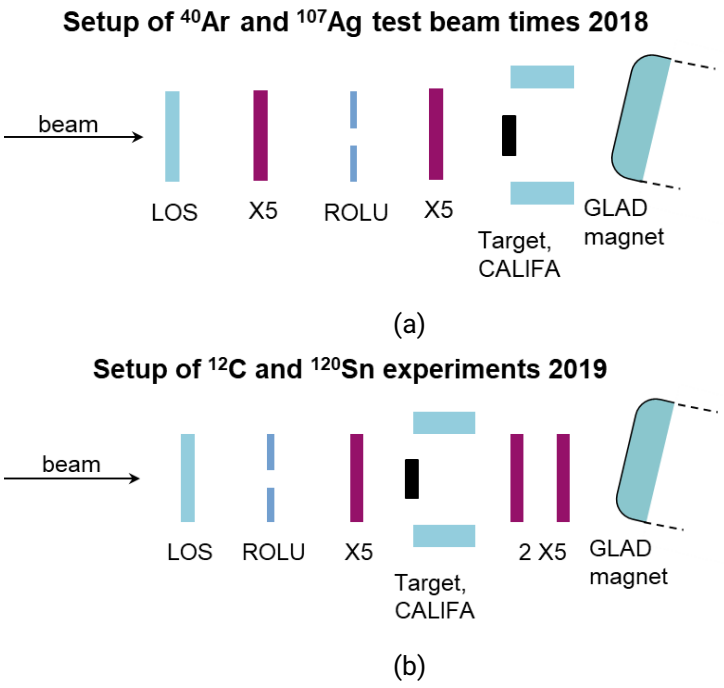

Figure D.1.: R^{3}B setup in front of the GLAD magnet during (a) the test beam time in 2018, where tracking detectors were tested with an Ar and an Ag beam, and (b) the first FAIR Phase-0 experiments in 2019 that were performed with C and Sn beams. The prototype PSPs used during both beam times are called X5.

D.1. Working Principle and Detector Design

The PSPs are semiconductor detectors made from silicon. The specialty of semiconductor materials is that the gap between the valence and the conduction energy band is small, making it easy to excite electrons with, for example, ionizing radiation. The excited electron leaves a hole in the valence band. The hole acts as a positive charge and can move freely in the valence band - similar to the electron in the conduction band - contributing to the conduction. The conduction with one of the charge carriers can be prioritized by modifying the material, known as ”doping”. In the doping process, atoms with an additional or one less valence electron are added to the material. If silicon is doped with a donor material, called n-type semiconductor, an extra level filled with electrons close to the conduction band is added. These electrons can be easily excited making them the dominant charge carriers. Doping with acceptor materials that have one valence electron less, called p-type semiconductor, adds an empty level close to the valence band. The dominant charge carriers in this case are the holes in the valence band, as the electrons that are excited to the extra energy level are not able to move due to the localization of the doping material.

To detect ionizing radiation with a silicon detector, a sensitive area is necessary. Placing an n- and p-type material together, will create a depletion zone. In this case, the electrons from the n-type material will diffuse to the p-type material and the holes vice versa. As the electrons and the holes recombine in the depletion zone and the semiconductor is initially being neutral, an electric field is formed stopping the diffusion eventually. Across this junction no mobile charge carriers are left. This

area can be used to detect ionizing radiation. An incident ionizing particle will create electron-hole pairs that get separated by the electric field and can be measured. The intrinsic electric field can be increased by applying a reverse bias voltage, enlarging the active area of the detector for radiation detection. A silicon detector can be used to measure the energy loss and thus the charge of the incident particle, as the number of created electron hole pairs is proportional to the deposited energy in the material.

Silicon detectors can also be used to measure the position of the incident particle. This is done by segmenting the surface into thin strips, with the position information given by the strip that was hit. Alternatively, a resistive layer can be added to the surface of the silicon. The charge carriers created in the depletion zone will split up due to the resistance of the surface. A schematic illustration of a position sensitive strip using resistive charge collection is shown in Fig. D.2a. These two approaches for the position measurement can also be combined as it is done for the silicon detectors currently used in the R^{3}B setup. Here, a resisitive layer is added to the strips and each strip is read out on both ends. The charge collected at the anode E_B (contact B in Fig. D.2a) depends on the distance to the hit position x with the following relation

$$E_B = E \cdot \frac{x}{L}, \tag{D.1}$$

where L is the length of the strip and E is the total energy deposited at the detector. More information about semiconductor detectors and their applications can be found in [Leo94; Kno10].

In the current R^{3}B setup, the silicon detectors have two sides with 32 strips on each side. They were produced by the manufacturer Micron Semiconductor Ltd and are of type X5 [Ltd15]. The active area is 9.57 x 9.57 cm^2, leading to a strip width of 2.99 mm. The technical drawing of the X5 detector is shown in Fig. D.2b. It is available in two different thicknesses of about 200 µm and 300 µm. Each strip is read out on both ends, leading to 128 channels per detector. The strips on the front and back side are arranged perpendicular to each other, making a simultaneous x and y position measurement with one detector possible. In addition, the surface of the silicon wafer is covered with the resistive layer to allow for an exact position determination within each strip. Thus, the position within the strip with length L can be reconstructed from the ratio of the signals on both ends E_1 and E_2, respectively, using

$$x = L \cdot \frac{E_1 - E_2}{E_1 + E_2}. \tag{D.2}$$

For the total energy, the two signals of each strip are added up

$$E = E_1 + E_2. \tag{D.3}$$

Combining the segmentation into strips and the resistive charge division method makes an accurate position determination with a resolution of $\approx$ 100 µm and a small number of electronic channels possible.

As already mentioned above, PSP stands for Position-Sensitive Pin detector. Although, the detector does not have pins anymore, the name is still used. In past R^{3}B experiments, the PSP detectors had

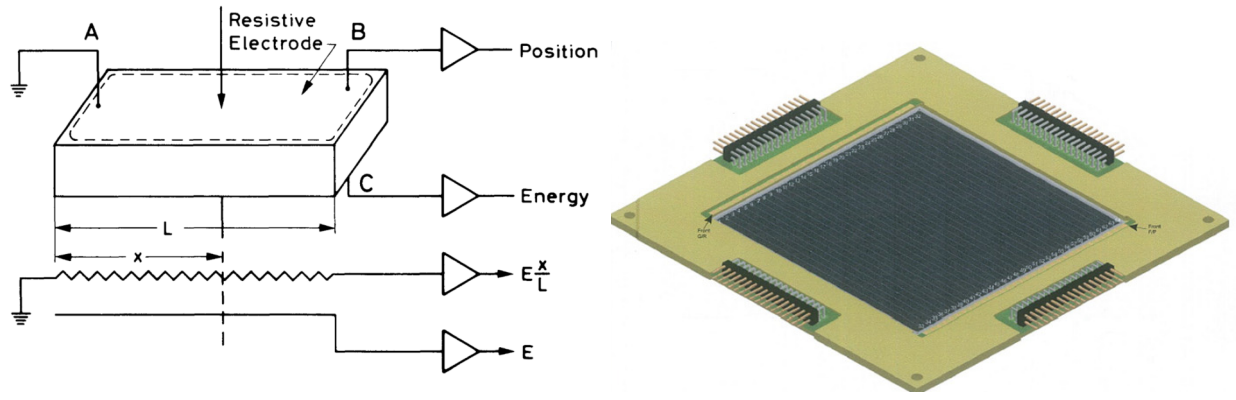

(a) (b)

Figure D.2.: (a) Sketch of an one-dimensional position sensitive strip using resistive charge division. The charge E_B collected at contact B is proportional to the energy of the incident particle and to the resistance of the electrode. The sketch is taken from [Leo94]. (b) Technical drawing of the X5 silicon detector. The front side with 32 strips that are read out on both sides is shown. The technical drawing is taken from [Ltd15].

four pins, one in each corner, on the resistive surface from which the position could be reconstructed. More details about this type of PSP detector can be found in [Syn14].

The predecessor of the X5 type, is the X1 type. This detector has an active area of 5 x 5 cm^2. It has 16 strips on only one side, where the measurement principle is the same as for the X5. Both ends of each strip are read out and with the resistive surface method the position within the strip can be reconstructed. The back side is used for an energy measurement only, since it has no resistive surface. More details about the X1 PSP can be found in [Sto15].

As the X5 detector is a prototype, it is still under investigation. For this and other prototype detectors of the R^3B setup, several test beam times were performed. An overview of the different PSP detectors that were used during the test beam times in 2018 and the experiments in 2019 which will be analyzed in this chapter, is summarized in Tab. D.1. In 2018 two PSP detectors were tested with an ^{40}Ar beam at 500 MeV/u and an ^{107}Ag beam at 400 MeV/u. In 2019 the first R^3B experiments after the upgrade of the accelerator and the R^3B magnet GLAD were performed as part of the FAIR Phase-0 campaign. As the FRagment Separator (FRS) of GSI was not available at the time, the beam times were performed with primary beam from the synchrotron (SIS18). The first experiment in 2019 was a commissioning beam time, called s444, for the key components of the R^3B setup, *i.e.*, CALIFA, GLAD, the tracking system, and NeuLAND. Here, a ^{12}C beam at various energies between 400 MeV/u and 900 MeV/u were used. s444 was followed by the s473 experiment, at which the accurate cross sections (total reaction, charge-changing, and neutron-removal) of ^{120}Sn was measured. The ^{120}Sn beam had various energies between 400 MeV/u and 900 MeV/u. During these beam times, the X5 detector was used in physics experiments for the first time.

As described in Tab. D.1, PSP 3126-9 was additionally used with ^{12}C beam at 90 MeV/u. The detector was tested in a beam time at the KVI-Center for Advanced Radiation Technology (KVI-CART) in Groningen together with other detectors with the goal of characterizing the heavy-ion tracking detectors for R^3B. The data of this beam time was analyzed by I. Syndikus [Syn18] and the results are explained in Sec. D.3.

Table D.1.: Overview of the detectors used in the test beam time in 2018 and the experiments in 2019. All available PSPs are p-type detectors. The operation voltage V_{op} is around 30 V larger than the depletion voltage V_{dep}.

Detector	3126-9	2433-20	2433-21
Thickness	209 µm	314 µm	313 µm
V_{dep}	43 V	75 V	75 V
V_{op}	75 V	105 V	105 V
Used in beam time with	^{12}C, 90 MeV/u ^{40}Ar, 500 MeV/u ^{107}Ag, 400 MeV/u ^{12}C, 400 - 900 MeV/u ^{120}Sn, 400 - 900 MeV/u	^{40}Ar, 500 MeV/u ^{107}Ag, 400 MeV/u ^{12}C, 400 - 900 MeV/u ^{120}Sn, 400 - 900 MeV/u	^{12}C, 400 - 900 MeV/u ^{120}Sn, 400 - 900 MeV/u

D.2. Calibration Procedure

Before the performance of the X5 detectors can be investigated, the data has to be calibrated. This is done within the `R3BRoot` framework [Ber11]. `R3BRoot` is based on `ROOT` and `FairROOT` [Ber+08; Al-+12] and has R^{3}B specific detector classes implemented. The raw data is stored in `lmd` files which can be converted into `root` files using the unpacking program unpack & check every single bit (`ucesb`) [Joh22]. The calibration is done in several steps in `R3BRoot` which will be described in the following.

`MAPPED`

The *mapped* level is the lowest data level in `R3BRoot`. At this level the basic information of the detector such as detector number, channel number, and energy loss measured by each channel is available. Mapping the channel number to the corresponding strip side is done during the `ucesb` unpacking. Energies in this level are given in ADC channels.

`PRECAL`

The *precal* level contains the strip number and the two energy variables corresponding to the energies measured at the ends of the strips. The energies are still given in ADC channels. The energies are calibrated relative to each other to guarantee that the center of the detector matches a hit position of zero.

`CAL`

On the *cal* level the energy calibration is finished and all values are converted to energy units of MeV. For this level a gain is determined that matches the measured energy value in ADC channels to the expected value in MeV.

`HIT`

On the last level, *hit*, the variables u and v give the hit position in detector specific coordinates, *i.e.*, the total range of the position varies between -1 arb.u. and 1 arb.u.. The hit position is also available

in x and y coordinates corresponding to the real hit position in cm. The energies of both ends of the strip are added up to the total energy of the hit.

After the beam time in 2019, the PSP class in `R3BRoot` was rewritten by M. Holl. The structure of the individual data levels *mapped*, *precal*, *cal*, and *hit* remained but detector number is not a variable anymore. This means, in the new class the detectors are listed individually and not summarized in one variable. Additionally, the signals from front and back side are available separately, *i.e.*, each detector has the data levels for both sides listed. The reconstructed position in detector specific coordinates is available already at *cal* level and the strip number is available on the *mapped* level already. The advantage of the new data structure is that it is easier to look at the data directly from the `root`-file which is very useful during a beam time. One can look at interstrip events and correlations without using an additional script. The calibration processes is the same as for the previous data class.

The calibration is performed with external scripts in which the calibration parameters are determined. In the first calibration step from *mapped* to *precal*, the calibration parameter is a gain factor. The goal of the first step is to match the central hits with the center of the detector. It might be the case that the energies measured at the ends of the strip have slightly different amplification due to effects in the electronics. To correct for this, a gain factor is applied to the energy on one side of the strip. The gain factor is determined using so-called ”interstrip” events. Interstrip events are events that hit the detector between adjacent strips. In this case the deposited energy is shared between the four channels of the two strips next to the interstrip area. The interstrip events are selected by choosing events for which two neighboring strips on one side and one strip on the other side of the detector fired, leading to six channels in total. The center of the detector is determined by selecting the central interstrip area between strip 16 and 17. The peak might have a position slightly off zero that can be corrected by applying a gain factor to the energy measured on one side of the strip. If it is not possible to determine a gain factor for a strip, for example because the beam did not hit this area, the gain factor is set to 1. Additionally, a threshold can be applied to each side of the strip to cut off noise.

The next calibration step converts the data from *precal* to *cal* level. The calibration parameter of this step is again a gain factor for each strip but this time the energy is matched among the strips and not within one strip. Events, in which one strip on the front and one on the back were hit, are selected. The total energy of one strip is calculated using Eq. D.3. The total energy peak of each strip is fitted with a Gaussian function to determine the mean position of the distribution. The gain factor can then be calculated to match the energy distributions among the strips with an arbitrary value or it can be used to already convert the energy from ADC channels to MeV. This step has to be repeated for each isotope and beam energy.

The last calibration step converts hit position into physical units using a slope and an offset parameter. Additional parameters for an energy conversion are available which can be used if the energy was not converted into physical units during the previous step. The calibration parameters of this step are defined for each strip separately as

$$x_{\text{exp}} = \text{offset} + \text{slope} \cdot x_{\text{meas}}. \tag{D.4}$$

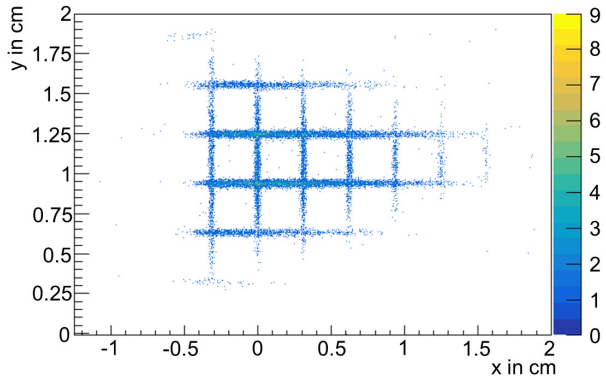

Figure D.3.: Position distribution of interstrip events of an Ar beam. After the calibration, the interstrip grid has a regular shape, meaning the interstrip areas are in line. Each square corresponds to an intersection of a strip on the front and back and has a size of $2.99 \times 2.99\,\mathrm{mm}^2$.

The measured position x_{meas} is given in detector specific coordinates whereas the expected position x_{exp} is given in cm ranging from -5 cm to 5 cm. The calibration parameters are determined using the interstrip areas again. For each strip, the interstrip events of the other side of the detector are selected and fitted with a Gaussian function to determine the mean of each peak, x_{meas}. The distance between the interstrip peaks and thus the expected positions x_{exp} are known from the design of the detector. A linear fit provides the conversion parameters offset and slope. The position distribution of the interstrip events after the calibration is shown in Fig. D.3 for an Ar beam from the tests in 2018, c.f. Sec. D.5.

The energy resolution is determined by selecting events with a multiplicity of 1 on each side, *i.e.*, only one strip was hit per side. From a Gaussian fit, the mean μ and the standard deviation σ are determined. The resolution is then given by $\sigma/\mu \mathrel{\widehat{=}} \Delta E/E$. The position resolution is determined using the interstrip events. The position of a particle hitting an interstrip area is well known, as the interstrip area is very thin. The width (standard deviation) of the interstrip peaks is used as a measure for the position resolution, see data in Sec. D.5.

D.3. Electronic Readout

During the tests and the experiments, the PSP detectors were mounted in a vacuum chamber. The detector has a total of four 34 pin connectors, two for each side, see Fig. D.2b. The signals are guided with a feed-through to the outside of the chamber where they are connected to mesytec preamplifiers of type MPR-32 [Gmb22b]. The energy range of the preamplifiers depends on the energy loss of the particle in the detector, meaning that for different projectiles the preamplifier has to be adjusted. The charge sensitive preamplifier converts the charge collected at the anode into a signal with a height proportional to the deposited energy. The output of the preamplifier is a differential signal which is connected to the Front-End Board with optical link EXtension 3b (FEBEX3b) module. The FEBEX3b is an ADC which was developed by the GSI electronics department [FEB22]. The FEBEX3b module determines the pulse height of the signal which is read out by the DAQ system. As explained

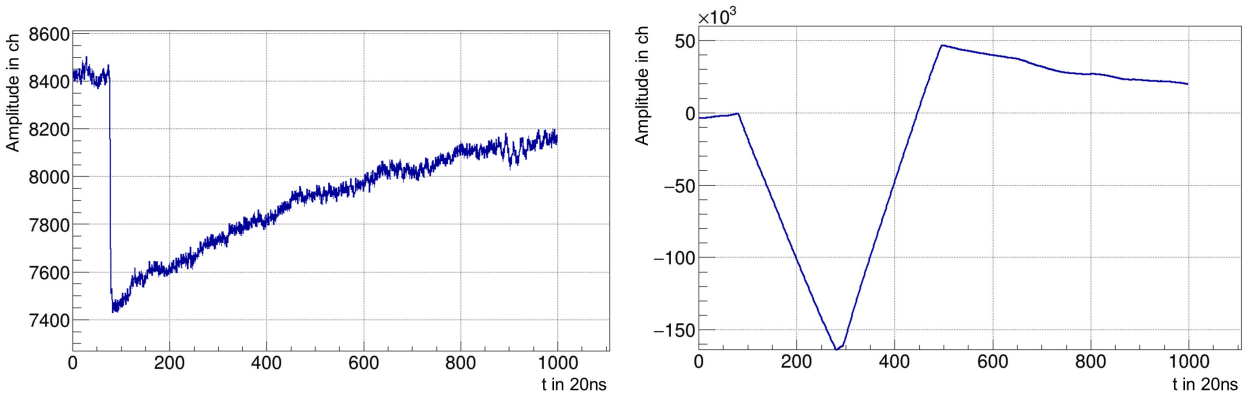

(a) (b)

Figure D.4.: (a) Pulse shape after the preamplifier of the PSP detector from an α-source. The signal has a fast falling edge and a slow decay. (b) FEBEX3b output signal. The filter signal has a trapezoidal shape with a flat top from which the pulse height is determined.

in Sec. D.1, a bias voltage is applied to the detector using a mesytec MHV-4 high voltage module [Gmb22a].

The FEBEX3b uses a moving sum filter to determine the signal height. This filter consists of two time windows of length $w \cdot \Delta t$ for which the signal is integrated, with a gap $g \cdot \Delta t$ in between. The output signal is the difference of the two time windows. The length of the gap g and length of the time window w can be selected in the FEBEX3b settings. The FEBEX3b ADC has a sampling rate of 50 MHz, leading to a time span of $\Delta t = 20$ ns between samples. The signal shape before and after the filter is shown in Fig. D.4. The original pulse has a fast rising edge, or in case of a negative signal a fast falling edge, and a slow decaying edge, as a result of the preamplifier specifications. As the detector is double-sided with an electric field gradient in between and both sides are read out, the signals from one side will be positive and the ones from the other side negative. The filter signal has the shape of a trapeze where the height corresponds to the signal height of the original pulse and the length of the flat top corresponds to the length of the gap g between the windows. The maximum allowed filter length of the FEBEX3b is $2w + g < 1000$. The pulse shape shown in Fig. D.4 was taken during a test with an α-source. As the signal height from an alpha particle is low due to the small energy deposition, the signal-to-noise ratio plays an important role when working with this kind of detector. The fluctuation of the baseline of the filtered signal is resulting from the noise on the original pulse. If the signal becomes too noisy, the top of the trapezoidal filter signal will not be sharp anymore and a precise charge measurement becomes impossible.

D.4. Findings from Previous Tests at KVI-CART

I. Syndikus found in her work [Syn18] that the choice of the window w and the gap g parameter has an influence on the position and energy resolution. A summary of her findings will be presented in the following as they are the starting point of the investigations described in Sec. D.5.

A X5 type detector was tested with a 90 MeV/u ^{12}C beam at KVI-CART in 2018. The expected

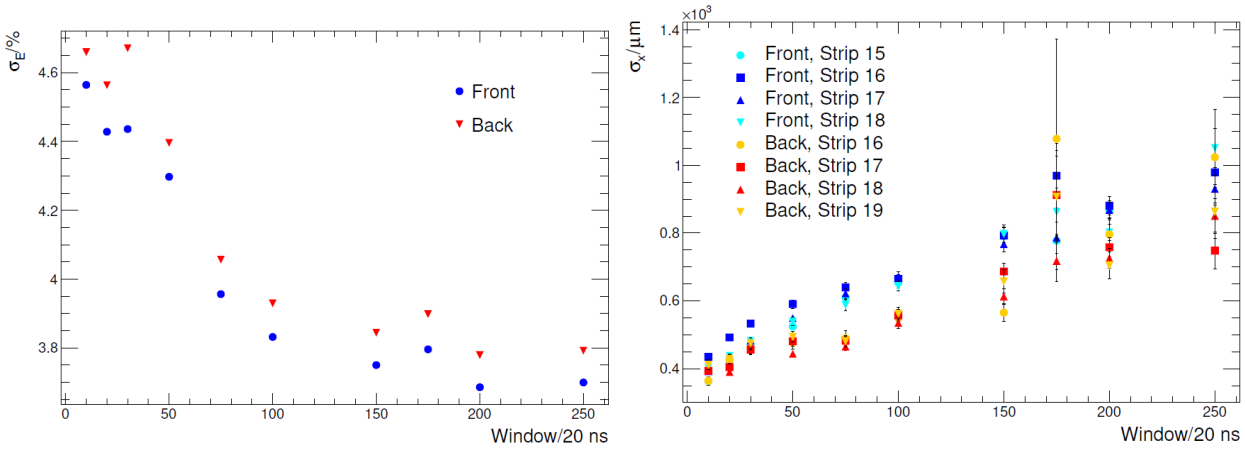

(a) (b)

Figure D.5.: (a) Dependence of the energy resolution on the window length w of the moving sum filter, for a fixed gap parameter $g = 12$. A clear trend is visible where the resolution improves towards long window lengths. (b) Dependence of the position resolution on the window length w with a fixed gap length of $g = 12$. The best position resolution is achieved with the smallest window length of $w = 10$. Both figures are taken from [Syn18]

energy loss in the PSP detector of $\Delta E = (11.63 \pm 0.40)$ MeV during this beam time was determined from simulations which lead to an expected energy resolution of 3.43 %. During the tests, the FEBEX3b parameters w and g were varied with a similar amount of events for each setting. The energy resolution, determined as described in Sec. D.2, is investigated for window lengths w between 10 and 250 with a constant gap of $g = 12$. The results are shown in Fig. D.5a. The resolution improves with an increasing window length. This trend is broken for $w = 175$, for which additional noise from the environment was introduced into the PSP signal. The optimal energy resolution is achieved at $w = 200$. Afterwards, the gap parameter g was varied between 12 and 35 with a fixed window length of $w = 250$. The variation of this parameter did not have a large influence on the energy resolution (see [Syn18]). The same effect was observed for the data from an α-source where the energy resolution is best for a long window length.

The position resolution is determined as described in Sec. D.2 using interstrip events. To investigate the dependence of the resolution on the parameters, the window length w was again varied between 10 and 250 for a fixed gap of $g = 12$, whereas the gap g was varied between 5 and 25 for a window length of $w = 10$. The result for the former is shown in Fig. D.5b. The position resolution is better for smaller window lengths. The best position resolution is achieved for the smallest value tested $w = 10$. For the variation of the gap parameter, a similar behavior was observed which was however not as significant as for the window length. The large uncertainty of the position resolution is an effect of low statistics. Since many different filter settings had to be tested, the duration of the recorded runs were short. For the position resolution, a strong multiplicity cut was necessary in contrast to the energy resolution for which the statistics was not a problem.

Additionally, the difference in resolution between air and vacuum was tested for detector 3126-9. This difference is in the order of the difference in resolution between the two different detectors

tested: No. 3126-9 and No. 3126-7. Therefore, the detector can be operated in both, air and vacuum, and it can be decided based on the availability of a vacuum or light-tight chamber and the needs of surrounding detector systems if vacuum is used. The second detector tested, No. 3126-7, was returned to the manufacturer after the beam time at KVI-CART as some of the bonds between the connector and the strips were broken, and therefore it was not available for the tests described in Sec. D.5.

One reason for the different behavior for the energy and position resolution is the ballistic deficit. Ballistic deficit describes the effect that the signal amplitude can be lost due to too short integration times [Leo94]. In the PSP detector, an additional time constant $\tau_D = R_D \cdot C_D$ is introduced through the resistance of the surface R_D and the capacitance of the depletion area C_D. This means that the rise time of the signal is position dependent, as the active resistance depends on the hit position. For hits close to the edge of a strip, the signal is a step function and becomes less sharp for hit positions further away from the edge, c.f. [Syn18]. In the case of the X5 detector the surface resistance is $R_D \approx 1\,\mathrm{k\Omega}$ and the capacitance of a single strip is $C_D \approx 150\,\mathrm{pF}$, leading to a time constant of $\tau_D \approx 150\,\mathrm{ns}$. It was found that for a position independent position determination an integration time of $t > 0.35\,\tau_\mathrm{D}$, and for the energy determination an integration time of $t > 0.45\,\tau_\mathrm{D}$ is necessary. This leads to a window length of $w > 4$, corresponding to a time of 80 ns with the FEBEX3b module.

However, a stronger effect comes from the decay characteristic of the pulse. To investigate this, the signal shape is recorded for each event. The events are grouped together depending on the perpendicular strip that was hit on the other side, so that hits with similar positions are in the same group. The pulses in these groups are averaged and Eq. D.2 and Eq. D.3 are applied to obtain the shape of the position and energy pulse. The resulting pulse shapes are shown in Fig. D.6 with different colors corresponding to different hit positions within a strip. The energy pulse shape does not show any dependence on the hit position. The energy resolution with a long filter is therefore better, since noise contributions are averaged out with a longer integration time. The position pulse shapes show a clear difference in decay time depending on the hit position. This means that a short integration time is favorable for a precise position determination since a long integration time would influence the result significantly. In conclusion, two different filter settings are necessary for the PSP detectors to measure the position and energy simultaneously with optimal resolutions.

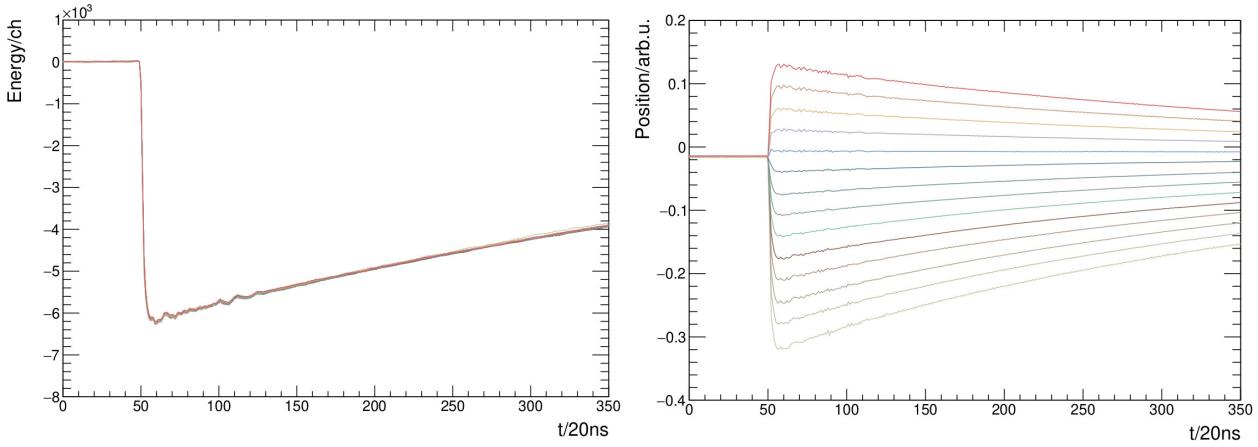

(a) (b)

Figure D.6.: Averaged (a) energy and (b) position pulse shapes. Different hit positions within a strip are shown in different colors. For the energy pulse shape no dependence on the hit position is visible in contrast to the position pulse shapes. Here, the decay time of the falling edge changes with different hit positions. Both figures are taken from [Syn18].

D.5. In-Beam Detector Tests at R^{3}B

The first part of the in-beam detector tests was performed in 2018 with an ^{40}Ar beam at 500 MeV/u and an ^{107}Ag beam at 400 MeV/u. Two X5 detectors were used, No. 3126-9 and No. 2433-20. They were mounted in two different vacuum chambers in front of the target. The first detector in the setup, in front of the first PSP, was the LOS detector. Between the first and the second PSP, the ROLU detector was installed, see Fig. D.1a. The Multi Branch System (MBS) DAQ was running in stand-alone mode, since various FEBEX3b settings were tested and a change of the parameters required a DAQ restart at the time.

The second part of the detector tests was performed in 2019 at the beginning of the R^{3}B experiments s444 and s473 where a ^{12}C beam and a ^{120}Sn beam at different energies were used. One PSP, No. 3126-9, was mounted in front of the target and two additional PSPs, No. 2433-21 and No. 2433-20, were mounted behind the target, see Fig. D.1b. For the tests, the PSP DAQ was running in stand-alone mode, but was integrated into the main DAQ later for the physics runs.

In both setups, the PSP signal was split after the preamplifier. For this, the electronics workshop at TU Darmstadt developed a splitter which is plugged into two FEBEX3b modules in parallel. With this additional component, the signal of each event can be processed twice, making it possible to use a ”position filter” and an ”energy filter”. Splitting the signal to have two filters was necessary, as the standard FEBEX3b module has only one filter implemented. Due to the limited storage of the FEBEX3b Field Programmable Gate Aarray (FPGA), it is not possible to implement and read out a second moving sum filter with this firmware.

The behavior of the position resolution agrees with the results observed during the KVI-CART measurements (see Sec. D.4): short integration times correspond to better position resolutions as shown in Fig. D.7b for Ag and Sn. However, if the integration time is too short, $w = 5$, the position resolution increases. The optimal value was found at $w = 10$ with a gap parameter of $g = 10$. The

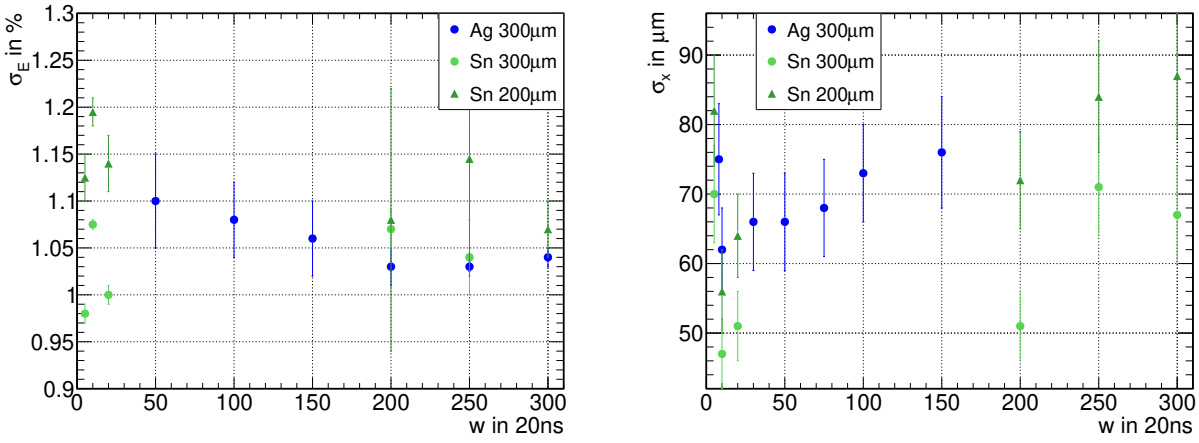

(a) (b)

Figure D.7.: (a) Energy and (b) position resolution for different window lengths w of the FEBEX3b filter. The position resolution is best for small filter length. For the energy resolution no clear trend is visible for the Sn beam. The Ag beam shows a slight trend to longer filters.

energy resolution dependence of the integration time is shown in Fig. D.7a. For the Ag data a slight trend to longer integration times is visible. The Sn data does not show a clear dependence, since also a filter with a small integration time provides a good energy resolution. The reason why a longer filter setting is preferable for the energy determination, was to reduce the influence of noise. The same effect could be observed for the Ar beam, for which the energy resolution did not show a clear trend with changing integration times, whereas an accurate position determination needs a short integration time. The C data was analyzed by M. Holl [Hol19]. The position resolution could not be determined from the data and for the energy resolutions only several long filters could be tested for which no clear difference was visible. The filter settings during the experimental beam time with C were chosen according to the findings in Sec. D.4. The optimal filter settings, determined for the Sn beam, were used in the physics runs performed after the tests. As the energy resolution does not show a significant trend, an integration time of $w = 200$ was chosen for the energy filter. In addition, also the position filter can be used for the energy measurement during the analysis if necessary, since both filters are available in the data.

It can be concluded that for heavy ion beams with $Z \gtrapprox 18$, the energy determination can be performed with short filters with a similar energy resolution as for long filters. This can be attributed to the improved signal-to-noise ratio for heavy beams. As the energy deposition in the detector according to the Bethe-Bloch formula, c.f. Eq. 3.4, and thus the detector signal will be larger, the influence of the noise is less significant. For the same reason, both resolutions are better for the thicker detector with 300 µm. In this case, a compromise between resolution and material budget along the beamline has to be made. For future experiments with heavy ion beams, it is not recommended to split the signal. A short filter provides both a good position and energy resolution at the same time while splitting the signal decreases the signal-to-noise ratio. For light ion beams like C ($Z = 6$), two filters are still necessary for sufficient resolutions. Furthermore, the energy resolution of $\approx 1\,\%$

Table D.2.: Summary of the results of the detector tests during the beam times in 2018 and 2019. Resolutions are given for the back side only or the back (front) side of the detectors. The values for the C beam were determined by M. Holl [Hol19].

Detector	3126-9		2433-21		2433-20	
	σ_E in %	σ_x in µm	σ_E in %	σ_x in µm	σ_E in %	σ_x in µm
Ar	2.5	99	not used		not used	
Ag	problem with leakage current		not used		1.04 (1.09)	53 (70)
C	7.5 (7.5)	-	6.8 (7.3)	-	7.1 (7.1)	-
Sn	1.3 (1.4)	51 (81)	1.05 (1.08)	55 (63)	1.26 (1.24)	48 (69)
α	-		0.8	-	-	

for the Sn data meets the design goal of the X5 detectors [Col14]. A summary of the resolutions determined during the tests is shown in Tab. D.2. It can be seen that the resolution of the front side is generally worse. Therefore, it is recommended to use this side for the less important position measurement, which is usually the y direction. The energy measurement from front and back side is redundant, so the side with the better resolution can be used for the analysis of the physics data. In addition, the resolutions for PSP 3126-9 is worse than the others, as it was already used in many experiments and has suffered from radiation damage. The values given in Tab. D.2 for the Sn beam time were determined at the beginning of the experiment. Towards the end of the experiment, the energy resolution decreased to 1.6 (1.5) % for No. 3126-9.

Measuring light ions, like C, is not ideal with the X5 as the energy deposition is quite small and the noise has a big influence on the signal. A lot of time during the installation of the detector into the setup has to be spend on noise reduction. The detector being connected to the electronics will create an electronic loop that cannot be avoided but captures a lot of noise from surrounding detectors or devices, like the drive of a neighboring detector or the target wheel. The signals from the detector to the feed-through of the vacuum chamber are not yet amplified and the cables are most sensitive to capturing noise. In the current setup a 34 pin flat cable is used. It is recommended that this kind of connection is improved for future experiments. Due to this behavior, is it not possible to measure ions with $Z < 6$.

D.6. Ongoing Activities

In 2021, the s515 beam time was performed which is the continuation of of the experiment s473. It continues the investigation of different cross sections for neutron-rich Sn isotopes. During the preparation for this beam time, it was tested if a different firmware of the FEBEX3b can be used to incorporate two filters at the same time. A new FEBEX3b firmware was developed for the CALIFA detector which implements a moving average filter usable for the X5 signal. In addition, a second process, called Quick Particle IDentification (QPID), is available which could possibly be used as a second filter. T. Wiewesiek investigated the use of the firmware in his Bachelor's thesis [Wie19] with α-source measurements. He found that the filter from the GSI firmware could be reproduced but the QPID is not suitable to be used as a second moving sum filter. As the CALIFA firmware behaved

more stable than the GSI firmware during the tests, it was decided to use the CALIFA firmware for the s515 experiment. The data analysis of this experiment is still ongoing and performed by E. Kudaibergenova.

During the beam times in 2018/19, the leakage current of one of the detectors was not stable. Eventually, this behavior could be attributed to a broken component of one of the preamplifiers. Nevertheless, it will be interesting to investigate the influence of cooling on the behavior of the leakage current and the resolutions. The infrastructure in the vacuum chamber to cool the detector is already available. In addition, cooling of the electronics outside of the chamber can be considered, as the setup might run more stable. A cooling test was already performed in 2014 with the X1 type detector, where the noise level of a setup with and without cooling was compared. During the test with cooling, the preamplifiers were mounted into the vacuum chamber together with the detector. The result was that the cooling power was not sufficient to compensate for the additional heat produced by the electronics inside the chamber. Therefore, the data taken without cooling showed a lower noise level despite the longer connections between the detector and the preamplifiers. More details can be found in [Sto15].

Another goal of future tests is the investigation of the position resolution independent on the interstrip events. Currently, they are used as a measure of the position resolution. To be independent on the interstrip events, a second detector could be used to determine the position resolution. For this, a pixel mask which consists of a plastic sheet with scintillating fibers glued into a certain pattern was produced. This detector will be mounted directly in front of the PSP. The position resolution will be determined from the width of the signal in coincidence with the pixel detector, as the size of the fibers is known. The detector was already build but could not be tested yet.

List of Figures

List of Tables

List of Abbreviations

ADC	Analog-to-Digital Converter
ALADIN	A Large Acceptance DIpole magNet
BDC	Beam Drift Chamber
BigRIPS	RIKEN Projectile Fragment Separator
CALIFA	CALorimeter for In-Flight Gamma-ray and PArticle Detection
CATANA	Caesium Iodide Array for γ-ray Transitions in Atomic Nuclei at high Isospin Asymmetry
CERN	European Organization for Nuclear Research
DAQ	Data AcQuisition
DSAM	Doppler Shift Attenuation Method
ECR	Electron Cyclotron Resonance
FAIR	Facility for Antiproton and Ion Research
FDC	Forward Drift Chamber
FEBEX3b	Front-End Board with optical link EXtension 3b
FPGA	Field Programmable Gate Aarray
FRS	FRagment Separator
GEANT4	GEometry ANd Tracking
GLAD	GSI Large-Acceptance Dipole
GSI	Helmholtzzentrum für Schwerionenforschung
HODF	HODoscope for Fragments
ICB	Ion Chamber for Beam
IRC	Intermediate-stage Ring Cyclotron
KVI-CART	KVI-Center for Advanced Radiation Technology
MBS	Multi Branch System

MoNA Modular Neutron Array

MSU Michigan State University

MWDC Multi-Wire Drift Chamber

NEBULA NEutron Detection System for Breakup of Unstable Nuclei with Large Acceptance

NeuLAND new Large Area Neutron Detector

NSCL National Superconducting Cyclotron Laboratory

PGS PhotoGrammetry System

PID Particle IDentification

PMT PhotoMultiplier Tube

PPAC Parallel Plate Avalanche Counter

PSP Position-Sensitive Pin detector

QDC Charge(Q)-to-Digital Converter

QPID Quick Particle IDentification

R^{3}B Reactions with Relativistic Radioactive Beams

RARF RIKEN Accelerator Research Facility

RIBF Rare Isotope Beam Factory

RIKEN formal japanese name Rikagaku Kenkyūjo, translates in english to Institute of Physical and Chemical Research

RILAC RIKEN Linear Accelerator

RMS Root Mean Square

RRC RIKEN Ring Cyclotron

SAMURAI Superconducting Analyzer for MULti-particles from RAdio Isotope Beams

SBT Scintillators for Beam Time-of-Flight

SOFIA Studies On FIssion with ALADIN

SRC Superconducting Ring Cyclotron

STQ Superconducting Triplet Quadrupole

TDC Time-to-Digital Converter

ToF Time-of-Flight

ucesb unpack & check every single bit

Bibliography

[Acc22] RIKEN Nishina Center for Accelerator-Based Science Homepage: Facilities at the RIBF. accessed: August 2022. URL: https://www.nishina.riken.jp/facility/RIBFfacility_e.html.

[Ago+03] S. Agostinelli et al. "Geant4—a simulation toolkit". In: *Nuclear Instruments and Methods in Physics Research Section A: Accelerators, Spectrometers, Detectors and Associated Equipment* 506.3 (July 2003), pp. 250–303. DOI: 10.1016/s0168-9002(03)01368-8.

[Ahn+19] D. S. Ahn et al. "Location of the Neutron Dripline at Fluorine and Neon". In: *Physical Review Letters* 123.21 (Nov. 2019). DOI: 10.1103/physrevlett.123.212501.

[Al-+12] M Al-Turany et al. "The FairRoot framework". In: *Journal of Physics: Conference Series* 396.2 (Dec. 2012), p. 022001. DOI: 10.1088/1742-6596/396/2/022001.

[Bab+10] H. Baba et al. "New data acquisition system for the RIKEN Radioactive Isotope Beam Factory". In: *Nuclear Instruments and Methods in Physics Research Section A: Accelerators, Spectrometers, Detectors and Associated Equipment* 616.1 (Apr. 2010), pp. 65–68. DOI: https://doi.org/10.1016/j.nima.2010.02.120.

[Ber+04] C. A. Bertulani and P. G. Hansen. "Momentum distributions in stripping reactions of radioactive projectiles at intermediate energies". In: *Physical Review C* 70 (Sept. 2004), p. 034609. DOI: 10.1103/PhysRevC.70.034609.

[Ber+08] D. Bertini et al. "The FAIR simulation and analysis framework". In: *Journal of Physics: Conference Series* 119.3 (July 2008), p. 032011. DOI: 10.1088/1742-6596/119/3/032011.

[Ber+10] C. A. Bertulani and C. De Conti. "Pauli blocking and medium effects in nucleon knock-out reactions". In: *Physical Review C* 81.6 (June 2010), p. 064603. DOI: 10.1103/physrevc.81.064603.

[Ber+19] C. A. Bertulani and J. Valencia. "Neutron skins as laboratory constraints on properties of neutron stars and on what we can learn from heavy ion fragmentation reactions". In: *Physical Review C* 100 (July 2019), p. 015802. DOI: 10.1103/PhysRevC.100.015802.

[Ber+21] C. A. Bertulani and P. Danielewicz. *Introduction to Nuclear Reactions*. 2nd ed. Graduate student series in physics. CRC Press, 2021.

[Ber+92] C. A. Bertulani and K. W. McVoy. "Momentum distributions in reactions with radioactive beams". In: *Physical Review C* 46.6 (Dec. 1992), pp. 2638–2641. DOI: 10.1103/physrevc.46.2638.

[Ber11] D. Bertini. “R3BRoot, simulation and analysis framework for the R3B experiment at FAIR”. In: *Journal of Physics: Conference Series* 331.3 (Dec. 2011), p. 032036. DOI: 10.1088/1742-6596/331/3/032036.

[Ber21] C. A. Bertulani. *Private Communication*. 2021.

[Bet+08] K. Bethge, G. Walter, and B. Wiedemann. *Kernphysik*. 3rd ed. Springer Berlin Heidelberg, 2008. DOI: 10.1007/978-3-540-74567-9.

[Bev+03] P. R. Bevington and D. K. Robinson. *Data Reduction and Error Analysis for the Physical Sciences*. 3rd ed. New York: McGraw-Hill, 2003.

[Big22] Technical Information of BigRIPS. accessed: August 2022. URL: https://ribf.riken.jp/BigRIPSInfo/.

[Bir51] J. B. Birks, ed. *Scintillations from Organic Crystals: Specific Fluorescence and Relative Response to Different Radiations*. Vol. 64. Proceedings of the Physical Society. Section A. 1951.

[Bor+21] K. Boretzky et al. “NeuLAND: The high-resolution neutron time-of-flight spectrometer for R3B at FAIR”. In: *Nuclear Instruments and Methods in Physics Research Section A: Accelerators, Spectrometers, Detectors and Associated Equipment* 1014 (Oct. 2021), p. 165701. DOI: 10.1016/j.nima.2021.165701.

[Bru+97] R. Brun and F. Rademakers. “ROOT — An object oriented data analysis framework”. In: *Nuclear Instruments and Methods in Physics Research Section A: Accelerators, Spectrometers, Detectors and Associated Equipment* 389.1 (Apr. 1997), pp. 81–86. DOI: https://doi.org/10.1016/S0168-9002(97)00048-X.

[Cae+13a] C. Caesar et al. “Beyond the neutron drip line: The unbound oxygen isotopes ^{25}O and ^{26}O”. In: *Physical Review C* 88 (3 Sept. 2013), p. 034313. DOI: 10.1103/PhysRevC.88.034313.

[Cae+13b] C. Caesar et al. *Measurement of the neutron-decay lifetime of the ^{26}O ground state at the SAMURAI setup at RIBF*. RIBF proposal NP1306-SAMURAI20. 2013.

[Cha23] The Colourful Nuclide Chart. Accessed: January 2023. URL: https://people.physics.anu.edu.au/~ecs103/chart/.

[Col11a] The R^{3}B Collaboration. *Technical Report for the Design, Construction and Commissioning of NeuLAND: The High-Resolution Neutron Time-of-Flight Spectrometer for R^{3}B*. 2011.

[Col11b] The R^{3}B Collaboration. *Technical Report for the Design, Construction and Commissioning of the CALIFA Barrel*. Nov. 2011.

[Col14] The R^{3}B Collaboration. *Technical Report for the Design, Construction and Commisioning of the Tracking Detectors for R^{3}B*. 2014.

[Erl+12] J. Erler et al. “The limits of the nuclear landscape”. In: *Nature* 486.7404 (June 2012), pp. 509–512. DOI: 10.1038/nature11188.

[FEB22] FEBEX3b. GSI electronics department. https://www.gsi.de/work/forschung/experimentelektronik/digitalelektronik/digitalelektronik/module/font_end_module/febex/febex3b, Accessed: November 2022.

[Fuk+13] N. Fukuda et al. “Identification and separation of radioactive isotope beams by the BigRIPS separator at the RIKEN RI Beam Factory”. In: *Nuclear Instruments and Methods in Physics Research Section B: Beam Interactions with Materials and Atoms* 317 (Dec. 2013), pp. 323–332. DOI: http://dx.doi.org/10.1016/j.nimb.2013.08.048.

[Gaš17] I. Gašparić. *Private Communication*. 2017.

[Gio+02] J. Giovinazzo et al. “Two-Proton Radioactivity of ^{45}Fe”. In: *Physical Review Letters* 89.10 (Aug. 2002). DOI: 10.1103/physrevlett.89.102501.

[Gmb22a] mesytec GmbH & Co. KG. *MHV-4*. Accessed: November 2022. URL: http://www.mesytec.com/products/nuclear-physics/MHV-4.html.

[Gmb22b] mesytec GmbH & Co. KG. *MPR-16*. Accessed: November 2022. URL: http://www.mesytec.com/products/nuclear-physics/MPR-16.html.

[Gri+11] L. V. Grigorenko et al. “Two-neutron radioactivity and four-nucleon emission from exotic nuclei”. In: *Physical Review C* 84 (2 Aug. 2011), p. 021303. DOI: 10.1103/PhysRevC.84.021303.

[Gri+13] L. V. Grigorenko, I. G. Mukha, and M. V. Zhukov. “Lifetime and Fragment Correlations for the Two-Neutron Decay of ^{26}O Ground State”. In: *Physical Review Letters* 111 (4 July 2013), p. 042501. DOI: 10.1103/PhysRevLett.111.042501.

[Gri+18] L. V. Grigorenko, J. S. Vaagen, and M. V. Zhukov. “Exploring the manifestation and nature of a dineutron in two-neutron emission using a dynamical dineutron model”. In: *Physical Review C* 97.3 (Mar. 2018). DOI: 10.1103/physrevc.97.034605.

[Gui+90] D. Guillemaud-Mueller et al. “Particle stability of the isotopes ^{26}O and ^{32}Ne in the reaction 44 MeV/nucleon ^{48}Ca+Ta”. In: *Physical Review C* 41.3 (Mar. 1990), pp. 937–941. DOI: 10.1103/physrevc.41.937.

[Hag+16] K. Hagino and H. Sagawa. “Decay dynamics of the unbound ^{25}O and ^{26}O nuclei”. In: *Physical Review C* 93.3 (Mar. 2016). DOI: 10.1103/physrevc.93.034330.

[Hax+49] O. Haxel, J. H. D. Jensen, and H. E. Suess. “On the ”Magic Numbers” in Nuclear Structure”. In: *Physical Review* 75.11 (June 1949), pp. 1766–1766. DOI: 10.1103/physrev.75.1766.2.

[Hof+08] C. R. Hoffman et al. “Determination of theN=16Shell Closure at the Oxygen Drip Line”. In: *Physical Review Letters* 100.15 (Apr. 2008). DOI: 10.1103/physrevlett.100.152502.

[Hof+09] C.R. Hoffman et al. “Evidence for a doubly magic 24O”. In: *Physics Letters B* 672.1 (Feb. 2009), pp. 17–21. DOI: 10.1016/j.physletb.2008.12.066.

[Hol19] M. Holl. *Private Communication*. 2019.

[Iso13] T. Isobe. “ANAROOT: new online/offline framework for RIBF data analysis based on ROOT”. In: *Poster presented at the RIBF Users Meeting 2013*. 2013.

[Joh22] H. T. Johansson. *ucesb - unpack & check every single bit*. Accessed: November 2022. URL: http://fy.chalmers.se/~f96hajo/ucesb/.

[Kah+16] J. Kahlbow et al. “NeuLAND demonstrator at SAMURAI: commissioning and efficiency studies”. In: *RIKEN Accel. Prog. Rep.* 49:17 (2016).

[Kah+17a] J. Kahlbow et al. “Experimental campaign using the NeuLAND demonstrator at SAMURAI”. en. In: *GSI Sci. Rep.* 216:151-155 (2017). DOI: 10.15120/GSI-2017-01856.

[Kah+17b] J. Kahlbow et al. “Neutron radioactivity—Lifetime measurements of neutron-unbound states”. In: *Nuclear Instruments and Methods in Physics Research Section A: Accelerators, Spectrometers, Detectors and Associated Equipment* 866 (Sept. 2017), pp. 265–271. DOI: 10.1016/j.nima.2017.06.002.

[Kah18] J. Kahlbow. *Private Communication*. 2018.

[Kah19] J. Kahlbow. “The low-Z Shore of the Island of Inversion: Invariant-mass Spectroscopy of the heavy Fluorine Isotopes ^{29}F* & ^{30}F at SAMURAI with NeuLAND”. PhD thesis. Technische Universität Darmstadt - D17, 2019.

[Kan+09] R. Kanungo et al. “One-Neutron Removal Measurement Reveals ^{24}O as a New Doubly Magic Nucleus”. In: *Physical Review Letters* 102.15 (Apr. 2009), p. 152501. DOI: 10.1103/physrevlett.102.152501.

[Kno10] Glenn F. Knoll. *Radiation Detection and Measurement*. 4th ed. John Wiley & Sons, Inc. New York, 2010.

[Kob+13] T. Kobayashi et al. “SAMURAI Spectrometer for RI Beam Experiments”. In: *Nuclear Instruments and Methods in Physics Research Section B: Beam Interactions with Materials and Atoms* 317 (Dec. 2013), pp. 294–304. DOI: http://dx.doi.org/10.1016/j.nimb.2013.05.089.

[Koh+13] Z. Kohley et al. “Study of Two-Neutron Radioactivity in the Decay of ^{26}O”. In: *Physical Review Letters* 110.152501 (Apr. 2013). DOI: 10.1103/PhysRevLett.110.152501.

[Kon+15] Y. Kondo et al. *Spectroscopy of unbound oxygen isotopes II*. RIBF proposal NP1312-SAMURAI21, publication in preparation. 2015.

[Kon+16] Y. Kondo et al. “Nucleus ^{26}O: A Barely Unbound System beyond the Drip Line”. In: *Physical Review Letters* 116.10 (Mar. 2016). DOI: 10.1103/PhysRevLett.116.102503.

[Kon17] Y. Kondo. *Private Communication*. 2017.

[Kra88] K. S. Krane. *Introductory Nuclear Physics*. John Wiley & Sons, Inc., 1988.

[Kub03] T. Kubo. “In-flight RI beam separator BigRIPS at RIKEN and elsewhere in Japan”. In: *Nuclear Instruments and Methods in Physics Research Section B: Beam Interactions with Materials and Atoms* 204 (May 2003), pp. 97–113. DOI: 10.1016/s0168-583x(02)01896-7.

[Kum+13] H. Kumagai et al. “Development of Parallel Plate Avalanche Counter (PPAC) for BigRIPS fragment separator”. In: *Nuclear Instruments and Methods in Physics Research Section B: Beam Interactions with Materials and Atoms* 317 (Dec. 2013), pp. 717–727. DOI: http://dx.doi.org/10.1016/j.nimb.2013.08.050.

[Lab22] Brookhaven National Laboratory. *National Nuclear Data Center*. Accessed: December 2022. URL: https://www.nndc.bnl.gov/nudat3/.

[Leh21] C. Lehr. "Low-energy dipole response of the halo nuclei ^{6,8}He". PhD thesis. Technische Universität Darmstadt - D17, 2021.

[Leo94] W. R. Leo. *Techniques for Nuclear and Particle Physics Experiments: A How-to Approach*. Springer Berlin Heidelberg, 1994. DOI: 10.1007/978-3-642-57920-2.

[Ltd15] Micron Semiconductor Ltd. *Design X5, readout across strip length*. Technical drawing number A-4381, provided by manufacturer with the detector purchase. 2015.

[Lun+12] E. Lunderberg et al. "Evidence for the Ground-State Resonance of ^{26}O". In: *Physical Review Letters* 108.14 (Apr. 2012). DOI: 10.1103/physrevlett.108.142503.

[Map22] SAMURAI Magnet Field Maps. *https://ribf.riken.jp/SAMURAI/index.php?Magnet*. Accessed: October 2022.

[Mar+15] J. Martin et al. "Studies on fission with ALADIN". In: *The European Physical Journal A* 51.12 (Dec. 2015). DOI: 10.1140/epja/i2015-15174-0.

[Mar+21] F. M. Marqués and J. Carbonell. "The quest for light multineutron systems". In: *The European Physical Journal A* 57.3 (Mar. 2021). DOI: 10.1140/epja/s10050-021-00417-8.

[May02] T. Mayer-Kuckuk. *Kernphysik*. 7th ed. Vieweg & Teubner Verlag, 2002. DOI: 10.1007/978-3-322-84876-5.

[May49] M. Goeppert Mayer. "On Closed Shells in Nuclei. II". In: *Physical Review* 75.12 (June 1949), pp. 1969–1970. DOI: 10.1103/physrev.75.1969.

[Nak+16] T. Nakamura and Y. Kondo. "Large acceptance spectrometers for invariant mass spectroscopy of exotic nuclei and future developments". In: *Nuclear Instruments and Methods in Physics Research Section B: Beam Interactions with Materials and Atoms* 376 (June 2016), pp. 156–161. DOI: 10.1016/j.nimb.2016.01.003.

[Nol+79] P. J. Nolan and J. F. Sharpey-Schafer. "The measurement of the lifetimes of excited nuclear states". In: *Reports on Progress in Physics* 42.1 (Jan. 1979), pp. 1–86. DOI: 10.1088/0034-4885/42/1/001.

[Obe+21] A. Obertelli and H. Sagawa. *Modern Nuclear Physics*. Springer, 2021.

[Ots+01] T. Otsuka et al. "Magic Numbers in Exotic Nuclei and Spin-Isospin Properties of the NN Interaction". In: *Physical Review Letters* 87.8 (Aug. 2001). DOI: 10.1103/physrevlett.87.082502.

[Ots+10] T. Otsuka et al. "Three-Body Forces and the Limit of Oxygen Isotopes". In: *Physical Review Letters* 105.3 (July 2010), p. 032501. DOI: 10.1103/physrevlett.105.032501.

[Ots+20] T. Otsuka et al. "Evolution of shell structure in exotic nuclei". In: *Reviews of Modern Physics* 92.1 (Mar. 2020). DOI: 10.1103/revmodphys.92.015002.

[Pfü+02] M. Pfützner et al. “First evidence for the two-proton decay of ^{45}Fe”. In: *The European Physical Journal A* 14.3 (July 2002), pp. 279–285. DOI: 10.1140/epja/i2002-10033-9.

[Pfü+12] M. Pfützner et al. “Radioactive decays at limits of nuclear stability”. In: *Reviews of Modern Physics* 84.2 (Apr. 2012), pp. 567–619. DOI: 10.1103/revmodphys.84.567.

[Pfü13] M. Pfützner. “Particle radioactivity of exotic nuclei”. In: *Physica Scripta* T152 (Jan. 2013), p. 014014. DOI: 10.1088/0031-8949/2013/t152/014014.

[Pro22] Geodetic Systems Inc. V-STARS Program. *https://www.geodetic.com/v-stars/*. Accessed: August 2022.

[Red+20] T. Redpath et al. “New segmented target for studies of neutron unbound systems”. In: *Nuclear Instruments and Methods in Physics Research Section A: Accelerators, Spectrometers, Detectors and Associated Equipment* 977 (Oct. 2020). DOI: 10.1016/j.nima.2020.164284.

[Red19] T. Redpath. “Measuring the half-life of ^{26}O”. PhD thesis. Michigan State University, 2019.

[Rut11] E. Rutherford. “LXXIX. The scattering of α and β particles by matter and the structure of the atom”. In: *The London, Edinburgh, and Dublin Philosophical Magazine and Journal of Science* 21.125 (May 1911), pp. 669–688. DOI: 10.1080/14786440508637080.

[Sak+99] H. Sakurai et al. “Evidence for particle stability of ^{31}F and particle instability of ^{25}N and ^{28}O”. In: *Physics Letters B* 448.3-4 (Feb. 1999), pp. 180–184. DOI: 10.1016/s0370-2693(99)00015-5.

[SAM22] SAMURAIsimulator. *http://be.nucl.ap.titech.ac.jp/~nebula/simulator.php*. Accessed: October 2022.

[Sch+68] A. Z. Schwarzschild and E. K. Warburton. “The Measurement of Short Nuclear Lifetimes”. In: *Annual Review of Nuclear Science* 18.1 (Dec. 1968), pp. 265–290. DOI: 10.1146/annurev.ns.18.120168.001405.

[Sch15] P. Schrock. “The Electric Dipole Response of ^{132}Sn”. PhD thesis. Technische Universität Darmstadt - D17, 2015.

[Sch17] F. Schindler. “Total reaction, charge-changing, and neutron-removal cross sections of the heavy, neutron-rich nuclei ^{124}Sn, ^{128}Sn, ^{132}Sn, and ^{134}Sn measured with large acceptance at R^{3}B”. PhD thesis. Technische Universität Darmstadt - D17, 2017.

[Shi+11] Y. Shimizu et al. “SAMURAI Project at RIBF”. In: *Journal of Physics: Conference Series* 312.5 (2011), p. 052022. URL: http://stacks.iop.org/1742-6596/312/i=5/a=052022.

[Shi+13] Y. Shimizu et al. “Vacuum system for the SAMURAI spectrometer”. In: *Nuclear Instruments and Methods in Physics Research Section B: Beam Interactions with Materials and Atoms* 317 (Dec. 2013), pp. 739–742. DOI: 10.1016/j.nimb.2013.08.051.

[Sto15] S. Storck. *Analysis of Position Sensitive Silicon Detectors from In-beam Measurements with the R^{3}B Setup*. B.Sc. Thesis. 2015.

[Sto18] S. Storck. “Lifetime Measurement of the ^{26}O ground state at SAMURAI”. MA thesis. Technische Universität Darmstadt, 2018.

[Sua16] M. L. Cortes Sua. “Inelastic Scattering of Ni and Zn Isotopes off a Proton Target”. PhD thesis. Technische Universität Darmstadt - D17, 2016.

[Syn14] I. Syndikus. “Testing of Position Sensitive Silicon Detectors for the R^{3}B-Setup”. MA thesis. Technische Universität Darmstadt, 2014.

[Syn18] I. Syndikus. “Proton-Knockout Reaction from Neutron-Rich N Isotopes at R^{3}B”. PhD thesis. Technische Universität Darmstadt - D17, 2018.

[Tan+85] I. Tanihata et al. “Measurements of Interaction Cross Sections and Nuclear Radii in the Light p-Shell Region”. In: *Physical Review Letters* 55.24 (Dec. 1985), pp. 2676–2679. DOI: 10.1103/physrevlett.55.2676.

[Tar+97] O. Tarasov et al. “Search for ^{28}O and study of neutron-rich nuclei near the N = 20 shell closure”. In: *Physics Letters B* 409.1-4 (Sept. 1997), pp. 64–70. DOI: 10.1016/s0370-2693(97)00901-5.

[Tay72] J. R. Taylor. *Scattering Theory: The Quantum Theory on Nonrelativistic Collisions*. John Wiley & Sons, Inc., 1972.

[Tei+22] E. A. Teixeira et al. “Nuclear fragmentation reactions as a probe of neutron skins in nuclei”. In: *The European Physical Journal A* 58.10 (Oct. 2022). DOI: 10.1140/epja/s10050-022-00849-w.

[Tho+13] M. Thoennessen et al. “Novel techniques to search for neutron radioactivity”. In: *Nuclear Instruments and Methods in Physics Research Section A: Accelerators, Spectrometers, Detectors and Associated Equipment* 729 (Nov. 2013), pp. 207–211. DOI: 10.1016/j.nima.2013.07.035.

[Tho04] M Thoennessen. “Reaching the limits of nuclear stability”. In: *Reports on Progress in Physics* 67.7 (June 2004), pp. 1187–1232. DOI: 10.1088/0034-4885/67/7/r04.

[Wap91] A. H. Wapstra. “Criteria that must be satisfied for the discovery of a new chemical element to be recognized”. In: *Pure and Applied Chemistry* 63.6 (Jan. 1991), pp. 879–886. DOI: 10.1351/pac199163060879.

[Wie19] T. Wiewesiek. *Charakterisierung einer digitalen Ausleseelektronik für segmentierte Siliziumdetektoren*. B.Sc. Thesis. 2019.

[Yan04] Y. Yano. “RI Beam Factory Project at RIKEN”. In: *Proc. 17th Int. Conf. on Cyclotrons and Their Applications, Tokyo, Japan* (2004).

[Zha+19] Z. Y. Zhang et al. “New Isotope ^{220}Np: Probing the Robustness of the $N = 126$ Shell Closure in Neptunium”. In: *Physical Review Letters* 122.19 (May 2019). DOI: 10.1103/physrevlett.122.192503.

Acknowledgement

I would like to thank all the people who supported me during my PhD. First, I want to thank Thomas Aumann for giving me the opportunity to perform this exciting work in his group and to travel to many interesting conferences and experiments, especially my participation in the experiment at RIKEN. I thank Christoph Caesar who made my participation in the S20 experiment possible. Additionally, I want to thank everyone who participated in the beamtime, helped setting up detectors, taking shifts and contributed to a successful experimental campaign.

I appreciate the help of Julian Kahlbow very much to get the analysis started and learn about the SAMURAI detectors. Additionally, I would like to thank Carlos Bertulani who provided the theory input for my work and Valerii Panin for his support to find the best strategy for the simulation. I want to thank Meytal Duer, Dominic Rossi and Christoph Caesar for proofreading my thesis and giving me many valuable comments. Without them the thesis would be much harder to read. A special thank you goes to Dominic Rossi as my mentor who was always available for some fruitful discussions.

I want to thank the whole group, past and present members, for creating an enjoyable working environment. I am very happy I got to know you all and I enjoyed the time at the various social events that we shared. I would like to mention my fellow Samurais Chris, Meytal and Marco who were always available for helpful discussions and funny trips to Japan and Norway; Vadim and Sebastian, for fighting my coding problems with me; Ashton and Andrea who survived the stressful times of GSI experiments with me; Ina who supervised me during my Bachelor and introduced me to the noisy world of PSPs that I inhibited alone for while and was then able to share again with Matthias and Eleonora. A special thanks goes to Ashton who became a very close friend during the past years. I enjoyed our time together when we were able to travel to Italy and Scotland but also when we had to stay at home and could only meet online. I don't want to forget Patrick, Mathy, Nikolina, Philipp, and Fabia for all the fun times during coffee and ice cream breaks but also outside of work during travels, game nights and summer BBQs.

Ich möchte mich bei meiner Familie und meinen Freunden außerhalb der Arbeit bedanken, die mich immer unterstützt haben. Ein besonderer Dank geht an meine Eltern, die das Studium erst möglich gemacht haben und immer an mich geglaubt haben. Ich danke meinen ältesten Freunden Laura, Helen und Deniz für all den Rückhalt und die Ablenkung von der Wissenschaft.

Und zuletzt danke ich Manuel. Danke, dass du dich dafür entschieden hast, Teil meines Lebens zu sein. Ich kann nicht in Worte fassen, was du mir bedeutest.


中性子数
096

Erklärungen laut Promotionsordnung

§8 Abs. 1 lit. c PromO

Ich versichere hiermit, dass die elektronische Version meiner Dissertation mit der schriftlichen Version übereinstimmt.

§8 Abs. 1 lit. d PromO

Ich versichere hiermit, dass zu einem vorherigen Zeitpunkt noch keine Promotion versucht wurde. In diesem Fall sind nähere Angaben über Zeitpunkt, Hochschule, Dissertationsthema und Ergebnis dieses Versuchs mitzuteilen.

§9 Abs. 1 PromO

Ich versichere hiermit, dass die vorliegende Dissertation selbstständig und nur unter Verwendung der angegebenen Quellen verfasst wurde.

§9 Abs. 2 PromO

Die Arbeit hat bisher noch nicht zu Prüfungszwecken gedient.

Darmstadt, 07.02.2023

S. Storck-Dutine